Durham E-Theses

A Hard X-ray View of the Distant Active Galactic Nucleus Population with NuSTAR

LANSBURY, GEORGE,BENJAMIN

How to cite:

Use policy

A Hard X-ray View of the Distant Active Galactic Nucleus Population with NuSTAR

George Benjamin Lansbury

A Thesis presented for the degree of

Doctor of Philosophy

Durham University

Centre for Extragalactic Astronomy
Department of Physics
University of Durham
England

September 2016

A Hard X-ray View of the Distant Active Galactic Nucleus Population with NuSTAR

George Benjamin Lansbury

Abstract

Active galactic nuclei (AGNs), the sites of mass accretion onto supermassive black holes, have been hosted by most galaxies at some point in their lifetime. X-rays are a direct and efficient means of identifying AGNs and measuring their intrinsic properties reliably. A recent breakthrough in this regard is the *Nuclear Spectroscopic Telescope Array* (*NuSTAR*), the first space satellite observatory with the ability to focus high-energy (i.e., "hard"; $\gtrsim 10$ keV) X-ray photons. In this thesis I use *NuSTAR* to study the distant hard X-ray emitting AGN population, with a view to improving the cosmic census of AGNs as well as understanding their demography and evolution. In addition to these broad goals, a more specific focus is to identify elusive Compton-thick (CT) AGNs, which may represent an important phase of hidden black hole growth. Two overall approaches are taken: (1) optically selected Type 2 quasars suspected to be CT (i.e., candidate CTQSO2s) are deliberately targetted with *NuSTAR*; and (2) a large and unbiased serendipitous survey of ≈ 500 X-ray sources is performed using almost all of the science data taken with the *NuSTAR* observatory over a 40-month period. For both of these complementary samples, the broad-band X-ray and multiwavelength properties are studied. For the candidate CTQSO2s, the addition of $\gtrsim 10$ keV *NuSTAR* data provides an improvement compared to constraints with *Chandra* and *XMM-Newton* alone (i.e., with the most sensitive observatories at $\lesssim 10$ keV), generally allowing significantly higher column densities (N_{H}) and intrinsic AGN luminosities (L_{X}) to be constrained, and providing strong evidence for CT absorption in some cases. Implications for the N_{H} distribution of Type 2 quasars are discussed. For the *NuSTAR* serendipitous survey, an extensive ground-based followup program has been undertaken, which was crucial to obtain spectroscopic redshifts and classifications for the bulk of the sample. The serendipitous survey AGNs cover a redshift range of $z = 0.002$ to 3.4 (median of $\langle z \rangle = 0.56$) and a hard X-ray luminosity range of $\log(L_{10-40\mathrm{keV}}/\mathrm{erg\ s^{-1}}) \approx 39$ to 46. Singling out the most extreme likely-CT sources in the serendipitous survey gives an insight into the prevalence of such extreme systems within the general AGN population.

Declaration

The work in this thesis is based on research carried out between October 2012 and September 2016 under the supervision of Prof. David M. Alexander, at the Centre for Extragalactic Astronomy, Department of Physics, University of Durham, England. No part of this thesis has been submitted elsewhere for any other degree or qualification. The thesis is all my own work unless referenced to the contrary in the text. Contributions from others to Chapters 3–5 are summarised in Section 1.4.

Acknowledgements

Contents

List of Figures

List of Tables

Chapter 1

Introduction

In this first introductory chapter, I provide the context for the research undertaken in this thesis. The structure is as follows: Section 1.1 provides the historical context for extragalactic astronomy and AGN research; Section 1.2 describes the physical structures and processes in AGNs and how these relate to the observed radiative emission; Section 1.3 describes how telescopic surveys are used to obtain a census on the AGN population, and how best to hunt for elusive highly obscured AGNs; and Section 1.4 provides an overview of the subsequent thesis chapters. The material is presented from the perspective of an (extragalactic) observational astronomer, and is biased towards the phenomena of highest relevance to this thesis.

1.1 Historical context

1.1.1 Extragalactic astronomy

One could argue that the beginning of extragalactic astronomy was in 1750, when an astronomer and garden designer from county Durham, England speculated (in a theological context) that nebulous objects in the sky might be collections of stars beyond our own Milky Way galaxy (Wright 1750). Immanuel Kant would later describe these nebulous objects as "island universes" (Kant 1755). In the same century, around 100 nebulae and star clusters were catalogued by Messier (1781) and others. Although this catalogue included what are now known to be distant galaxies, at the time they were simply "nui-

sance" objects to be avoided in the search for comets. Soon after, William Herschel used his famous telescopes to push the number of catalogued nebulae into the thousands (e.g., Herschel 1786). In hindsight, it is clear that the technological limitations of the times would have made it challenging to realise the fundamental difference between the Galactic (e.g., planetary) nebulae and extragalactic galaxies. Further hints came when the 3rd Earl of Rosse built the "Leviathan of Parsonstown", a 72-inch reflecting telescope which remained the largest in the world for seventy years. The resulting drawings clearly reveal spiral structure and distinct point sources of light (now known to be stellar associations) within some nebulae (e.g., Rosse 1850). Spectroscopic observations provided further evidence that these spiral nebulae were stellar systems, unlike the gaseous planetary nebulae (e.g., Huggins & Miller 1864; Scheiner 1899), and that some of the spiral nebulae appeared to be moving at unprecedentedly large (radial) velocities relative to our galaxy (e.g., Slipher 1913, 1915). In the early twentieth century, several independent approaches demonstrated that spiral nebulae like Andromeda (Messier 31 or M31) were ∼hundreds of kiloparsecs distant from our galaxy (e.g., Curtis 1917; Opik 1922). The debate was settled using George Ellery Hale's 100-inch Hooker telescope (then the world's largest) to study Cepheid variable stars, utilising their period-luminosity relation to firmly measure the distance to M31 (e.g., Hubble 1929b). With the advance in telescope engineering, also came the means to begin a classification system for statistical samples of "extragalactic nebulae" (i.e., galaxies; Hubble 1926) and to begin establishing the expanding nature of the Universe (e.g., Hubble 1929a). The field of extragalactic astronomy has continued to be driven by technological advances to this date. We now know the observable Universe hosts a diverse population of $\sim 2 \times 10^{11}$ (i.e., ~ 200 billion) galaxies, and that a significant fraction of these have a rather strange beast residing at the galaxy centre: an extremely bright and energetic, but densely packed, object called an "active galactic nucleus".

1.1.2 A brief history of active galactic nuclei (AGNs)

In 1908, astronomers performing optical spectroscopy of nearby galaxies at the Lick observatory (E. Fath and V. Slipher) noticed that one "spiral nebula" (Messier 77; now more commonly referred to as NGC 1068) had an atypical spectrum, showing multiple strong emission lines (see Figure 1.1). This was one of the earliest identifications of an active
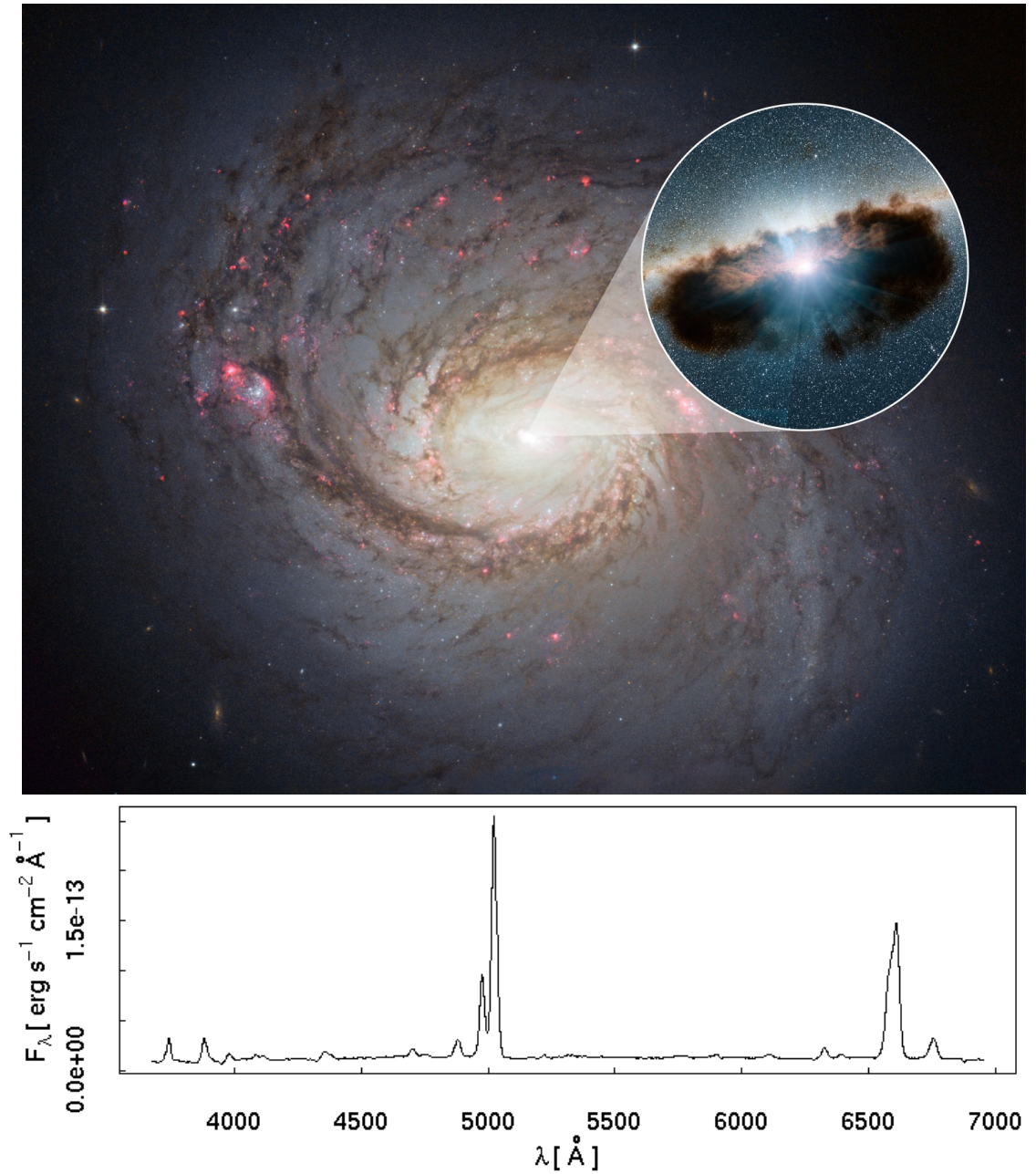
Figure 1.1: Upper image: the nearby galaxy NGC 1068, as seen with the Hubble Space Telescope (HST). The inset shows an artist impression zoom-in on the central active galactic nucleus (AGN). The AGN in NGC 1068 is highly obscured, meaning that gas and dust clouds around the central black hole shield it from our direct view. Image credit: NASA/ESA/JPL-Caltech. Lower graph: optical spectrum of the nuclear region of NGC 1068 (Moustakas & Kennicutt 2006), showing the strong emission lines (e.g., [O III] at 5007Å) which are characteristic of AGNs.

galactic nucleus (a term which was not coined until decades later). Later, Carl Seyfert identified similar high-excitation emission lines in the nuclei of multiple nearby galaxies (Seyfert 1943), and such systems have since become known as "Seyfert galaxies". As time went on, many more Seyfert galaxies were identified, and their observational properties became better constrained. They all exhibited extremely bright nuclear regions, with the bright emission limited to a very compact area (within 100 pc of the galaxy centre). Resolving this bright nuclear emission spectroscopically and temporally, the Seyferts all showed remarkably strong emission lines, and highly time-variable optical–UV continua, respectively. Importantly, it also became clear that within the Seyfert galaxy population, there appeared (observationally) to be two main sub-classes with distinctly different emission line spectra: "Type 1" Seyferts, where the permitted lines (e.g., the Hydrogen Balmer series) are much broader than the forbidden lines (e.g., [O III] and [N II]); and "Type 2" Seyferts, where the permitted lines have the same width as the forbidden lines (Weedman 1970; Khachikian & Weedman 1971). Modern studies estimate that ≈ 5–15% of all galaxies in the local Universe have a Seyfert nucleus (e.g., Maiolino & Rieke 1995).

Meanwhile, radio telescopes pushed forwards an independent line of discovery. The first radio surveys, such as the third Cambridge (3C) catalogue (Edge et al. 1959), identified hundreds of distinct radio sources, some of which could be matched to galaxies, but others of which appeared to be associated with star-like point sources in the optical photographic plate coverage (such as 3C 48 and 3C 273; e.g., Matthews & Sandage 1963). Using George Ellery Hale's 200-inch telescope at Palomar observatory (the world's largest effective optical telescope for a period of 45 years) Maarten Schmidt (1963a) revolutionised the understanding of the latter class of star-like radio sources. Performing spectroscopy for 3C 273, he had the epiphany that bumps in the optical spectrum were in fact emission lines corresponding to the Hydrogen Balmer lines, Mg II, and [O III], except redshifted to longer (i.e., redder) photon wavelengths (the redshift of 3C 273 is $z = \Delta\lambda/\lambda_0 = 0.158$, where $\Delta\lambda$ is the shift in photon wavelength observed for an emission line relative to the laboratory wavelength, λ_0). The implication was that these "quasistellar radio sources" (i.e., "quasars") were not stars, but unprecedentedly distant (many hundreds of megaparsecs) and extraordinarily luminous objects of unknown origin. Since then the number of spectroscopically identified quasars has risen dramatically (now over

$300,000$; e.g., Véron-Cetty & Véron 2010; Pâris et al. 2016), with some being identified as far back as $z \approx 7$ (i.e., when the Universe was only $\sim 5\%$ of its current age; e.g., Mortlock et al. 2011). Another important early discovery from radio astronomy was that some galaxies (e.g., Centaurus A) showed bright non-thermal emission from large-scale jet and lobe structures (e.g., Baade & Minkowski 1954). Despite the vast scales over which these impressive radio structures were extended (e.g., many tens of kpc), their properties suggested an origin at the very centres of the galaxies (e.g., Burbridge 1963; other falsified theories included galaxy collisions).

Today, we understand that the optically discovered Seyferts and the radio-discovered quasars are fundamentally similar, and the main distinction between them is simply that quasars are more powerful (e.g., they can outshine all of the stars in their host galaxies by a factor of $\gtrsim 100$), and consequently more rare, than the Seyferts (which have similar luminosities to their host galaxies; e.g., $\sim 10^{11} \ L_\odot$). Furthermore, the various historic classifications (e.g., Seyfert 1, Seyfert 2, quasar, radio galaxy) and more modern classifications (e.g., Seyfert 1.8,[1] X-ray obscured, X-ray unobscured), may be related by a single unifying physical model (see below and Section 1.2). The astronomy community now commonly use a generic term to bring together all of the different object classes: "active galactic nuclei" (AGNs).

AGNs are a fascinating observational phenomenon, but were initially perplexing and problematic to understand. Many physical theories were readily falsified by the extreme observational characteristics. An initially popular idea, for instance, was that the intense nuclear emission resulted from stellar light. Such a system would need many millions of (normal) stars within the central nucleus of the galaxy to match the observed luminosity (e.g., Woltjer 1959), which alone sounds feasible. However, AGN light varies on day-to-day timescales, by many factors in brightness. The millions of stars would therefore have to be "conspiring" together to vary in the close synchronisation required to achieve

---

[1]For sources which appear to be intermediate between Seyfert 1s and 2s, a more detailed classification scheme has been introduced. The class numbers decrease with the increasing relative strength of the broad (compared to narrow) lines: in Seyfert 1.9s, only Hα shows a broad component; Seyfert 1.8s are like 1.9s but with a weak broad component to Hβ; and Seyfert 1.5s have comparable strengths for the narrow and broad components of Hβ.

such brightness variations. Furthermore, based on light travel time arguments, all of the stars would have to be compressed into a region of space no larger than the solar system. Such a dense arrangement of stars would not be sustainable against gravitational collapse. After much debate on the origin of AGNs, the successful model to emerge was one of mass *accretion* onto a massive and dense object (e.g., Salpeter 1964; see also Hoyle & Fowler 1963 regarding the idea of accretion onto a hypermassive star). It was a potentially elegant solution; for example, Lynden-Bell (1969) demonstrated that a very reasonable mass accretion of just $1\ M_\odot\ \mathrm{yr}^{-1}$ (i.e., one solar mass per year) onto the massive dense object would result in a sufficient radiative release of gravitational energy to explain the high luminosity of Seyfert galaxy nuclei. Such models successfully resolved the apparent tension between the enormous power of AGNs and their small physical scales.

The current consensus is that the massive and dense object in an AGN is a supermassive black hole (SMBH), with a mass of $\sim 10^5$–$10^{10}\ M_\odot$ (i.e., $100,000$ to 10 billion times the mass of our Sun).[2] The concept of such light-trapping objects ("dark stars") were speculated about as early as the eighteenth century (e.g., Michell 1783; Laplace 1796), but thereafter ignored until Schwarzschild's solution to the Einstein field equations (of the general theory of relativity; Einstein 1916) in 1916 highlighted black holes[3] as a mathematical point of interest. The existence of black holes in our Universe has since become increasingly accepted due to their requirement in many astrophysical phenomena, such as AGNs (see above), X-ray binaries in the Milky Way (e.g., Cygnus X1), the collapse of massive stellar cores (e.g., see Oppenheimer & Volkoff 1939 for an early example), and gravitational wave emitting black hole mergers (e.g., Abbott et al. 2016). Today, there is clear evidence that SMBHs reside at the centres of most (if not all) galaxies. Some of the strongest (indirect) evidence comes from dynamical studies at the centres of galaxies, using starlight, line-emitting gas, and water masers; high velocities observed in the relatively small nuclear region suggest an extremely massive and dense central object (e.g., see Kormendy & Richstone 1995 for a review). In the local Universe, we have

---

[2]All of the black holes referred to in this thesis are "supermassive". These are many orders of magnitude more massive than stellar mass black holes (the product of the collapsed cores of massive stars, found scattered throughout the galaxy).

[3]The term "black hole" was not actually used until its popularisation by John Wheeler in 1967.

now robustly identified a central SMBH for ~ 100 galaxies (including our own Milky Way galaxy; e.g., see Kormendy & Ho 2013 for a review). Furthermore, there is a remarkably tight correlation between SMBH masses and the properties of their host galaxy (specifically, with the mass and stellar velocity dispersion of the host galaxy spheroidal component; e.g., Magorrian et al. 1998; Ferrarese & Merritt 2000; Gebhardt et al. 2000; Marconi & Hunt 2003; see Kormendy & Ho 2013 for a review). We understand based on this empirical evidence, as well as theoretical evidence from galaxy formation models (e.g., Bower et al. 2006), that there is an evolutionary connection between SMBHs and star formation, and that all (or most) massive galaxies in the Universe (i.e., many billions of galaxies) are likely to host SMBHs at their centres. Almost any galaxy thus has the potential to appear observationally as an AGN– all that's needed is mass accretion onto the central SMBH.

1.2 The physical structure and radiation of AGNs

In this section I summarise the basic physical properties of AGNs and how they relate to the broad-band radiative emission, in order to provide context for the observational measurements in this thesis. Radio and gamma ray emission (e.g., from relativistic jets) are an important aspect of AGNs. However, given the focal areas of this thesis, this section will not detail these extreme ends of the AGN spectral energy distribution (SED). Rather, I will focus on the infrared–X-ray portion of the AGN SED, and its related phenomena. Figure 1.2 provides a schematic AGN model as a reference point, illustrating the approximate physical layout and scales of the phenomena discussed below.

1.2.1 The accretion disk, X-rays, and other aspects of the standard AGN model

In the standard model of AGNs, cold material from the host galaxy arrives at the sphere of influence of the central SMBH with non-zero angular momentum, and forms an orbiting, optically thick *accretion disk* around the SMBH (at radial scales of $\lesssim 0.01$ pc; see Figure 1.2). This physical system has an unparalleled efficiency for converting matter into radiation. The luminosity (L; i.e., the rate at which radiative energy is emitted, dE/dt) is
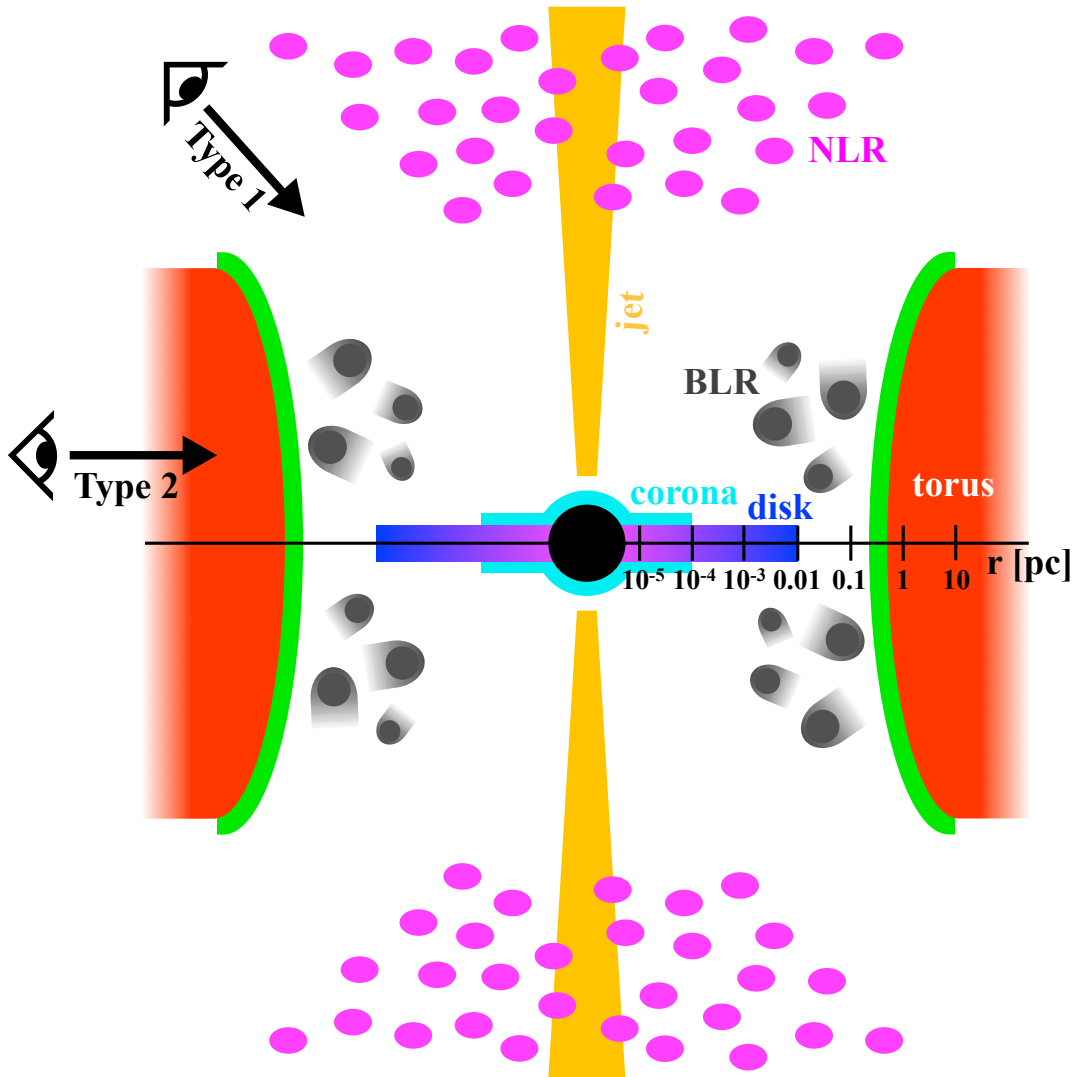
Figure 1.2: Schematic showing an example physical layout for the standard AGN model (Section 1.2.1). The black arrows show how this relates to the unified model of AGNs (Section 1.2.2): distant observers, oriented at different inclination angles with respect to the AGN geometry, will see different observational features (e.g., either Type 1 or Type 2 optical spectra). The horizontal *log-scale* axis gives an idea of the approximate radial physical scales (in parsecs) of the different components. The size scales are approximate, and depend on the black hole mass and accretion rate. The NLR can be extended on ~ 10–10^4 pc scales. The colours of the jet, torus, disk, and corona components match up to those of the corresponding emission curves shown in Figure 1.3.

related to the rate of mass accretion ($\dot{M} = dM/dt$) by the following:

$$L = dE/dt = \epsilon\dot{M}c^2 \tag{1.2.1}$$

where c is the speed of light, and ϵ is a constant which quantifies the efficiency of the mass-to-energy conversion. A typical value for this constant for non-rotating black holes is $\epsilon = 0.1$, which is over 10 times more efficient than the stellar fusion of hydrogen to helium. For instance, a luminosity of $\approx 5 \times 10^{45}$ erg s^{-1} can be achieved for a mass accretion rate of just $1 M_\odot$ yr^{-1}. Even higher efficiencies ($\epsilon \approx 0.4$) may be reached for spinning black holes (e.g., Thorne 1974). The majority of the rest mass (not converted to radiative energy) eventually gets swallowed by the black hole, contributing to its mass growth.

A detailed discussion of the many physical processes important to accretion disks (e.g., gravity, viscosity, hydrodynamics, magnetic fields) is beyond the scope of this thesis introduction. However, the basic essential concept is that as material spirals inwards, frictional forces heat it to high temperatures resulting in the emission of electromagnetic radiation (primarily black-body radiation). The spectral shape of such radiation is dependent on the temperature of the material, with higher temperatures resulting in spectra peaked at lower wavelengths (i.e., higher frequencies/energies). Since the innermost region of the accretion disk is relatively hot (due to increased matter velocities and frictional heating), the dominant wavelength of light is UV ($\lambda \sim 100$–4000Å). At further distances from the black hole (i.e., lower accretion disk temperatures), the photons shift towards the optical band ($\lambda \sim 4000$–9000Å). The overall thermal component of the accretion disk spectrum is therefore a composite of the black-body spectra for all radii, which results in a power-law spectral shape, cut-off in the UV due to the Wien tail of the hottest accretion disk gas.[4] This classic view of accretion disks was established by Pringle & Rees (1972) and Shakura & Sunyaev (1973). The blue dash-dotted line in Figure 1.3 shows the accretion disk at optical–UV wavelengths and how it fits in to the overall spectral energy distribution (SED) of an AGN.

---

[4]We typically cannot observe the UV cut-off due to photoelectric absorption in the ISM of our galaxy, and in the distant host galaxy, creating uncertainty for accretion disk studies and bolometric luminosity estimates (e.g., Collinson et al. 2015).
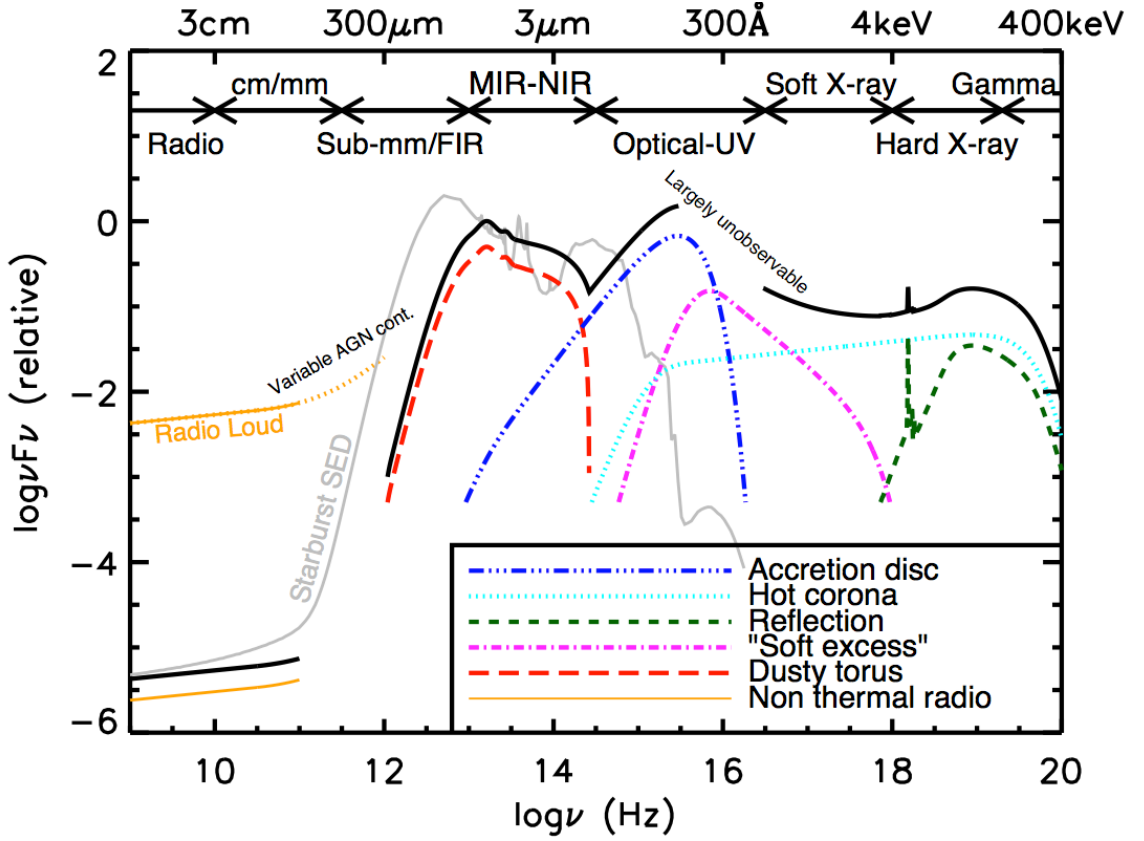
Figure 1.3: Illustration of the spectral energy distribution (SED) of an unobscured AGN. The black curve shows the total SED for a radio-quiet quasar (e.g., Elvis et al. 1994; Richards et al. 2006), and the coloured curves show individual components (see the legend for component descriptions). The primary accretion disk emission peaks at UV wavelengths. Primary emission from the corona dominates at X-ray energies, with a reflected continuum becoming more prominent at higher X-ray energies. Host galaxy star light dominates over the AGN at mm–far-IR wavelengths, for all but the most luminous quasars and powerful radio-loud AGNs. The thicker orange line illustrates the dramatically higher radio flux that can be observed for radio-loud (relative to radio-quiet) AGNs. The background grey curve shows an example radio-UV SED for a star-forming galaxy (M82; Silva et al. 1998). Figure taken from C. M. Harrison (2014) thesis.

An extremely hot ($T \sim 10^9$ K), optically thin "corona" is believed to lie above the AGN accretion disk (e.g., Done et al. 2012). High-energy, relativistic electrons in the corona, bathed in photons from the accretion disk, can boost the photon energies through the process of inverse Compton scattering. This physical scenario was first proposed by Katz (1976) for AGNs, and is supported by variability arguments (e.g., Ghisellini et al. 1993), although certain details of the corona (e.g., its exact location and origin) are still under discussion. The photon energies resulting from the inverse Compton scattering are large, and mostly emerge in the X-ray energy regime ($\sim$ 0.1–300 keV), where the spectrum takes the form of a power law:

$$F_E \propto E^{-\Gamma} \tag{1.2.2}$$

Here, F_E is the photon flux, E is photon energy and Γ is the "photon index". The range of typical photon indices observed, $1.7 < \Gamma < 2.3$ (e.g., Nandra & Pounds 1994; Mateos et al. 2010; Scott et al. 2011), is dictated by the velocity distribution of the coronal electrons. The above power law spectrum is modified by an exponential cutoff at high X-ray energies, due to a drop-off in the coronal electron energy distribution (this "high energy cutoff" lies at $\sim$ 100–300 keV; e.g., Risaliti & Elvis 2004). I will refer to this power-law spectrum, arising from the corona, as the "primary" X-ray continuum. This primary continuum is typically the dominant component of the X-ray emission that we observe (especially for unobscured or lightly obscured AGNs), as illustrated by the cyan dotted line in Figure 1.3. For obscured AGNs where the primary continuum is suppressed toward lower X-ray energies, there is sometimes a soft component detected with a similar photon index as the primary continuum. This is commonly interpreted as emission which has been Thomson-scattered by distant ionised gas (e.g., Krolik & Kriss 1995), but could also result from partial covering (i.e., leaking of photons through the line-of-sight obscuring material). In later chapters I refer to this component as "scattered" AGN continuum (not to be confused with the reflection/Compton-scattered continuum described below).

Another physical process which imprints on the X-ray spectrum of AGNs is "reflection" (e.g., George & Fabian 1991). Reflection refers to the X-ray spectrum produced (and scattered into the observer's line-of-sight) by the photon–matter interactions which occur

when dense, cold[5] gas in the vicinity of the black hole is irradiated by the primary X-ray power law photons (from the corona; see above). Such cold gas can be associated with the accretion disk itself (or possibly the BLR) or with obscuring structures such as the AGN "torus" (see Section 1.2.2). Firstly, the incident X-ray photons may be Compton-scattered by electrons (free and bound), to lower photon energies. Secondly, an incident X-ray photon can interact with an atom through photoelectric absorption, liberating a bound electron. When a higher-shell electron moves down to fill the vacancy, energy is released in the form of either a radiated photon or an Auger electron. The chance of photon radiation is particularly high for the iron K-shell (i.e., the closest shell to the atomic nucleus), due to the combination of iron's high abundance and the iron K-shell's high fluorescence yield (i.e., the relative likelihood of photon, rather than Auger electron, emission is comparatively high). As such, a dominant feature in the reflection spectrum is the Fe Kα emission line at 6.4 keV (fainter Kα lines are also seen for other abundant metals). Another imprint of photoelectric absorption on the reflected continuum is a sharp downturn in flux toward lower X-ray energies (where the photons are less likely to re-emerge from the cold gas). The exact shape of the overall reflection spectrum (Compton-scattering plus fluorescent line emission plus photoelectric absorption), depends on the geometry of the material, the observer's line-of-sight, the ionization level, and the abundances, but the spectrum generally peaks at high energies (~ 30 keV). The decrease in flux at energies higher than the reflection peak results from Compton down-scattering (e.g., Comastri 2004). An example of this X-ray reflection component is shown as a green dashed curve in Figure 1.3.

In the circumnuclear environment, there is strong evidence for a geometrically thick, axisymmetric distribution of dust and gas, located at larger scales than the accretion disk. Since it is optically thick, this dusty material can obscure the primary accretion disk photons from the distant observer (see Section 1.2.2). This same emission heats the dust which thermally radiates (typically at $T \sim 50$–1000 K) at infrared (IR; $\lambda \sim 1$–1000μm) wavelengths, with a spectral shape that peaks in the mid-IR (at $\sim 30\mu$m; e.g., Pier & Krolik 1992; Sanders 1999). An example AGN IR dust spectrum is shown in Figure 1.3 (dashed red line). At the shorter wavelength end of this thermal spectrum, there is a drop-

---

[5]Here, "cold" is a relative term meaning that the metal atoms are almost neutral, but hydrogen and helium are largely ionised.

off in emission due to the sublimation of dust (at ~ 1500 K). At longer wavelengths (in the far-IR and sub-mm wavelength regimes) there is substantial emission from the host galaxy due to cooler dust being heated by star formation (e.g., see the grey background curve in Figure 1.3), and it thus becomes hard or impossible to identify the AGN against the host galaxy light.

Thus far I have primarily dealt with continuum emission in the standard model of AGNs. However, since the earliest observations (e.g., see Section 1.1.2), luminous emission lines have been appreciated as an important and unique aspect of the AGN spectrum. There are two main, physically distinct regions from which the lines arise. The innermost of these is known as the broad line region (BLR), due to the broad ($1000 \lesssim \mathrm{FWHM} \lesssim 10{,}000$ km s^{-1}) permitted lines (e.g., the Balmer series) observed. In this region dense, hot ($T \sim 10^4$ K; e.g., Kallman & Mushotzky 1985) gas clouds, thought to be excited by high energy (UV) accretion disk photons, move at high velocity in the gravitational field of the central SMBH. The characteristic radius of the region (e.g., deduced from broad line variability) ranges from ~ 10 light-days to a few light-years (i.e., ~ 0.01–1 pc), with the upper limit corresponding to luminous quasars. Unlike the NLR (see below) strong forbidden lines are not observed in the BLR due to the high electron densities ($n_{\mathrm{e}} \gtrsim 10^8$ cm^{-3}), which result in the collisional de-excitation of the transitions before radiative de-excitation can occur. The second line-emitting region is extended on larger scales (~ 10–10^4 pc) and is known as the narrow line region (NLR) due to the fact that the permitted (and forbidden) lines produced are narrow ($\mathrm{FWHM} \lesssim 1000$ km s^{-1}). Low density ($n_{\mathrm{e}} \lesssim 10^6$ cm^{-3}), hot ($T \sim 10^4$ K) gas in this extended region is ionized by high energy photons from the inner AGN regions. The geometry of the central obscuring structure (e.g., see Section 1.2.2) means that the ionized NLR gas can be anisotropically distributed (in an "ionization cone", for instance; e.g., see Figure 1.2). Both permitted lines and forbidden lines (e.g., [O III] and [N II]) are strongly radiated from the NLR. The large physical scale of the NLR is supported by the lack of line variability, and observations for low redshift galaxies which actually resolve the NLR. Section 1.2.2 describes how the observational Type 1 and Type 2 classifications[6] can be understood by consider-

---

[6]The historic classifications of "Seyfert 1" and "Seyfert 2" refer specifically to optically identified low-luminosity AGNs. When referring to the general AGN population at any luminosity (e.g., Seyferts or

ing together the properties of the accretion disk, BLR and NLR regions, and the obscuring material in AGNs.

1.2.2 Obscuring material around the central black hole

The unified model

Not all of the features described above (Section 1.2.1) are observed in all AGNs. For instance, many AGNs exhibit Type 1 optical spectra with clear accretion disk emission, while others show Type 2 spectra and no evidence for the accretion disk. As another example, some AGNs have strongly absorbed X-ray spectra, while others appear X-ray unobscured. The simplest picture for understanding this is one where a structure of optically thick material (intrinsically the same for all AGNs) exists on larger scales than the primary light-emitting regions, and contains openings such that the passage of light to a distant observer will be unhindered for some randomly-oriented systems but not others. This idea is known as AGN "unification" (e.g., Antonucci 1993; Urry & Padovani 1995). The most widely applied version of the obscuring structure is a donut-shaped, axisymmetric torus (e.g., see Elitzur 2008 and Netzer 2015 for reviews).

One of the most important early observational evidence for such an obscuring structure came from optical spectropolarimetry of NGC 1068 (Antonucci & Miller 1985), a classic nearby Type 2 AGN (see Section 1.1.2). Scattered light in the nuclear region revealed broad lines, just like those seen ubiquitously for Type 1 AGNs. This suggested that Type 1 and Type 2 AGNs are intrinsically the same, but the broad line region (BLR) of Type 2s is hidden from view. The narrow line region (NLR), on the other hand, is extended on sufficiently large scales that it is seen for both Type 1s and Type 2s. Another important observable was the extended radio emission (jets and lobes) around some AGNs, the geometry and morphologies of which added support to a simple axisymmetric central structure like the torus (e.g., Antonucci 1982). The diversity of radio spectral properties observed also supported a unified model (e.g., Orr & Browne 1982), with BL Lac (and blazar) type objects corresponding to face-on geometries, where the observer's line-

---

quasars, or both), we use the general classifications of "Type 1" and "Type 2" to similarly distinguish between sources with or without broad ($\gtrsim 1000 \, \mathrm{km \, s^{-1}}$) emission lines in their optical spectra, respectively.

of-sight passes directly through the relativistic polar jets.

X-ray observations have been crucial to the development of the unified model, since they provide arguably the most accurate way to measure the line-of-sight column density ($N_{\rm H}$) through gaseous mediums.[7] X-ray photons travelling from the inner regions of the AGN are lost due to photoelectric absorption by intervening gas. The absorption is stronger towards lower X-ray energies, resulting in a sharp cutoff to the power law spectrum (see Figure 1.4). Modelling of the X-ray spectrum therefore allows one to estimate $N_{\rm H}$. This thesis refers to sources with $N_{\rm H} < 10^{22}$ cm^{-2} as "unobscured", since these column densities approach the low values that can be produced as the X-rays pass through our own Galaxy (see the purple and blue lines in Figure 1.4). Sources with $N_{\rm H} \geq 10^{22}$ cm^{-2} are referred to as "obscured" (see the green and yellow lines in Figure 1.4). Very highly obscured systems, with column densities exceeding the inverse of the Thomson scattering cross-section ($N_{\rm H} \gtrsim 1.5 \times 10^{24}$ cm^{-2}), are known as "Compton-thick" (hereafter CT) systems. In these cases, the large majority of the primary X-ray continuum at < 10 keV is absorbed (or scattered), and reflected continuum or fluorescent lines (the process of X-ray reflection is discussed in the above subsection) can start to become prominent (see the orange line in Figure 1.4). At higher column densities still, of $N_{\rm H} > 10^{25}$ cm^{-2} (i.e., for heavily CT systems), all of the primary X-ray photons are absorbed (or down-scattered and absorbed; e.g., Comastri 2004), regardless of energy. However, it is still possible to detect any reflected emission which is indirectly scattered into the line-of-sight (the $\gtrsim 4$ keV portion of the red line in Figure 1.4 is essentially a reflection-only or "pure reflection" spectrum). The fact that X-ray obscured (versus unobscured) classifications *broadly* agree with optical Type 2 (versus Type 1) classifications is evidence that the X-ray absorbing gas is largely coincident (at least in the projected geometry) with optical/UV-extinguishing dust, and thus belongs to a common obscuring structure (e.g., Maiolino & Risaliti 2007). There are of course exceptions to the above, such as strong X-ray absorption in BAL quasars (which are optically unobscured), and warm absorbers associated with ionised, rather than cold, gas (which may absorb UV and

---

[7]$N_{\rm H}$ represents the column density of hydrogen, but we are really measuring the column density of metals, since hydrogen is highly ionised (resulting in a relatively low interaction cross-section compared to the less-ionised metals).
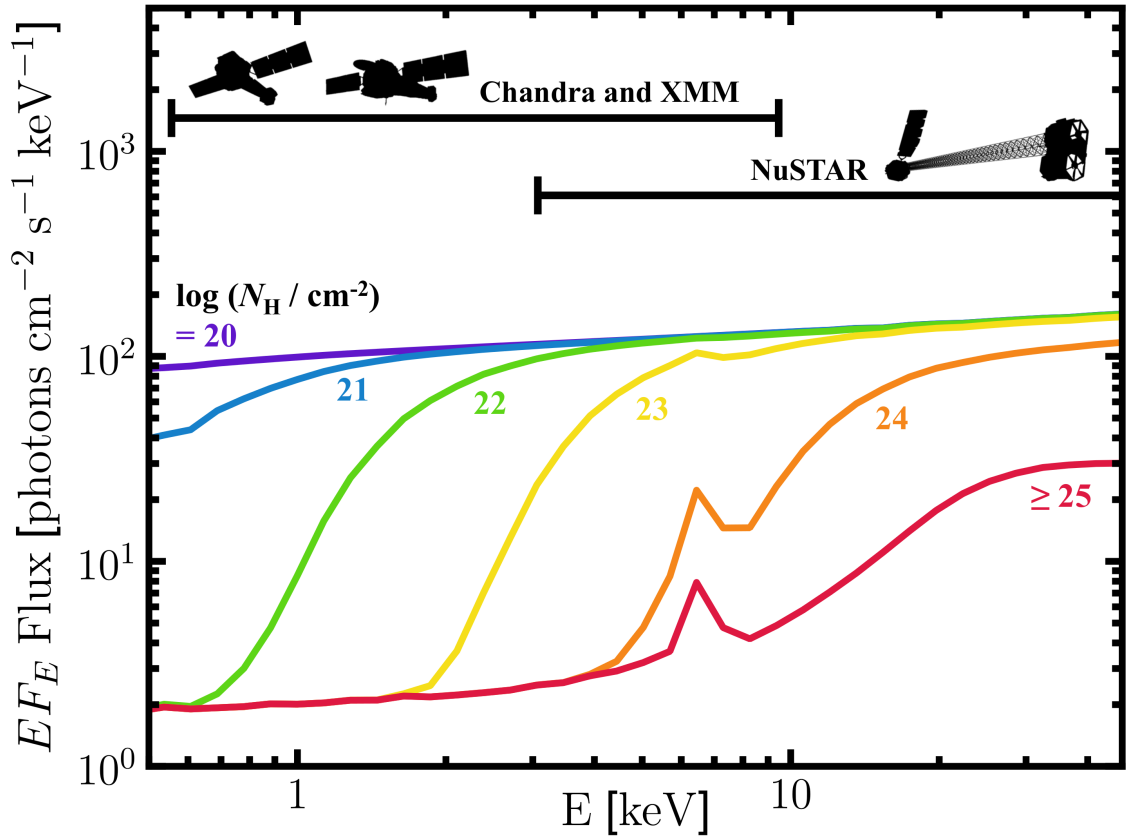
Figure 1.4: An example $\Gamma = 1.9$ AGN X-ray spectrum (flux versus rest-frame energy) for different amounts of absorbing column densities from $N_H = 10^{20}$ cm^{-2} (purple) to 10^{25} cm^{-2} (red). High energy (> 10 keV) observations (e.g., with *NuSTAR*, *Swift* BAT, or *INTEGRAL*) can effectively probe the primary (unabsorbed) X-ray continuum for all but the most heavily absorbed AGNs ($N_H >$ a few $\times 10^{24}$ cm^{-2}), and thus provide one of the "cleanest" ways to identify AGNs, free from complicated selection effects. For highly absorbed "Compton-thick" (CT; $N_H \gtrsim 10^{24}$ cm^{-2}) AGNs, broad-band coverage (including > 10 keV data) is especially important to reliably classify AGNs. The approximate energy ranges for *Chandra*, *XMM-Newton*, and *NuSTAR* (i.e., sensitive focusing X-ray space telescopes) are marked by the black lines. It should be emphasised that this is just one example X-ray spectrum (based on the Brightman & Nandra 2011 toroidal model), and more variety is seen in X-ray spectra across the overall AGN population. For instance, here we have adopted a value of 2% for the soft X-ray scattering fraction (i.e., the relative normalisation of scattered AGN continuum with respect to the primary continuum), hence the residual flux observed below ≈ 4 keV for the CT spectra. Also, different physical geometries (e.g., different covering factors and inclination angles) for the circumnuclear material will result in different relative strengths for the Compton reflection features (i.e., the ≈ 6.4 keV Fe line complex, and the > 10 keV Compton reflection "hump").

X-ray light; e.g., Blustin et al. 2005), but disagreement between optical and X-ray classifications is not greater than the $\approx 30\%$ level (e.g., Panessa & Bassani 2002; Perola et al. 2004; Tozzi et al. 2006; Merloni et al. 2014). Also, for at least some systems, some highly absorbing gas appears to be associated with smaller-scales (e.g., with the BLR) rather than (or in addition to) the obscuring torus (based on variability measurements; e.g., Risaliti et al. 2005, 2007).

X-ray reflection features (observed for obscured AGNs) are important in the context of the unified model, since they imply the existence of extended cold material. A natural assumption is that the reflection material is associated with the obscuring structure itself. This assumption forms the basis of Monte Carlo simulation-based X-ray spectral models designed to explain the X-ray spectra of AGNs in a physically self-consistent manner (e.g., Murphy & Yaqoob 2009; Brightman & Nandra 2011). Considering a uniform toroidal geometry, for instance, if the observer's line-of-sight to the accretion disk region is obstructed by the torus (e.g., resulting in the complete CT suppression of the primary continuum), for certain torus inclination angles reflected X-rays can still reach the observer along an indirect path. For example, primary X-rays may be reflected off the inner edge of the far side (i.e., the backside) of the torus, and into the observers line-of-sight through a lower-density gas column. The fluorescent Fe Kα reflection feature can be very strong for CT AGNs, with an emission line equivalent width of $\mathrm{EW_{FeK\alpha}} \gtrsim 1$ keV (for comparison, reflection off an accretion disk typically results in $\mathrm{EW_{FeK\alpha}} \lesssim 300$ eV). Such high equivalent widths can only be observed for highly obscured systems, otherwise this reflection feature is diluted by the primary X-ray continuum (as is the case for unobscured or moderately obscured AGNs). Detailed studies of the X-ray spectrum for obscured AGNs can potentially place constraints on the geometry of the obscuring structure, since the reflection continuum and Fe line strength are sensitive to the geometry of the reflecting medium (e.g., Awaki et al. 1991; Brightman & Nandra 2011; Baloković et al. in prep.).

A now generally accepted aspect of the torus is that it probably isn't composed of smooth, uniformly distributed gas and dust, but is rather composed of inhomogeneously distributed molecular "clumps" (e.g., Krolik & Begelman 1988; Pier & Krolik 1992; Nenkova et al. 2008a,b). Amongst the observational evidence for clumpy tori (or al-

ternatively an inner clumpy region somewhere between the torus and the BLR) are AGNs which vary in column density (over multiple, and up to multi-month, timescales; e.g., Risaliti et al. 2002; Markowitz et al. 2014). At the present we are moving towards being able to directly image the torus, through high resolution infrared imaging and interferometry. For instance, dust structures on parsec scales have been identified for some nearby AGNs (e.g., Circinus; e.g., Prieto et al. 2004; Burtscher et al. 2013). The infrared luminosity for this parsec-scale torus appears to be a good tracer of the intrinsic AGN power, tightly correlated with the intrinsic X-ray luminosity (e.g., Gandhi et al. 2009; Asmus et al. 2015).

A more complex picture: moving away from the simple unified model

After leaving the central regions of the host galaxy, the AGN emission still has to pass through the galaxy before being detected by the distant observer. The host galaxy itself can therefore imprint absorption features on the observed AGN SED, which need to be disentangled from nuclear absorption. Optical light (e.g., AGN continuum or emission lines like Hα and [O III]) can be easily extinguished by galactic-scale dust (this is increasingly likely for more edge-on galaxy orientations), but X-rays are unlikely to be significantly affected by galactic-scale gas. To demonstrate the latter, the column density along the line-of-sight through Sgr A* (i.e., through the Milky Way centre) is $N_\mathrm{H} \approx 10^{22}$ cm^{-2}, a rough upper limit to the galactic absorption that could occur for an AGN in a Milky Way-like galaxy. This column density is low enough that most X-rays would remain detectable post-absorption (see Figure 1.4). Higher column densities in the CT regime ($N_\mathrm{H} \gtrsim 10^{24}$ cm^{-2}) are unlikely to be produced by gas outside the 10 pc radius (e.g., Risaliti et al. 1999).

There is observational evidence for a decrease in the fraction of obscured AGNs with increasing luminosity, suggesting a modification to the unified model. Similar luminosity dependences have been found using independent approaches: X-ray classifications (e.g., Ueda et al. 2003), optical classifications (e.g., Simpson 2005), and using the dust covering factor as a proxy for the obscured fraction (e.g., Maiolino et al. 2007). To explain these observations, "receding torus" models (e.g., Lawrence 1991) have been invoked. In these models, the inner radius of the dusty torus correlates with the power of the central accret-
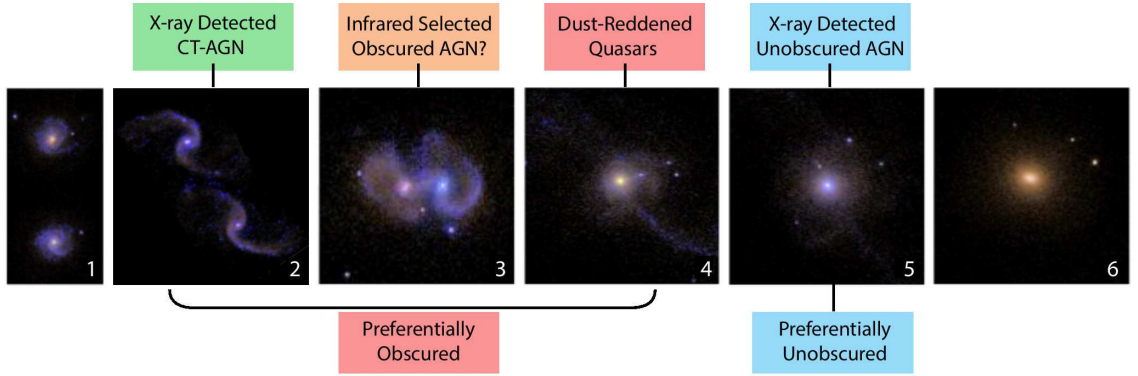
Figure 1.5: A pictorial example of a possible AGN-galaxy co-evolutionary sequence from Kocevski et al. 2015.

ing black hole, since a higher luminosity raises the temperature at a given radius, pushing the dust sublimation radius outwards. The result is a lower covering factor for individual AGNs, and therefore a lower obscured AGN fraction for overall luminous samples. However, there are also observational hints of a reversion back to high obscured fractions for the most powerful quasars in the Universe (e.g., $L_{\rm IR} \gtrsim 10^{13} L_\odot$; e.g., Treister et al. 2010b; Assef et al. 2015). Some studies also find at an increase in the obscured fraction with redshift for luminous AGNs (e.g., Iwasawa et al. 2012; but this is a debated issue), which may be related to an increase in the dust and gas content of the host galaxies.

It is possible, at least in some systems, that the obscuration state of the AGN is related to some evolutionary scenario. As a notable example, Sanders et al. (1988; also, later developed by Hopkins et al. 2008) suggested an evolutionary picture to connect ultraluminous infrared galaxies with luminous optical quasars, where the two represent consecutive phases of an evolutionary sequence (e.g., see Figure 1.5). The former is suggested (based on observational evidence) to result from the major merger of two gas-rich galaxies (stages 1–3 in Figure 1.5), which triggers star formation and drives gas to the central SMBH(s). There is then a dust-enshrouded phase of rapid black hole growth (e.g., Draper & Ballantyne 2010; Treister et al. 2010a), where the quasar is mostly hidden from the observer, followed later by an optical quasar phase (stage 5 in Figure 1.5), once radiation pressure or winds from the AGN have expelled the enshrouding material. A basic observational prediction from the above models is that CT AGNs should have different host galaxy environments (e.g., higher merger fractions) than less obscured AGNs. Ob-

servational evidence for highly obscured AGNs being preferentially associated with the major merger stage of the BH-galaxy evolutionary sequence is scarce. However, some recent studies do find (at a relatively low significance level) that in samples of X-ray selected AGNs, the host galaxies show a higher frequency of galaxy major mergers for CT AGNs (e.g., Kocevski et al. 2015; Koss et al. 2016a). There are similar hints toward such a connection within the distant hard X-ray selected AGN population (see Chapter 6).

1.3 The cosmic census of black hole growth

Identifying AGNs is more than a stamp collecting exercise. Undeniably, individual AGNs are fascinating on their own, each acting as a natural astrophysical laboratory to test the behaviour of matter and light in intense physical conditions. However, on a broader scale, gaining a complete census of the AGN population is the only way to know the extent and the cosmic history of black hole accretion. Below, I briefly describe a particularly relevant, specific motivation for completing the census– the Cosmic X-ray Background (CXB). Section 1.3.1 then provides a description of some of the main survey and identification approaches which can be used to find AGNs, while Section 1.3.2 describes the problems involved in identifying the most highly obscured AGNs, and the techniques that can be used to identify them.

The cosmic X-ray background (CXB)

One of the earliest hints of the need for an AGN census came from the cosmic X-ray background (CXB). This diffuse background was discovered about half a century ago in the first rocket-based astronomical X-ray observations (Giacconi et al. 1962), several years before the cosmic microwave background (CMB) was discovered. Later observations with orbiting X-ray satellite missions (e.g., *HEAO*) found that the CXB above the plane of the Milky Way was uniformly distributed across the sky, implying an extragalactic origin, and spanned a large energy range (primarily $\approx$ 1–500 keV; e.g., Fabian & Barcons 1992). Understanding the origin of this X-ray glow has since been one of the primary goals of high energy astrophysics, and remains a dynamic area of research. Thanks to deep X-ray surveys (with *Chandra* and *XMM-Newton*) we now know the < 10 keV CXB

to be composed of the light from many individual AGNs, and we have resolved a large fraction ($\sim 80\%$) of the CXB at these energies into individual X-ray sources (e.g., Giacconi et al. 2002; Hasinger 2004; Brandt & Hasinger 2005; Worsley et al. 2005; Hickox & Markevitch 2006). However, the CXB peaks at higher energies (≈ 20–$30\,\mathrm{keV}$), for which the technology necessary to resolve a high fraction of the CXB sources has only recently arrived (i.e., with *NuSTAR*; see Chapter 2). Setti & Woltjer (1989) initially suggested that the hard (i.e., rising to high energies) shape of the CXB spectrum could result from the combined emission from a varied population of AGNs, some relatively unobscured (and therefore with "soft" X-ray spectra) and some obscured by material along the line-of-sight (and therefore with "hard" X-ray spectra). Since then, there has been an industry of population synthesis modelling, which aims to explain the shape and normalisation of the CXB (e.g., Comastri et al. 1995; Treister & Urry 2005; Gilli et al. 2007; Treister et al. 2009). A key prediction from these CXB models is that extremely obscured AGNs, largely hidden from us by CT gas column densities along the line-of-sight (see Section 1.2.2 and Figure 1.4), constitute a sizeable fraction of the AGN population. However, the fraction of CT sources in CXB models is well known to be degenerate with the prominence of the X-ray reflection spectral component (e.g., Treister et al. 2009; Akylas et al. 2012). The true abundance of the hidden AGNs therefore needs to be directly constrained by observing and identifying individual CT AGNs, which can be extremely challenging (see Section 1.3.2).

1.3.1   Surveying AGNs

Here I describe the relative merits of the main techniques used in the identification of AGNs. The conclusion that can be drawn from the following subsections is that a truly complete census of cosmic black hole growth requires multiple complementary approaches at different parts of the electromagnetic spectrum (at least given the limitations of current-generation telescopes and instruments). However, if the completeness selection function is known for a given survey then it is possible to correct for missing AGNs.

Optical/UV continuum

Since the optical–UV continuum is produced directly from the accretion disk (see Section 1.2.1), it would (if not for severe observational hinderances; see below) provide the most reliable observational tracer of the accretion power. The typical colours of the optical–UV continua are different for quasars and galaxies, and can thus be used to identify luminous AGNs (e.g., Schmidt & Green 1983; Boyle et al. 1990; Richards et al. 2001). Since there is high quality optical photometric coverage of large swathes of the sky, large quasar samples can be obtained in this manner (there are over 10^6 photometric quasar candidates in the Sloan Digital Sky Survey, for instance; e.g., Richards et al. 2009). Such selections are highly incomplete, however, since extinction (from the circumnuclear environment or the host galaxy; see Section 1.2.2) is strong at these wavelengths and the emission for fainter AGNs is typically diluted by host galaxy starlight.

Optical emission lines

Optical emission lines arise from line-emitting gas under the influence of the intense radiation (for the BLR and NLR) and gravitational (for the BLR) fields of the AGN (see Section 1.2.1). In Type 1 AGNs the presence of an AGN is made clear by the detection of broad emission lines from the BLR. For Type 2 AGNs the narrow emission line spectrum must be distinguished from non-AGN galaxy spectra. This is possible because the photoionizing spectra of AGNs produce different emission line intensity ratios compared to star forming regions. Baldwin et al. (1981) initiated such a classification scheme, now known as the "BPT diagram". In this scheme, AGNs are identified as having high [N II] $\lambda6583$Å / Hα and [O III] $\lambda5007$Å / Hβ ratios ($\gtrsim 0.5$ and $\gtrsim 3$, respectively; the former is sensitive to metallicity and the hardness of the ionizing continuum, and the latter is sensitive to the hardness of the ionizing continuum). Certain forbidden lines require such a hard ionizing continuum (e.g., [Ne V]) that the line detection alone gives strong evidence for an AGN. Using these techniques, or simply identifying luminous or broad (FWHM $\gtrsim 1000$ km s^{-1}) emission lines, optical spectroscopic surveys thus have the power to identify relatively large samples of (primarily unobscured) AGNs, more reliably than photometric selections. A breakthrough project in this vein is the Sloan Digital Sky Survey (York et al. 2000; Abazajian et al. 2009), an enormous ground-based optical

program which has reliably spectroscopically identified many $100,000$s of Type 1 AGNs (e.g., Pâris et al. 2012, 2016) and 1000s of Type 2 AGNs (e.g., Zakamska et al. 2003; Reyes et al. 2008; Heckman & Best 2014).

An advantage of optical line-based techniques for selecting AGNs, relative to those which measure the direct/primary emission (optical/UV continuum, and X-ray observations) is that the bulk of the narrow line (e.g., [O III]) emission originates from material at large scales (see Section 1.2.1), and is therefore relatively unaffected by the circumnuclear obscuring material (see Section 1.2.2). A selection based on the observed (e.g., [O III]) line luminosity should therefore trace the intrinsic black hole power/luminosity, and provide an unbiased AGN selection.

A disadvantage of the targetted nature of spectroscopic surveys is the complicated selection function, which can be difficult to correct for. Also, the observations become especially challenging for $z \gtrsim 1$ if the same emission lines are to be used as for $z < 1$ (e.g., Hα, Hβ, [O III], [N II]), since IR spectrographs (e.g., KMOS; Sharples et al. 2013) must be used, which can be challenging due to Earth's atmosphere, and are currently more limited in their capabilities than optical spectrographs (especially towards longer wavelengths). Furthermore, host-galaxy-related effects result in poorly understood sample completeness; optical emission lines can be attenuated by dust in the host galaxy, and dilution by host galaxy light is common for less luminous AGNs. Regarding the latter point, the high-ionization lines themselves are relatively uncontaminated by line emission in star forming regions, but the AGN lines can still be easily swamped/outshone by the galaxy continuum. As an example, some well-studied galaxies in the local Universe, now known to harbor hidden powerful AGNs at their centres, are classified as starbursts in the optical (e.g., Iwasawa et al. 1993; Armus et al. 2006). Another approach is using longer wavelength emission lines in the infrared (e.g., [Ne V] at 14.3μm) where dust extinction is much less severe, allowing the identification of optically-unidentified AGNs (e.g., Goulding & Alexander 2009), although this is observationally expensive.

Infrared

Infrared (IR) photons arise from circumnuclear dust which has reprocessed the primary AGN emission (see Section 1.2.1). A common approach to identify AGNs in the infrared

is through a photometric colour selection. This method exploits the red power-law shape of the reprocessed continuum to separate AGNs from other astrophysical sources (e.g., Lacy et al. 2004; Mateos et al. 2012; Stern et al. 2012). Very high source yields can be obtained with such colour selections. An impressive example is the *WISE* all-sky survey, which is estimated to have identified several million obscured quasars (e.g., Stern et al. 2012; Assef et al. 2013; Donoso et al. 2014). A significant limitation of photometric IR selections, however, is host galaxy dilution (e.g., Cardamone et al. 2008; Kirkpatrick et al. 2013): contamination from star formation-related IR light means that colour selections become increasingly incomplete toward lower luminosities (especially at $L_{\rm X} \lesssim 10^{44}$ erg s^{-1}; e.g., see Figure 1.3). A more reliable (but more resource-intensive) approach to identify AGNs in the IR, which helps minimise the above dilution problem, is SED modelling of the IR (and neighbouring waveband) photometry. This typically involves using template libraries (e.g., Assef et al. 2008, 2010; Mullaney et al. 2011) to fit the AGN SED, and disentangle AGN emission from star formation (e.g., see Chapters 3 and 4).

Since the reprocessed IR emission is largely isotropic, there should be little to no bias against obscured AGNs. On the other hand, it is difficult to distinguish between unobscured and obscured AGNs based on the IR data alone, so followup observations (e.g., at X-ray energies) are typically required to reliably classify the AGNs. IR surveys nevertheless provide a promising way to even find luminous, deeply buried AGNs (e.g., $N_{\rm H} \gg 10^{24}$ cm^{-2}) which are elusive in X-ray surveys (e.g., Donley et al. 2008, 2012).

Radio

Multiple physical processes are responsible for the radio output of AGNs. In radio-loud AGNs (e.g., $f_{\rm 5GHz}/f_B > 10$; Kellermann et al. 1989), jets and lobes primarily dominate the observed radio emission, whereas for radio-quiet AGNs the observed AGN emission is more confined to the compact nuclear region (where the emission is possibly related to smaller-scale jets or an accretion disk corona; e.g., Laor & Behar 2008). Radio surveys have generated large samples of AGNs (e.g., Edge et al. 1959; Ekers 1969; Laing et al. 1983; Wall & Peacock 1985; Becker et al. 1995; Condon et al. 1998). Due to the orders of magnitude difference in radio flux between the two radio classes (e.g., see Figure 1.3), these surveys are generally highly biased towards detecting radio-loud AGNs, which only

account for $\sim 10\%$ of the overall AGN population. Also, for radio-quiet AGNs, the radio emission can be outshone by recent star formation in the host galaxy. The latter emission is a combination of synchrotron radiation from relativistic electrons and free-free Bremsstrahlung emission from HII regions (e.g., see Figure 1.3; see Condon 1992 for a review). Depending on the origin of the radio emission in radio-quiet AGNs, and the ability to distinguish from star formation (e.g., using very high resolution radio interferometry or the radio–far-IR correlation for starforming galaxies; e.g., Del Moro et al. 2013), radio surveys have the potential to be one of the most reliable ways to select AGNs, unbiased by the effects of obscuration.

X-ray

Like optical/UV continuum light, X-rays are transmitted directly from the immediate environment of the black hole (see Section 1.2.1). The first orbiting X-ray observatories in the early 1970s (e.g., *Uhuru* and *Ariel-V*) detected the first samples of extragalactic X-ray sources, and it quickly became apparent that X-ray emission is likely to be a ubiquitous feature of AGNs (e.g., Giacconi et al. 1974; Elvis et al. 1978). Since then, X-ray surveys have provided fundamental advances in our understanding of AGNs (e.g., see Brandt & Alexander 2015 for a review). Next-generation missions (e.g., *HEAO-1*, *Einstein/HEAO-2*, *EXOSAT*, and *Ginga*) had sufficient energy resolution that the X-ray spectra of AGNs could be characterised in detail (e.g., Reichert et al. 1985; Turner & Pounds 1989; Edge & Stewart 1991; Nandra & Pounds 1994). Current generation high-sensitivity X-ray missions (particularly *Chandra* and *XMM-Newton*, the two most sensitive X-ray observatories at $\lesssim 10$ keV) have pushed the field forwards, providing large samples of distant AGNs (1000s of objects in the deep fields, and $100,000$s for wide-area serendipitous surveys).[8] In the deepest surveys (such as the *Chandra* deep fields, and others; e.g., Brandt et al. 2001; Giacconi et al. 2002; Rosati et al. 2002; Alexander et al. 2003; Xue et al. 2011) *Chandra* and *XMM-Newton* find source densities of AGNs ($\sim 15,000$ deg^{-2}; e.g., Bauer et al. 2004; Lehmer et al. 2012), which exceed the AGN number densities found for the

---

[8]There have been many other X-ray missions, not mentioned here. An important example is *ROSAT*, which surveyed the entire sky at < 2.4 keV, detecting $\sim 100,000$ X-ray sources (e.g., Voges et al. 1999, 2000).

deepest optical surveys by over an order of magnitude (e.g., Treister & Urry 2012). Large serendipitous survey programs performed in the blank-sky background regions of archival X-ray data (e.g., 2XMM and 3XMM; Watson et al. 2001, 2009; Rosen et al. 2016) provide complementary coverage to the deep field surveys, better sampling low–medium redshift sources and rare populations due to the large areal coverage (e.g., $\sim 400 \deg^2$ for 2XMM; Watson et al. 2009) and cosmic volume. In terms of obtaining initial X-ray source identifications and analyses, serendipitous surveys are very economical, requiring zero ks of targetted telescope exposure time. However, the multiwavelength coverage is generally lower quality than for dedicated survey fields, meaning that large followup programs (e.g., optical spectroscopic followup to obtain redshifts) are necessary to realise the potential of the X-ray data.

Since X-ray detectors can distinguish the energies of individual photons (e.g., see Section 2), X-ray data has the additional advantage of providing at least basic spectra for all sources, which can be used to constrain source properties such as the line-of-sight absorption, corrections for which are crucial to accurately constrain the intrinsic AGN power (e.g., see Chapter 4). On the other hand, this absorption means that X-ray surveys (especially with < 10 keV missions such as *Chandra* and *XMM-Newton*) have a selection function which is biased against the detection of obscured AGNs, and are strongly biased against the identification of Compton-thick AGNs (although much less so than the optical/UV; e.g., see Figure 1.4). Surveys with observatories sensitive to higher energy (> 10 keV) X-ray photons can help alleviate this problem, being unbiased against all but the CT systems. Such high-energy surveys have been undertaken with non-focusing X-ray space missions such as *Swift* BAT and *INTEGRAL*, which have surveyed the entire (or close to the entire) sky. However, the objects detected with these non-focusing X-ray missions are primarily limited to the very local Universe ($z < 0.05$), due to their limited flux sensitivity. A recent breakthrough in the high energy regime is *NuSTAR*, the first X-ray space mission capable of focusing > 10 keV X-ray photons. As the primary X-ray observatory used in this thesis, a detailed description of *NuSTAR* is provided in Section 2. Extragalactic surveys with *NuSTAR* during the first four years of the mission have provided the first statistical samples of high energy selected AGNs beyond the nearby universe (e.g., Alexander et al. 2013; Mullaney et al. 2015; Civano et al. 2015;

Aird et al. 2015b; Harrison et al. 2016; Lansbury et al. 2016, submitted; Chapter 5 of this thesis). Furthermore, in the deep field surveys covered by *Chandra* and *XMM-Newton* (e.g., ECDFS and COSMOS), the addition of *NuSTAR* data significantly improves the constraints on the intrinsic properties (e.g., N_H and L_X) of the *NuSTAR*-detected AGNs (e.g., Del Moro et al. 2014; Civano et al. 2015).

Another point to note about the advantage of X-ray surveys with respect to other wavelengths, is the comparatively low dilution of the AGN emission from other light-emitting processes (e.g., star formation). Indeed, there is almost no dilution, down to low AGN luminosities ($L_X \approx 10^{41-42}$ erg s^{-1}; e.g., Ptak et al. 1999; Norman et al. 2004). However, since the galaxy emission is typically comparably soft in the X-ray band, even in the presence of strong star formation, the AGN will often dominate at $\gtrsim 4$ keV. High energy X-ray surveys at $\gtrsim 10$ keV therefore provide one of the cleanest methods to select AGNs.

1.3.2 Completing the census: hidden AGNs and how to find them

One of the main challenges in AGN research is to identify "hidden" AGNs which are obscured by Compton-thick (CT; $N_H \gtrsim 1.5 \times 10^{24}$ cm^{-2}) gas columns. It is important to understand how much CT AGNs contribute to the overall growth of black holes, and to explore whether they are just the most obscured and highly inclined subset of the AGN population or if they represent a rapid SMBH growth phase within the evolution of galaxies (e.g., Figure 1.5). This thesis largely focuses on these issues in the distant Universe probed with *NuSTAR* ($z > 0.1$). However, it should be emphasised that even in the local Universe ($z < 0.1$), where the galaxies are brighter, better-resolved, and generally more amenable to study, we appear to be far from having a complete census on AGNs, especially in the CT regime (e.g., Annuar et al. 2016, submitted).

The cosmological evolution and luminosity functions of CT AGNs are generally poorly known. In the local Universe, a large fraction ($\approx 75\%$) of AGNs are obscured, and many of the obscured AGNs are CT (e.g., $\sim 50\%$ of local Type 2s; e.g., Maiolino & Rieke 1995; Bassani et al. 1999; Risaliti et al. 1999; Burlon et al. 2011). Currently, the majority of the unambiguous identifications of CT AGNs are limited to the local Universe ($z < 0.05$). Here there are ≈ 30–50 or so AGNs which have been classed as "bona fide"

CT systems (e.g., Della Ceca et al. 2008; Burlon et al. 2011; Gandhi et al. 2014; Ricci et al. 2015). Interestingly, two of the three AGNs closest to us are CT (NGC 4945 and Circinus). However, these are mostly low luminosity Seyfert-type systems that, although numerically dominant, only account for a small fraction of the black hole growth. It is instead during rare *luminous obscured quasar* phases that most of the integrated black hole growth is thought to occur (e.g., Fabian 1999; Gilli et al. 2007; Treister et al. 2009). At quasar luminosities (e.g., $L_X > 10^{44}$ erg s^{-1}), our census of highly obscured AGNs appears to be incomplete. In the optical band, the number of robustly spectroscopically identified Type 2 quasars is still in the 1000s (e.g., Zakamska et al. 2003; Reyes et al. 2008), in contrast to the situation for unobscured quasars ($\gtrsim 300,000$; e.g., Pâris et al. 2012, 2016), and at X-ray energies we are only just beginning to robustly identify distant CT quasars (e.g., Comastri et al. 2011; Gilli et al. 2011; Gandhi et al. 2014; Lansbury et al. 2015).

As described above, and illustrated in Figure 1.4, the penetrating hard ($\gtrsim 10$ keV) X-ray bandpass can arguably provide one of the most complete AGN selection approaches, with less bias against highly obscured systems than other approaches (see Section 1.3.1). However, even at high X-ray energies, the flux loss resulting from high absorption (e.g., $\sim 50\%$ of the 15–55 keV flux can be lost for $N_H > 10^{24.5}$ cm^{-2}; Ghisellini et al. 1994) means that there is still a significant bias against CT AGNs. Reflecting this, of the 100s of AGNs identified in the all-sky hard X-ray surveys of *INTEGRAL* and *Swift* BAT, only $\approx 5\%$ are CT (e.g., Burlon et al. 2011), which is low compared to the intrinsic fractions predicted by CXB population synthesis models. The bias increases with distance (i.e., with redshift), due to the limited flux sensitivity, meaning that most of the identified CT AGNs in these surveys are limited to very low redshifts ($z < 0.05$; e.g., Ricci et al. 2015). *NuSTAR*, the first focusing > 10 keV X-ray mission (Harrison et al. 2013), is about two orders of magnitude more sensitive than the aforementioned missions, and is thus able to identify highly obscured AGNs at significantly larger distances (e.g., see Chapters 3–6).

At high redshifts ($z > 1$), the sensitive focusing soft (< 10 keV) X-ray observatories (*Chandra* and *XMM-Newton*) perform relatively well in identifying CT systems, since the features of absorption are redshifted into the observed energy window (e.g., Brightman et al. 2014). At redshifts of $z < 1$, however, hard (> 10 keV) X-ray coverage

is essential to reliably measure high columns ($N_H \gtrsim 5 \times 10^{23}$ cm^{-2}; e.g., see Figure 1.4). For X-ray-bright AGNs, the photon statistics are sufficiently high (i.e., at least a few hundred individual photon counts), over a sufficiently broad energy range (e.g., ≈ 0.5–30 keV), that detailed X-ray spectral modelling can be used to reliably measure N_H, and thus identify CT systems. Modelling approaches allow the photoelectric cutoff, the fluorescent line emission, and any high energy Compton reflection continuum to be modelled together in a self-consistent manner (e.g., Murphy & Yaqoob 2009; Brightman & Nandra 2011). However, for X-ray-faint AGNs (such as many CT AGNs) the photon count-rates are typically very low ($\lesssim 10^{-3}$ counts s^{-1}), meaning that even for nearby AGNs (e.g., $z \approx 0.05$) long exposure times (~ 100 ks) with the most sensitive X-ray telescopes (e.g., *Chandra*, *XMM-Newton*, and *NuSTAR*) can be required to obtain sufficient photon counts for spectral modelling (e.g., see Chapters 4 and 6). In the absence of detailed X-ray spectral modelling, empirical evidence for strong absorption can be obtained from X-ray spectra in two main ways. Firstly, low observed photon indices (e.g., $\Gamma_{\rm eff} \lesssim 0.5$;[9] but this depends on the X-ray energy range and redshift) indicate either a CT transmission-dominated spectrum (with a strong photoelectric absorption cutoff), or a CT reflection-dominated spectrum (e.g., George & Fabian 1991). Secondly, high Fe Kα line equivalent widths ($\rm EW_{FeK\alpha} > 1$ keV) suggest CT line-of-sight columns (e.g., see Section 1.2.2; Maiolino et al. 1998; Comastri 2004). Neither of these identification techniques are complete, however (e.g., a fraction of CT AGNs have $\rm EW_{FeK\alpha} < 1$ keV; e.g., Della Ceca et al. 2008; Gandhi et al. 2016), and neither are likely to accurately constrain N_H on their own.

Since CT AGNs are often only weakly detected or undetected at X-ray energies, the *direct* absorption constraints from the X-ray data (see above) are often uninformative. For this reason, *indirect* estimates of absorption have become common. In these indirect methods, the observed X-ray luminosity is compared to a proxy for the intrinsic AGN power such as high-ionization lines (e.g., [O III] or [Ne V]), or the MIR emission from circumnuclear dust (e.g., see Chapters 3–6). If the observed X-ray luminosity is lower than expected based on the intrinsic power proxy, then absorption is inferred. While the

---

[9]A convenient proxy for $\Gamma_{\rm eff}$, historically employed in X-ray surveys, is the X-ray band ratio. This is simply the ratio of count rates between a hard X-ray band and a soft X-ray band.

uncertainties in such estimates are relatively large, they are a useful way of highlighting extreme outlying sources, and obtaining useful information for X-ray-undetected sources.

1.4   Thesis overview

This thesis uses the *Nuclear Spectroscopic Telescope Array* (*NuSTAR*) observatory to study the distant hard X-ray emitting AGN population. While focused on *NuSTAR*, the work also makes extensive use of new and existing multiwavelength data sets. For instance, an extensive campaign of ground-based optical followup has been performed with multiple observatories to followup *NuSTAR* sources (as described in Chapter 5). The work in this thesis can be separated into two main components: (1) pointed *NuSTAR* observations of SDSS-selected highly obscured, candidate CT Type 2 quasars (CTQSO2s); and (2) the *NuSTAR* serendipitous survey. The former is described in Chapters 3–4, and the latter is described in Chapters 5–6. Specific introductory material is provided at the start of each of the individual science chapters. The chapters can be summarised as follows:

- **Chapter 2 – The Nuclear Spectroscopic Telescope Array (*NuSTAR*)**

  An overview and context for the *NuSTAR* observatory are provided. The instrumental components and scientific performance of the telescope are described, as well as the data processing procedures adopted in this thesis.

- **Chapter 3 – *NuSTAR* observations of heavily obscured quasars at $z \sim 0.5$**

  This chapter presents exploratory *NuSTAR* observations of three Type 2 quasars at $z \approx 0.4$–0.5, optically selected from the Sloan Digital Sky Survey (SDSS). Although the quasars show evidence for being CT systems on the basis of the 2–10 keV to [O III] luminosity ratio and multiwavelength diagnostics, their X-ray absorbing column densities ($N_{\rm H}$) are poorly known. The high energy X-ray coverage of *NuSTAR* is used to better constrain $N_{\rm H}$, and the physical properties of the sources are further characterized through broad-band near-UV to mid-IR spectral energy distribution (SED) analyses. One of the quasars is detected with *NuSTAR* at > 8 keV, and the estimated column density is $N_{\rm H} \gtrsim 5 \times 10^{23}$ cm^{-2}. The other two quasars are undetected, but indirect constraints suggest CT absorption

($N_{\rm H} \gtrsim 10^{24}$ cm^{-2}). The author is responsible for all of the work presented, except the running of the MIR–UV SED modelling algorithm (performed by R. J. Assef). The work in Chapter 3 is published in Lansbury et al. (2014).

- **Chapter 4 – *NuSTAR* reveals extreme absorption in $z < 0.5$ Type 2 quasars**
  Informed by the results of Chapter 3, additional SDSS-selected $z < 0.5$ Type 2 quasars were chosen to be targetted with *NuSTAR*. This chapter reports on the total sample of nine candidate CT Type 2 quasars (CTQSO2s) observed with *NuSTAR*. Overall, five sources are detected by *NuSTAR* at > 8 keV, and three of these have sufficient counts for relatively detailed X-ray spectral modelling. For the detected sources the column densities measured are ≈ 2.5–1600 times higher and the intrinsic (unabsorbed) X-ray luminosities measured are ≈ 10–70 times higher than pre-*NuSTAR* constraints from *Chandra* and *XMM-Newton*. Based on these results, I make a correction to the $N_{\rm H}$ distribution for optically selected type 2 quasars, predicting a CT fraction of $f_{\rm CT} = 36^{+14}_{-12}$ %. The author is responsible for all of the work presented, except for the running of the MIR–UV SED modelling algorithm (performed by R. J. Assef) and the X-ray analysis of SDSS J1034 (performed by P. Gandhi; Gandhi et al. 2014). The source selection was jointly performed by the author and P. Gandhi. The work in Chapter 4 is published in Lansbury et al. (2015).

- **Chapter 5 – The *NuSTAR* serendipitous survey: the 40 month catalogue and the properties of the distant high energy X-ray source population**
  In this chapter I present a catalogue and science results for the *NuSTAR* serendipitous survey. This 40-month catalogue contains 497 sources detected over a total sky area of 13 deg^2. An extensive ground-based followup campaign has been undertaken to obtain new source redshifts and classifications for 222 sources (bringing the total spectroscopically identified sample to 276 sources). The serendipitous survey AGNs cover a large range in redshift ($z = 0.002$ to 3.4) and luminosity [$\log(L_{10-40\rm keV}/\rm erg\,s^{-1}) \approx 39$ to 46]. The X-ray, optical, and infrared source properties are studied. I show that a significant fraction of the *NuSTAR*-selected AGN population would be missed by commonly applied mid-IR AGN selection techniques, even at the highest luminosities ($L_{\rm X} > 10^{44}$ erg s^{-1}). There is tentative

evidence for a higher optically obscured (i.e., Type 2) fraction for hard (> 10 keV) X-ray selected AGNs compared to those selected by < 10 keV X-ray missions. The author is responsible for all of the work presented, from data processing all the way through to interpretation of results, with the following exceptions where others have made notable contributions. Source detection and photometry algorithms were jointly developed by the author and J. Aird; the algorithm adopted for the primary catalogue was written by J. Aird, and that adopted for the secondary catalogue was written by the author. Many ground-based observing runs were undertaken for this chapter (see Section 5.3.3). For all of these runs, the author was involved at some level: as a minimum contribution the author provided the target lists and source information necessary for successful followup by other observers (primarily D. Stern); as a maximum contribution (in the case of the NTT runs), the author was responsible for all aspects of the observing run. In the southern hemisphere, the majority of the spectroscopic followup has been achieved through an NTT program lead by the author (see Section 5.3.3). In the northern hemisphere (i.e., with Keck and Palomar), the spectroscopic followup program was lead by D. Stern (see Section 5.3.3). Due to the nature of ground-based followup programs, many other individuals (including students and research staff) have helped on-location with the execution of observations. With regards to the spectroscopic data processing, the Keck and Palomar data were processed by D. Stern, the NTT data were processed by the author, and the Magellan and Gemini data were processed by C. Fuentes. The author has manually investigated all of the optical spectra resulting from these observing runs (see Section A.2). The work in Chapter 5 has been submitted for publication in ApJ.

- **Chapter 6 – The *NuSTAR* serendipitous survey: hunting for the most extreme sources**

  In this chapter, I identify candidate CT AGNs by searching for extremely hard sources in the *NuSTAR* serendipitous survey (Chapter 5). Ten such extreme *NuSTAR* AGNs are investigated. Based on X-ray spectral analyses (which incorporate data from < 10 keV missions), the large majority of the sources are at least moderately obscured, with line-of-sight column densities ranging from $N_{\mathrm{H}} \approx 10^{23}$ to

$> 10^{24}$ cm^{-2}. Three of the sources are robust CT AGNs at low redshift ($z < 0.1$), and two more higher redshift AGNs are likely CT. The observed CT AGN number counts are compared with model predictions based on previous X-ray missions. A high fraction of the likely-CT *NuSTAR* AGNs are hosted by galaxy major mergers, possibly hinting at a connection between CT phases and the merger stage of galaxy evolution. The author is responsible for all of the work presented. This work is being prepared for journal submission.

- **Chapter 7 – Conclusions and future work**

  An overall summary of the work is provided, and future projects are discussed which have the potential to further the research presented in this thesis.

Chapter 2

The Nuclear Spectroscopic Telescope Array (*NuSTAR*)

This chapter gives context for, and an overview of, the primary observatory which is used in this thesis: the Nuclear Spectroscopic Telescope Array (*NuSTAR*). Firstly I describe the general approach taken by X-ray missions to focus and detect X-rays (Section 2.1). Then Section 2.2 describes the *NuSTAR* observatory, its main instrumental components, and its scientific performance. Finally, I detail the general *NuSTAR* data processing procedures adopted in this thesis (Section 2.3).

2.1   Focusing and counting X-rays

Since X-rays are absorbed by Earth's atmosphere, any observatory hoping to detect cosmic X-rays must be at a very high altitude (above $\approx$ 99–99.9999% of the atmosphere, depending on the X-ray photon energy). The other challenge in obtaining high quality data is that X-ray photons are very difficult to focus; they are readily absorbed by the mirror material used by UV, optical, and infrared telescopes (rather than being reflected). Focusing X-rays is nevertheless possible through the use of special "grazing incidence" mirrors (Figure 2.1). The chance of an X-ray reflection increases for very small incidence angles (i.e., "grazing angles"; typically at the level of $\sim$ 0.1–1°), where the incoming photon is travelling almost parallel to the mirror. The reflection efficiency is generally higher for smaller grazing angles, lower X-ray photon energies, and for higher densities
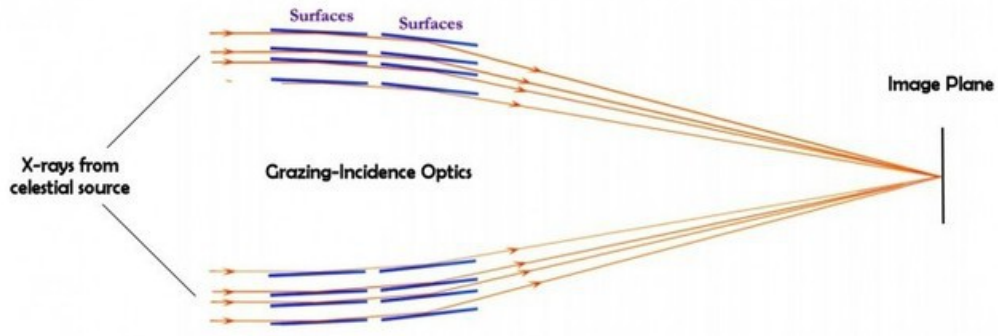
Figure 2.1: Schematic showing the path of X-ray photons from a distant celestial source (e.g., an AGN) through nested grazing-incidence mirrors, and to the focal point in the image plane. In the Wolter Type I design adopted for many X-ray telescopes (e.g., *NuSTAR*), the first and second reflecting surfaces are paraboloid and hyperboloid in shape, respectively. Image credit: *NuSTAR*/Caltech.

of the reflecting material. A paraboloid surface alone will effectively focus X-ray photons to a point, but coma effects (i.e., distortions of the image/point-sources off-axis) are severe. Adding a second reflector in the form of a hyperboloid surface allows an image to be produced at the focal plane, with a usable field of view (e.g., Wolter 1952). A popular version of paraboloid–hyperboloid optics employed in X-ray telescopes is the Wolter Type I design, which also has the practical advantage of a reduced focal length (e.g., ≈ 10m). Since the effective collecting area of a single grazing-incidence mirror is small, the common design approach is to nest multiple shells of grazing-incidence mirrors inside one another, increasing the effective area (e.g., see Figures 2.1 and 2.4).

The first focusing X-ray telescope with full imaging capabilities was *Einstein* (or *HEAO-2*), launched in 1978. *Einstein* used nested shells of Wolter Type 1 mirrors to focus $\lesssim 4$ keV X-ray photons. The same basic design has been adopted for the most sensitive X-ray telescopes in operation today (*Chandra* and *XMM-Newton*), which can focus X-rays up to photon energies of ≈ 10 keV. Focusing even higher energy (> 10 keV) X-rays with a similar telescope design required new technological developments (e.g., in the mirror and detector properties) to allow the higher energy photons to be focused over a sufficiently small focal length. These developments were achieved relatively recently through balloon-borne experiments carrying grazing-incidence optics: the High-Energy Focus-

ing Telescope (HEFT; Harrison et al. 2005), HERO (Ramsey et al. 2002), and InFOCμS (Tueller et al. 2005). The balloon-borne missions set the scene for the first orbiting satellites hosting focusing hard X-ray telescopes: *NuSTAR* (launched in 2012, and likely to continue operation into the 2020s; see Harrison et al. 2013 and Section 2.2 below) and *Hitomi* (launched in February 2016; Takahashi et al. 2012). Technical information for the *NuSTAR* optics is provided in Section 2.2.

A unique aspect of astronomical X-ray data (compared to other wavelengths such as UV, optical, and IR) is that *individual* photons can be counted, have their sky coordinates recorded, have their energies measured, and be temporally constrained. Consequently, a single X-ray observation not only provides spatial imaging for X-ray sources, but also spectroscopic data and variability information. This photon-counting ability is partly thanks to the low background, but also relies on the X-ray detector technology. The detecting instruments used in modern X-ray telescopes are solid state detectors or charge-coupled devices (CCDs). In these instruments, the incident X-ray photon ionises atoms in a detector pixel (or multiple neighbouring pixels), resulting in electron production. The resulting charge (which is proportional to the incident photon energy) is then measured and converted to digital units. In the absence of incident X-ray photons, the pixels have no charge. Section 2.2 gives a more detailed account of how scientific information is drawn from the detector output, for the specific devices installed on *NuSTAR*.

2.2 Description of the NuSTAR X-ray observatory

Launched in June 2012 from a Pegasus (Orbital Sciences) rocket as part of the NASA Small Explorer (SMEX) satellite program, the Nuclear Spectroscopic Telescope Array (*NuSTAR*; Harrison et al. 2013) is the first orbiting X-ray observatory with the ability to focus $\gtrsim 10$ keV photons. This focusing ability results in a two orders of magnitude improvement in sensitivity and over an order of magnitude improvement in angular resolution with respect to previous > 10 keV missions (as illustrated in Figure 2.2, with a comparison to the non-focusing X-ray observatory *Swift* BAT). The observatory is sensitive to photon energies of 3–78.4 keV. Figure 2.3 shows a comparison of the *NuSTAR* effective collecting area (as a function of energy) with other focusing X-ray observatories
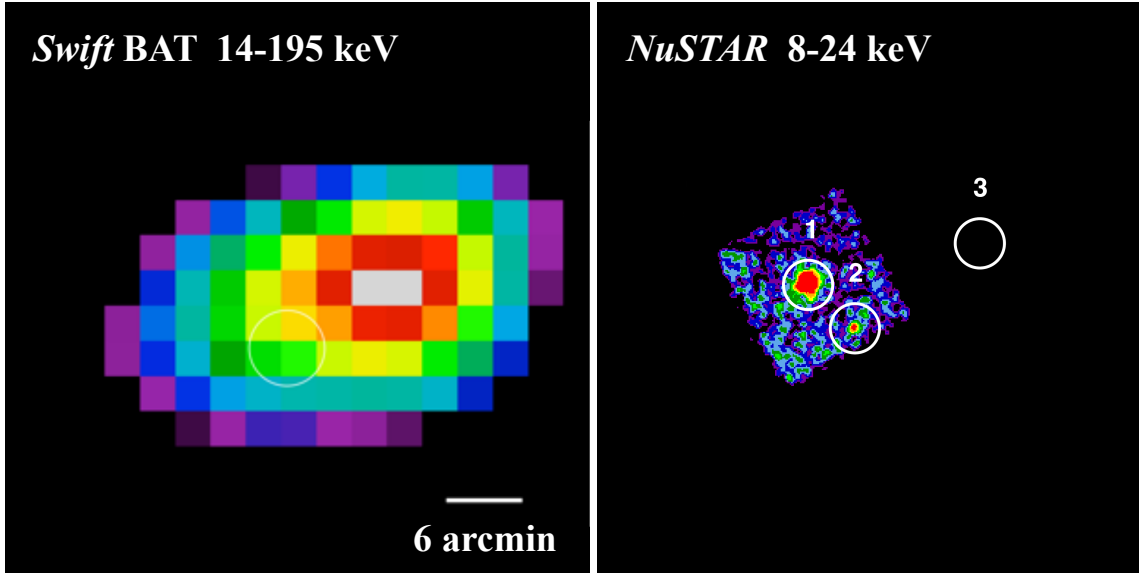
Figure 2.2: Imaging comparison between *Swift* BAT (left; a non-focusing hard X-ray telescope; image provided by M. Koss) and *NuSTAR* (right; a focusing hard X-ray telescope; image from the *NuSTAR* serendipitous survey data set, studied in Chapters 5–6 of this thesis). The images are matched in sky coordinates. *Swift* BAT detects a single "blob", while the high resolution (and high sensitivity) of *NuSTAR* clearly separates this into three distinct point-sources. The faintest source (#2) is NuSTAR J150645+0346.2, a highly obscured nearby CT AGN (in a galaxy major merger) discovered in the *NuSTAR* serendipitous survey, previously unidentified as an X-ray AGN (see Chapter 6). Source #3 is outside the FoV, but known from other observations to be a bright AGN.
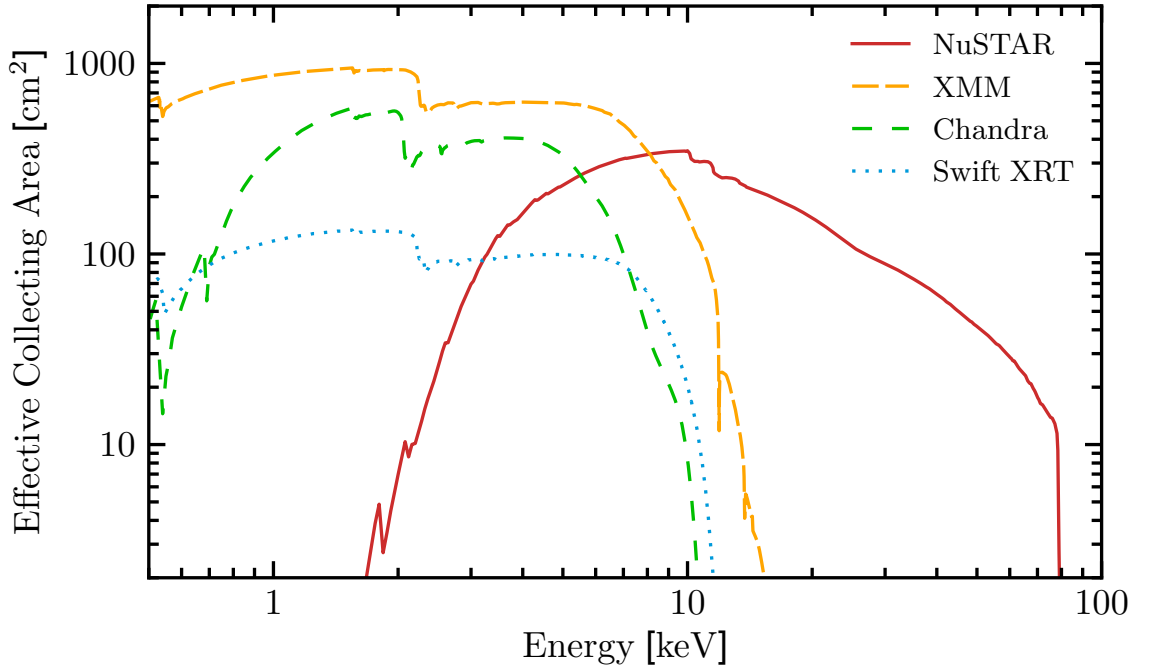
Figure 2.3: Example effective area curves for the focusing X-ray telescopes used in this thesis. For *NuSTAR* (solid red line), the curve represents the response for an individual focal plane module (i.e., FPMA or FPMB individually). The *XMM-Newton* ARF (long-dashed orange line) is for the PN instrument (which is more sensitive than the individual MOS instruments). For *Chandra* (dashed green line), the ARF corresponds to the ACIS (rather than the HRC) instrument, and to the ACIS-S CCD array (as opposed to ACIS-I). The *Swift* XRT spectral response shown (dotted blue line) is for the PC (rather than the WT) mode. *NuSTAR* is the first focusing mission with high sensitivity at > 10 keV.

currently in operation (all of which operate at $\lesssim 10$ keV). Below I describe the *NuSTAR* observatory and its instrumental components (illustrations and photographs of the main components are shown in Figure 2.4).

The 350 kg, 600 W observatory is based on a LeoStar-2 (Orbital Sciences) spacecraft bus, and orbits the Earth once every 97 minutes at an altitude of ≈ 630 km. *NuSTAR* carries two coaligned and independent telescopes ("A" and "B"; identical in design), each with its own focal plane module (FPM; the two individual units are referred to as "FPMA" and "FPMB") and optics module (OM; the two individual units are referred to as "OMA" and "OMB"). Uniquely to *NuSTAR*, a long extendable (carbon-fibre, aluminium, and steel) mast (see Figure 2.4f) was deployed in orbit to separate the optics modules
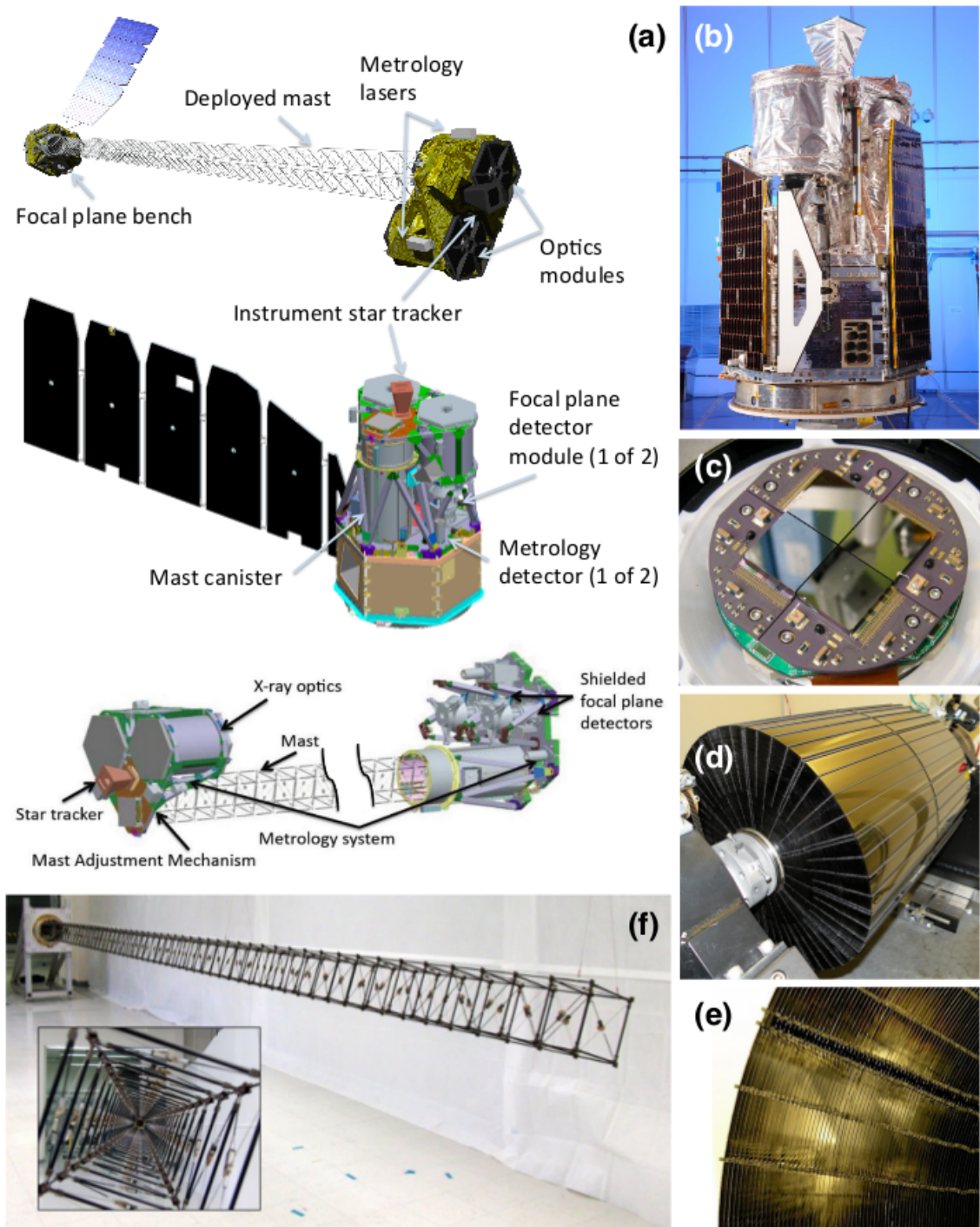
Figure 2.4: Illustrations and photos of the *NuSTAR* observatory and its instrumental components. (a): Illustrations of the observatory in various configurations (the middle graphic shows the observatory prior to mast deployment). The other three star trackers on the spacecraft bus are not labelled here. (b): The stowed observatory, pre-launch. (c): One the two FPM detectors. (d): One of the two optics modules. (e): A zoom in on one of the optics modules, showing the component shells. (f): The deployable mast, during a pre-launch test. Individual image credits: *NuSTAR*/NASA/Caltech; Harrison et al. (2013).

from the FPMs, to achieve the 10.14m focal length. The observatory attitude (i.e., the orientation with respect to the celestial sphere) is determined using one star tracker mounted on the optics bench and three star trackers on the spacecraft bus (the former are used to determine telescope pointing; the latter are used to keep the spacecraft fixed in inertial space, and to slew the observatory; e.g., Roberts et al. 2014). Slight mast bending during orbital cycles (due to Sunlight and Earth shadow) results in focal point movements at the level of $\approx$ 1–3mm (approximately translating to angular movements of ≈ 30–$60''$) on the detectors, tracked using laser metrology between the optics and the main bus (Liebe et al. 2012). The telescope calibration (e.g., of the effective area and vignetting) was performed using the Crab nebula and other objects (Madsen et al. 2015).

Each optical module follows a grazing incidence (see Section 2.1) Wolter-I conical approximation design (Petre & Serlemitsos 1985), and is comprised of 133 shells (Koglin et al. 2009; Hailey et al. 2010; Craig et al. 2011). The glass shells (Titanium-glass-epoxy-graphite composites; 0.2 mm thick) are each comprised of multiple glass segments (Zhang 2009), and coated with multiple layers of W/Si and Pt/C (for the outer and inner shells, respectively) to enhance reflectivity and thus facilitate higher grazing-incidence angles for high energy photons ($\gtrsim$ 15 keV; Madsen et al. 2009; Christensen et al. 2011). The upper drop-off in sensitivity at 78.4 keV results from the Pt K absorption edge (due to the Pt/C coating). The minimum and maximum grazing angles are 1.34 mrad and 4.7 mrad, respectively. The optics are designed such that focused photons undergo two reflections (see Figure 2.1). However, some photons at shallow or steep angles (primarily if there happens to be a bright source at 3–40$'$ off-axis) can be singly reflected onto the detector. These are referred to as "ghost rays". Additionally, some unfocused photons can make it to the detector, since there are some specific light paths (from bright sources at 3–6° off-axis) which are not blocked by the aperture stop or optics bench (Wik et al. 2014). This is referred to as "stray light".

The *NuSTAR* point spread function (PSF; shown in Figure 2.5) is centrally sharp, with a FWHM of 18$''$, and has broad wings (the half power diameter is 58$''$). A 45$''$ radius circular aperture (a typical size employed for source extraction) encloses $\sim 65\%$ of the full PSF energy. The PSF is largely smooth and symmetric; the slight spatial inhomogeneities, which are visible in Figure 2.5, result from the titanium support spiders (at the top and
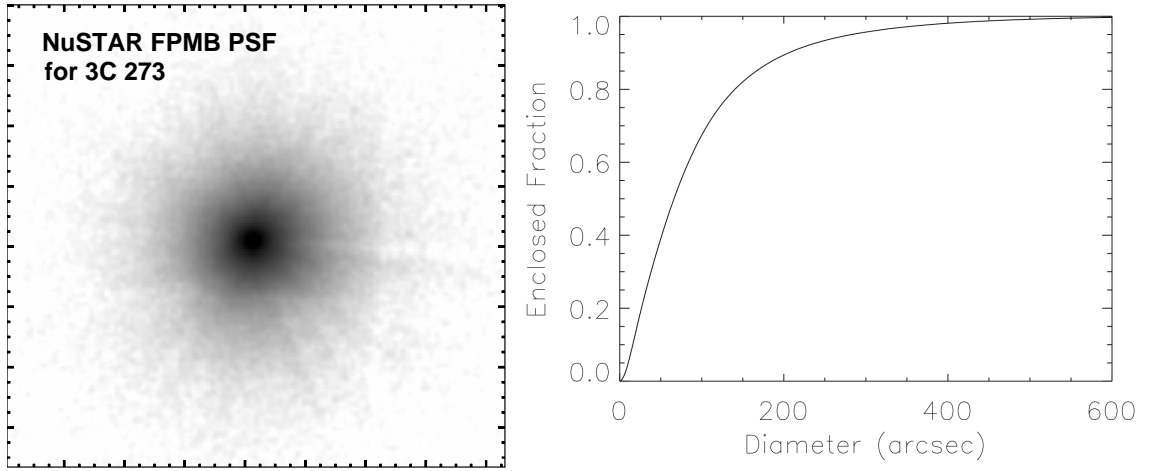
Figure 2.5: Left panel: An example near-on-axis *NuSTAR* point spread function (PSF) for FPMB (for the bright quasar 3C 273). The image is smoothed with a gaussian of three-pixel radius, and is shown in log-scaling (with a contrast- and bias-adjusted colourmap). The major ticks show steps in sky coordinates of 1 arcmin (the horizontal and vertical axes show R.A. and Decl., respectively). Right panel (from Harrison et al. 2013): The encircled energy fraction of the *NuSTAR* PSF as a function of diameter (for a circular source extraction region).

bottom of each optics module) and gaps between the glass sections of the optics. There is little variation in the PSF as a function of energy, although it slightly decreases in half power diameter towards higher energies. Additionally, the encircled energy fraction of the PSF does not strongly vary as a function of off-axis angle, although the detailed 2D shape of the PSF does vary.

Each FPM has a photon counting detector comprised of four individual CdZnTe (CZT) crystal detectors in a 2×2 grid with an overall field of view (FoV) size of $12.45' \times 12.45'$ (e.g., Kitaguchi et al. 2011, 2014). Each of the four crystal detectors is $2\text{cm} \times 2\text{cm}$ with a 32×32 pixel array. The image sampling scale (after running the software pipeline) is a factor of five finer than these crystal pixels, resulting in an effective pixel scale of $2.46''$ for the post-pipeline imaging (see Section 2.3). The detector readout is triggered by individual X-ray events. Each detector is surrounded by CsI anti-coincidence active shielding, which reduces detector background at $\gtrsim 10$ keV by flagging events which are recorded simultaneously by the shield and the detector (implying a travel direction other than the optical axis). The detector achieves a reasonably high spectral energy resolution, with $\mathrm{FWHM} = 0.4$ keV at 10 keV (and $\mathrm{FWHM} = 0.9$ keV at 68 keV).

Part of the breakthrough with *NuSTAR* is due to the low background (< 1 counts s^{-1} per FPM) with respect to previous missions (e.g., *Swift* BAT), largely due to the focusing nature of the optics (a PSF spread over a smaller physical area is naturally subject to fewer contaminating background events). Figure 2.6 shows an example *NuSTAR* background spectrum, and the main background sub-components: the "aperture background", from some unfocused CXB passing through the aperture stops (i.e., similar to the stray light mentioned above); focused and ghost ray CXB (labelled as "fCXB" in Figure 2.6); reflected solar X-rays; instrument Compton-scattered continuum; and instrument emission lines. In this thesis I primarily limit to energies of ≤ 24 keV. Except for some comparatively bright sources, the large majority of the *NuSTAR* sources in this thesis are faint and undetected at $\gtrsim 24$ keV, due to a combination of the decreasing sensitivity and the strong instrument background at these energies. As shown in Figure 2.6, the aperture background component dominates the background for the energies studied in this thesis. This background component is spatially non-uniform, appearing gradient-like across the FoV, and its spatial distribution is different for FPMA and FPMB.
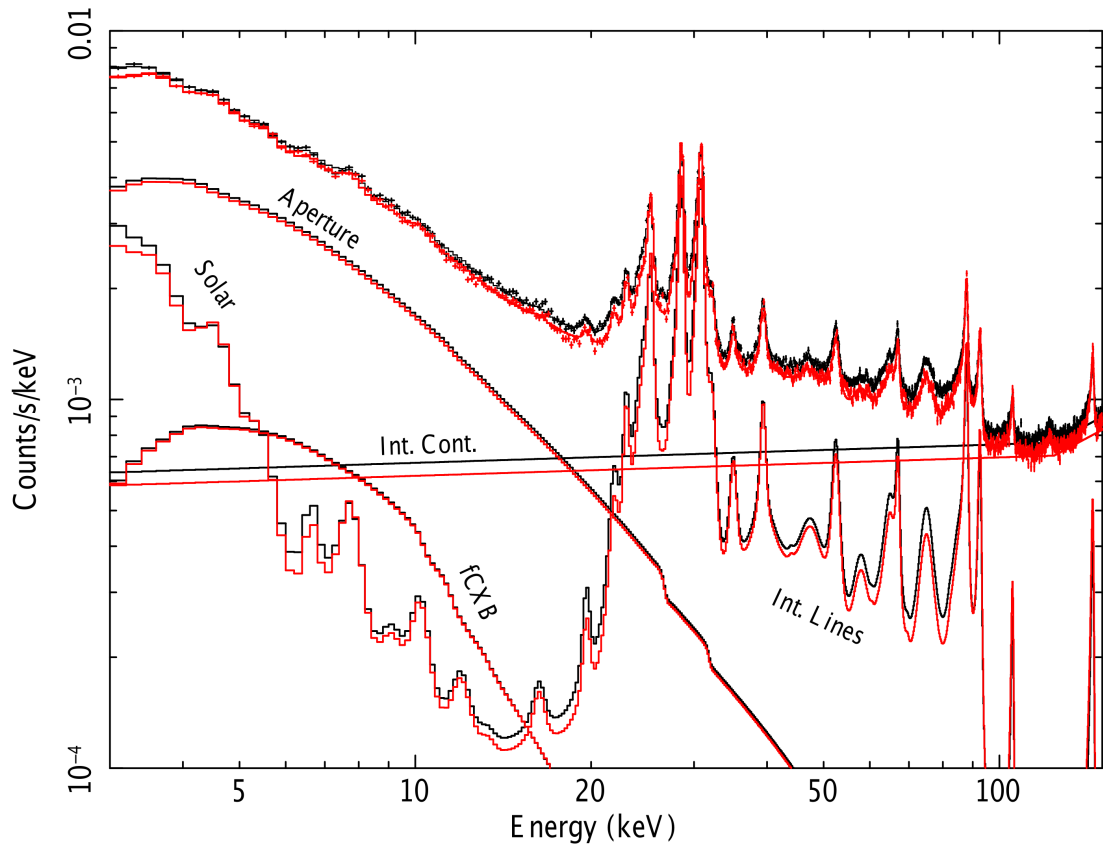
Figure 2.6: Figure from Wik et al. (2014) showing an example *NuSTAR* background spectrum (upper data points) compared to the individual components (individually labelled). The black and red correspond to FPMA and FPMB, respectively.

2.3 Data processing

Here I describe the *NuSTAR* data processing procedures applied in this thesis. Figure 2.7 shows a flow chart schematic, illustrating the data processing steps for a given *NuSTAR* field (i.e., a small region of sky with one *NuSTAR* observation or multiple spatially overlapping *NuSTAR* observations). In the serendipitous survey (Chapter 5) there are 331 individual fields to which these steps are applied. This section is intended to give a basic guide to the general data processing procedures, some of which vary slightly between chapters (for instance, Chapter 3 does not use the combined FPMA+B data). The reader is therefore also referred to the data, source detection, and other relevant sections of the individual Chapters 1–3.

The starting point is the level 1 data, which is the telemetry data from the space satellite processed into the FITS format. For the first data processing stage [(i) in Figure 2.7], I reduce the level 1 data using the NuSTARDAS task `nupipeline`.[1] This task is broken down into two main sub-stages: (1) data calibration; and (2) data screening. Summarised below are the processing steps for the calibration stage, which make use of instrument calibration data from the calibration database (CALDB).

- Data from the onboard laser metrology system (e.g., see Figure 2.4) are used to process information tracking temporal changes in the relative alignment of the optics and the focal plane detectors (which are connected by the ≈ 10m mast; see Figure 2.4).

- Attitude data is processed, using information from the star trackers (the star tracker on the optics bench provides a pointing accuracy of $\pm 8''$).

- Known bad pixels and detected hot pixels are flagged, to be excluded at the screening stage.

- The events in the level 1 data each have a 3×3 nine-pixel signal pattern (the centre of which is the pixel with the largest registered pulse height). For each event, pulse height amplitude (PHA; i.e., the charge in electronic units) information is processed, and a "grade" is assigned which characterises the morphology of the 3×3

---

[1]For further details the reader is referred to the NuSTARDAS guide (Perri et al., Version 1.9.0).

For each field:

**Level 1 raw FPMA and FPMB
event lists for the individual
obsID(s)**

i) Event list reduction pipeline

**Level 2 cleaned, calibrated
event lists**

ii) Split into 3 energy bands,
convert data to image format,
and create exposure maps

**Images (data and exp. maps)
Coadded = FPMA + FPMB**

iii) If $N_{obs} > 1$, merge the
obsIDs for each energy band

Science mosaics

iv) Source detection

Source lists

v) Merge

Final source list

For individual sources:

vi) Source photometry

vii) Spectral extraction

Figure 2.7: Flow chart schematic illustrating the data processing steps (detailed in Section 2.3) applied for a given *NuSTAR* field (e.g., this procedure is applied to 331 individual fields for the *NuSTAR* serendipitous survey; Chapter 5). "ObsID" refers to an individual *NuSTAR* exposure; there can be multiple obsIDs (i.e., multiple exposures) for a given field (i.e., $N_{obs} > 1$). "A", "B", and "C" correspond to FPMA, FPMB, and the coadded FPMA+B data, respectively. The coloured (blue, red, and green) shapes represent data which is filtered in energy to the three main *NuSTAR* bands adopted in this thesis (3–24, 3–8, and 8–24 keV).

signal pattern (from grade 0 to grade 32). Grades 27–32 are excluded at the screening stage (these particular four and five pixel patterns are less likely to be caused by real X-ray events).

- A gain correction (or energy correction) is performed for each event to convert from PHA to pulse invariant units (PI; i.e., the charge in physical energy units). The conversion is dependent on the pixel, the grade, and the detector temperature. PI is related to photon energy (E; in units of keV) by the following:

$$\text{PI} = \frac{E - 1.6}{0.04} \tag{2.3.1}$$

- An "interaction depth" threshold is applied to flag internal background and cosmic ray events (to be excluded at the screening stage). $E < 60$ keV events from focused astrophysical sources have shallow interaction depths.

- The physical coordinates of each event are converted to sky coordinates (Harp et al. 2010 details the pointing reconstruction procedure). First focal plane bench frame coordinates (`DET1X`, `DET1Y`) are assigned probabilistically based on the grade and the detector pixel coordinates (`RAWX`, `RAWY`). Next the `DET1` coordinates are converted to optics bench frame coordinates (`DET2X`, `DET2Y`) based on the mast aspect solution (from the laser metrology information; see above). The `DET1` and `DET2` coordinate systems use integer coordinates with effective pixel sizes which are finer by a factor of five than the raw detector pixels (meaning an effective pixel size of $12.3''/5 = 2.46''$ in the focal plane). Finally, the `DET2` coordinates are converted to celestial sky coordinates (`X`, `Y`) using attitude information (see above).

The above results in a calibrated (level 1a) event list, to which the screening stage is then applied. This involves excluding "bad" time intervals, including: when the Earth is in the FoV; when the telescope boresight is pointed $\leq 3°$ from the Earth's limb; when the observatory is passing through the South Atlantic Anomaly (SAA); when the attitude reconstruction is not from the optics bench star tracker, or its quality is low; when at least one of the mast-tracking laser spots is outside its associated position sensing detector grid; or when there is instrument dead time, due to the event-processing time of the focal plane module electronics or due to an anti-coincidence shield veto (which either prevents

event triggering, or interrupts event processing; e.g., Bachetti et al. 2015). Additionally, bad events are excluded: those associated with bad or hot pixels; those with grades ≥ 27; those with large interaction depths; and those with PI values outside of the standard range. The above results in a cleaned and calibrated (level 2) event list.

From this point on I use my own bespoke data processing procedure as illustrated in Figure 2.7 [stages (ii) to (vii)] and described below. First, I apply image analysis procedures to the level 2 data, which are schematically illustrated in Figure 2.8 using real *NuSTAR* data (for an example serendipitous survey field). From the level 2 event list, counts images are produced [step (ii) in Figure 2.7]. This is done separately for each obsID, each FPM (FPMA and FPMB), and each energy band (3–24, 3–8, and 8–24 keV), using the CIAO (Fruscione et al. 2006) task `dmcopy`. This results in $N_{\mathrm{obs}} \times 6$ different images (i.e., 3 energy bands per FPM) for each *NuSTAR* field (where N_{obs} is the number of independent exposures/observations for a given field). In addition, the FPMA and FPMB images are coadded for each energy band to increase sensitivity (this is referred to as the FPMA+B data), increasing the number of images per field to $N_{\mathrm{obs}} \times 9$. All X-ray image coadding is performed using `XIMAGE`.[2] Exposure maps (corresponding to the $N_{\mathrm{obs}} \times 6$ FPMA and FPMB images), which assign an effective exposure time to each pixel, are produced using the NuSTARDAS task `nuexpomap`. This task uses information from the calibration stage above (such as mast and attitude variations; thus accounting for the natural dither of the telescope during the observation), accounts for chip-gaps and bad pixels, and accounts for vignetting (i.e., the loss in sensitivity which increases as a function of off-axis angle). Non-vignetting-corrected exposure maps are additionally produced for the purposes of source detection in Chapter 5. As for the counts images, the FPMA and FPMB exposure maps are coadded for each energy band, to yield FPMA+B exposure maps (resulting in a total of $N_{\mathrm{obs}} \times 9$ exposure maps per field). For fields with multiple observations ($N_{\mathrm{obs}} > 1$), the images and exposure maps from step (ii) are merged across all observations [for each FPM and energy band; step (iii) in Figure 2.7], resulting in nine image mosaics and nine associated exposure map mosaics for each field. Source detection is performed using these mosaics [steps (iv) and (v) in Figure 2.7]. The exact

---

[2]https://heasarc.gsfc.nasa.gov/xanadu/ximage/ximage.html
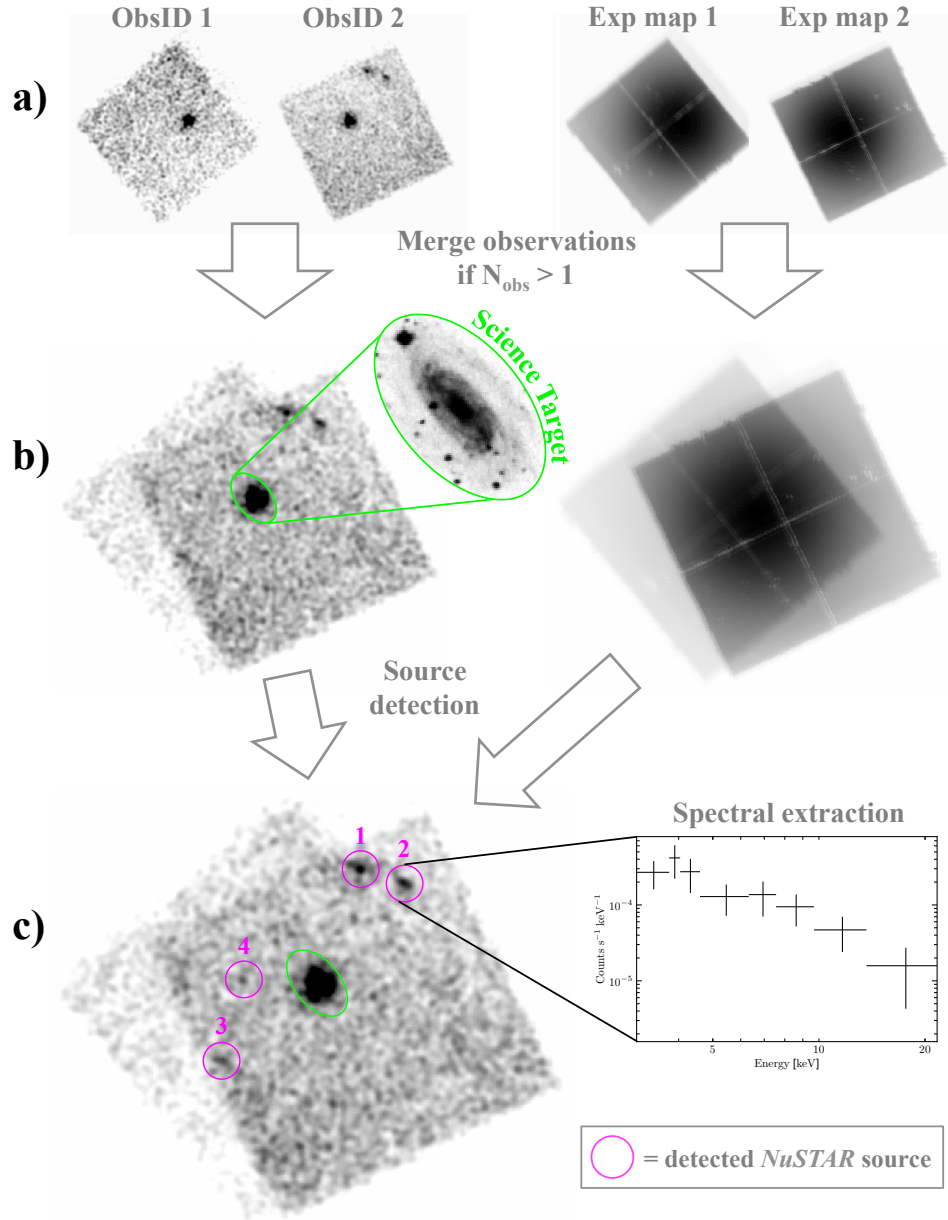
Figure 2.8: Schematic showing real counts images and exposure maps associated with stages (iii) to (v) of Figure 2.7. This example is for the IC 2560 field, which is included as one of the 331 fields in the *NuSTAR* serendipitous survey (Chapter 5). The data shown are for FPMA and the 3–24 keV energy band only. In general, the illustrated procedure is followed for FPMA, FPMB, and the coadded FPMA+B data, and for each of the three adopted *NuSTAR* bands (3–24, 3–8, and 8–24 keV). In this example there are two separate *NuSTAR* observations of the field, with different orientations and exposure times [(a)], the data from which are merged together [(b)]. Here IC 2560 is highlighted in green (the zoom-in inset shows a coordinate-matched optical image). Source detection is then performed, using information from both the counts image mosaic and the exposure map mosaic [(c)]. Since IC 2560 was the science target of the *NuSTAR* observation, it is excluded from the source detection. Although it appears faint here, source #4 (magenta circle) is significantly detected due to the increase in sensitivity gained from merging multiple exposures and from the combined FPMA+FPMB data. An example binned FPMA spectrum extracted for source #2 is shown [illustrating stage (vii) of Figure 2.7].

source detection procedure varies for the different studies presented in this thesis. For the *NuSTAR* serendipitous survey (Chapters 5 and 6) "blind" detection approaches are adopted, whereas for the targetted observations of obscured quasars (Chapters 3 and 4) the source detection uses prior knowledge of the source positions. As such, the reader is referred to the source detection sections of the individual chapters for details. The general procedure for source photometry [step (vi) in Figure 2.7] involves the following steps: (1) the gross (source plus background) counts are measured in a circular aperture (e.g., a $30''$ radius circle centred on the source position); (2) background counts are measured in a larger aperture (e.g., an annulus centred on the source position) and scaled down to estimate the background counts in the source aperture; and (3) the scaled background counts are subtracted from the gross counts to yield net source counts (from which count-rates, fluxes, and luminosities are estimated). Details of the photometry procedures adopted in Chapters 3–5 are provided in Sections 3.3.1, 4.3.1, and 5.2.4.

Once individual *NuSTAR* sources have been identified in the imaging data, spectra can be extracted from the level 2 event file. To achieve this, source and background extraction regions are defined (as for the photometry above) and the NuSTARDAS task `nuproducts` is run to extract a source spectrum, a background spectrum, an ancillary response function (ARF; e.g., see Figure 2.3) and a redistribution matrix file (RMF). Source and background light curves are also produced, although these are not used in this thesis (the generally low photon counts for the distant, faint sources studied here are not well suited to temporally resolved analyses). The difference in effective exposure between the source and background regions is accounted for using the sub-task `nubackscale`, which assesses the difference using an internally produced exposure map (the result is recorded using the "BACKSCAL" keyword). The RMF file accounts for the discrete nature of the PI channels, describing how photons of a given energy will be redistributed into PI channels. The ARF file describes the spectral response (i.e., the effective area) as a function of photon energy (as a result of the optics, the detector efficiency, and additional factors). `nuproducts` produces the ARF by taking a CALDB ARF file and correcting for the effects of vignetting, the natural dither, and the detector gaps relevant for the given observation and source FoV position. Since the X-ray sources presented in this thesis are point-sources, a PSF correction is applied to the ARF (the ARF is re-scaled by the

fraction of the PSF contained within the source extraction region). The overall response is the product of the ARF and RMF, which is used to translate between unfolded and folded spectra (i.e., the spectra before and after the effects of the telescope/instrumental response, respectively) when doing spectral modelling. For a given *NuSTAR* source, I extract the spectra for each available observation, with separate extractions for FPMA and FPMB, then coadd the spectra across all observations (separately for FPMA and FPMB) using `addascaspec`.[3] Finally, the spectra are binned to a minimum of 3 counts per bin (for use with `statistic cstat` in XSPEC) or 20–40 counts per bin (for use with `statistic chi` in XSPEC), using `grppha`.[4] The spectroscopic data are then fitted with physically motivated models using XSPEC to constrain the observed and intrinsic spectral properties of sources (see Chapters 4 and 6 for more details).

In this thesis, I apply the above data processing procedures to two main *NuSTAR* data sets: (a) ≈ 300 ks of data from a *NuSTAR* program targetting optically selected CT-candidate Type 2 quasars (Chapters 3–4); (b) ≈ 20 Ms of data for the *NuSTAR* serendipitous survey (Chapters 5–6).

---

[3]https://heasarc.gsfc.nasa.gov/docs/asca/adspecinfo.html
[4]http://heasarc.gsfc.nasa.gov/docs/journal/grppha4.html

Chapter 3

NuSTAR observations of heavily obscured quasars at $z \sim 0.5$

Abstract

We present *NuSTAR* hard X-ray observations of three Type 2 quasars at $z \approx 0.4$–0.5, optically selected from the Sloan Digital Sky Survey (SDSS). Although the quasars show evidence for being heavily obscured Compton-thick systems on the basis of the 2–10 keV to [O III] luminosity ratio and multiwavelength diagnostics, their X-ray absorbing column densities (N_{H}) are poorly known. In this analysis: (1) we study X-ray emission at > 10 keV, where X-rays from the central black hole are relatively unabsorbed, in order to better constrain N_{H}; (2) we further characterize the physical properties of the sources through broad-band near-UV to mid-IR spectral energy distribution (SED) analyses. One of the quasars is detected with *NuSTAR* at > 8 keV with a no-source probability of $< 0.1\%$, and its X-ray band ratio suggests near Compton-thick absorption with $N_{\mathrm{H}} \gtrsim 5 \times 10^{23}$ cm^{-2}. The other two quasars are undetected, and have low X-ray to mid-IR luminosity ratios in both the low energy (2–10 keV) and high energy (10–40 keV) X-ray regimes that are consistent with extreme, Compton-thick absorption ($N_{\mathrm{H}} \gtrsim 10^{24}$ cm^{-2}). We find that for quasars at $z \sim 0.5$, *NuSTAR* provides a significant improvement compared to lower energy (< 10 keV) *Chandra* and *XMM-Newton* observations alone, as higher column densities can now be directly constrained.

3.1 Introduction

Quasars are the sites of the most rapid black hole growth in the universe (Salpeter, 1964; Soltan, 1982). They represent the luminous end of the active galactic nucleus (AGN) population, often outshining their host galaxies. The first unobscured ('Type 1') quasars were discovered over 50 years ago (Schmidt, 1963b; Hazard et al., 1963), and more than one hundred thousand have now been spectroscopically identified (e.g., Véron-Cetty & Véron 2010; Pâris et al. 2012). For obscured ('Type 2') quasars[1] the situation is not as advanced. Similar to the early Type 1 quasars, Type 2 quasars were initially identified from radio selection (e.g., Minkowski 1960), and over the following decades several hundred powerful 'radio galaxies' (as such radio-selected Type 2 quasars are typically called) were identified (for reviews, see McCarthy 1993; Miley & De Breuck 2008). However, it is only in the past decade that radio-quiet Type 2 quasars have been found in large numbers. Such sources are generally identified on the basis of either their relatively hard X-ray spectral slopes (e.g., Norman et al. 2002; Stern et al. 2002), optical spectral features (e.g., Steidel et al. 2002; Zakamska et al. 2003), or mid-infrared (mid-IR) colours (e.g., Lacy et al. 2004; Stern et al. 2005). Importantly, mid-IR colour selection of Type 2 quasars using the all-sky *Wide-Field Infrared Survey Explorer* (*WISE*; Wright et al. 2010) survey identifies several million Type 2 quasars, roughly down to the bolometric luminosity of the primary Sloan Digital Sky Survey (SDSS; York et al., 2000) Type 1 quasar spectroscopic survey (Stern et al., 2012; Assef et al., 2013; Donoso et al., 2014).

The exact nature of Type 2 quasars is still under debate. A simple extension of the orientation-driven unified model of AGN (Antonucci, 1993; Urry & Padovani, 1995) to high luminosities can account for their existence. However, there is also observational evidence for an evolutionary link to Type 1 quasars (e.g., Sanders et al., 1988; Hopkins et al., 2008). The importance of Type 2 quasars to the cosmic evolution of AGN is further demonstrated by their requirement in models of the cosmic X-ray background

---

[1]We define Type 2 quasars as AGN with $L_{2-10\mathrm{keV}} \geq 10^{44}$ erg s^{-1}, X-ray absorbing column densities $N_{\mathrm{H}} > 10^{22}$ cm^{-2}, and optical spectra that show narrow line emission without broad (Hα or Hβ) components. This $L_{2-10\mathrm{keV}}$ threshold is consistent with: (1) the classical optical quasar definition, $M_B \leq -23$, when the α_{OX} relation of Steffen et al. (2006) and the composite quasar spectrum of Vanden Berk et al. (2001) are assumed; (2) the $L_{\mathrm{X},*}$ value derived by Hasinger et al. (2005) for unobscured AGN.

(CXB) (e.g., Treister & Urry, 2005; Gilli et al., 2007; Treister et al., 2009). However, the observed X-ray properties of Type 2 quasars are poorly constrained at present. Consequently, the column density ($N_{\rm H}$) distribution[2] and Compton-thick[3] fraction of quasars are poorly known, which has implications for both AGN and CXB models (e.g., Fabian et al., 2008; Draper & Ballantyne, 2010).

To date, the largest sample of spectroscopically confirmed (radio-quiet) Type 2 quasars at $z \lesssim 1$ is that of Zakamska et al. (2003) and Reyes et al. (2008). Zakamska et al. (2003) selected 291 Type 2 quasars at redshift $0.2 \lesssim z \lesssim 0.8$ from the SDSS based on their optical properties: high [O III] $\lambda 5007$ line power and narrow emission lines. Reyes et al. (2008) used the same approach and more recent SDSS data to extend the sample to 887 objects. While X-ray selections of Type 2 quasars at $\lesssim 10$ keV are biased against the most heavily obscured sources (e.g., Maiolino et al., 1998), [O III] emission is mostly produced on ~ 100 pc scales and is thus relatively unaffected by nuclear obscuration, allowing larger numbers of the heavily obscured, X-ray faint objects to be found. Following up [O III] selected, rather than X-ray selected, objects with X-ray observations thus gives a less biased estimate of the $N_{\rm H}$ distribution of AGN (e.g., Risaliti et al., 1999).

The X-ray properties of the Zakamska et al. (2003) and Reyes et al. (2008) Type 2 quasar sample have been studied using *Chandra* and *XMM-Newton* observations (Ptak et al., 2006; Vignali et al., 2006, 2010; Jia et al., 2013). Vignali et al. (2006, 2010) measured column densities for a handful of sources through 'direct' means (i.e., using X-ray spectroscopic analysis). The highest column densities measured in this manner were $N_{\rm H} \approx 3 \times 10^{23}$ cm^{-2}. However, distant obscured quasars are X-ray weak and in most cases direct constraints are not feasible. Instead, an 'indirect' approach to estimating column densities can be used where the observed X-ray emission is compared with a proxy for intrinsic AGN power (e.g., the mid-IR continuum emission from hot dust or high-excitation emission lines; Bassani et al., 1999; Lutz et al., 2004; Heckman et al., 2005; Alexander et al., 2005b, 2008; Cappi et al., 2006; Panessa et al., 2006; Meléndez et al., 2008; Gandhi et al., 2009; LaMassa et al., 2009, 2011; Gilli et al., 2010; Goulding

---

[2]X-rays emitted from the immediate black hole environment are absorbed by circumnuclear gas, and thus provide constraints on $N_{\rm H}$.

[3]Compton-thick absorption is that with $N_{\rm H} \geq \sigma_{\rm T}^{-1} \approx 1.5 \times 10^{24}$ cm^{-2}.

et al., 2011). Vignali et al. (2006, 2010) were limited to indirect absorption constraints for the majority of their Type 2 quasar sample, and found in every case that Compton-thick absorption (i.e., $N_{\mathrm{H}} > 1.5 \times 10^{24}$ cm^{-2}) is required to explain the X-ray suppression in these sources. To first order, there appears to be a bimodal N_{H} distribution for optically selected Type 2 quasars, with $\sim 40\%$ having $N_{\mathrm{H}} = 10^{22}$–3×10^{23} cm^{-2} and $\sim 60\%$ being Compton-thick. This is interesting given that a continuous N_{H} distribution is measured for Type 2 Seyferts (e.g., Bassani et al., 1999; Risaliti et al., 1999; LaMassa et al., 2009, 2011), although the differences may be reconciled by considering the different methods used to estimate N_{H} (LaMassa et al., 2011). To better constrain the N_{H} distribution of Type 2 quasars, more robust identifications of Compton-thick absorption must be obtained through either: (i) measurement of strong Fe Kα emission, with EW ≥ 1 keV, which results from the Fe Kα line being viewed in reflection against a suppressed continuum (e.g., Ghisellini et al., 1994; Levenson et al., 2002); or (ii) measurement of high column densities through spectroscopic analysis at high energies above the photoelectric absorption cutoff (i.e., above observed-frame 8 keV for $z \sim 0.5$ and $N_{\mathrm{H}} \sim 10^{24}$ cm^{-2}), where X-ray emission is relatively unabsorbed.

The recent launch of the *Nuclear Spectroscopic Telescope Array* (*NuSTAR*) will see a breakthrough in our understanding of heavily obscured AGN and the CXB population in general (see Chapter 2 for a detailed description of *NuSTAR*). The high energy range at which *NuSTAR* operates (3–79 keV) means that the intrinsic, unabsorbed emission of AGN is observed for all but the most heavily obscured, Compton-thick objects. At $z \lesssim 1$, it is now possible to directly constrain column densities an order of magnitude higher than those achievable with *Chandra* and *XMM-Newton* alone (e.g., Luo et al., 2013).

In this chapter, we present exploratory *NuSTAR* observations of three optically selected Type 2 quasars at $z \approx 0.4$–0.5. All three have been identified as Compton-thick candidates in previous studies (Vignali et al., 2006, 2010; Jia et al., 2013). We use X-ray data from *NuSTAR*, *Chandra* and *XMM-Newton*, and near-UV to mid-IR data from other observatories to determine the physical properties of the quasars. In particular, we use a combination of direct and indirect methods to constrain the absorbing column densities. The chapter is organized as follows: our sample selection is detailed in Section 3.2; we describe the observations, data reduction and data analysis in Section 3.3; our main re-

sults regarding X-ray absorption constraints are presented in Section 3.4; we summarize our main conclusions in Section 3.5. The cosmology adopted throughout this work is $(\Omega_M, \Omega_\Lambda, h) = (0.27, 0.73, 0.71)$.

3.2 Sample Selection

First, we selected objects at $z \approx 0.4$–0.5 from the *Chandra* and *XMM-Newton* studies of SDSS selected Type 2 quasars by Vignali et al. (2006, 2010) and Jia et al. (2013). Although the objects have narrow Hβ line emission, the Hα line lies outside the SDSS spectral range at these redshifts. Therefore, we cannot rule out that these quasars are luminous versions of the Type 1.9 Seyferts that show evidence for a broad Hα component but no broad Hβ component (Osterbrock, 1981). Second, we selected quasars with low observed X-ray to [O III] luminosity ratios, $L_{2-10\mathrm{keV}}/L_{[\mathrm{OIII}]} < 2.5$. This threshold corresponds to a two orders of magnitude suppression of the observed X-ray luminosity, assuming the Mulchaey et al. (1994) relation between [O III] and intrinsic 2–10 keV flux (taking into account the variance of the relation), which is consistent with Compton-thick absorption. This is a conservative selection, since the Mulchaey et al. (1994) relation was calibrated for Type 2 Seyferts, and Type 2 quasars typically have larger X-ray to [O III] luminosity ratios (Netzer et al., 2006). Third, we made sub-selections of three quasars which show evidence for extreme obscuration on the basis of different diagnostics:

- SDSS J001111.97+005626.3 ($z = 0.409$, $L_{2-10\mathrm{keV}} = 3.1 \times 10^{42}$ erg s^{-1}, $L_{[\mathrm{OIII}]} = 1.8 \times 10^{42}$ erg s^{-1}; Reyes et al., 2008; Jia et al., 2013) has a flat X-ray spectral slope at observed-frame 0.3–10 keV ($\Gamma = 0.6^{+1.17}_{-1.15}$; Jia et al., 2013), which suggests that the X-ray emission is rising steeply towards high energies (> 10 keV). Unlike the other two quasars, there is no mid-IR spectroscopy available.

- SDSS J005621.72+003235.8 ($z = 0.484$, $L_{2-10\mathrm{keV}} = 8.9 \times 10^{41}$ erg s^{-1}, $L_{[\mathrm{OIII}]} = 6.8 \times 10^{42}$ erg s^{-1}; Reyes et al., 2008; Vignali et al., 2010) has the deepest 9.7 μm silicate (Si) absorption of the sample of Type 2 quasars observed with *Spitzer*-IRS in Zakamska et al. (2008). Such strong Si features are typically found in Compton-thick AGN (e.g., Shi et al., 2006; Georgantopoulos et al., 2011b; Goulding et al., 2012).

- SDSS J115718.35+600345.6 ($z = 0.491$, $L_{2-10\mathrm{keV}} < 1.5 \times 10^{42}$ erg s^{-1}, $L_{[\mathrm{OIII}]} = 1.6 \times 10^{43}$ erg s^{-1}; Reyes et al., 2008; Vignali et al., 2010) is the most luminous quasar in the Vignali et al. (2010) sample at mid-IR wavelengths, but is undetected by *Chandra* (Vignali et al., 2006). The extremely low X-ray to mid-IR luminosity ratio is likely due to Compton-thick absorption (Vignali et al., 2010). The *Spitzer*-IRS spectrum for this source shows it to be quasar-dominated at mid-IR wavelengths, but that it also hosts ultraluminous star formation [$\log(L_{\mathrm{SF}}/L_\odot) = 12.3$, Zakamska et al. 2008]. There is no evidence for significant Si-absorption; however, $\approx 50\%$ of the best studied Compton-thick AGN do not have significant Si-absorption (e.g., Goulding et al., 2012).

3.3 NuSTAR and Multiwavelength Data

In our analysis of the three Type 2 quasars, we used *NuSTAR* observations in conjunction with lower energy X-ray observations from *Chandra* and *XMM-Newton*, and near-UV to mid-IR data primarily from large-area public surveys. Hereafter we refer to the quasars using abbreviated SDSS object names.

3.3.1 NuSTAR Observations

The Type 2 quasars, SDSS J0011+0056, SDSS J0056+0032 and SDSS J1157+6003, were observed by *NuSTAR* with nominal exposure times of 19.6 ks, 23.5 ks and 23.3 ks, respectively. Details of the observations, including net exposure times, are provided in Table 3.1. We processed the data using the *NuSTAR* Data Analysis Software (NuSTARDAS) v. 1.3.0. Calibrated and cleaned event files were produced using the NUPIPELINE script and the *NuSTAR* CALDB 20131007 release with the standard filter flags.

Photometry and Source Detection

To characterize the high energy X-ray emission and determine whether sources are detected, we performed photometry in the observed-frame 3–24 keV, 3–8 keV, and 8–24 keV bands for both of the *NuSTAR* FPMs following Alexander et al. (2013). We avoided using photons above 24 keV, where the drop in effective area and the prominent background

Table 3.1: X-ray Observation Log

Object Name	z	NuSTAR				Lower Energy X-ray Observations			
		Observation ID	UT Date	Exposure	Observatory	Observation ID	UT Date	Exposure
(1)	(2)	(3)	(4)	(5)	(6)	(7)	(8)	(9)
SDSS J001111.97+005626.3	0.409	60001065002	2013 Jan 27	18.3 ks	XMM-Newton	0403760301	2006 Jul 10	25.7 ks
SDSS J005621.72+003235.8	0.484	60001061002	2013 Jan 27	21.9 ks	Chandra	7746	2008 Feb 08	9.91 ks
SDSS J115718.35+600345.6	0.491	60001071002	2012 Oct 28	21.7 ks	Chandra	5698	2005 Jun 03	6.97 ks

NOTE. – (1): Full SDSS object name. (2): Redshift. (3) and (4): *NuSTAR* observation ID and start date. (5): Net on-axis *NuSTAR* exposure time. This value applies to both FPMA and FPMB. (6) Lower energy X-ray observatory data used (*Chandra* or *XMM-Newton*). (7), (8) and (9): *Chandra* or *XMM-Newton* observation ID, observation start date, and net on-axis exposure time, corrected for flaring and bad events.

features (see Figure 2 and 10 of Harrison et al. 2013, respectively) hinder the analysis of faint X-ray sources such as Type 2 quasars. We split the *NuSTAR* event files into individual band images using DMCOPY, part of the *Chandra* Interactive Analysis Observations software (CIAO, v4.4; Fruscione et al. 2006).[4] We extracted the gross source counts (S) from a $45''$ radius aperture centred on the SDSS position. For a source at the *NuSTAR* aim point, and for the energy range (3–24 keV) and spectral slopes ($\Gamma = 0.6$–1.8) used in this study, this aperture encloses $\approx 65\%$ of the full PSF energy. We extracted the background counts (B) from an annulus with an inner radius $90''$ from the source and an outer radius $150''$ from the source, which allowed the local background to be sampled while minimising contamination from the source. To obtain the background counts in the source extraction region (B_{src}), we multiplied B by the area scaling factor between the source and background regions (A_S/A_B). Net source counts were calculated as $S - B_{\mathrm{src}}$, and corresponding 68.3% confidence level uncertainties were taken as $\sqrt{S + B(A_S/A_B)^2}$. For non detections, we calculated 99.7% confidence level upper limits using the Bayesian method of Kraft et al. (1991). The *NuSTAR* photometry is given in Table 3.2.

To test whether the quasars are detected in the individual *NuSTAR* band images, we looked for significant source signals at their SDSS positions. We assumed binomial statistics and calculated false probabilities, or 'no-source' probabilities (P), using the following equation:

$$P(x \geq S) = \sum_{x=S}^{T} \frac{T!}{x!(T-x)!} p^x \left(1 - p\right)^{T-x},$$
(3.3.1)

where $T = S + B$ and $p = 1/(1 + B/B_{\mathrm{src}})$. P is the probability that, assuming there is no source at the SDSS position, the measured gross counts in the source aperture (S) are purely due to a background fluctuation (Weisskopf et al., 2007).

Given that the three Type 2 quasars are faint at 3–8 keV (see Table 3.2 for *Chandra* and *XMM-Newton* fluxes and upper limits), and likely have flat X-ray spectra with emission rising steeply to higher energies, *NuSTAR* is most likely to detect the sources above 8 keV (observed-frame). At these energies *Chandra* and *XMM-Newton* have little to no sensitivity. In Figure 3.1, we show the S and B_{src} values measured with *NuSTAR* for the

---

[4]http://cxc.harvard.edu/ciao/index.html

Table 3.2: X-ray Photometry

Object Name	Net Counts (FPMA)			Net Counts (FPMB)			Flux (*NuSTAR*)			Flux (other)
(1)	(2)			(3)			(4)			(5)
	3–24	3–8	8–24	3–24	3–8	8–24	3–24	3–8	8–24	3–8
0011+0056	17.5 ± 7.7	< 16.3	16.8 ± 6.4	< 24.7	< 18.3	< 19.7	0.99	< 0.74	1.32	0.18
0056+0032	< 19.1	< 10.9	< 20.9	< 23.5	< 17.8	< 19.6	< 1.14	< 0.52	< 1.58	< 0.16
1157+6003	< 31.4	< 16.6	< 29.1	< 23.3	< 20.0	< 17.7	< 1.35	< 0.63	< 1.68	< 0.22

NOTE. – (1): Abbreviated SDSS object name. The 'SDSS J' prefix and all RA and Dec digits after the first four have been truncated. (2) and (3): Net source counts in the observed-frame 3–24, 3–8 and 8–24 keV bands for FPMA and FPMB, respectively. 68.3% confidence level uncertainties, and 99.7% confidence level upper limits are given. (4): Aperture-corrected *NuSTAR* flux in units of 10^{-13} erg s^{-1} cm^{-2} (for a power-law model with $\Gamma = 1.8$), in the observed-frame 3–24, 3–8 and 8–24 keV bands. For SDSS J0011+0056 the fluxes are for FPMA only, while for SDSS J0056+0032 and SDSS J1157+6003 the fluxes are averaged over FPMA and FPMB. (5): Aperture-corrected observed-frame 3–8 keV flux in units of 10^{-13} erg s^{-1} cm^{-2} (for a power-law model with $\Gamma = 1.8$), as measured using lower-energy X-ray data. *XMM-Newton* data have been used for SDSS J0011+0056, and *Chandra* data have been used for SDSS J0056+0032 and SDSS J1157 +6003. 99.7% confidence level upper limits are given.

8–24 keV band (filled symbols), and the no-source probabilities to which they correspond (dashed lines).[5] For the purposes of this figure, Poisson statistics have been assumed; for our sources, B is large and the Poisson integral thus provides a good approximation of Equation 3.3.1 (Weisskopf et al., 2007). Taking binomial no-source probabilities greater than 1% to indicate non detections, neither SDSS J0056+0032 nor SDSS J1157+6003 are detected in either FPM. SDSS J0011+0056, on the other hand, is detected in FPMA with a binomial no-source probability of 0.093%.[6] The *NuSTAR* image corresponding to this detection is shown in Figure 3.2. The source is not detected in FPMB, which has higher background noise relative to FPMA for this observation; indeed the net source counts for FPMA are consistent with the upper limit for FPMB (see Table 3.2). SDSS J0011+0056 is also weakly detected in the 3–24 keV band for FPMA, with a binomial no-source probability of 0.58%. Aside from this, none of the quasars are detected in the 3–8 keV and 3–24 keV bands.

The no-source probability is sensitive to the background region sampled. To partially address this we also measured the background from model background maps produced using NUSKYBGD (Wik et al. 2014), summing counts within the $45''$ radius source aperture. These measurements are shown as empty symbols in Figure 3.1. SDSS J0011+0056 is still detected in FPMA using this approach, with a no-source probability of 0.033% at 8–24 keV.

Flux Calculation

For each *NuSTAR* energy band we determined the conversion factor between net count rate and source flux using XSPEC v12.8.1j (Arnaud, 1996), taking into account the Response Matrix File (RMF) and Ancillary Response File (ARF) for each FPM. We assumed a power-law model with $\Gamma = 1.8$, consistent with that found for AGN at observed-frame 3–24 keV (Alexander et al., 2013). We corrected fluxes to the 100% encircled-energy fraction of the PSF. The *NuSTAR* fluxes are given in Table 3.2.

---

[5]We avoid overplotting the errors for individual S and B_{src} measurements, since these are not used in the calculation of no-source probabilities.

[6]We note that, in this case, using a $50''$ (as opposed to $45''$) source aperture results in a lower no-source probability of 0.049%.
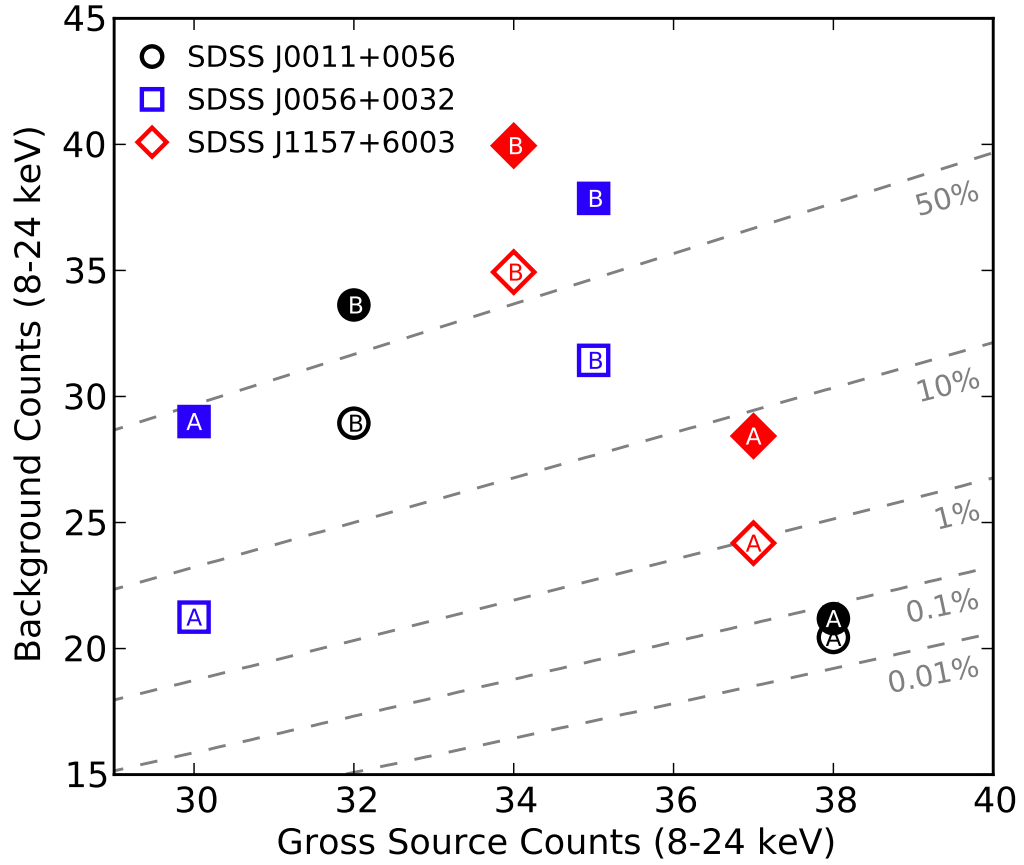
Figure 3.1: Gross source counts (S) versus scaled background counts (B_{src}) at observed-frame 8–24 keV for SDSS J0011+0056, SDSS J0056+0032 and SDSS J1157+6003 (circles, squares and diamonds, respectively). Background counts were measured using two approaches: direct measurement from the *NuSTAR* images (filled symbols), and from model background maps (empty symbols). The A and B labels correspond to FPMA and FPMB, respectively. The dashed lines indicate Poisson no-source probabilities. There is one significant detection: SDSS J0011+0056 is detected with FPMA.
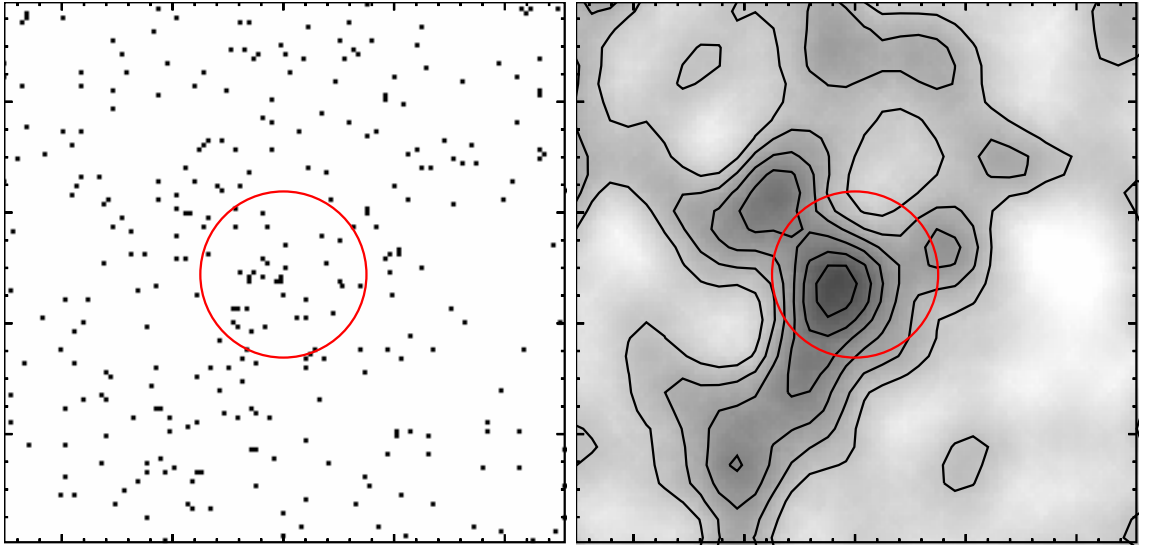
Figure 3.2: *NuSTAR* FPMA 8–24 keV image centred on the SDSS position of SDSS J0011+0056. Left panel: Unsmoothed image. Right panel: Image smoothed with a Gaussian of radius 14 pixels ($34.5''$), and with overlaid contours of constant pixel values. The smoothing and contours are for display purposes only. A $45''$ radius aperture is shown (red circle), centred on the SDSS position. The horizontal and vertical axes are right ascension (RA) and declination (Dec), respectively. The major ticks indicate 1 arcmin offsets.

For the *NuSTAR*-detected quasar, SDSS J0011+0056, we measure an observed-frame 8–24 keV flux of 1.32×10^{-13} erg s^{-1} cm^{-2}. This value is consistent with extrapolations from the *XMM-Newton* 0.5–10 keV count rate given the photon index constraints of Jia et al. (2013), $\Gamma = 0.6^{+1.17}_{-1.15}$, and assuming a simple unabsorbed power-law model. Additionally, as we later show in Section 3.4.2, our X-ray flux measurement for SDSS J0011 +0056 is consistent with that expected from its 6 μm luminosity, which is assumed to result from the reprocessing of AGN emission by obscuring dust.

3.3.2 Lower Energy X-ray Data

For SDSS J0011+0056 we used the archival *XMM-Newton* EPIC observation, first published in Jia et al. (2013). We analysed the Pipeline Processing System (PPS) data products for this observation using the *Science Analysis Software*[7] (SAS v.12.0.1). The MOS1 and MOS2 data were coadded with the SAS task EPICSPECCOMBINE. The PN data were excluded, since SDSS J0011+0056 is close to a chip gap. The source counts were extracted from a $15''$ radius aperture and the background counts were extracted using an $80''$ radius source-free aperture, selected to sample the local background while avoiding chip gaps and nearby serendipitous sources. We used XSPEC to convert from count rate to flux, assuming a power-law model with $\Gamma = 1.8$ and using the *XMM-Newton* RMF and ARF. Throughout this work, we neglect the cross-calibration constants between MOS and *NuSTAR* as the current best estimates are $\sim 7 \pm 5\%$ (Madsen et al. 2015), and a change on this scale does not affect our results.

For SDSS J0056+0032 and SDSS J1157+6003 we used the archival *Chandra* observations, first published in Vignali et al. (2006, 2010). We reprocessed the data using CHANDRA_REPRO,[8] a CIAO pipeline, to create event files. The source counts were extracted from a $3''$ radius aperture, and the background counts were extracted from an annulus with an inner radius $10''$ from the source and an outer radius $30''$ from the source. As SDSS J0056+0032 and SDSS J1157+6003 are non detections at observed-frame 3–8 keV, we calculated 99.7% confidence level upper limits for the source counts using the

---

[7]http://xmm.esa.int/sas/

[8]http://cxc.harvard.edu/ciao/ahelp/chandra_repro.html

Bayesian method of Kraft et al. (1991). To calculate fluxes, we converted from *Chandra* count rates with the HEASARC tool WebPIMMs[9] (v4.6b) assuming a power-law model with $\Gamma = 1.8$, and corrected to the 100% encircled-energy fraction of the PSF.

As the Type 2 quasars are faint at X-ray wavelengths, we are unable to fit the spectra accurately. For instance, SDSS J0011+0056 is detected with *XMM-Newton*, but using the combined MOS1+MOS2 data we only extract 5.6 and 20.6 net source counts in the observed-frame 0.5–3 keV and 3–8 keV bands, respectively. We list the *Chandra* and *XMM-Newton* 3–8 keV fluxes and upper limits in Table 3.2.

3.3.3 Near-UV to Mid-IR Data and SED Decomposition

To investigate the multiwavelength properties of the three Type 2 quasars, in particular the mid-IR emission from the AGN, we collected photometric data at 0.3–30 μm (i.e., at near-UV through mid-IR wavelengths). We used imaging data from public large-area surveys, primarily the Sloan Digital Sky Survey (SDSS; York et al., 2000), the UKIRT Infrared Deep Sky Survey (UKIDSS; Lawrence et al., 2007), and the *WISE* all-sky survey (Wright et al., 2010). Additionally, for SDSS J0056+0032 and SDSS J1157+6003, we used *Spitzer* photometry from the *Spitzer* Enhanced Imaging Products Source List.[10] The photometric dataset, not corrected for Galactic extinction, is provided in Table 3.3. We note that since the observations are not contemporaneous, AGN variability may affect the SED analysis at longer wavelengths, where the AGN is bright with respect to the host galaxy.

We used the near-UV through mid-IR photometric data to produce broad-band spectral energy distributions (SEDs) for our sample. We modelled the SEDs using the Assef et al. (2010) 0.03–30 μm empirical low-resolution AGN and galaxy templates. Each SED was modelled as a best-fit combination of an elliptical, a spiral and an irregular galaxy component, plus an AGN. We refer the reader to Assef et al. (2008, 2010, 2013) for further details. In Fig. 3.3 we present the SEDs and best-fitting model solutions. For SDSS J1157 +6003 we also show the *IRAS* 60 μm flux measured by Zakamska et al. (2004, green

---

[9]http://heasarc.gsfc.nasa.gov/Tools/w3pimms.html

[10]http://irsa.ipac.caltech.edu/data/SPITZER/Enhanced/Imaging/

Table 3.3: Near-Ultraviolet to Mid-Infrared Source Properties

Object Name[a]	0011+0056	0056+0032	1157+6003
u (0.355 μm)[b]	23.51 ± 0.99	23.25 ± 0.71	20.53 ± 0.06
g (0.468 μm)[b]	21.50 ± 0.05	21.60 ± 0.069	20.10 ± 0.01
r (0.616 μm)[b]	20.26 ± 0.05	20.72 ± 0.05	19.61 ± 0.02
i (0.748 μm)[b]	19.60 ± 0.04	19.82 ± 0.04	18.90 ± 0.01
z (0.892 μm)[b]	19.25 ± 0.09	19.81 ± 0.12	19.02 ± 0.05
Y (1.03 μm)[c]	18.25 ± 0.04	–	–
J (1.25 μm)[c]	17.70 ± 0.03	18.42 ± 0.07	–
H (1.63 μm)[c]	16.81 ± 0.04	17.31 ± 0.07	–
K (2.20 μm)[c]	–	16.64 ± 0.05	–
WISE (3.4 μm)[d]	14.94 ± 0.04	15.53 ± 0.05	12.78 ± 0.02
WISE (4.6 μm)[d]	14.45 ± 0.07	14.51 ± 0.08	11.24 ± 0.02
WISE (12 μm)[d]	10.62 ± 0.09	9.77 ± 0.05	8.0 ± 0.02
WISE (22 μm)[d]	–	6.55 ± 0.07	5.37 ± 0.03
Spitzer (3.6 μm)[e]	–	0.173 ± 0.003	2.860 ± 0.009
Spitzer (4.5 μm)[e]	–	0.220 ± 0.003	4.511 ± 0.010
Spitzer (5.8 μm)[e]	–	0.591 ± 0.009	8.215 ± 0.017
Spitzer (8.0 μm)[e]	–	2.474 ± 0.016	13.165 ± 0.022
Spitzer (24 μm)[f]	–	18.088 ± 0.058	57.318 ± 0.062
IRAS (60 μm)[g]	–	–	260.0 ± 46.0
$\hat{a}$[h]	0.590 ± 0.029	0.946 ± 0.003	0.977 ± 0.001
$L_{6\mu\mathrm{m}}$[h]	1.14 ± 0.15	15.19 ± 0.60	51.44 ± 1.12

NOTE. – [a] Abbreviated SDSS object name; [b] SDSS DR7 Fiber magnitudes in the AB sinh system; [c] UKIDSS DR9 2.8″ diameter aperture magnitudes in the Vega system; [d] *WISE* profile-fit magnitudes in the Vega system; [e] *Spitzer* 3.8″ diameter aperture flux densities in units of mJy; [f] *Spitzer* PSF-fit flux densities in units of mJy; [g] *IRAS* flux density in units of mJy (Zakamska et al., 2004). This data point was not used in the SED modelling; [h] best-fit parameters (corrected for dust reddening) from the SED decomposition described in Section 3.3.3: $\hat{a}$ is the fractional contribution of the AGN to the 0.1–30 μm emission; $L_{6\mu\mathrm{m}}$ is the rest-frame 6 μm luminosity (νL_ν) of the AGN in units of 10^{44} erg s^{-1}. The uncertainties are standard deviations, derived from the Monte Carlo re-sampling of the photometric data.
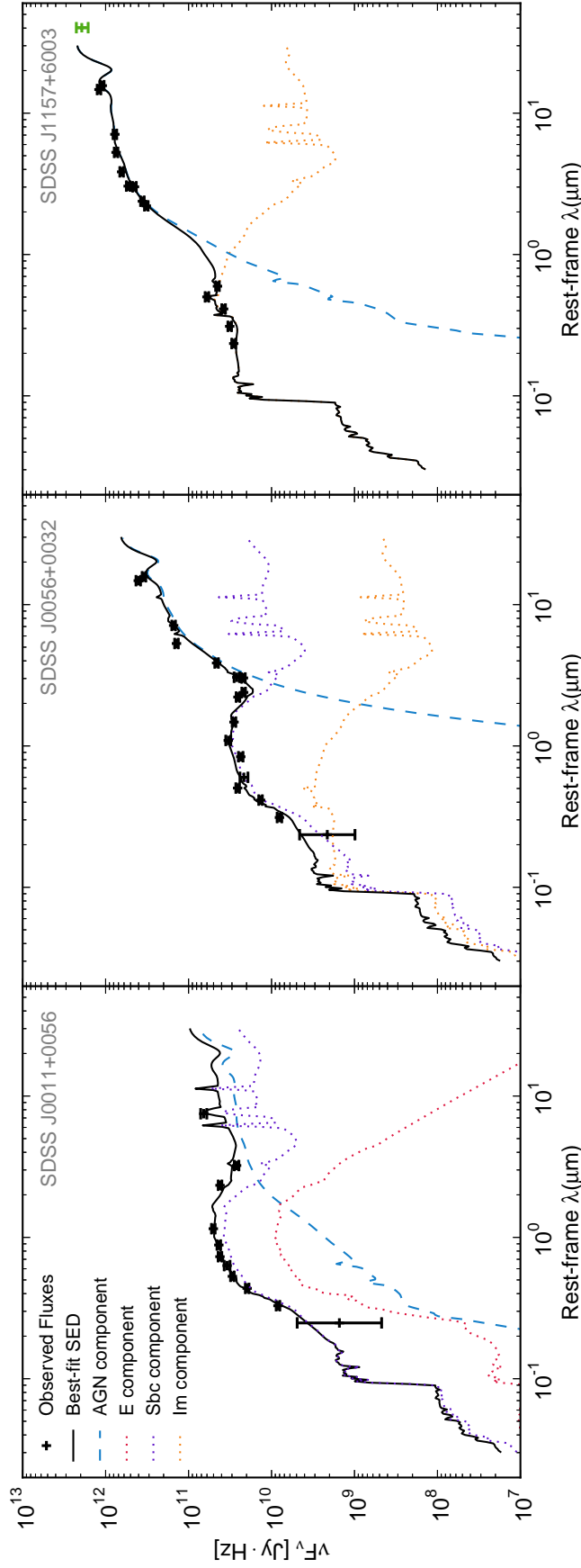
Figure 3.3: Near-UV to mid-IR SEDs for the three Type 2 quasars. The best-fitting model solutions (black line) were achieved using the AGN (blue dashed line) and galaxy (elliptical: red dotted line, spiral: purple dotted line, irregular: orange dotted line) templates of Assef et al. (2010). The photometric data (black data points) and best-fitting parameters are given in Table 3.3. The *IRAS* 60 μm flux for SDSS J1157 +6003 (green data point) was not used in the SED decomposition.

data point in Fig. 3.3), which lies beyond the wavelength range of the galaxy templates and was therefore excluded from the SED modelling. The data point is consistent with a simple extrapolation of the best-fitting model from shorter wavelengths. Zakamska et al. (2004) also detect SDSS J0056+0032 at 60 μm, but at a low significance level (80% confidence). In Table 3.3 we provide the best-fitting parameters $\hat{a}$ (the fractional contribution from the AGN component to the 0.1–30 μm emission after correction for dust reddening; Assef et al. 2010) and $L_{6\mu m}$ (the luminosity of the AGN component at rest-frame 6 μm after correction for dust reddening; νL_ν). The uncertainties on $\hat{a}$ and $L_{6\mu m}$ are standard deviations, derived from the Monte Carlo re-sampling of the data according to the photometric uncertainties. Both parameters are well constrained.[11] Since our SED modelling uses a single AGN template, it does not account for the fact that AGN show a range of heated dust emission relative to the bolometric emission of the accretion disk. For instance, assuming the distribution of quasar covering factors found by Roseboom et al. (2013) would introduce an additional uncertainty to the 6 μm luminosities of $\approx$ $\pm 0.5 L_{6\mu m}$. Our three Type 2 quasars have high $\hat{a}$ values, which indicates that they are AGN-dominated at 0.1–30 μm. For SDSS J0056+0032 and SDSS J1157+6003 this is in agreement with the *Spitzer*-IRS spectroscopy of Zakamska et al. (2008), which shows the sources to be AGN-dominated at mid-IR wavelengths (for SDSS J0011+0056 there is no mid-IR spectroscopy available).

3.4 Results

The three Type 2 quasars in this work bear the signatures of heavily obscured, Compton-thick AGN based on multi-wavelength diagnostics (see Section 2 of this work; Zakamska et al., 2008; Vignali et al., 2010; Jia et al., 2013). Here we present the results of our analysis, which is aimed at assessing the prevalence of extreme absorption in these systems.

X-rays provide a direct measure of AGN emission that has been subject to circum-nuclear absorption. As such, the characterisation of X-ray spectra is necessary to obtain

---

[11]Constraining $\hat{a}$ and $L_{6\mu m}$ is the primary purpose of our SED analysis. We do not read deeply into the host-galaxy properties of the best fitting solutions.

reliable estimates of absorbing column densities (N_H).[12] For SDSS J0011+0056 we detect X-rays over the observed-frame 3–24 keV energy range, and for SDSS J0056+0032 and SDSS J1157+6003 we place upper limits on the 3–24 keV emission (see Table 3.2). As the quasars are at best weak detections at 3–24 keV, detailed modelling of their X-ray spectra is unfeasible. For SDSS J0011+0056 we characterize the observed-frame 3–24 keV X-ray spectrum using the ratio of hard (8–24 keV) to soft (3–8 keV) emission, which provides a direct absorption constraint (see Section 3.4.1). For the remaining two quasars we are limited to indirect absorption constraints from the comparison of the observed X-ray emission with the intrinsic X-ray emission implied by infrared measurements (see Section 3.4.2).

3.4.1 Direct (X-ray) Absorption Constraints

SDSS J0011+0056 is detected with *NuSTAR* in the 8–24 keV band, but not in the 3–8 keV band. We measure a 99.7% confidence level lower limit for the *NuSTAR* X-ray band ratio (i.e., the ratio of 8–24 keV counts to 3–8 keV counts), of > 1.0. In Figure 3.4 we show the *NuSTAR* band ratio against redshift for SDSS J0011+0056 and the first 10 sources detected in the *NuSTAR* extragalactic survey (Alexander et al., 2013); the SDSS J0011 +0056 band ratio is amongst the most extreme. We compare the band ratio with predictions from a simple absorbed power-law (ZWABS·POW) model and the MYTORUS model (Murphy & Yaqoob, 2009), both of which are implemented in XSPEC. MYTORUS is a self-consistent physical model that is valid for the energy range 0.5–500 keV, and for column densities of $N_\mathrm{H} = 10^{22}$–10^{25} cm^{-2}. It is more suitable than the ZWABS·POW model for column densities of $N_\mathrm{H} \gtrsim 5 \times 10^{23}$ cm^{-2}, where a careful treatment of scattering and reflection is needed (for instance, see Figure 3.5). In the MYTORUS model, an obscuring torus reprocesses X-rays from a central source, and the resulting X-ray spectrum has both transmitted and scattered components. In the current implementation of MYTORUS, the half-opening angle of the obscuring medium is fixed to $60°$ (i.e., a covering factor of 0.5),

---

[12]All N_H values in this Section are line-of-sight column densities unless otherwise stated. In the MY-TORUS model, N_H is related to the equatorial column density ($N_{\mathrm{H,eq}}$) via Equation 1 in Murphy & Yaqoob (2009).
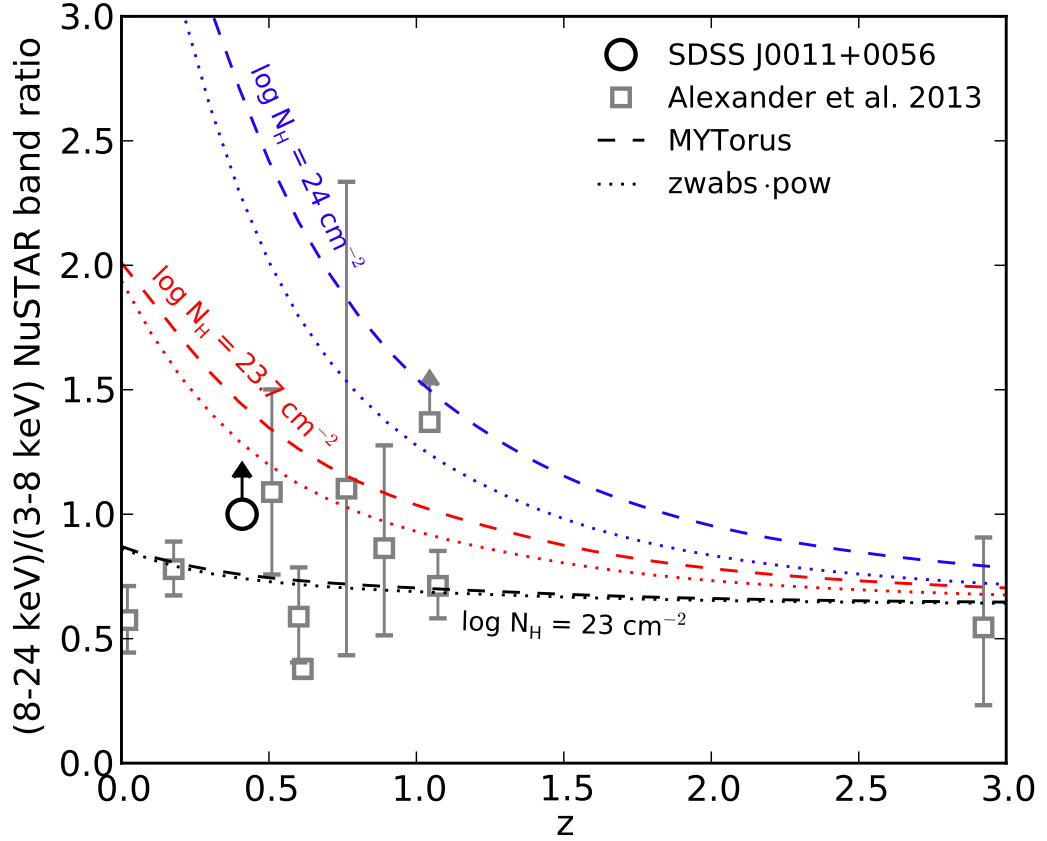
Figure 3.4: *NuSTAR* X-ray band ratio (8–24 keV to 3–8 keV counts ratio) against redshift for SDSS J0011+0056 (black circle), and the *NuSTAR*-detected sources in Alexander et al. (2013) (grey squares). The dashed and dotted lines show band ratio predictions from MY-TORUS and simple ZWABS·POW models respectively, for a variety of column densities, and assuming a spectral slope of $\Gamma = 1.8$. Varying θ_{obs} makes a negligible difference to the MYTORUS tracks. Based on the 99.7% lower limit for the *NuSTAR* band ratio, SDSS J0011+0056 is consistent with being heavily obscured.

a value inferred from the obscured AGN fraction of Seyfert galaxies. We note that a larger half-opening angle could be more appropriate in this study of Type 2 quasars, since the obscured AGN fraction is observed to decrease with luminosity (e.g., Ueda et al., 2003; Lusso et al., 2013). We assume a specific MYTORUS model with an intrinsic photon index of $\Gamma = 1.8$ (typical value for AGN at observed-frame 3–24 keV; Alexander et al. 2013) and an inclination angle of $\theta_{\mathrm{obs}} = 70°$, referred to as *Model A* hereafter. Varying θ_{obs} between 65° and 90°, where 90° corresponds to an edge-on view through the equatorial plane of the torus, makes a negligible difference to the MYTORUS band ratio tracks in Figure 3.4. We avoid using θ_{obs} values close to 60°, below which the line-of-sight X-ray emission does not intercept the torus and the MYTORUS model therefore describes an unobscured AGN. As shown in Figure 3.4, the *NuSTAR* band ratio lower limit for SDSS J0011+0056 corresponds to an absorbing column density of $N_{\mathrm{H}} \gtrsim 2.5 \times 10^{23}$ cm^{-2}. This implies heavy, but not necessarily Compton-thick, absorption.

Since *XMM-Newton* is more sensitive than *NuSTAR* at < 8 keV, we also measure an X-ray band ratio for SDSS J0011+0056 using the *XMM-Newton* 3–8 keV data and *NuSTAR* 8–24 keV data, which gives a *NuSTAR/XMM-Newton* band ratio of 1.2 ± 0.6 (68.3% confidence level). One limitation of the measurement is that we are unable to assess whether the X-ray emission of SDSS J0011+0056 has varied significantly in the ~ 6.5 years between the *XMM-Newton* and *NuSTAR* observations; if the *XMM-Newton* count rate is relatively low, we overestimate the band ratio, and vice versa. In Figure 3.5, we compare the measured *NuSTAR/XMM-Newton* band ratio with predictions from the MYTORUS and ZWABS·POW models as a function of column density. We fixed the model redshifts to that of SDSS J0011+0056 ($z = 0.409$), used a range of intrinsic photon indices corresponding to those observed for unobscured AGN ($1.7 < \Gamma < 2.3$; e.g., Mateos et al., 2010; Scott et al., 2011), and used a range of inclination angles in the MYTORUS model ($65° < \theta_{\mathrm{obs}} < 90°$). The resulting tracks in Figure 3.5 suggest that SDSS J0011+0056 is absorbed by $N_{\mathrm{H}} \gtrsim 5 \times 10^{23}$ cm^{-2}, which is consistent with the *NuSTAR* band ratio analysis (Figure 3.4). Assuming *Model A* ($\Gamma = 1.8$ and $\theta_{\mathrm{obs}} = 70°$), the observed *NuSTAR/XMM-Newton* band ratio for SDSS J0011+0056 implies a column density of $N_{\mathrm{H}} = (8.1^{+2.9}_{-3.4}) \times 10^{23}$ cm^{-2} (i.e. heavy, but not clearly Compton-thick, absorption is required to produce the observed 3–24 keV X-ray spectrum). This result is consistent with column density
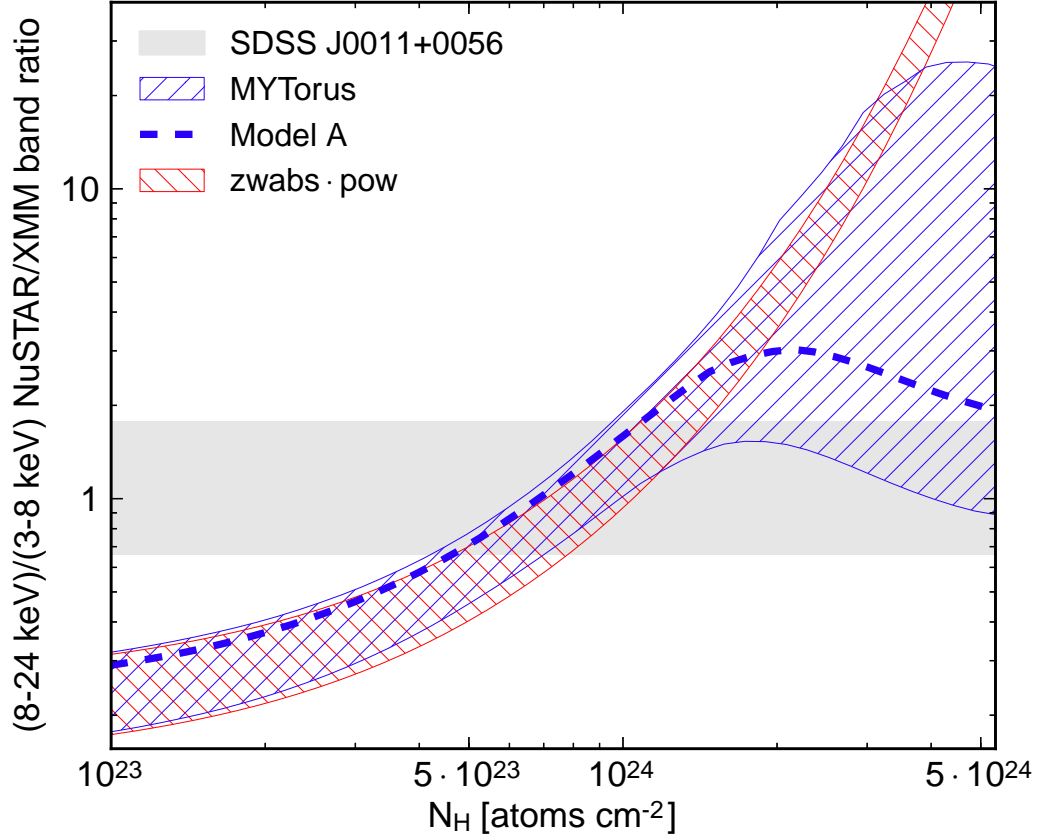
Figure 3.5: *NuSTAR/XMM-Newton* X-ray band ratio (*NuSTAR* 8–24 keV to *XMM-Newton* 3–8 keV count-rate ratio) against line-of-sight X-ray absorbing column density (N_H). The grey shaded area shows the 68.3% confidence level region for the observed band ratio of SDSS J0011+0056. The hashed regions show the range of band ratios predicted with MYTORUS (blue) and a simple ZWABS·POW model (red) for $z = 0.409$, and for a range of intrinsic photon indices ($1.7 < \Gamma < 2.3$). The MYTORUS region was computed for a range of inclination angles ($65° < \theta_\mathrm{obs} < 90°$). According to these models, SDSS J0011 +0056 is absorbed by $N_\mathrm{H} \gtrsim 5 \times 10^{23}$ cm^{-2}. We also show band ratio predictions for a specific MYTORUS model with $\Gamma = 1.8$ and $\theta_\mathrm{obs} = 70°$ (*Model A*; dashed blue line); on the basis of *Model A*, SDSS J0011+0056 is absorbed by $N_\mathrm{H} = (8.1^{+2.9}_{-3.4}) \times 10^{23}$ cm^{-2}.

estimates from indirect methods, as shown in Section 3.4.2. For comparison, the highest column densities directly constrained by Vignali et al. (2006, 2010) in their < 10 keV analysis of SDSS-selected Type 2 quasars are $N_H \approx 3 \times 10^{23}$ cm^{-2}.

The above N_H constraint for SDSS J0011+0056 must be treated with a degree of caution, since it depends on the assumed X-ray spectral model. Here we assess the impact on our result of two spectral complexities, both of which are important in the case of Type 2 quasars. First, a soft 'scattered' power law component is commonly observed for obscured AGN which may be either nuclear emission scattered by hot gas (e.g., Turner et al., 1997), or 'leakage' of nuclear emission due to partial covering (e.g., Vignali et al., 1998; Corral et al., 2011). Adding a scattered component which is 2% of the primary transmitted power law (a typical X-ray scattering fraction for Type 2 Seyferts; e.g., Turner et al., 1997) to *Model A*, we obtain a consistent result: $N_H > 4.9 \times 10^{23}$ cm^{-2} (68.3% confidence level lower limit). Second, the absorbing medium may have a complex geometry (e.g., a clumpy torus) that requires the equatorial and line-of-sight column densities of the MYTORUS model ($N_{H,eq}$ and N_H, respectively) to be treated independently. Decoupling these two parameters in *Model A* and setting $N_{H,eq}$ to the maximum possible value of 10^{25} cm^{-2} yields a consistent result: $N_H = (7.7^{+2.8}_{-3.4}) \times 10^{23}$ cm^{-2}. Last, we emphasize that although MYTORUS is a relatively complex model, the N_H constraints do not differ significantly from those using a simple ZWABS·POW model in the Compton-thin regime (see Figure 3.5). We conclude that the inferred N_H for SDSS J0011+0056 does not change significantly with the assumed spectral model.

3.4.2 Indirect Absorption Constraints

The X-ray emission in heavily obscured AGN is subject to significant absorption along the line of sight. The mid-IR emission, on the other hand, has been reprocessed by the dust obscuring the AGN and is less sensitive to extinction. The mid-IR luminosity therefore provides an estimate of the intrinsic AGN power. As such, the presence of absorption in an AGN can be inferred from the observed X-ray to mid-IR luminosity ratio (e.g., Lutz et al., 2004; Alexander et al., 2008; LaMassa et al., 2009; Goulding et al., 2011; LaMassa et al., 2011). We note that the mid-IR emission is also significantly absorbed for $\approx 50\%$ of Compton-thick AGN (e.g., Bauer et al., 2010; Goulding et al., 2012). Indeed, SDSS

J0056+0032 has significant Si-absorption at 9.7 μm, in contrast to SDSS J1157+6003 (see Section 3.2). To account for this, we have corrected our mid-IR luminosities for dust reddening (see Section 3.3.3). In Figure 3.6 we compare the rest-frame X-ray luminosities ($L_{\rm X}$) of our three Type 2 quasars with the rest-frame 6 μm luminosities ($L_{6\mu\rm m}$), exploring both the low energy (2–10 keV) and high energy (10–40 keV) X-ray regimes. For SDSS J0011+0056, $L_{2-10\rm keV}$ was obtained through photometry in the rest-frame 2–10 keV band using *XMM-Newton* data (see Section 3.3.2). For SDSS J0056+0032 and SDSS J1157 +6003, $L_{2-10\rm keV}$ was obtained through photometry in the observed-frame 0.5–8 keV band using *Chandra* data (see Section 3.3.2), and an extrapolation to the rest-frame 2–10 keV band assuming a power-law model with $\Gamma = 1.8$. The $L_{10-40\rm keV}$ values were obtained through a photometric analysis in the rest-frame 10–40 keV band using *NuSTAR* data (see Section 3.3.1). The 6 μm luminosities are from SED fitting (Section 3.3.3) and relate specifically to the emission from the AGN.

In the rest-frame 2–10 keV band, the Type 2 quasars fall below the intrinsic X-ray–mid-IR luminosity relation found for AGN in the local universe (Lutz et al., 2004); see Figure 3.6*a*. For comparison, we also show the non-beamed sources detected in the *NuS-TAR* extragalactic survey (Alexander et al., 2013), which lie within the scatter of the Lutz et al. (2004) relation. The 2–10 keV luminosity suppression of the three Type 2 quasars is expected given our selection and has previously been demonstrated for SDSS J0056 +0032 and SDSS J1157+6003 (Vignali et al., 2006, 2010). Assuming the suppression of the X-ray emission is due to absorption, as opposed to intrinsic X-ray weakness, we estimate the column densities of these systems by comparing with the X-ray to mid-IR luminosity ratios for AGN absorbed by $N_{\rm H} = 10^{24}$ cm^{-2} and $N_{\rm H} = 5 \times 10^{24}$ cm^{-2} (dash-dotted and dashed lines in Figure 3.6*a*, respectively). On the basis of this analysis, the 2–10 keV luminosities of SDSS J0056+0032 and SDSS J1157+6003 are consistent with being absorbed by a factor of $\gtrsim 300$, and therefore lie well within the Compton-thick region with $N_{\rm H} \gtrsim 5 \times 10^{24}$ cm^{-2}. The X-ray emission from SDSS J0011+0056, on the other hand, is suppressed by a factor of ≈ 7, but is still consistent with being Compton-thick or near Compton-thick ($N_{\rm H} \approx 10^{24}$ cm^{-2}). Since our 2–10 keV luminosities were calculated assuming a $\Gamma = 1.8$ power-law, which is probably not consistent with heavy absorption at $z \sim 0.5$, we repeated the flux calculations in Section 3.3.2 assuming $\Gamma = 0.6$ (the spectral
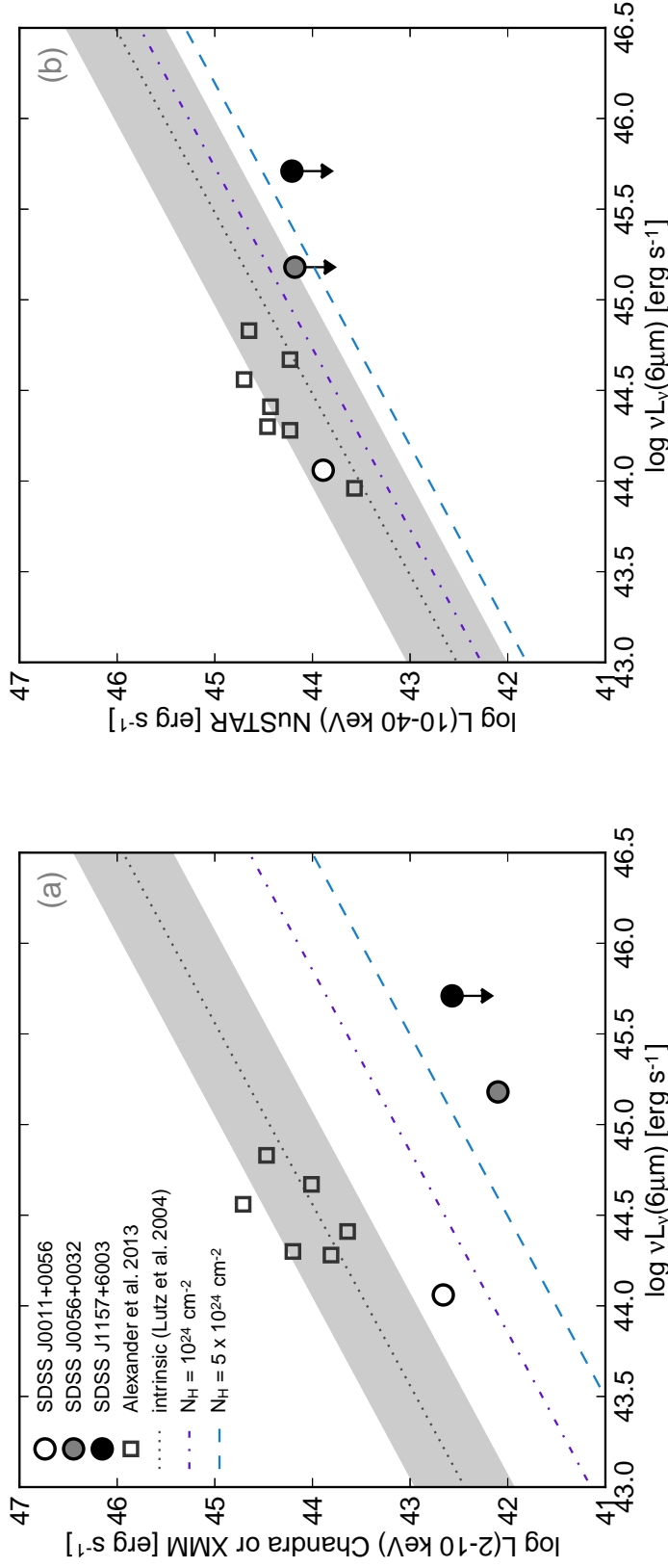
Figure 3.6: Rest-frame X-ray luminosity against rest-frame 6 μm luminosity for: (a) 2–10 keV luminosities calculated using *XMM-Newton* or *Chandra* data; and (b) 10–40 keV luminosities calculated using *NuSTAR* data. The X-ray luminosities are not corrected for absorption. SDSS J0011+0056, SDSS J0056+0032 and SDSS J1157 +6003 are shown as white, grey and black circles, respectively. We compare with sources detected as part of the *NuSTAR* extragalactic survey (open squares; Alexander et al., 2013). We also compare with an intrinsic relation for 2–10 keV, calibrated using local AGN (dotted line, with a shaded region indicating the scatter; Lutz et al., 2004). This relation has been extrapolated to the 10–40 keV band assuming $\Gamma = 1.8$, and to relations for AGN absorbed by $N_{\mathrm{H}} = 10^{24}$ cm^{-2} (dash-dotted line) and $N_{\mathrm{H}} = 5 \times 10^{24}$ cm^{-2} (dashed line) assuming a MYTORUS model with $\Gamma = 1.8$ and $\theta_{\mathrm{obs}} = 70°$. If we assume that low X-ray luminosities are due to absorption, sources that lie below the $N_{\mathrm{H}} = 10^{24}$ cm^{-2} tracks may be Compton-thick.

slope of SDSS J0011+0056 as measured by Jia et al. (2013); see Section 3.2). This results in $L_{2-10\text{keV}}$ values which are higher by a factor of ≈ 1.9; not enough to significantly change the conclusions drawn from Figure 3.6*a*.

In the rest-frame 10–40 keV band, the X-ray emission is only strongly suppressed for column densities of $N_{\text{H}} \gtrsim 5 \times 10^{24}$ cm^{-2}, and therefore *NuSTAR* observes the intrinsic X-ray emission for all but the most heavily obscured AGN; see Figure 3.6*b*. For comparison, Matsuta et al. (2012) studied *Swift*/BAT-detected AGN and found that for 14–195 keV, only $\approx 60\%$ of Compton-thick objects have significant X-ray suppression with respect to the intrinsic X-ray to mid-IR luminosity ratio. The results in Figure 3.6*b* suggest that the X-ray emission from SDSS J0011+0056 is not significantly suppressed at 10–40 keV, and is absorbed by $N_{\text{H}} \lesssim 10^{24}$ cm^{-2}. This is consistent with the X-ray band ratio analysis in Section 3.4.1. SDSS J0056+0032 is consistent with being Compton-thick, with $N_{\text{H}} \gtrsim 10^{24}$ cm^{-2}. SDSS J1157+6003 is the strongest candidate for being Compton-thick based on this analysis. Its 10–40 keV luminosity is consistent with being absorbed by a factor of $\gtrsim 10$, despite the high X-ray energies being probed, which again suggests an extreme column density of $N_{\text{H}} \gtrsim 5 \times 10^{24}$ cm^{-2}. Assuming $\Gamma = 0.6$, rather than $\Gamma = 1.8$, for the *NuSTAR* count rate to flux conversion (Section 3.3.1) results in $L_{10-40\text{keV}}$ values which are a higher by a factor of ≈ 1.4; again, not enough to significantly change the conclusions drawn from Figure 3.6*b*. As an independent test, we repeated our indirect analyses using [O III] luminosity as a measure of intrinsic AGN power (i.e., using $L_{\text{X}}/L_{[\text{OIII}]}$). This yielded very similar results; *NuSTAR* observes the intrinsic X-ray emission of SDSS J0011+0056, while SDSS J0056+0032 and SDSS J1157+6003 are consistent with being heavily Compton-thick ($N_{\text{H}} \gtrsim 5 \times 10^{24}$ cm^{-2}). However, since our sample was originally selected on the basis of high [O III] luminosity (Zakamska et al., 2003; Reyes et al., 2008), we consider the $L_{\text{X}}/L_{6\mu\text{m}}$ results to be more reliable. Nevertheless, the $L_{\text{X}}/L_{6\mu\text{m}}$ ratio alone is not a robust indicator of Compton-thick absorption, even if the 6 μm emission accurately reflects the intrinsic power of the AGN. First, some quasars can be intrinsically X-ray weak (e.g., Gallagher et al. 2001; Wu et al. 2011; Luo et al. 2013; Teng et al. 2014). Second, inferred column densities depend on the assumed X-ray spectral model (e.g., Yaqoob & Murphy, 2011; Georgantopoulos et al., 2011a). For instance, adding an additional soft scattered component, with a scattering fraction of 2%, to the MYTORUS

model predicts a $L_{2-10\mathrm{keV}}/L_{6\mu\mathrm{m}}$ ratio for $N_{\mathrm{H}} = 5 \times 10^{24}$ cm^{-2} which is a factor of three higher than that shown in Figure 3.6*b*. However, this is not enough to change our broad conclusions regarding the column densities of SDSS J0056+0032 and SDSS J1157+6003. Ultimately, deeper X-ray observations, with simultaneous coverage at low and high energies, are required to directly constrain N_{H} and provide more robust evidence for or against the presence of Compton-thick absorption in these Type 2 quasars.

3.5   Summary and Future Work

We have presented the first sensitive high energy (> 10 keV) analysis of optically selected Type 2 quasars. The sample consists of three objects that show evidence for Compton-thick absorption ($N_{\mathrm{H}} > 1.5 \times 10^{24}$ cm^{-2}) on the basis of different diagnostics (see Section 3.2). To summarize our main results:

- One of the Type 2 quasars, SDSS J0011+0056, is detected by *NuSTAR* with 16.8 ± 6.4 counts in the 8–24 keV band. The remaining two, SDSS J0056+0032 and SDSS J1157+6003, are not detected by *NuSTAR*; see Section 3.3.1.

- For SDSS J0011+0056, we characterize the 3–24 keV spectrum using the X-ray band ratio and find evidence for near Compton-thick absorption with $N_{\mathrm{H}} \gtrsim 5 \times 10^{23}$ cm^{-2}; see Section 3.4.1. This is consistent with the column densities inferred from the 2–10 keV to mid-IR ratio, the 10–40 keV to mid-IR ratio, and the X-ray to [O III] ratios; see Section 3.4.2.

- For SDSS J0056+0032 and SDSS J1157+6003, we find evidence for a significant suppression of the rest-frame 10–40 keV luminosity with respect to the mid-IR luminosity. If due to absorption, this result implies that these Type 2 quasars are extreme, Compton-thick systems with $N_{\mathrm{H}} \gtrsim 10^{24}$ cm^{-2}; see Section 3.4.2.

The characterisation of distant heavily obscured AGN is clearly an extremely challenging pursuit. Nevertheless, as we have demonstrated, the sensitive high energy observations of *NuSTAR* provide a significant improvement compared to *Chandra* or *XMM-Newton* observations alone; for quasars at $z \sim 0.5$, high column densities of $N_{\mathrm{H}} \gtrsim$

5×10^{23} cm^{-2} can now be directly constrained. Based on the results obtained in this exploratory study, we are now extending the analysis of optically selected Type 2 quasars to a larger sample which is currently being observed by *NuSTAR*. Furthermore, *NuSTAR* is undertaking deep surveys in the ECDFS (Mullaney et al. 2015) and COSMOS (Civano et al. 2015) fields, along with a large-area serendipitous survey (Alexander et al., 2013), that are likely to uncover a number of heavily obscured quasars. These upcoming studies will provide a leap forward in our understanding of the column density distribution of distant luminous AGN.

3.6 An Iron Line in the X-ray Spectrum of SDSS J0011

Here we discuss the identification of a strong Fe Kα line in the *XMM-Newton* spectrum of SDSS J0011+0056. The < 10 keV X-ray spectrum of SDSS J0011+0056 was first presented in J13. In this chapter we have extended the X-ray analysis to high energies and used the *NuSTAR/XMM-Newton* band ratio to identify heavy, close to CT, absorption ($N_{\mathrm{H}} \approx 8 \times 10^{23}$ cm^{-2}). Although we did not perform detailed spectral modelling, due to the low source counts (≈ 25 net source counts), studying the *XMM-Newton* 0.5–10 keV spectrum we find evidence for an excess at observed-frame ≈ 4.5 keV (i.e., rest-frame ≈ 6.4 keV). Modelling the continuum emission with a power law and the excess with a Gaussian component, the rest-frame line centroid energy is in good agreement with that expected for Fe Kα line emission ($E_{\mathrm{line}} = 6.4 \pm 0.1$ keV), and the rest-frame equivalent width is large (EW$_{\mathrm{Fe\ K\alpha}} = 2.9^{+2.5}_{-2.2}$ keV). This strong Fe Kα emission suggests CT absorption, and it adds confidence to the high column density measured.

Chapter 4

NuSTAR reveals extreme absorption in $z < 0.5$ Type 2 quasars

Abstract

The intrinsic column density ($N_{\rm H}$) distribution of quasars is poorly known. At the high obscuration end of the quasar population and for redshifts $z < 1$, the X-ray spectra can only be reliably characterized using broad-band measurements which extend to energies above 10 keV. Using the hard X-ray observatory *NuSTAR*, along with archival *Chandra* and *XMM-Newton* data, we study the broad-band X-ray spectra of nine optically selected (from the SDSS), candidate Compton-thick ($N_{\rm H} > 1.5 \times 10^{24}$ cm^{-2}) Type 2 quasars (CTQSO2s); five new *NuSTAR* observations are reported herein, and four have been previously published. The candidate CTQSO2s lie at $z < 0.5$, have observed [O III] luminosities in the range $8.4 < \log(L_{\rm [O\ III]}/L_\odot) < 9.6$, and show evidence for extreme, Compton-thick absorption when indirect absorption diagnostics are considered. Amongst the nine candidate CTQSO2s, five are detected by *NuSTAR* in the high energy (8–24 keV) band: two are weakly detected at the $\approx 3\sigma$ confidence level and three are strongly detected with sufficient counts for spectral modelling ($\gtrsim 90$ net source counts at 8–24 keV). For these *NuSTAR*-detected sources *direct* (i.e., X-ray spectral) constraints on the intrinsic AGN properties are feasible, and we measure column densities ≈ 2.5–1600 times higher and intrinsic (unabsorbed) X-ray luminosities ≈ 10–70 times higher than pre-*NuSTAR* constraints from *Chandra* and *XMM-Newton*. Assuming the *NuSTAR*-detected type 2 quasars are representative of other Compton-thick candidates, we make a correction to

the N_{H} distribution for optically selected type 2 quasars as measured by *Chandra* and *XMM-Newton* for 39 objects. With this approach, we predict a Compton-thick fraction of $f_{\mathrm{CT}} = 36^{+14}_{-12}$ %, although higher fractions (up to 76%) are possible if indirect absorption diagnostics are assumed to be reliable.

4.1 Introduction

Much of the cosmic growth of supermassive black holes is thought to occur during a phase of luminous, heavily obscured accretion: an obscured quasar phase (e.g., Fabian, 1999; Gilli et al., 2007; Treister et al., 2009). However, our current census of obscured quasars appears highly incomplete. While unobscured quasars were first discovered over 50 years ago (Schmidt, 1963b; Hazard et al., 1963), it is only in the last decade that (radio-quiet) obscured quasars have been discovered in large numbers (e.g., Zakamska et al., 2003; Hickox et al., 2007; Reyes et al., 2008; Stern et al., 2012; Assef et al., 2013; Donoso et al., 2014). Furthermore, it is only very recently that the most heavily obscured Compton-thick (with absorbing column densities of $N_{\mathrm{H}} > 1.5 \times 10^{24}$ cm^{-2}; hereafter CT) quasars have begun to be robustly identified at X-ray energies (e.g., Comastri et al., 2011; Gilli et al., 2011; Gandhi et al., 2014; Lanzuisi et al., 2015a).

Identifying and characterizing heavily obscured quasars is important for various reasons. Firstly, many less luminous AGNs in the local Universe appear to be CT ($\sim$ 20–30% of the total population; e.g., Risaliti et al. 1999; Burlon et al. 2011). While observational constraints are challenging for distant quasars, a significant population of luminous CT AGNs are expected from models of the cosmic X-ray background (CXB) spectrum (e.g., Comastri et al., 1995; Gilli et al., 2007; Treister et al., 2009; Draper & Ballantyne, 2010; Akylas et al., 2012; Ueda et al., 2014). Secondly, while the orientation-based unified model (e.g., Antonucci, 1993; Urry & Padovani, 1995) can account for the relative fractions of unobscured, obscured and CT AGNs observed in the local Universe, it is unclear whether a unified model or some evolutionary scenario (e.g., Sanders et al., 1988; Hopkins et al., 2008) is more appropriate at higher luminosities and redshifts. Indeed, the observed dependence of AGN obscuration on luminosity suggests a departure from the unified model (e.g., Ueda et al. 2003; Simpson 2005; Treister et al. 2010b; Iwasawa et al.

2012; Assef et al. 2015; Buchner et al. 2015; Lacy et al. 2015; but see also Mayo & Lawrence 2013). The above issues can be addressed using X-ray studies which aim to measure the column density (N_H) distribution and CT fraction of obscured quasars, important components of CXB models and important tools for understanding AGN models (e.g., Fabian et al., 2009; Draper & Ballantyne, 2010).

X-ray studies of heavily obscured quasars are extremely challenging. For instance, to-date very few optically selected obscured quasars (i.e., "Type 2" quasars or "QSO2s"; the definition of this term is provided in Section 4.2.1) have been unambiguously confirmed as CT using broad-band X-ray measurements extending to high energies (> 10 keV; e.g., Gandhi et al. 2014). Including the high-energy data is crucial. Firstly, the number of counts is inherently low at < 10 keV, due to photoelectric absorption of the X-ray continuum, which restricts the accuracy of X-ray spectral modelling and may lead to an underestimate of the absorbing column density and intrinsic luminosity. Secondly, important diagnostic features can be missed if the observed X-ray energy window is narrow. Such features include the photoelectric absorption cut-off (e.g., at ≈ 10 keV for a $z = 0.2$ AGN absorbed by $N_H = 10^{24}$ cm^{-2} gas), and features of Compton reflection/scattering from cold, dense gas. The latter become prominent when CT levels of photoelectric absorption deeply suppress the primary continuum, revealing strong Fe Kα fluorescent line emission at 6.4 keV and a Compton reflection "hump" at > 10 keV (e.g., George & Fabian, 1991), and may arise from an extended structure such as the torus of the unified model (e.g., Ghisellini et al., 1994).

NuSTAR (see Chapter 2) has further opened our window on the X-ray spectra of obscured AGNs, with sensitivity up to 78.4 keV. Recent studies have demonstrated that, in the case of heavily obscured quasars, the most accurate constraints on the absorbing column density and intrinsic X-ray luminosity come from a combination of both *NuSTAR* and *XMM-Newton*/*Chandra* data, which provide the broadest possible energy band pass for X-ray spectral modelling (e.g., Luo et al., 2013; Baloković et al., 2014; Del Moro et al., 2014; Lansbury et al., 2014; Gandhi et al., 2014).

In this chapter, we extend the work of Lansbury et al. (2014; hereafter L14; see Chapter 3 of this thesis) and Gandhi et al. (2014; hereafter G14), using *NuSTAR* to study the high-energy emission of SDSS-selected QSO2s which are candidates for being CT

(i.e., candidate "CTQSO2s"). The targets were initially selected based on [O III] λ5007 line emission (Zakamska et al., 2003; Reyes et al., 2008), thought to be an unbiased indicator of intrinsic AGN power (e.g., Heckman et al. 2005; LaMassa et al. 2010; but see also Hainline et al. 2013), and subsequently identified as CT candidates within the detection capabilities of *NuSTAR* using the low-energy X-ray data available (e.g., Jia et al., 2013). L14 (Chapter 3) looked at an exploratory sample of three $z = 0.41$–0.49 candidate CTQSO2s: one was weakly detected and shown to have a high column density of $N_H \gtrsim 5 \times 10^{23}$ cm^{-2}; the remaining two were undetected but shown to have suppressed X-ray luminosities in the high-energy regime, suggestive of CT absorption. G14 showed the lower redshift object SDSS J1034+6001 (also known as Mrk 34; $z = 0.05$) to have a column density and intrinsic power an order of magnitude greater than those measured with the pre-*NuSTAR* X-ray data, unambiguously revealing the object to be a CTQSO2.

We present new results for a further five targets, bringing the *NuSTAR*-observed SDSS-selected candidate CTQSO2 sample to a total size of nine objects. For the brightest two sources we model the broad-band X-ray spectra, for one weakly detected source we characterize the spectrum using the X-ray band ratio, and for all targets (including non-detections) we use the X-ray:mid-IR ratio to infer the intrinsic AGN properties. The chapter is organised as follows: Section 4.2 details the sample selection; Section 4.3 describes the X-ray and multiwavelength data, along with data reduction and analysis procedures; Section 4.4 presents the results of X-ray spectral and multiwavelength analyses; and Section 4.5 discusses the results for the full sample of nine *NuSTAR*-observed candidate CTQSO2s in the context of the parent QSO2 population, including an estimation of the N_H distribution and CT fraction for $z < 0.5$. The cosmology adopted is (Ω_M, Ω_Λ, h) = (0.27, 0.73, 0.71). Uncertainties and limits quoted throughout the chapter correspond to the 90% confidence levels (CL), unless otherwise stated.

4.2   The QSO2 Sample

4.2.1   Definitions

Quasars are rapidly accreting black holes which emit large amounts of radiation, and have luminosities which typically place them above the knee of AGN luminosity func-

tion. Multiple thresholds exist in the literature for separating quasars from less luminous AGNs (e.g., "Seyferts"). According to the classical threshold of Schmidt & Green (1983), quasars are those objects with absolute B–band magnitudes of $M_B < -23$. Thus far we have used the term "obscured" rather loosely, since it has different implications depending on the wavelength regime in question. In the optical band, objects are identified as obscured if they show narrow line emission without broad (e.g., Hα or Hβ) components, a result of the central broad line region being hidden from the observer. These objects are classed as type 2s, or QSO2s if the luminosity is at quasar levels (in type 1s the broad line components are visible). At X-ray energies, objects are identified as obscured or "absorbed" if their X-ray continua show evidence for being absorbed by gas along the line-of-sight, with column densities of $N_{\rm H} > 10^{22}$ cm^{-2}. The objects in this work originate from a sample of optically-identified QSO2s (Zakamska et al., 2003; Reyes et al., 2008). Several X-ray studies at < 10 keV have now provided evidence that these optically-identified QSO2s are also absorbed at X-ray energies, with many objects showing indirect evidence for being absorbed by column densities in excess of $N_{\rm H} = 1.5 \times 10^{24}$ cm^{-2} (i.e., CT columns; Vignali et al. 2006, 2010; Jia et al. 2013). In this chapter we look at the *direct* evidence for CT absorption in these optically-identified QSO2s, from X-ray analyses which incorporate spectral information at > 10 keV.

4.2.2 Sample Selection

When selecting a sample of obscured quasars to observe at X-ray energies, it is important to select based on an indicator of the intrinsic AGN luminosity such that the sample is unbiased and as representative of the general population as possible. The [O III] $\lambda 5007$ line, one of the strongest emission lines readily visible in the optical, is a suitable choice since such emission arises from gas on large (~ 100 pc) scales, minimizing the effect of nuclear obscuration. Reyes et al. (2008, hereafter R08; see also Zakamska et al. 2003) presented the largest sample of [O III]-selected QSO2s, consisting of 887 objects selected from the SDSS. R08 defined quasars as having observed (i.e., not corrected for extinction) [O III] luminosities of $L_{\rm [O\ III]} > 2 \times 10^8 L_\odot$, and identified the quasars as type 2s (i.e., QSO2s) following the standard optical definition. For comparison, the classical absolute magnitude cut of Schmidt & Green (1983, $M_B < -23$) corresponds approximately to

$L_{[\text{O III}]} > 3 \times 10^8 L_\odot$ for type 1 sources (Zakamska et al., 2003). Subsequent *Chandra* and *XMM-Newton* studies (e.g., Ptak et al., 2006; Vignali et al., 2006, 2010; Jia et al., 2013; LaMassa et al., 2014) have investigated the soft X-ray (< 10 keV) properties of subsamples of the R08 sample, with the largest subsample (71 objects) investigated by Jia et al. (2013, hereafter J13). Figure 4.1 shows redshift versus $L_{[\text{O III}]}$ for the R08 and J13 samples.

For our study, we select from the J13 sample. The latter is a sample of 71 Type 2 quasars which was obtained by cross-correlating the Reyes et al. (2008) SDSS-selected Type 2 quasar sample with the public *Chandra* and *XMM-Newton* archives (the 71 sources include both X-ray detections and non-detections). In order to infer information about the overall optically selected QSO2 population, we desire a parameter space for which the J13 sample is broadly representative of the R08 sample. As such we apply redshift and luminosity cuts of $z < 0.5$ and $L_{[\text{O III}]} > 2.5 \times 10^8 L_\odot$, respectively (see Figure 4.1). For these z and $L_{[\text{O III}]}$ ranges: (1) the z and $L_{[\text{O III}]}$ distributions of the J13 sample and the R08 sample are consistent according to the Kolmogorov-Smirnov (KS) test ($p = 0.64$ and 0.09 for z and $L_{[\text{O III}]}$, respectively); (2) the majority (74%) of the J13 sample are either serendipitous sources in the soft X-ray (*Chandra* and *XMM-Newton*) data or were targeted based on their [O III] properties, and should therefore be relatively unbiased with respect to the X-ray properties of the R08 sample. We exclude SDSS J0913+4056 ($z = 0.442$; $L_{[\text{O III}]} = 2.1 \times 10^{10} L_\odot$), since this infrared bright AGN is an extreme outlier and has been targeted for *NuSTAR* separately (D. Farrah et al., in preparation). The above cuts leave 42 QSO2s from J13, 39 of which are detected at < 10 keV (according to J13 and Vignali et al. 2006, 2010).

From the J13 subsample above, we first targeted an initial three candidate CTQSO2s at $z \approx 0.4$–0.5 (this subselection is described in Chapter 3). Since these three objects were weakly or not detected with *NuSTAR*, for the succeeding targets described herein greater consideration was given to the predicted *NuSTAR* 8–24 keV count rate.[1] The predictions (shown in Figure 4.2; these Figures are not published in Lansbury et al. 2015) were achieved by extrapolating from the < 10 keV data, assuming a variety of physically mo-

---

[1]The 8–24 keV band is the standard hard band defined for the *NuSTAR* extragalactic surveys (Alexander et al., 2013).
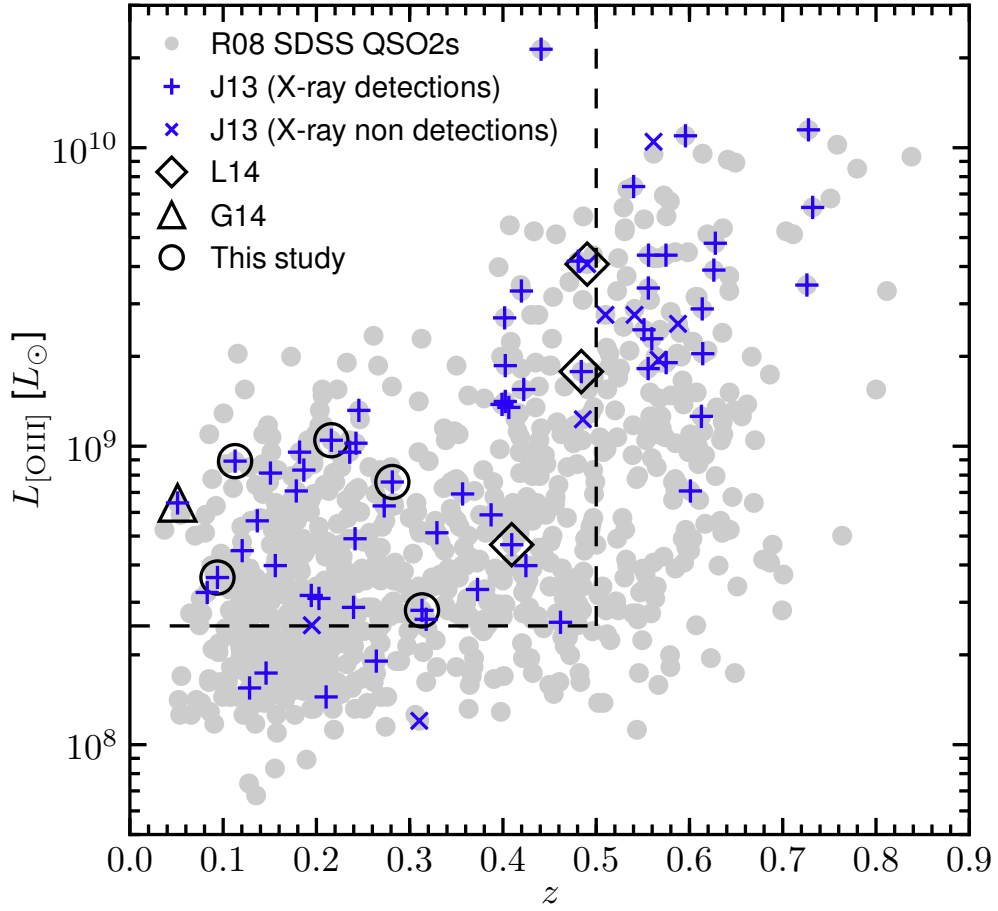
Figure 4.1: Observed (i.e., extinction-uncorrected) [O III] λ5007 line luminosity ($L_{\text{[O III]}}$) versus redshift (z). The R08 sample of SDSS-QSO2s is shown as grey dots. The J13 sample of *Chandra*- and *XMM-Newton*-observed objects is indicated in blue, with '+' and '×' symbols indicating < 10 keV detections and non detections, respectively (according to X-ray analyses in J13 and Vignali et al. 2006, 2010). The dashed lines mark out the parameter space used in this work ($z < 0.5$ and $L_{\text{[O III]}} > 2.5 \times 10^8 L_\odot$), for which the J13 sample is broadly representative of the R08 sample. Our *NuSTAR*-observed subsample of candidate CTQSO2s is highlighted by black points, with circles marking the five recently observed objects presented in this study, diamonds marking the three $z \approx 0.4$–0.5 objects presented in Chapter 3, and the triangle marking the low redshift ($z = 0.05$) object presented in G14.
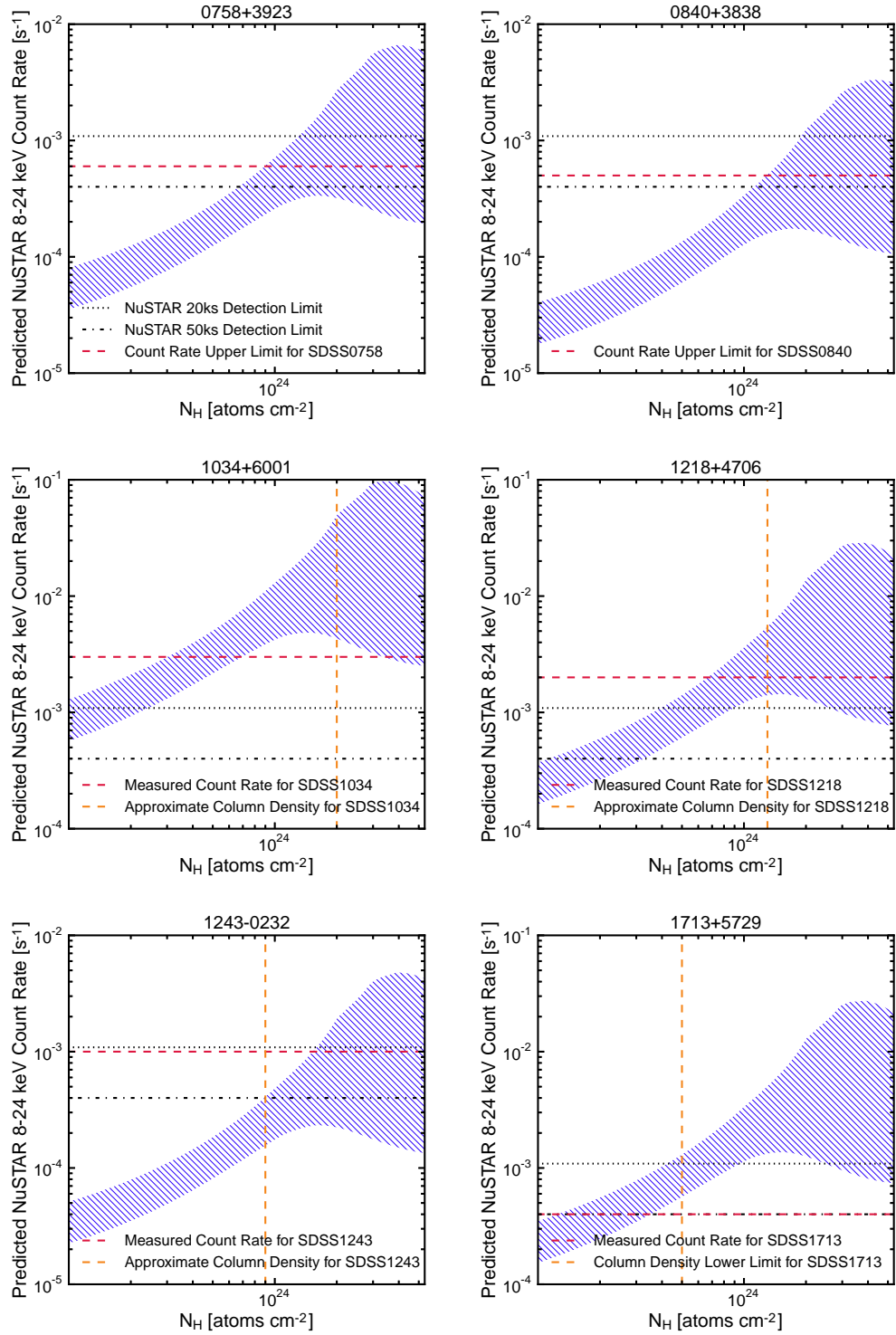
Figure 4.2: *NuSTAR* 8–24 keV count-rate predictions (blue hatched regions). These were achieved by extrapolating from the < 10 keV (e.g., *Chandra* or *XMM-Newton*) count-rates, assuming a variety of MY-TORUS models which cover a range of column densities ($10^{23} < N_H < 10^{25}$ cm^{-2}), intrinsic photon indices ($1.7 < \Gamma < 2.3$), and torus inclination angles (65–90°). We compare to the approximate *NuSTAR* detection limits (per FPM) for 20 ks and 50 ks exposures (dotted and dash-dotted lines, respectively), and to the post-observation count-rate and N_H constraints (red and orange dashed lines, respectively).

tivated torus models which cover a range of column densities ($10^{23} < N_{\mathrm{H}} < 10^{25}$ cm^{-2}). To the remainder of the J13 subsample above, we applied a cut in observed X-ray:[O III] luminosity ratio of $L^{\mathrm{obs}}_{2-10 \ \mathrm{keV}}/L_{\mathrm{[O\ III]}} < 1$ (a conservative threshold for targeting the most obscured candidates; see section 4.5 in J13), which leaves 12 CT candidates. From this selection, six objects were observed with *NuSTAR*, with preference being given to the objects with high 8–24 keV count rate predictions. These include the one object presented in G14 and the five presented in this chapter, bringing the *NuSTAR*-observed SDSS-selected candidate CTQSO2 sample to a total size of nine objects.

In this work we present results for the five recently observed candidate CTQSO2s SDSS J0758+3923, 0840+3838, 1218+4706, 1243–0232 and 1713+5729. For the other four previously-studied objects (SDSS J0011+0056, 0056+0032, 1034+6001 and 1157 +6003) the detailed reductions and data analyses are presented in L14 (Chapter 3) and G14. Redshifts and [O III] luminosities for the five new objects are listed in Table 4.1. The low-energy (< 10 keV) X-ray spectra have previously been characterized by J13, who fit the existing *Chandra* and *XMM-Newton* data with absorbed power law models. For SDSS J1218+4706, the column density constrained by J13 using this *direct* (i.e., X-ray spectral) approach is high, but less than CT ($N_{\mathrm{H}} = 8.0^{+5.6}_{-4.1} \times 10^{23}$ cm^{-2}). In the other four cases, the directly constrained column densities are comparatively low ($N_{\mathrm{H}} < 3 \times 10^{22}$ cm^{-2}). This is in strong disagreement with the extremely low X-ray:[O III] ratios, which imply CT absorption. J13 recognised this, and thus used indirect diagnostics to estimate the absorption levels. The low N_{H} measurements from direct spectral fitting can be explained as due to a combination of the limited energy ranges of *Chandra* and *XMM-Newton*, low source counts, and (especially in the case of SDSS J1713+5729; see Section 4.4.1 for further details) strong contamination at lower energies from other processes such as star formation, AGN photoionization, or scattered AGN emission. In Section 4.7 we give individual object information for the five candidate CTQSO2s presented in this chapter, including relevant multiwavelength properties and indicators of heavy absorption.

Table 4.1: X-ray Observation Log

			NuSTAR Observations				Soft X-ray Observations			
Object Name	z	$L_{[\text{O III}]}$	Observation ID	UT Date	t_{on}	t_{eff}	Observatory	Observation ID	UT Date	t
(1)	(2)	(3)	(4)	(5)	(6)	(7)	(8)	(9)	(10)	(11)
SDSS J075820.98+392336.0	0.216	9.02	60001131002	2014:255	48.3	41.2	*XMM-Newton*	0305990101	2006:108	9.1
								0406740101	2006:295	14.2
SDSS J084041.08+383819.8	0.313	8.45	60001132002	2014:121	50.5	38.4	*XMM-Newton*	0502060201	2007:289	19.0
SDSS J121839.40+470627.7	0.094	8.56	60001135002	2014:145	41.8	34.0	*XMM-Newton*	0203270201	2004:153	40.8
								0400560301	2006:321	43.2
SDSS J124337.34−023200.2	0.281	8.88	60001136002	2014:211	55.5	46.0	*Chandra*	6805	2006:115	10.0
SDSS J171350.32+572954.9	0.113	8.95	60001137002	2014:120	54.5	45.3	*XMM-Newton*	0305750401	2005:174	4.4

NOTE. – (1): Full SDSS object name. (2): Redshift. (3): Gaussian fit [O III] λ5007 line luminosity [$\log(L_{[\text{O III}]}/L_{\odot})$], as reported in R08. (4) and (5): *NuSTAR* observation ID and start date (YYYY:DDD), respectively. (6): Total on-source time (ks). (7): Effective on-axis exposure time (ks). This is the net value for the 3–24 keV band, and at the celestial coordinates of the target, after data cleaning. We have accounted for vignetting; despite the sources being "on-axis", there is a small loss of exposure due to the natural dither of the observatory. (8), (9) and (10): Soft X-ray observatory with available data, corresponding observation ID(s) and start date(s) (YYYY:DDD), respectively. (11): Net on-axis, flaring-corrected exposure time(s) (ks). For *XMM-Newton*, the quoted value corresponds to the EPIC detector used with the longest net exposure time.

4.3 Data

This section details the pointed *NuSTAR* observations and data analysis procedures for the five newly observed SDSS-selected candidate CTQSO2s (Section 4.3.1), which bring the *NuSTAR*-observed sample to a total of nine such objects. We also detail the archival *Chandra* and *XMM-Newton* data (Section 4.3.2), which facilitate a broad-band X-ray analysis when combined with the *NuSTAR* data. In addition, near-UV to mid-IR data from large-area surveys are presented in order to characterize the spectral energy distributions (SEDs) of the objects and disentangle AGN and host galaxy emission in the mid-IR (Section 4.3.3).

4.3.1 NuSTAR Data

Table 4.1 provides details, including dates and exposure times, for the most recent five *NuSTAR* observations of SDSS-selected candidate CTQSO2s. The data were processed as for the L14 sample (Chapter 3), using the *NuSTAR* Data Analysis Software (NuS-TARDAS) version 1.3.0. For the detected sources, the NUPRODUCTS task was used to extract spectra and response files. Following other recent *NuSTAR* studies (Alexander et al. 2013; L14; Luo et al. 2014), we perform photometry in the 3–24 keV, 3–8 keV, and 8–24 keV bands.[2] The photometry is performed for each FPM separately and also for combined FPMA+FPMB data (referred to hereafter as "FPMA+B"), to increase sensitivity. For source detection, we use prior knowledge of the SDSS coordinates and calculate no-source probabilities assuming binomial statistics (P_B), defining non detections as $P_\mathrm{B} > 1\%$ (i.e., $\lesssim 2.6\sigma$). For non detections we calculate upper limits on the net source counts using the Bayesian approach outlined in Kraft et al. (1991). For a detailed description of the source detection and aperture photometry procedures, we refer the reader to Chapter 3.

Table 4.2 summarizes the *NuSTAR* photometry. Two of the quasars, SDSS J1218 +4706 and 1243–0232, are strongly detected; the net source counts for FPMA+B in the 8–24 keV band are 188 and 90, respectively. Figure 4.3 shows the 8–24 keV no-source prob-

---

[2]The combination of the *NuSTAR* instrumental background and decrease in effective area with increasing energy means that 3–≈24 keV is the most useful energy band for faint sources.

Table 4.2: X-ray Photometry: *NuSTAR* Counts

Object Name	Net Counts (3–24 keV)			Net Counts (3–8 keV)			Net Counts (8–24 keV)		
SDSS J	FPMA	FPMB	FPMA+B	FPMA	FPMB	FPMA+B	FPMA	FPMB	FPMA+B
0758+3923	$30.4^{+17.9}_{-16.4}$	< 14.8	< 43.8	< 29.3	< 7.2	< 18.1	< 30.4	< 21.8	< 45.0
0840+3838	< 25.2	< 17.1	< 28.4	< 14.6	< 8.8	< 13.4	< 19.1	< 21.5	< 31.5
1218+4706	$122.9^{+20.8}_{-19.3}$	$127.2^{+21.6}_{-20.2}$	$249.9^{+29.5}_{-28.0}$	$32.4^{+12.6}_{-11.1}$	$32.4^{+13.3}_{-11.8}$	$64.7^{+17.8}_{-16.4}$	$91.4^{+17.1}_{-15.6}$	$96.7^{+17.7}_{-16.2}$	$188.0^{+24.1}_{-22.6}$
1243-0232	$56.8^{+19.9}_{-18.4}$	$60.4^{+21.7}_{-20.2}$	$116.9^{+28.9}_{-27.5}$	< 32.4	< 31.8	$33.8^{+18.8}_{-17.3}$	$40.0^{+15.8}_{-14.3}$	$49.6^{+17.2}_{-15.7}$	$89.6^{+22.8}_{-21.3}$
1713+5729	< 43.1	< 33.5	< 67.4	< 18.1	< 13.3	< 21.5	< 33.9	< 36.3	$38.1^{+19.6}_{-18.1}$

NOTE. – *NuSTAR* net source counts for the candidate CTQSO2s. FPMA and FPMB are the individual focal plane modules belonging to the two telescopes which comprise *NuSTAR*. "FPMA+B" refers to the combined FPMA+FPMB data.

abilities for the three fainter sources, SDSS J0758+3923, 0840+3838 and 1713+5729. Poisson, rather than binomial, no-source probabilities have been adopted for the purposes of the figure only, to aid inter-object comparison; these provide a good approximation of the binomial no-source probabilities (P_{B}) since the background counts are large (Weiss-kopf et al., 2007). Although SDSS J0758+3923 is formally undetected at 8–24 keV, it is only just below the adopted detection threshold for this band and is weakly detected in the broader 3–24 keV energy band, but for FPMA only ($P_{\mathrm{B}} = 0.63\%$). SDSS J0840+3838 is a non detection. SDSS J1713+5729 is weakly detected with FPMA+B for the 8–24 keV band only ($P_{\mathrm{B}} = 0.22\%$). In general, the detected sources have more net source counts in the 8–24 keV band, where the focusing soft X-ray observatories (e.g., *Chandra* and *XMM-Newton*) have little to no sensitivity, than in the 3–8 keV band, where *NuSTAR* and the soft X-ray observatories overlap. This can occur for heavily obscured AGNs, which have extremely flat X-ray spectra and are therefore brighter at $\gtrsim 8$ keV. Indeed, the single candidate CTQSO2 to be detected with *NuSTAR* in Chapter 3, SDSS J0011+0056, was only detected in the 8–24 keV band. *NuSTAR* FPMA+B 8–24 keV image cutouts for the three new targets detected in this energy band are shown in Figure 4.4. None of these three sources are detected in the most sensitive *Swift* BAT all-sky catalogues (e.g., Baum-gartner et al., 2013), and direct examination of the 104 month *Swift* BAT maps shows no excess above 2σ (for details of the maps and procedures, see Koss et al. 2013). Therefore, *NuSTAR* has provided the first real detections of these targets at high energies (> 10 keV).

For the *NuSTAR*-detected sources, it is important to rule out confusion with and con-tamination from other nearby X-ray sources. Both of these are extremely unlikely: in the soft X-ray (*Chandra* and *XMM-Newton*) imaging of the *NuSTAR*-detected sources, the only neighbouring source detected within $88''$ (i.e., the radial distance containing an encircled-energy fraction of $\sim 85\%$ for the *NuSTAR* PSF) of the SDSS positions lies at an angular separation of $51''$ from SDSS J1218+4706 (i.e., outside our adopted source aperture radius) and is a factor of ≈ 20 fainter in the *XMM-Newton* energy band.

Table 4.3 lists the aperture-corrected *NuSTAR* fluxes and rest-frame 10–40 keV lumi-nosities ($L_{10-40\ \mathrm{keV}}$; uncorrected for absorption). The fluxes were obtained using pho-tometry, assuming an effective photon index (i.e., for an unabsorbed power law model) of $\Gamma_{\mathrm{eff}} = 0.3$ and using count rate to flux conversion factors which account for the *NuS-*
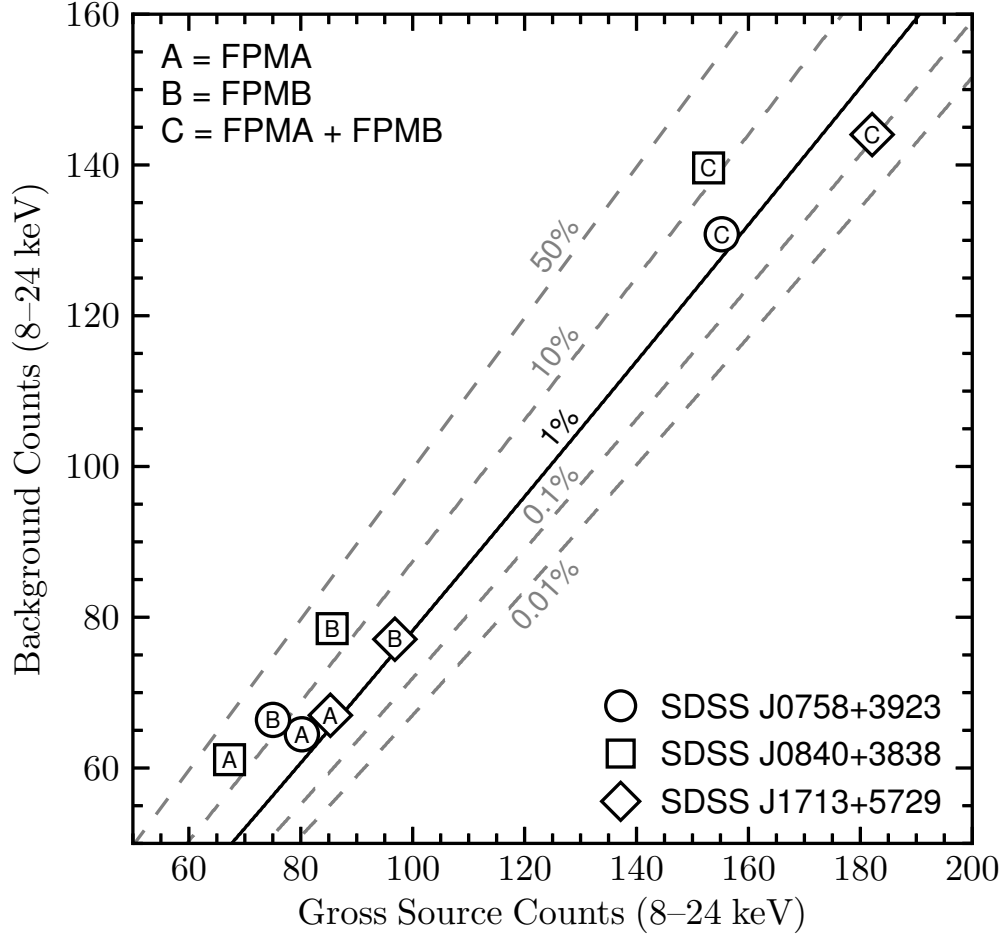
Figure 4.3: *NuSTAR* photometry at 8–24 keV for the faintest three sources, SDSS J0758 +3923, 0840+3838 and 1713+5729 (circles, squares and diamonds, respectively). Gross source counts and background counts (scaled to the source aperture) are shown. The dashed lines indicate tracks of constant Poisson no-source probability (a good approximation of P_B, given the large background counts considered here; Weisskopf et al. 2007). The solid black line shows our adopted detection threshold of $P_B = 1\%$. Only SDSS J1713+5729 is detected: while it is not detected in the individual FPMs, the increased sensitivity in FPMA+B (i.e., the combined FPMA+FPMB data) results in a significant detection, with $P_B = 0.22\%$.
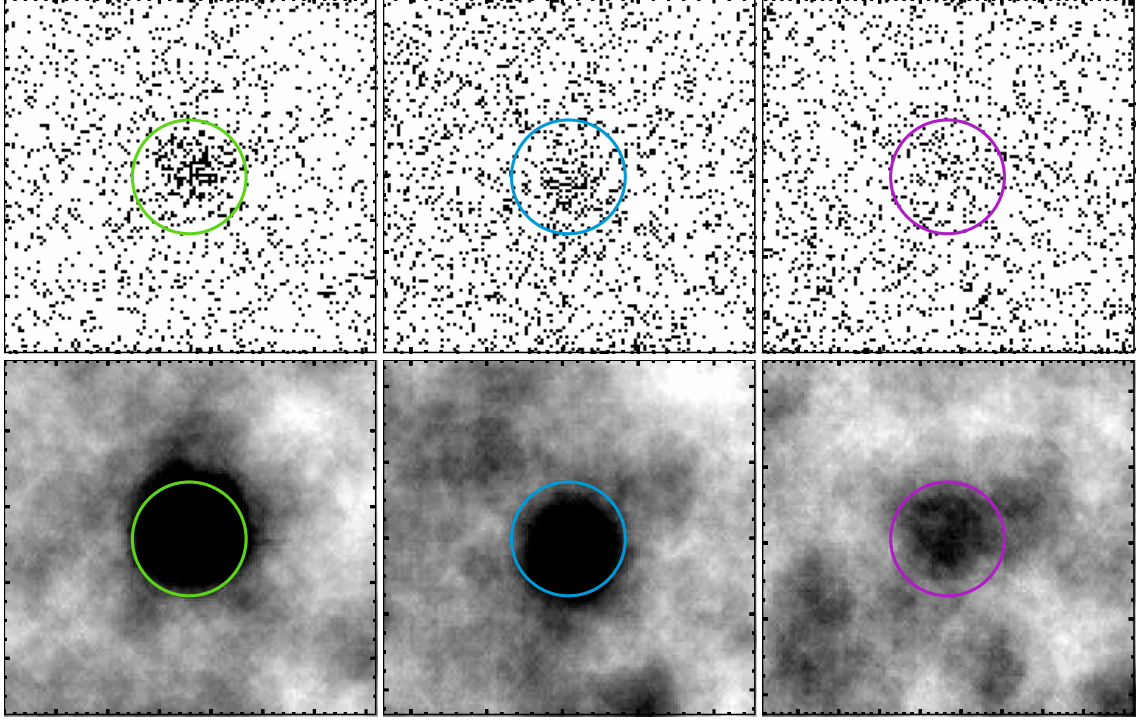
Figure 4.4: *NuSTAR* 8–24 keV images for the three objects detected in this energy band: SDSS J1218+4706, 1243–0232 and 1713+5729 (left to right, respectively). Top row: unsmoothed photon images. Bottom row: images smoothed with a top hat function of radius 14 pixels, corresponding to $34''\!.5$ (for aesthetic purposes only). The $45''$ radius source apertures are shown, centred on the SDSS positions. The major tickmarks indicate 1 arcmin offsets in right ascension (R.A.; horizontal axis) and declination (Decl.; vertical axis).

TAR response and effective area. Often $\Gamma_{\text{eff}} = 1.8$ (a typical value for the 3–24 keV emission of AGNs; e.g., Alexander et al. 2013) is assumed for such extrapolations, but the *NuSTAR*-detected candidate CTQSO2s have extremely flat observed spectral slopes at 3–24 keV (see Section 4.4), in agreement with $\Gamma_{\text{eff}} = 0.3$ in all cases. For each object our measured *NuSTAR* flux is in agreement with the soft X-ray observatory (*Chandra* or *XMM-Newton*) measurement at 3–8 keV, the energy band for which the observatories overlap. For the three faint or undetected sources (SDSS J0758+3923, 0840+3838 and 1713+5729), the $L_{10-40 \text{ keV}}$ values were obtained by extrapolating from the observed-frame 8–24 keV fluxes assuming $\Gamma_{\text{eff}} = 0.3$. For the two sources with good *NuSTAR* photon statistics (SDSS J1218+4706 and 1243–0232) the $L_{10-40 \text{ keV}}$ values were calculated using the best-fitting spectral models (Section 4.4.1).

4.3.2 Lower Energy X-ray Data

To incorporate lower energy (< 10 keV; or "soft") X-ray data in our study, we use archival *Chandra* and *XMM-Newton* observations, limiting the analysis to the 0.5–8 keV and 0.5–10 keV bands, respectively. Table 4.1 provides details of the archival soft X-ray observations, including dates and net exposure times. For the sources with poor photon statistics, we perform photometry using identical procedures to those for the *NuSTAR* photometry (see Section 4.3.1). For the sources with good photon statistics, we model the X-ray spectra with XSPEC (see Section 4.4.1). As mentioned in Section 4.3.1, source confusion is extremely unlikely: there are no neighbouring sources detected within $51''$ of the QSO2 positions. Measurements of the observed-frame 3–8 keV fluxes and rest-frame 2–10 keV luminosities (uncorrected for absorption) are listed in Table 4.3.

For the source with *Chandra* coverage (SDSS J1243–0232), we process the data using CHANDRA_REPRO.[3] The source events are extracted from a circular $2''.5$ radius aperture. The background events are extracted from a background source-free annulus centred on the source coordinates, with an inner radius of $8''$ and an outer radius of $80''$. Since SDSS J1243–0232 is on-axis, a large fraction ($\gtrsim 90\%$) of the source counts lie within the source aperture. Given this, and the extremely low net source counts measured (9),

---

[3]http://cxc.harvard.edu/ciao/ahelp/chandra_repro.html

Table 4.3: Multiwavelength Flux and Luminosity Measurements

Object	Observed-frame Flux (10^{-13} erg s^{-1} cm^{-2})				Rest-frame Luminosity (10^{42} erg s^{-1})				
	Chandra / XMM	NuSTAR			Chandra / XMM	NuSTAR	SED Modelling		
SDSS J	3–8 keV	3–8 keV	3–24 keV	8–24 keV	2–10 keV	10–40 keV	6 μm	$\hat{a}$ 0.1–30 μm	$\hat{f}_{6\mu m}$ 6 μm
(1)	(2)	(3)	(4)	(5)	(6)	(7)	(8)	(9)	(10)
0758+3923	$0.13^{+0.03}_{-0.02}$	< 0.12	< 0.69	< 0.93	$2.33^{+0.40}_{-0.35}$	< 23.22	347 ± 19	0.88 ± 0.01	0.97 ± 0.00
0840+3838	< 0.13	< 0.09	< 0.48	< 0.69	< 3.93	< 35.23	130 ± 10	0.63 ± 0.03	0.73 ± 0.04
1218+4706	$0.57^{+0.05}_{-0.47}$	$0.49^{+0.13}_{-0.12}$	$4.66^{+0.55}_{-0.52}$	$4.49^{+0.58}_{-0.54}$	$1.38^{+0.10}_{-1.13}$	$14.00^{+44.53}_{-1.17}$	73 ± 3	0.91 ± 0.01	0.99 ± 0.01
1243−0232	$0.15^{+0.08}_{-0.09}$	$0.19^{+0.11}_{-0.10}$	$1.65^{+0.41}_{-0.39}$	$1.62^{+0.41}_{-0.39}$	$5.74^{+0.69}_{-0.56}$	$54.60^{+5.22}_{-5.67}$	25 ± 4	0.30 ± 0.04	0.52 ± 0.07
1713+5729	< 0.30	< 0.12	< 0.95	$0.69^{+0.35}_{-0.33}$	< 1.07	$4.76^{+2.45}_{-2.26}$	305 ± 21	0.92 ± 0.02	$0.99^{+0.01}_{-0.03}$

NOTE. – Columns (2) to (7): Hard X-ray (*NuSTAR*) and soft X-ray (*Chandra* or *XMM-Newton*) fluxes and luminosities. The rest-frame X-ray luminosities are observed values, i.e. uncorrected for absorption, and are in units of 10^{42} erg s^{-1}. The *NuSTAR* fluxes are from photometry in three observed-frame energy bands, assuming $\Gamma_{\mathrm{eff}} = 0.3$. The rest-frame 10–40 keV luminosities are determined from the best-fitting spectral models (Section 4.4.1) for SDSS J1218+4706 and 1243−0232, and by extrapolating from the observed-frame 8–24 keV band (assuming $\Gamma_{\mathrm{eff}} = 0.3$) for SDSS J0758+3923, 0840+3838 and 1713+5729. The *Chandra* and *XMM-Newton* fluxes and luminosities are determined from spectroscopy for SDSS J0758+3923, 1218+4706 and 1243−0232, and from aperture photometry in the observed-frame 3–8 keV and rest-frame 2–10 keV bands for SDSS J0840+3838 and 1713+5729 (assuming $\Gamma_{\mathrm{eff}} = 0.3$). Columns (8) to (10): Best-fit parameters from the near-UV to mid-IR SED modelling in Section 4.3.3. The errors shown correspond to standard deviations from a Monte Carlo re-sampling of the photometric data. Column (8): rest-frame 6 μm luminosity for the AGN only, $L_{6\mu m}$ (νL_{ν}), in units of 10^{42} erg s^{-1}. This value is intrinsic (i.e., corrected for dust extinction). Column (9): The fractional contribution of the AGN to the total integrated intrinsic luminosity between 0.1 and 30 μm. Column (10): The fractional contribution of the AGN to the observed (i.e., uncorrected for dust extinction) monochromatic rest-frame 6 μm flux.

contamination of the background region by source counts is negligible.

For the sources with *XMM-Newton* coverage, we analyse data products from the Pipeline Processing System (PPS) using the *Science Analysis Software* (SAS v.13.5.0). To determine appropriate count rate thresholds for background flare subtraction, we visually examine the light curves. In all cases the fraction of exposure time removed is $\leq 30\%$, except in the case of obsID 0305750401 where the fraction is 49%. The exposure times in Table 4.1 are flaring-corrected. The source events are extracted from circular regions of 8–$20''$ radius (depending on source brightness and off-axis angle). The background events are extracted from regions of area $70 \times 70''$ to $140 \times 140''$, using either an annulus centred on the source position or an offset region if it is necessary to avoid chip-gaps or nearby sources. We combine the MOS1 and MOS2 data using the SAS task EPICSPECCOMBINE, and simultaneously fit the PN and MOS data when performing spectral analyses.

In the case of SDSS J1218+4706, we use the two archival *XMM-Newton* observations with the longest exposures and most recent start dates (obsIDs 0203270201 and 0400560301). For obsID 0203270201, SDSS J1218+4706 lies close to the on-axis position. In this instance we only use the MOS data, since the source lies on a chip-gap for PN. For obsid 0400560301, SDSS J1218+4706 lies far off-axis. In this case we only use the PN data, since the source lies on a chip-edge in MOS1, and there are relatively low net counts with MOS2 (65).

4.3.3 Near-UV to Mid-IR SED Analysis

Here we analyse near-UV to mid-IR (0.3–30 μm) spectral energy distributions (SEDs) for the five candidate CTQSO2s presented in this work, and the one presented in G14 (SDSS J1034+6001), with the primary aim of reliably measuring the AGN emission at mid-IR wavelengths. The photometric data (shown in Figure 4.5) are collated from the SDSS (Data Release 7; York et al., 2000), the *WISE* All-Sky source catalogue (Wright et al., 2010), and the *Spitzer* (Werner et al., 2004) Enhanced Imaging Products Source List (for SDSS J1243–0232 only). The SDSS fluxes are corrected for Galactic extinction. The photometric data adopted are provided in Section 4.8. In order to provide a consistent SED analysis across the full sample of nine *NuSTAR*-observed candidate CTQSO2s, we use the same SED decomposition procedure as that applied in Chapter 3 to the initial three
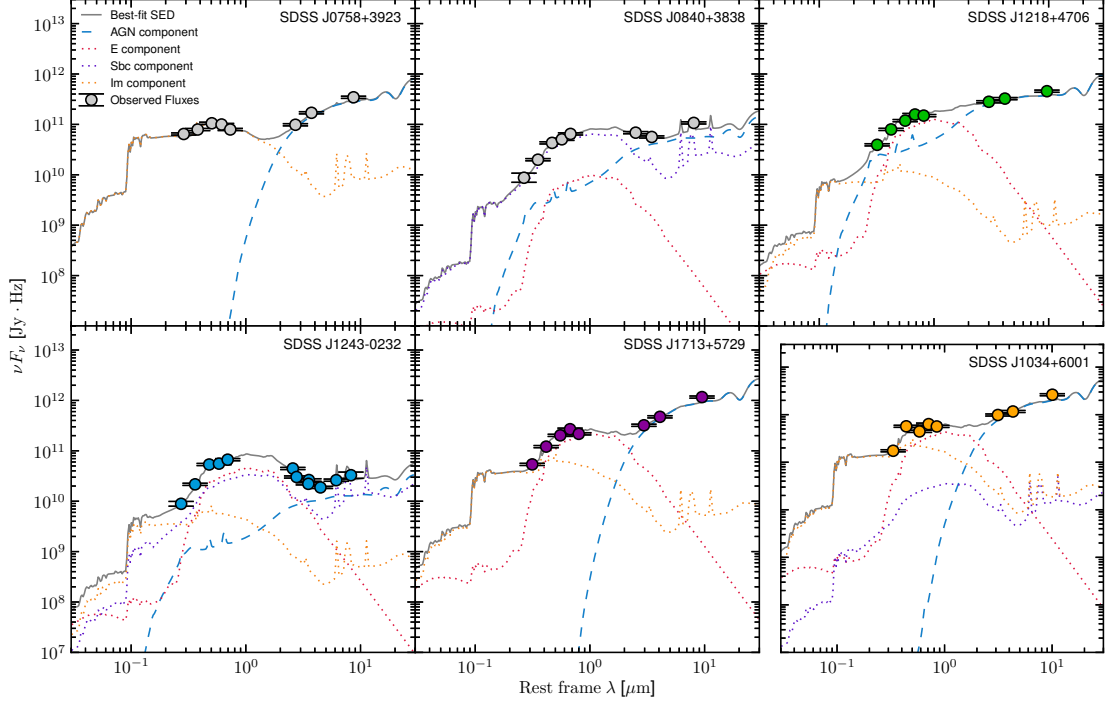
Figure 4.5: Near-UV to mid-IR spectral energy distributions (SEDs) for the five candidate CTQSO2s presented in this work, and the one (SDSS J1034+6001) presented in G14. AGN (blue dashed curve) and galaxy (dotted curves) templates were combined in the best-fit modelling of the photometric data (coloured circles for the sources detected at 8–24 keV with *NuSTAR*, and grey circles for the 8–24 keV non-detections), following Assef et al. (2008, 2010, 2013). The three galaxy templates correspond to an old stellar population ("elliptical" or E; red), ongoing star formation ("spiral" or Sbc; purple), and a starburst population ("irregular" or Im; orange). The gray curve shows the combined model solution. The systems are all AGN-dominated in the mid-IR waveband based on this analysis, except for SDSS J1243–0232, which has comparable contributions from the AGN and the host galaxy; see Table 4.3.

objects. Following the methodology detailed in Assef et al. (2008, 2010, 2013), each SED is modelled as the best-fit, non-negative, linear combination of four empirical templates (Assef et al., 2010), including one AGN template and three galaxy templates for: an old stellar population ("elliptical" or E), ongoing star formation ("spiral" or Sbc), and a starburst population ("irregular" or Im). The internal dust extinction of the AGN component is included as a free parameter in the modelling. The model solutions are shown in Figure 4.5, and the following best-fitting parameters are listed in Table 4.3: $\hat{a}$, the fractional contribution of the AGN to the total intrinsic (i.e., corrected for the dust extinction of the AGN component) integrated 0.1–30 μm luminosity; $\hat{f}_{6\mu\mathrm{m}}$, the fractional contribution of the AGN to the total observed (i.e., uncorrected for the dust extinction of the AGN component) monochromatic rest-frame 6 μm flux; and $L_{6\mu\mathrm{m}}$, the intrinsic AGN luminosity at rest-frame 6 μm (νL_ν). The errors represent standard deviations from a Monte Carlo re-sampling of the photometric data over $1\,000$ iterations, and thus account for possible model degeneracies. In all cases the integrated light properties (i.e., the total galaxy and AGN contributions) are well constrained, which is required to accurately determine $\hat{a}$, $\hat{f}_{6\mu\mathrm{m}}$ and $L_{6\mu\mathrm{m}}$. Since the primary goal of the SED modelling was to reliably measure these parameters, we do not make inferences about the host galaxy properties from the best-fit combination of host galaxy templates. SDSS J1034+6001, not shown in Table 4.3 since the X-ray analysis is presented in G14, has $L_{6\mu\mathrm{m}} = (1.20 \pm 0.09) \times 10^{44}$ erg s^{-1}, $\hat{a} = 0.90 \pm 0.02$, and $\hat{f}_{6\mu\mathrm{m}} = 0.98^{+0.02}_{-0.03}$.

The $\hat{a}$ constraints demonstrate that the candidate CTQSO2s in Figure 4.5 require an AGN component at a very high confidence level, and that in general the AGN contributes strongly to the intrinsic emission across the broad 0.1–30 μm wavelength range (all but one object have $\hat{a} \gtrsim 0.6$). The high $\hat{f}_{6\mu\mathrm{m}}$ values (all but one have $\hat{f}_{6\mu\mathrm{m}} \gtrsim 0.7$) indicate that the observed monochromatic 6 μm fluxes are AGN-dominated. The presence of an AGN at mid-IR wavelengths may also be inferred using *WISE* colour diagnostics. In Figure 4.6 we show the six objects from Figure 4.5, and the three from Chapter 3, on the *WISE* $W1$–$W2$ (i.e., [3.4 μm]–[4.6 μm]) versus $W2$–$W3$ (i.e., [4.6 μm]–[12.0 μm]) plane. Generally, sources with larger $W1$–$W2$ values have stronger AGN contributions. We compare with the AGN 'wedge' of Mateos et al. (2013) and the $W1$–$W2$ colour cut of Stern et al. (2012), which may be used to identify AGN-dominated systems. Out of

the total sample of nine candidate CTQSO2s, five are AGN-dominated according to both criteria, and one (SDSS J0056+0032) falls below the Mateos et al. (2013) wedge but lies above the Stern et al. (2012) cut. This is in good agreement with the SED modelling for these sources, where $\hat{a} \gtrsim 0.9$ in all cases. The remaining three sources (SDSS J0011 +0056, 0840+3838 and 1243–0232) fall below both of the selection regions, although SDSS J0840+3838 is consistent with satisfying the Stern et al. (2012) AGN selection criterion given the errors. This supports the SED modelling, from which it is concluded that these three sources are the least AGN dominated ($\hat{a} \approx 0.3$–0.6, and $\hat{f}_{6\mu m} \approx 0.5$–0.7). The *WISE* colours of the objects agree with the expectations; in general, the CTQSO2 population appears to follow the *WISE* colour distribution of the total QSO2 population, with a fraction of objects ($\sim 70\%$) lying within the AGN wedge (Mateos et al., 2013). In the local Universe, $\sim 40\%$ of the currently known bona fide CT AGNs lie within the wedge (Gandhi et al., 2015).

In addition to the near-UV to mid-IR SED, one of the candidate CTQSO2s presented in this work (SDSS J1713+5729) has a detection at far-IR wavelengths with *IRAS* which allows us to assess the extent to which star formation could contribute to the soft X-ray emission (Section 4.4.1).

4.4   Results

To summarise the *NuSTAR* source detection for the five SDSS-selected candidate CTQSO2s presented in this work: two are strongly detected, one is weakly detected, and two are un-detected by *NuSTAR* in the high energy band (8–24 keV). In Section 4.4.1 we present the results of X-ray spectral fitting with XSPEC for the three brightest objects. In Section 4.4.2 we present the X-ray band ratios of all of the *NuSTAR*-detected candidate CTQSO2s, comparing to model predictions. For the weakly detected source SDSS J1713+5729, this is an appropriate method for characterizing the broad-band X-ray spectrum. These two sections give *direct* (i.e., X-ray spectral) constraints on absorbing column densities ($N_{\rm H}$). In Section 4.4.3, we present *indirect* constraints from a multiwavelength diagnostic for the entire sample, including *NuSTAR* non-detections.

First we take a brief look at the overall X-ray spectral shapes for the full sample
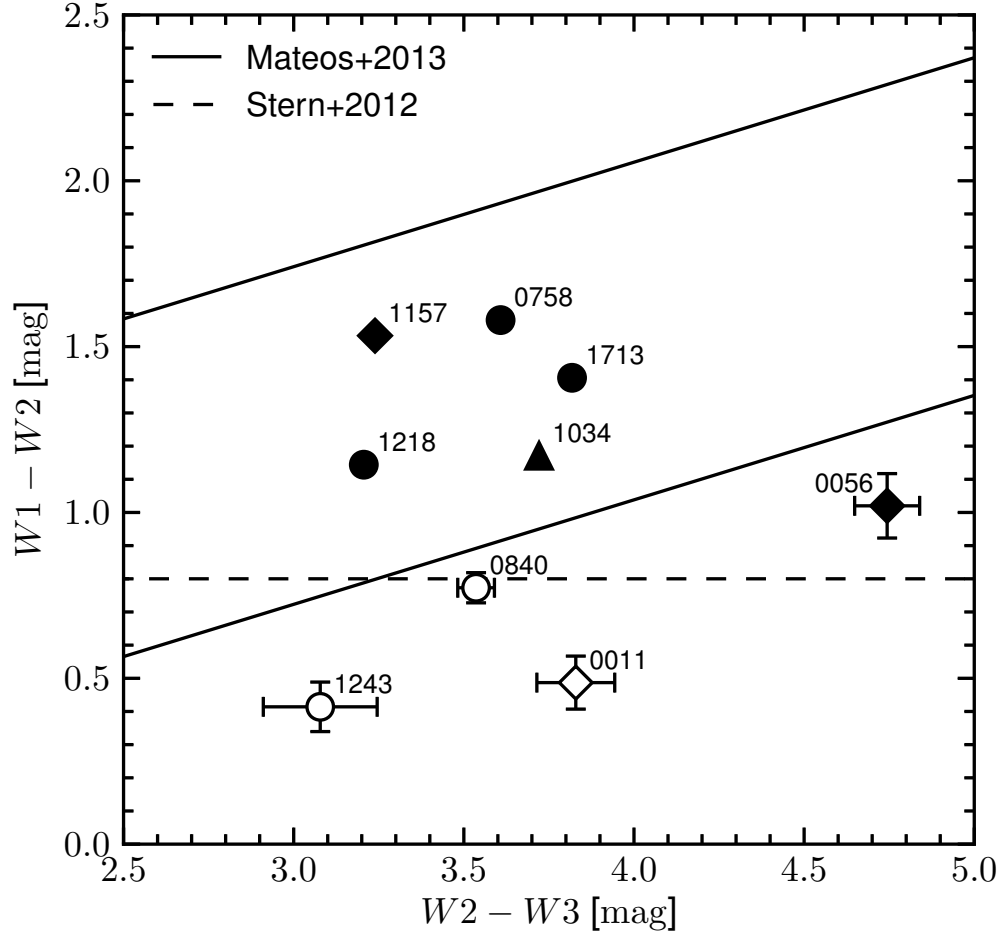
Figure 4.6: *WISE* colour–colour diagram for the *NuSTAR*-observed SDSS-selected candidate CTQSO2s from this study (circles), G14 (triangle) and Chapter 3 (L14; diamonds). We compare with the AGN colour cut of Stern et al. (2012; $W1$–$W2 \geq 0.8$) and the AGN 'wedge' of Mateos et al. (2013). The filled and empty symbols mark sources which are strongly AGN-dominated ($\hat{a} \gtrsim 0.9$) and less AGN-dominated ($\hat{a} \lesssim 0.6$), respectively, at mid-IR wavelengths according to our SED modelling. For the five objects that lie within the AGN wedge, the error bars are smaller than the symbols.

of nine *NuSTAR*-observed candidate CTQSO2s. Figure 4.7 shows the effective photon indices (Γ_{eff}), measured through unabsorbed power law fits to the individual *Chandra* or *XMM-Newton* (0.5–8 keV) and *NuSTAR* (3–24 keV) spectra. The spectral shapes observed by *Chandra* and *XMM-Newton* vary significantly over an order of magnitude in (non absorption corrected) rest-frame 2–10 keV luminosity. The increase in Γ_{eff} (0.5–8 keV) toward lower luminosities may reflect an increase in the relative contribution to the low-energy spectra from processes unrelated to the direct AGN emission, such as thermal plasma emission due to star formation or AGN-powered photoionization. In contrast, the spectra seen by *NuSTAR* are consistent with having the same effective photon index: excluding upper limits, the mean is Γ_{eff} (3–24 keV) ≈ 0.3.

4.4.1 X-ray Spectral Analysis: Best-fit Modelling

Here we use broad-band X-ray spectral modelling for the two brightest *NuSTAR*-detected sources presented in this chapter (SDSS J1218+4706 and SDSS J1243–0232) to measure intrinsic properties: the intrinsic absorbing column density (N_{H}), the intrinsic photon index (Γ), and the intrinsic X-ray luminosity (L_{X}). Additionally, we investigate the low energy X-ray spectrum of SDSS J1713+5729. The X-ray spectral fitting is performed using XSPEC version 12.8.1j (Arnaud, 1996). In all cases we account for Galactic absorption using a PHABS multiplicative component, with column densities fixed at values from Kalberla et al. (2005).

SDSS J121839.40+470627.7

SDSS J1218+4706 has the strongest *NuSTAR* detection in the 8–24 keV band, with net source counts of $S_{8-24\,\text{keV}} = 188$ for FPMA+B. The *NuSTAR* data are complemented by relatively high quality soft X-ray data, with two long *XMM-Newton* exposures (obsIDs 0203270201 and 0400560301; see Table 4.1). Below we analyse the broad-band (0.5–24 keV) *NuSTAR* plus *XMM-Newton* dataset (shown in Figure 4.8). The modelling approach taken is similar to that adopted by G14 for SDSS J1034+6001, the other brightest source in the *NuSTAR*-observed QSO2 sample, which has comparable photon statistics ($S_{8-24\,\text{keV}} = 182$). We group the data by a minimum of 20 counts per bin, and use χ^2 minimisation (statistic chi in XSPEC) to constrain parameters. We note that using,
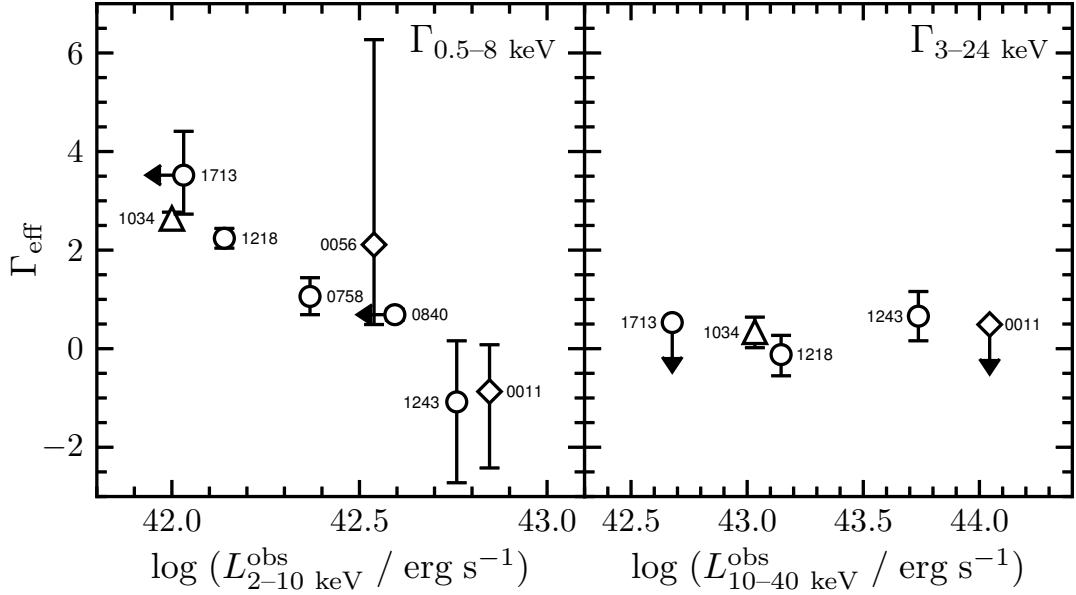
Figure 4.7: Observed X-ray properties of the *NuSTAR*-observed candidate CTQSO2 sample. Left panel: properties measured at low energies with *Chandra* and *XMM-Newton*. Right panel: properties measured at high energies with *NuSTAR*. Only detected sources are shown. Circles, diamonds and the triangle indicate the objects presented in this work, Chapter 3 (L14), and G14, respectively. The effective photon index (Γ_{eff}), which provides a basic description of the overall X-ray spectral shape, was obtained by fitting an unabsorbed power law model to the data for each source. The rest-frame X-ray luminosities ($L_{\mathrm{X}}^{\mathrm{obs}}$; bottom axis) are observed values, i.e. uncorrected for absorption. For the five objects presented in this chapter, the luminosities correspond to those in Table 4.3. For the L14 and G14 objects the luminosities have been calculated using the same methodology: spectral modelling where possible, or photometry following the procedure outlined in Section 4.3.1. In the cases of the X-ray faint sources SDSS J0011+0056 and SDSS J1713+5729, the Γ_{eff} for 3–24 keV was estimated from the *NuSTAR* band ratio ($\mathrm{BR_{Nu}}$; see Section 4.4.2).

instead, `statistic cstat` (applying the W statistic approach; e.g., see Section 4.4.1) results in essentially unchanged values for the key best-fit parameters (Γ and N_H change by less than 0.1 and 0.1×10^{24} cm^{-2}, respectively, for the models tested). The *XMM-Newton*:*NuSTAR* cross-normalization factor, when left as a free parameter, converges to slightly different values depending on the model being tested, but is always broadly consistent (given the uncertainties) with the current best calibration measurements of Madsen et al. (2015) of ≈ 0.93. We therefore fix the cross-normalization factor to this value throughout.

As shown in Figure 4.7, SDSS J1218+4706 has an extremely flat effective photon index over the *NuSTAR* band, $\Gamma_{3-24 \text{ keV}} = -0.15^{+0.40}_{-0.45}$. This is indicative of a spectrum dominated by Compton reflection, as a result of the primary continuum being heavily suppressed by CT levels of photoelectric absorption (e.g., George & Fabian, 1991). Another important diagnostic feature of reflection is fluorescent Fe Kα line emission, which occurs at rest-frame 6.4 keV and becomes increasingly prominent as the level of absorption increases (e.g., Risaliti, 2002). An equivalent width threshold of $\text{EW}_{\text{Fe K}\alpha} > 1$ keV is commonly used to identify CT AGNs; such high values are difficult to explain for less than CT columns (e.g., Maiolino et al., 1998; Comastri, 2004), and suggest a heavily reflection-dominated or pure reflection spectrum, where little to none of the directly transmitted AGN emission is visible.

For SDSS J1218+4706, there is a clear excess of emission at observed frame ≈ 6 keV, which has previously been interpreted as Fe Kα line emission (J13; LaMassa et al. 2012). To model this, we fit to the > 2 keV *NuSTAR* plus *XMM-Newton* dataset an unobscured power law and Gaussian component, fixing the line energy at $E_\text{line} = 6.4$ keV and the line width at $\sigma_\text{line} = 0.01$ keV. We measure an observed-frame equivalent width of $\text{EW}_{\text{Fe K}\alpha} = 1.7^{+0.7}_{-0.6}$ keV using the *XMM-Newton* spectra. This value is similar to but more tightly constrained than that published by J13, since they only use one of the archival *XMM-Newton* observations, while we use two here. The Fe Kα line equivalent width is above the commonly adopted threshold for CT AGNs ($\text{EW}_{\text{Fe K}\alpha} > 1$ keV), with a comparable value to that of the CT quasar SDSS J1034+6001 (Mrk 34; G14). Freeing the Gaussian line energy parameter, we obtain a best-fit value of $E_\text{line} = 6.40^{+0.24}_{-0.07}$ keV (rest frame), which adds further confidence that the excess emission is due to Fe Kα.

For the X-ray spectral modelling of SDSS J1218+4706, we first conduct a simple test to assess the nature of the AGN continuum; we fit the 7–24 keV *NuSTAR* data with two extreme models, one reflection-only spectrum and one transmission-only spectrum. Fitting the high energy data above 7 keV allows a clean measurement of the AGN continuum *independent* of how the potentially complex lower energy emission is chosen to be modelled; low energy X-ray emitting processes other than the reflected or directly transmitted AGN continuum can dominate up to energies of ≈ 4 keV (e.g., Gandhi et al., 2014, 2015), and fluorescent line emission (e.g., Fe Kα) can also strongly contribute at energies up to ≈ 7 keV. For the reflection-only model we use PEXRAV (Magdziarz & Zdziarski, 1995), with the reflection scaling factor set to -1 to produce a reflection-only spectrum (i.e., no directly transmitted component), and set all other parameters to the default values. This model provides a statistically acceptable fit to the *NuSTAR* data ($\chi^2/n = 11.3/12$; here, n is the number of degrees of freedom), and the intrinsic photon index is constrained to be $\Gamma = 1.35 \pm 0.46$. For the transmission-only model we use CABS $\cdot$ ZWABS $\cdot$ POW (in XSPEC formalism).[4] It is not possible to simultaneously constrain $N_{\rm H}$ and Γ in this case, so we fix the intrinsic photon index at $\Gamma = 1.8$ (a typical value for AGNs detected by *NuSTAR* at 3–24 keV; e.g., Alexander et al., 2013). Again, there is a statistically acceptable fit to the data ($\chi^2/n = 10.5/12$), for a best-fit column density of $N_{\rm H} = (1.9^{+0.7}_{-0.5}) \times 10^{24}$ cm^{-2}.

The above tests support the empirical evidence (from $\Gamma_{\rm eff}$ and $\rm EW_{Fe\,K\alpha}$) that extremely large, CT column densities are required to explain the X-ray spectrum of SDSS J1218+4706. In the most extreme case, the source is consistent with being fully reflection-dominated (no directly transmitted component), which would imply $N_{\rm H} \gg 1.5 \times 10^{24}$ cm^{-2}. In the least extreme case, the source is consistent with lying close to the CT threshold ($N_{\rm H} \approx 1.5 \times 10^{24}$ cm^{-2}). However, the latter model assumes a transmission-only spectrum (no Compton reflection), which is unlikely given the large measured equivalent width of Fe Kα. The reflection-only model tested (PEXRAV) is also limited in that the

---

[4]The model PLCABS (Yaqoob, 1997) is generally a preferable transmission model to use (over CABS $\cdot$ ZWABS $\cdot$ POW) for column densities of $N_{\rm H} >$ few $\times 10^{23}$ cm^{-2}. However, in our case PLCABS is not appropriate, since the energy range for which the model is valid depends on source column density ($E < 14.4$ keV for $N_{\rm H} \leq 10^{24}$ cm^{-2}; $E < 10$ keV for $N_{\rm H} \leq 5 \times 10^{24}$ cm^{-2}; Yaqoob 1997), which means not utilising the high energy *NuSTAR* data.

Table 4.4: Best-fit Models for the X-ray Spectrum of SDSS J1218+4706

	Model M	Model T
χ^2/n	31.9/38	33.0/39
Γ	$2.4^{+0.2}_{-0.3}$	$2.8^{+u}_{-0.4}$
$N_{\rm H}$ (10^{24} cm^{-2})	$2.0^{+u}_{-0.8}$	$2.2^{+1.2}_{-0.6}$
$\theta_{\rm tor}$ (°)	[60.0]	[60.0]
$\theta_{\rm inc}$ (°)	$63.7^{+8.5}_{-2.9}$	[87.0]
$kT_{\rm APEC}$ (keV)	$0.42^{+0.20}_{-0.11}$	$0.25^{+0.07}_{-0.05}$
$L^{\rm APEC}_{0.5-2{\rm keV}}$ (10^{41} erg s^{-1})	1.38	1.65
$L^{\rm obs}_{2-10{\rm keV}}$ (10^{44} erg s^{-1})	0.01	0.01
$L^{\rm obs}_{10-40{\rm keV}}$ (10^{44} erg s^{-1})	0.14	0.13
$L^{\rm int}_{2-10{\rm keV}}$ (10^{44} erg s^{-1})	0.85	1.70
$L^{\rm int}_{10-40{\rm keV}}$ (10^{44} erg s^{-1})	0.46	0.48

NOTE. – Best-fitting model parameters for the 0.5–24 keV spectrum of SDSS J1218+4706. The individual models are detailed in Section 4.4.1. The column densities ($N_{\rm H}$) quoted are defined along the line-of-sight of the observer.

geometry (a slab of material) and infinite optical depth assumed are not well motivated for obscured AGNs. Ideally, in the CT regime, any absorbed continuum, reflected continuum and fluorescent lines should be modelled in a self-consistent way, and assuming a well-motivated geometry. This is possible using the physical models MYTORUS (Murphy & Yaqoob, 2009) and torus (Brightman & Nandra, 2011), which were produced using Monte Carlo simulations of X-ray radiative transfer through toroidal distributions of gas, with the two models assuming different toroidal geometries. We proceed to analyse the broad-band (0.5–24 keV) *XMM-Newton* plus *NuSTAR* spectrum of SDSS J1218 +4706 using these two models.

Our MYTORUS-based model (Model M hereafter) has the following form:

$$\text{Model M} = \text{PHABS} \times (\text{MYTZ} \times \text{POW} + \text{MYTS} + \text{MYTL} + \text{APEC}).$$

Here, MYTZ reprocesses the zeroth-order transmitted continuum (POW) through photoelec-
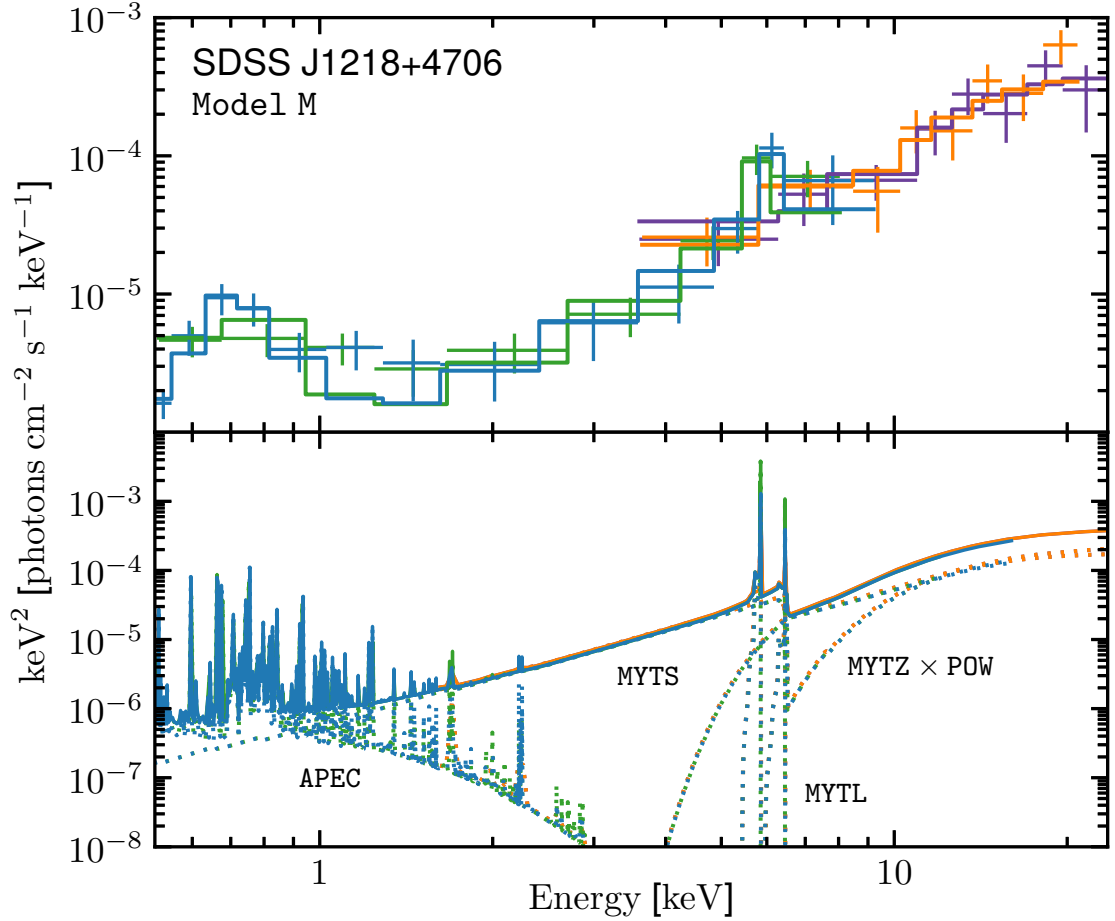
Figure 4.8: Unfolded *NuSTAR* plus *XMM-Newton* spectrum, in EF_E units, for SDSS J1218+4706. The data are shown in the upper panel, grouped to a minimum significance of 2σ per bin for visual purposes. The *NuSTAR* FPMA and FPMB data are shown in purple and orange, respectively. The MOS (obsID 0203270201) and PN (obsID 0400560301) data are shown in green and blue, respectively. The best-fit MYTORUS-based model (Model M; described in Section 4.4.1) is shown binned to match the data (solid lines, upper panel) and in full detail (lower panel).
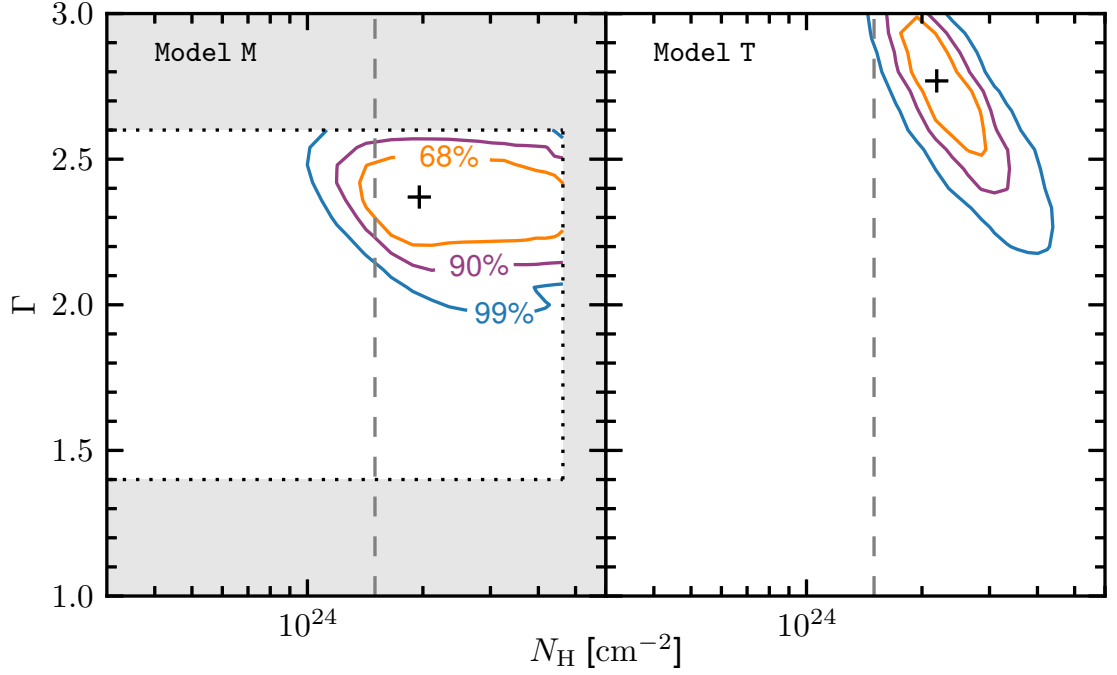
Figure 4.9: Intrinsic photon index (Γ) versus (line-of-sight) column density (N_{H}) confidence contours for SDSS J1218+4706. The contours outline the 68%, 90% and 99% confidence regions, and the best-fit value is marked by a black cross. We show results for two models (Model M and Model T; left and right panels). The individual models are detailed in Section 4.4.1. The gray shaded region indicates the parameter ranges for which Model M is not valid. The best-fit column densities are CT ($N_{\mathrm{H}} > 1.5 \times 10^{24}$ cm^{-2}), and the 90% CL lower N_{H} limits lie just below and just above the CT threshold (gray dashed line) for Model M and Model T, respectively.

tric absorption and the Compton scattering of X-ray photons out of the line-of-sight, MYTS is the scattered/reflected continuum produced by scattering X-ray photons into the line of sight, and MYTL is the fluorescent emission line spectrum (Murphy & Yaqoob, 2009). We use MYTORUS in the simplest form possible, tying the common parameters of MYTZ, MYTS and MYTL (N_H and θ_{inc}) together. The intrinsic (unprocessed) photon indices and normalizations are tied to those of the zeroth-order continuum (POW). The torus opening angle (θ_{tor}) is fixed at $60°$ in the current version of MYTORUS. APEC is a thermal plasma component (Smith et al., 2001) which we use to parameterize the low energy excess, fixing the abundance parameter at solar. This component is motivated by the steep spectral slope at low energies ($\Gamma_{0.5-2\,\mathrm{keV}} \approx 3.4$, measured using an unabsorbed power law model), which suggests contributions from processes such as star formation or AGN photoionization, although we lack the spectral detail required to distinguish between these processes. The best-fit model has $\chi^2/n = 32/38$ (see Table 4.4 for the model parameters and Figure 4.8 for the model spectrum). Since Γ and N_H are known to be degenerate, we compute their uncertainties from χ^2 contours in the Γ–N_H plane. Contours showing the 68%, 90% and 99% confidence regions for this parameter space are shown in Figure 4.9. These were computed with θ_{inc} left free to vary. Hereafter, the quoted uncertainties for N_H and Γ are taken from the 90% CL contours. The best-fit intrinsic photon index and line-of-sight column density are $\Gamma = 2.4^{+0.2}_{-0.3}$ and $N_H = (2.0^{+u}_{-0.8}) \times 10^{24}\ \mathrm{cm}^{-2}$ [corresponding to an equatorial column density of $N_{H,eq} = (4.2^{+u}_{-0.8}) \times 10^{24}\ \mathrm{cm}^{-2}$] for the best-fit inclination angle of $\theta_{inc} = 63.7^{+8.5°}_{-2.9}$. The modelling will not allow inclination angles of $\theta_{inc} < 60°$, since for these angles the observer has a direct, unobscured view of the central X-ray emitting source. The upper error on N_H is not constrained, which is in part due to the limited N_H range of MYTORUS ($N_H = 10^{22}$–$10^{25}\ \mathrm{cm}^{-2}$). The best-fit model spectrum is reflection-dominated, with the MYTS component dominating at ≈ 3–10 keV, and the MYTZ $\cdot$ POW and MYTS components contributing equally to the normalization and spectral shape at $\gtrsim 10$ keV. To assess whether the *NuSTAR* plus *XMM-Newton* spectrum is in agreement with being fully reflection dominated, we test two modifications of Model M where the MYTZ $\cdot$ POW component is removed and the inclination angle of the MYTS component is set to $0°$ and $90°$, corresponding to face-on and edge-on reflection. Both models provide statistically acceptable fits to the spectrum ($\chi^2/n = 29/35$ and $28/35$, respectively), with

flat χ^2 residuals, reasonable best-fit intrinsic photon indices ($\Gamma = 1.6^{+0.6}_{-u}$ and 1.9^{+u}_{-u}, respectively) and large column densities for the reflecting material [$N_{\mathrm{H,reflector}} = (3.1^{+u}_{-1.6})$ and $(1.5^{+1.0}_{-0.8}) \times 10^{24}$ cm^{-2}, respectively]. The broad-band X-ray spectrum of SDSS J1218 +4706 is therefore in agreement with being fully reflection dominated. Since no transmission component is required in these models, we may infer that the line-of-sight column density is consistent with having a value of $N_{\mathrm{H}} \gg 1.5 \times 10^{24}$ cm^{-2}.

Our `torus`-based model (`Model T` hereafter) has the following form:

$$\mathrm{Model\ T} = \mathrm{PHABS} \times (\mathrm{BNTORUS} + \mathrm{APEC}).$$

In the `torus` model, N_{H} is defined along the line of sight, and is independent of θ_{inc}. Initially, we fix the inclination at the maximum value of $\theta_{\mathrm{inc}} = 87°$, corresponding to an edge-on view of the torus. Since the opening angle for `Model T` is poorly constrained when left as a free parameter ($\theta_{\mathrm{tor}} < 72°$), we fix it to $60°$. The best-fit model has $\chi^2/n = 33/39$ (the model parameters are listed in Table 4.4, and the Γ–N_{H} contours are shown in Figure 4.9). N_{H} is well constrained at the 90% CL, with a best-fit value of $(2.2^{+1.2}_{-0.6}) \times 10^{24}$ cm^{-2}, and the intrinsic photon index has a relatively high value of $\Gamma = 2.8^{+u}_{-0.4}$. The upper error on Γ is not constrained due to the parameter limits of the `torus` model. Fixing the intrinsic photon index at a more reasonable value of $\Gamma = 2.3$, which is consistent with the χ^2 contours and is at the upper end of the range typically observed for unobscured AGNs (e.g., Mateos et al., 2010; Scott et al., 2011), results in a higher column density of $N_{\mathrm{H}} = (3.6^{+0.8}_{-0.7}) \times 10^{24}$ cm^{-2} and a reduced χ^2 value close to unity ($\chi^2/n = 39/40$). If the intrinsic photon index is fixed at $\Gamma = 1.8$, an extremely high column density of $N_{\mathrm{H}} > 5.1 \times 10^{24}$ cm^{-2} is required. We note that the modelling (with Γ left free) allows a large range of inclination angles ($\theta_{\mathrm{inc}} > 63°$), and re-modelling with θ_{inc} fixed at a lower value of $65°$ results in a similarly good fit ($\chi^2/n = 38/39$) with no significant change in N_{H} but a flatter photon index of $\Gamma = 2.5^{+0.3}_{-0.4}$. Furthermore, the statistical quality of the fit and the best-fit parameters are relatively unchanged when θ_{tor} is left as a free parameter.

To summarize, CT line-of-sight column densities are preferred for all of the models tested for SDSS J1218+4706. The broad-band X-ray spectrum shows evidence for having a dominant contribution from Compton reflection, with the primary continuum being heavily suppressed due to photoelectric absorption. This is in agreement with the ex-

pectations from the observation of strong fluorescent Fe Kα line emission (EW$_{\text{Fe K}\alpha} \approx$ 1.7 keV). The lowest limit allowed by the modelling for the line-of-sight column density is $N_{\text{H}} > 1.2 \times 10^{24}$ cm^{-2}, and there is no constraint at the upper end. The N_{H}, L_{X} and EW$_{\text{Fe K}\alpha}$ constraints and data quality for SDSS J1218+4706 ($z = 0.094$) are remarkably similar to those for the other low redshift QSO2 strongly detected by *NuSTAR*, SDSS J1034+6001 ($z = 0.051$; also known as Mrk 34), which was identified by G14 as a bona fide CT AGN. More complex models are possible (such as a clumpy torus; e.g., Bauer et al. 2015), but testing these is beyond the X-ray data quality.

SDSS J124337.34–023200.2

SDSS J1243–0232 is the third brightest *NuSTAR* detection in the SDSS-selected candidate CTQSO2 sample, after SDSS J1218+4706 (Section 4.4.1) and SDSS J1034+6001 (G14), but still has relatively low photon counts: $S_{8-24 \text{ keV}} \approx 90$ and $S_{3-8 \text{ keV}} \approx 34$ with *NuSTAR*, and $S_{0.5-8 \text{ keV}} \approx 9$ with *Chandra*. This emphasizes the challenge involved in studying these inherently faint X-ray sources. Due to the low photon statistics, we use `statistic cstat` in XSPEC, which is more appropriate than `statistic chi` in the case of Poisson distributed data (Nousek & Shue, 1989). In the case of unmodelled background spectra, `cstat` applies the W statistic (Wachter et al., 1979).[5] While the W statistic is intended for unbinned data, bins containing zero counts can lead to erroneous results,[6] so we group the *Chandra* and *NuSTAR* data by a minimum of 1 count and 3 counts per bin, respectively (e.g., Wik et al., 2014). We fix the *Chandra*:*NuSTAR* cross-normalization factor at 1.0, consistent with the value obtained when the cross-normalization factor is left as a free parameter in the modelling.

The *NuSTAR* spectrum of SDSS J1243–0232 has a flat effective photon index of $\Gamma_{3-24 \text{ keV}} = 0.66 \pm 0.50$, indicative of heavy absorption. Fitting the broad-band (0.5–24 keV) *NuSTAR* plus *Chandra* spectrum with a simple absorbed power law (ZWABS · POW) model, we obtain $N_{\text{H}} \approx 1.6 \times 10^{24}$ cm^{-2} and $\Gamma \approx 3$. This intrinsic photon index is discrepant with the expected range for AGNs, and the parameter is poorly constrained. We therefore fix the parameter to $\Gamma = 1.8$ (typical value in the 3–24 keV energy band for

---

[5]See also http://heasarc.gsfc.nasa.gov/docs/xanadu/xspec/wstat.ps
[6]See https://heasarc.gsfc.nasa.gov/xanadu/xspec/manual/XSappendixStatistics.html
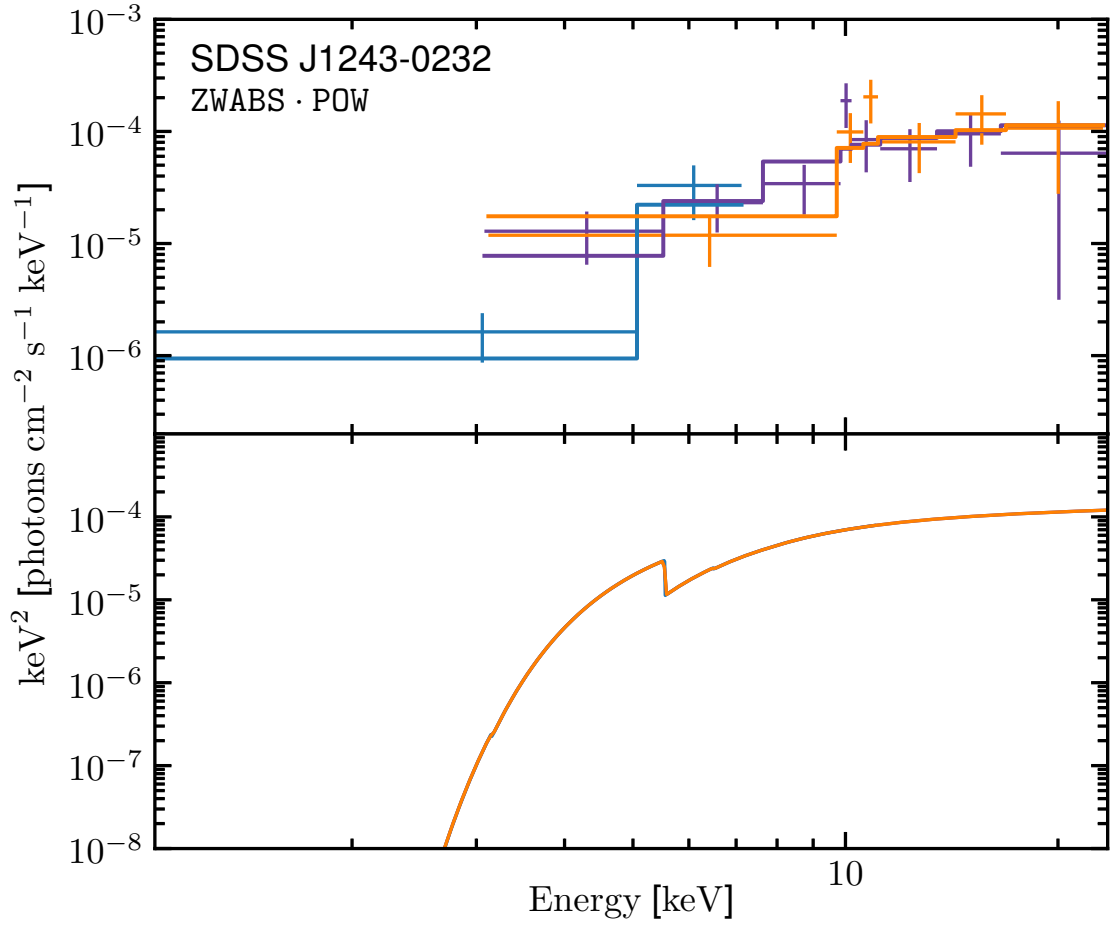
Figure 4.10: Unfolded *NuSTAR* (purple and orange for FPMA and FPMB, respectively) plus *Chandra* (blue) X-ray spectrum for SDSS J1243–0232. The best-fit absorbed power law (ZWABS · POW) model is shown. The panel layout, units and data binning follow that of Figure 4.8.

AGNs; e.g., Alexander et al. 2013). The best-fitting model has $\chi^2 = 101$ and a C-statistic value of $C = 123$, for $n = 130$. The unfolded spectrum and best-fitting model are shown in Figure 4.10. The column density, $N_{\mathrm{H}} = (0.90^{+0.36}_{-0.33}) \times 10^{24}$ cm^{-2}, is close to CT. The intrinsic luminosities in the low and high energy X-ray bands are $L^{\mathrm{in}}_{2-10\ \mathrm{keV}} = 0.6 \times 10^{44}$ erg s^{-1} and $L^{\mathrm{in}}_{10-40\ \mathrm{keV}} = 0.7 \times 10^{44}$ erg s^{-1}, respectively. The higher quality *NuSTAR* data dominate the fit, with similar results [$N_{\mathrm{H}} = (0.97^{+0.49}_{-0.38}) \times 10^{24}$ cm^{-2}] being obtained when the *Chandra* data are excluded. We note that `cstat` may also be used to model the unbinned, gross (i.e., combined source plus background) spectrum, in which case the Cash statistic (C statistic; Cash 1979) is applied. Characterizing the background spectra using double power law models (`POW + POW` in XSPEC), and including these as fixed components in the spectral modelling of the *NuSTAR* data, this C statistic approach yields very similar results to the W statistic approach, with $N_{\mathrm{H}} = (0.97^{+0.46}_{-0.37}) \times 10^{24}$ cm^{-2}.

Given the extremely flat effective photon index measured for this source, it is reasonable to test whether the spectrum is in agreement with a pure reflection continuum. As in Section 4.4.1, we use `PEXRAV` with the reflection scaling factor set to -1 to produce a reflection-only spectrum. The model produces a similarly good fit to the data as for the absorbed power law model above, with $\chi^2 = 117$ and $C = 120$, for $n = 130$. We infer that the line-of-sight column density is consistent with being CT, with $N_{\mathrm{H}} \gg 1.5 \times 10^{24}$ cm^{-2}. Unlike for the absorbed power law model, the intrinsic photon index is well constrained by the reflection-only model, with $\Gamma = 1.7 \pm 0.3$. To summarize, the *NuSTAR* data unambiguously reveal heavy absorption in this QSO2, with a column density lower limit of $N_{\mathrm{H}} > 0.6 \times 10^{24}$ cm^{-2} and no constraint at the high, CT absorption end. Higher quality X-ray data than those currently available, especially at < 10 keV, are required to reliably distinguish between less than CT, and reflection-dominated CT models. For instance, the current data are unable to provide informative constraints on Fe Kα line emission (see Section 4.7.4).

SDSS J171350.32+572954.9

For SDSS J1713+5729 there are too few *NuSTAR* counts for broad-band X-ray spectral modelling (see Table 4.2). Here we investigate the low energy (< 10 keV) spectrum observed with *XMM-Newton*. The object appears to have an extremely steep spectrum at

low energies, with PN (MOS) source counts of < 2 (< 5) at 2–10 keV and 12^{+6}_{-5} (18^{+7}_{-5}) at 0.5–2 keV, implying a photon index of $\Gamma = 3.5^{+1.0}_{-0.8}$ in the 0.5–10 keV energy band; J13 measure a slightly flatter, but consistent (within the uncertainties), value of $\Gamma = 2.5 \pm 0.4$. The steep spectral slope is not typical of an AGN, and would be inconsistent with the *NuSTAR* detection if produced as a result of direct AGN emission. To test whether the soft X-ray emission could be powered by star formation, we compare the 0.5–8 keV luminosity, $L_{0.5-8 \text{ keV}} = 1.4 \times 10^{42}$ erg s^{-1}, with the far-infrared (FIR) luminosity, $L_{\text{FIR}} < 4.0 \times 10^{44}$ erg s^{-1}, measured using *IRAS* fluxes following Lonsdale Persson & Helou (1987). The relatively high soft X-ray:FIR luminosity ratio of $L_{0.5-8 \text{ keV}}/L_{\text{FIR}} > 0.0035$, which is a conservative lower limit due to the poorly constrained *IRAS* 100μm flux, rules out star formation as the driver of the soft X-ray emission (e.g., see Figure 8 of Alexander et al. 2005a). We deduce that the soft X-rays detected with *XMM-Newton* are indirectly powered by the AGN (e.g., via photoionization or scattered AGN emission), and *NuSTAR* may have provided the first identification of the directly transmitted (or reflected) AGN continuum of this QSO2.

4.4.2 X-ray Spectral Analysis: Band Ratios

X-ray band ratios provide a basic description of the X-ray spectrum, and are useful when there are insufficient counts for detailed spectral modelling. We define the *NuSTAR* band ratio (BR_{Nu}) as the ratio of net source counts in the hard-band to those in the soft-band, $S_{8-24 \text{ keV}}/S_{3-8 \text{ keV}}$. Figure 4.11 shows BR_{Nu} against redshift (z) for the five (of the total nine) *NuSTAR*-observed candidate CTQSO2s which are detected at 8–24 keV, including the three presented in this chapter (SDSS J1218+4706, 1243–0232 and 1713+5729) and the two presented in Chapter 3 (L14) and G14 (SDSS J0011+0056 and 1034+6001, respectively). The tracks show the expected evolution of BR_{Nu} with z for four different fixed column densities (N_{H}), computed using a MYTORUS model with an intrinsic photon index of $\Gamma = 1.8$. We compare the measured BR_{Nu} values for the candidate CTQSO2s with these tracks in order to infer N_{H}. We note that producing the tracks with, instead, a simple ZWABS · POW model results in higher N_{H} values for the same BR_{Nu}. The *NuSTAR*-detected candidate CTQSO2s, in general, have high band ratios compared to AGNs detected in the *NuSTAR* extragalactic surveys (squares in Figure 4.11). In all cases
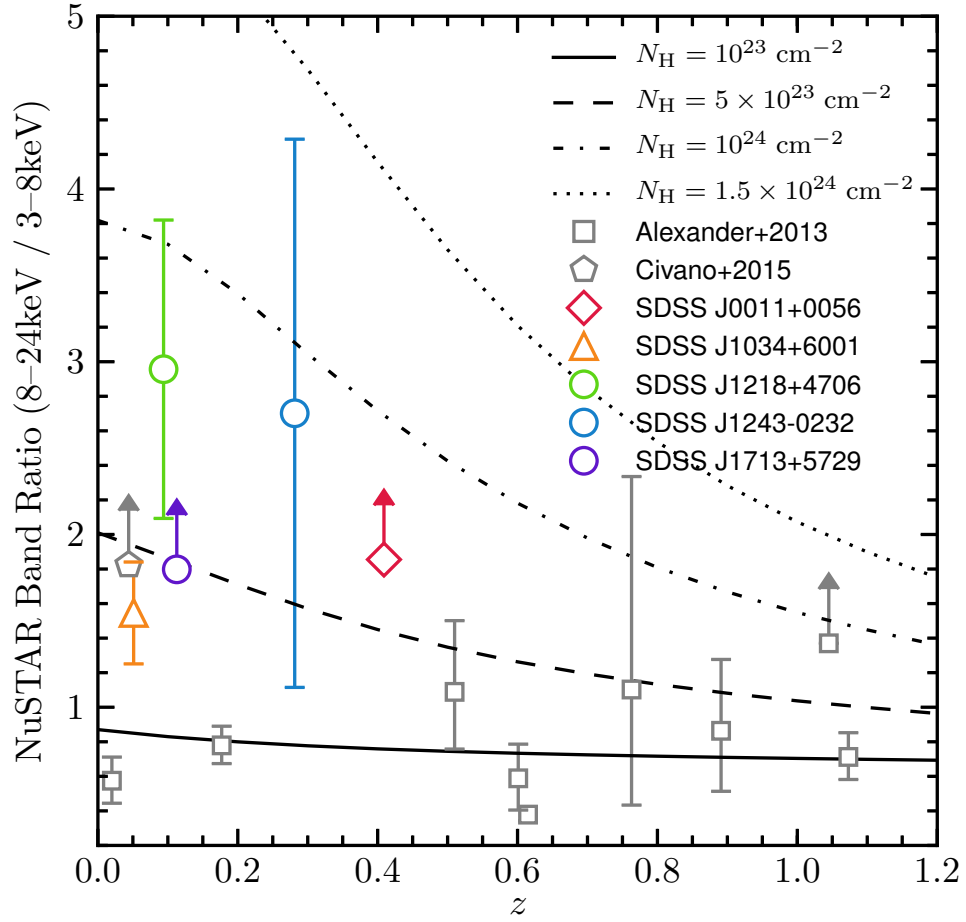
Figure 4.11: *NuSTAR* band ratio (BR_{Nu}) versus z. The circles, the diamond and the triangle indicate the candidate CTQSO2s presented in this work, Chapter 3 (L14) and G14, respectively, which are detected at 8–24 keV; 90% CL error bars and limits are shown. For comparison, gray squares show the first 10 AGNs detected in the *NuSTAR* serendipitous survey (Alexander et al., 2013); 68% CL error bars are shown. The gray pentagon marks a CT AGN identified with *NuSTAR* in the COSMOS field (Civano et al. 2015); a 90% CL lower limit is shown. The tracks show model predictions for BR_{Nu} for four absorbing column densities in the range $N_{H} = (0.1–1.5) \times 10^{24}$ cm^{-2}. The BR_{Nu} constraints for SDSS J1218+4706, 1243–0232 and 1713+5729 are higher than that of the confirmed CTQSO2 SDSS J1034+6001, and suggest large absorbing columns.

the BR_{Nu} values suggest $N_H > 10^{23}$ cm^{-2}.

For SDSS J1713+5729, a *NuSTAR*-detected object with too few counts for broad-band spectral modelling of the direct AGN continuum (see Section 4.4.1), the lower limit in BR_{Nu} suggests heavy absorption with $N_H \gtrsim 5 \times 10^{23}$ cm^{-2}. Our most direct measurement for the intrinsic X-ray luminosity of this QSO2 comes from using this N_H constraint. Taking the observed 10–40 keV luminosity constraint from Table 4.3, and assuming that the X-ray spectrum is an absorbed power law with $\Gamma = 1.8$, the lower limits obtained are $L_{2-10 \text{ keV}}^{\text{in}} > 4.6 \times 10^{42}$ erg s^{-1} and $L_{10-40 \text{ keV}}^{\text{in}} > 5.3 \times 10^{42}$ erg s^{-1}. As an alternative to the BR_{Nu} approach, N_H can be constrained using the *NuSTAR/XMM-Newton* band ratio (following Chapter 3). However, in this case the constraint ($N_H \gtrsim 2 \times 10^{23}$ cm^{-2}) is less stringent than that from BR_{Nu}, due to the comparatively poor quality of the available *XMM-Newton* data.

The N_H estimates made from BR_{Nu} using Figure 4.11 are relatively crude, since the individual X-ray spectra may have additional spectral complexities (e.g., line emission around ≈ 6.4 keV, a scattered power law, or a complex absorber geometry) not incorporated in our model predictions. To illustrate this, for the two sources with comparatively high quality *NuSTAR* spectra (SDSS J1034+6001 and 1218+4706), the less than CT column densities inferred from the BR_{Nu} analysis ($N_H \lesssim 5 \times 10^{23}$ cm^{-2} and $\lesssim 10^{24}$ cm^{-2}, respectively) are an underestimate of the column densities determined from X-ray spectral fitting ($N_H \gtrsim 1.5 \times 10^{24}$ cm^{-2}; see G14 and Section 4.4.1 of this chapter, respectively). Similarly, using the *NuSTAR* results for three CT reflection-dominated Seyfert 2s, Baloković et al. (2014) demonstrate that the above BR_{Nu} approach underestimates N_H for reflection-dominated AGNs. Nevertheless, BR_{Nu} provides first-order N_H constraints for weakly detected sources.

4.4.3 Indirect Constraints on X-ray Absorption

It is well-established that there is a tight relation between the mid-IR and intrinsic X-ray luminosities of AGNs (e.g., Lutz et al., 2004; Fiore et al., 2009; Gandhi et al., 2009; Lanzuisi et al., 2009; Ichikawa et al., 2012; Matsuta et al., 2012; Mateos et al., 2015; Stern, 2015). Mid-IR emission can therefore provide an indirect estimate of the intrinsic AGN power, especially useful when heavy absorption in the X-rays makes this information
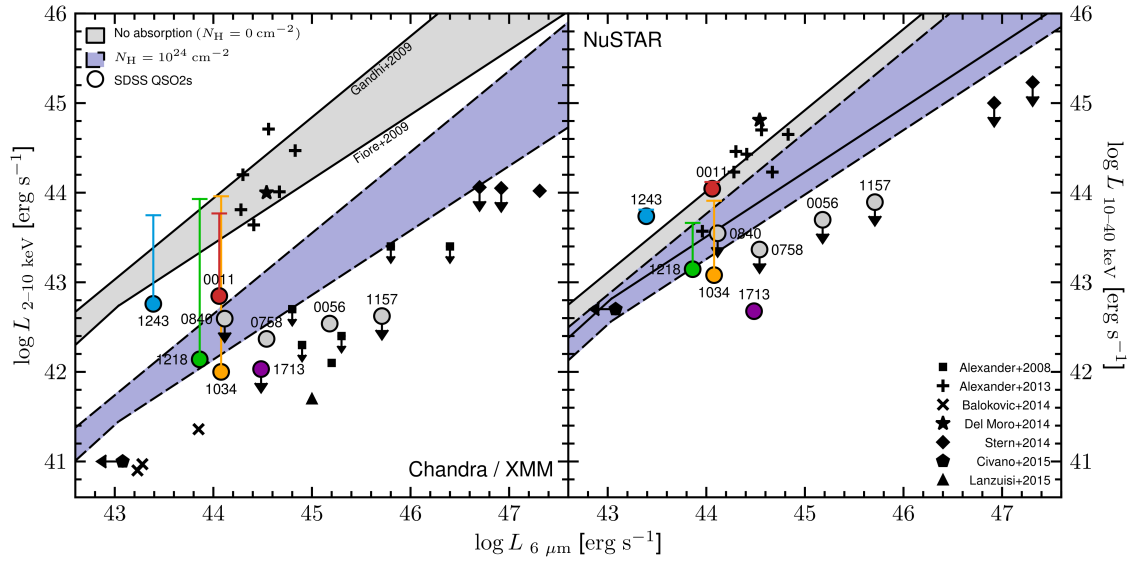
Figure 4.12: Observed (i.e., uncorrected for absorption) X-ray luminosity for the rest-frame 2–10 keV and 10–40 keV bands (left and right hand panels, respectively) versus rest-frame 6 μm luminosity (in νL_ν units). The circles indicate the *NuSTAR*-observed SDSS-selected candidate CTQSO2s presented in this work, Chapter 3 (L14), and G14 ($z = 0.05$–0.49); coloured circles mark the *NuSTAR*-detected sources. The X-ray luminosities for the candidate CTQSO2s are taken from best-fitting spectral models where possible. Otherwise, they have been determined from photometry, assuming an unabsorbed power law model with $\Gamma = 0.3$ (as described in Section 4.3.1). For the three objects from Chapter 3 (SDSS J0011+0056, 0056+0032 and 1157+6003), the values have been adjusted for consistency with this work. Other *NuSTAR*-observed objects are shown, including: *NuSTAR* extragalactic survey AGNs ('+' symbols; $z = 0.02$–2.92; Alexander et al., 2013), three CT Seyfert 2 AGNs ('×' symbols; $z \approx 0.01$; Baloković et al., 2014), a heavily obscured quasar identified in the ECDFS field (star; $z \approx 2$; Del Moro et al., 2014), three luminous and heavily obscured *WISE*-selected AGNs (diamonds; $z \approx 2$; Stern et al., 2014), and a CT AGN identified in the COSMOS field (pentagon; $z = 0.044$; Civano et al. 2015). For the latter object, we show an upper limit in $L_{6\mu m}$, since we have assumed that the mid-IR emission is AGN-dominated. Additionally, for the 2–10 keV band we compare with sources studied at < 10 keV with *Chandra* or *XMM-Newton*: the candidate CT quasars presented in Alexander et al. (2008; squares; $z \approx 2$), and a candidate heavily CT AGN identified in the COSMOS field (triangle; $z = 0.35$; Lanzuisi et al., 2015b). For four of the *NuSTAR*-observed candidate CTQSO2s, vertical lines indicate the intrinsic (i.e., corrected for absorption) X-ray luminosities obtained from X-ray spectral analyses. We compare all of the data with two intrinsic relations for the 2–10 keV band (solid black lines), those of Fiore et al. (2009) and Gandhi et al. (2009). Following Chapter 3 and Stern et al. (2014), the relations have been extrapolated to 10–40 keV assuming $\Gamma = 1.8$, and the dashed lines show the effect of absorption by $N_{\rm H} = 10^{24}$ cm^{-2} gas. The different X-ray:mid-IR ratios for the Fiore et al. (2009) and Gandhi et al. (2009) relations means that the former provides a more conservative estimate of the CT absorption threshold. The majority of the *NuSTAR*-observed candidate CTQSO2s have low X-ray:mid-IR ratios, suggesting CT levels of photoelectric absorption.

challenging to obtain (e.g., Vignali et al., 2010; Alexander et al., 2008; LaMassa et al., 2009, 2011; Goulding et al., 2011; Lanzuisi et al., 2015b). Following the approach used for other *NuSTAR* studies of faint, obscured AGNs (Chapter 3 of this thesis; L14; Stern et al. 2014), in Figure 4.12 we compare the observed X-ray:mid-IR luminosity ratios with intrinsic ratios for unobscured AGNs and those corresponding to X-ray absorption due to dense obscuring material ($N_{\rm H} = 10^{24}$ cm^{-2}), for both the low (2–10 keV) and high (10–40 keV) energy X-ray regimes. We show the full sample of nine *NuSTAR*-observed SDSS-selected candidate CTQSO2s, including the five presented in this work, the three from Chapter 3 (L14) and the one in G14. The X-ray luminosities ($L_{\rm X}^{\rm obs}$) are observed values (i.e., uncorrected for absorption), and the 6 μm luminosities ($L_{6\mu\rm m}$, in νL_ν units) are intrinsic values (i.e., corrected for dust extinction occuring in the system) for the AGN determined through SED modelling (Section 4.3.3), and both correspond to the values provided in Table 4.3. We note that for a large fraction of CT AGNs, potentially $\approx 50\%$ in the case of local CT AGNs, we expect significant absorption in the mid-IR (e.g., Bauer et al., 2010; Goulding et al., 2012). We have partially addressed this through dust corrections which are included in the SED modelling (Section 4.3.3). These corrections are small, however, with the luminosities changing by factors ranging from 1.03 to 1.46 (with a median of 1.17). For the four candidate CTQSO2s with constrained intrinsic X-ray luminosities ($L_{\rm X}^{\rm int}$), we plot the $L_{\rm X}^{\rm int}$ values obtained from X-ray spectral analyses (see Chapter 3, G14, and Sections 4.4.1 and 4.4.1 of this work). We conservatively adopt intrinsic X-ray luminosities from the models with lower best-fit column densities (e.g., `Model M` in the case of SDSS J1218+4706 and the absorbed power law model in the case of SDSS J1243–0232).

The two intrinsic relations utilized for comparison are those of Fiore et al. (2009) and Gandhi et al. (2009), which were both computed at 2–10 keV. In the case of the Gandhi et al. (2009) relation, we adjust the 12 μm (the mid-IR wavelength at which the relation was computed) νL_ν luminosities downwards by 7% to obtain 6 μm luminosities, based on the Assef et al. (2010) AGN template. The two relations predict slightly different X-ray:mid-IR ratios at low luminosities and diverge further towards higher luminosities, which is partly due to the different luminosity ranges over which the two relations were calibrated, but also reflects the uncertainty in such relations. Comparison to both allows

us to account for systematic effects in the derivation of these relations. We extrapolate the relations to the 10–40 keV band assuming $\Gamma = 1.8$ (typical value for AGNs; e.g., Alexander et al. 2013). An advantage of using 10–40 keV X-ray luminosities ($L_{10-40\ \mathrm{keV}}^{\mathrm{obs}}$), as opposed to 2–10 keV luminosities ($L_{2-10\ \mathrm{keV}}^{\mathrm{obs}}$), is that contamination from processes other than AGN continuum emission is negligible in this high-energy band. However, the suppression of the X-ray emission by absorbing gas is less dramatic in the 10–40 keV band, as demonstrated by the relative normalization of the $N_{\mathrm{H}} = 10^{24}\ \mathrm{cm}^{-2}$ lines in the left and right hand panels of Figure 4.12, which were computed assuming a MYTorus model with $\Gamma = 1.8$ and $\theta_{\mathrm{obs}} = 70°$ (following Chapter 3). Absorption by $N_{\mathrm{H}} = 10^{24}\ \mathrm{cm}^{-2}$ gas results in a suppression of the X-ray emission by factors of ≈ 20 and ≈ 2 in the 2–10 keV and 10–40 keV bands, respectively. We note that for the four candidate CTQSO2s with $L_{\mathrm{X}}^{\mathrm{int}}$ values constrained using X-ray spectral analyses, the intrinsic luminosities agree more closely with the Gandhi et al. (2009) relation than with the Fiore et al. (2009) relation.

In general, the overall sample of candidate CTQSO2s have extremely low X-ray:mid-IR ratios, with the observed 2–10 keV luminosities a factor of $\gtrsim 20$ lower than the intrinsic relations, suggesting CT absorption. This was already apparent from 2–10 keV luminosities published in the literature, but here we have demonstrated the 2–10 keV suppression using our own soft X-ray analysis. A similar conclusion is reached in the high-energy 10–40 keV band, where six out of nine of the objects have X-ray luminosities a factor of $\gtrsim 2$ lower than the intrinsic relations, consistent with CT obscuration. Our sample of SDSS-selected candidate CTQSO2s lies below the majority of the AGNs detected in the *NuSTAR* extragalactic surveys (Alexander et al., 2013), including a heavily obscured quasar detected in ECDFS (NuSTAR J033202–2746.8; $z \approx 2$; Del Moro et al. 2014).

Of the five new objects presented in this work, there is one, SDSS J1243–0232, which does not appear compatible with CT absorption based on this indirect analysis. For this object, the low N_{H} implied by the relatively high X-ray:mid-IR ratios is incongruous with the direct constraints from X-ray spectral modelling (Section 4.4.1), which suggest $N_{\mathrm{H}} \gtrsim 10^{24}\ \mathrm{cm}^{-2}$. A similar case where the N_{H} values inferred from X-ray spectral modelling and the X-ray:mid-IR ratio do not agree is that of NuSTAR J033202–2746.8 (star symbol in Figure 4.12; Del Moro et al. 2014). Despite the large column density measured for this source ($N_{\mathrm{H}} \approx 6 \times 10^{23}\ \mathrm{cm}^{-2}$; Del Moro et al. 2014), it lies high with

respect to the relations, which may in part be due to its significant Compton reflection component. It is possible that a strong reflection component also contributes to the high X-ray:mid-IR ratio observed for SDSS J1243–0232, especially given that a pure reflection spectrum well describes the data (see Section 4.4.1).

Of the *NuSTAR* targets detected at high energies (> 10 keV), SDSS J1713+5729 has the most extreme 10–40 keV:mid-IR ratio, with a $L^{\mathrm{obs}}_{10-40\ \mathrm{keV}}$ value suppressed by a factor of ≈ 35 with respect to the intrinsic relations (on average). The fact that the source lies even lower than the CTQSO2 SDSS J1034+6001 (G14) may be due to some combination of a heavily CT absorbing column ($N_{\mathrm{H}} \gg 10^{24}$ cm^{-2}) and a less prominent reflection component. For the non detections, SDSS J0758+3923 and SDSS J0840+3838, the $L^{\mathrm{obs}}_{10-40\ \mathrm{keV}}$ upper limits suggest that if the X-ray faintness is due to absorption, these sources are likely CT (for SDSS J0840+3838 this only applies for the Gandhi et al. 2009 relation). While heavy absorption seems the most likely explanation for the X-ray faintness of these non detections, we do not have broad-band X-ray spectral constraints and therefore cannot rule out the possibility of intrinsic X-ray weakness (e.g., Gallagher et al., 2001; Wu et al., 2011; Luo et al., 2014; Teng et al., 2014). However, intrinsic X-ray weakness is a phenomenon observed for type 1 sources where there is an unobscured view of the central nucleus, unlike for our QSO2s.

4.5   Discussion

In the following sections, we discuss the possible implications of the extremely high column densities and corresponding intrinsic luminosities measured for the *NuSTAR*-detected heavily obscured QSO2s presented in this chapter (SDSS J1218+4706, 1243–0232 and 1713+5729), Chapter 3 (SDSS J0011+0056), and G14 (SDSS J1034+6001), in the context of the overall quasar population.

4.5.1   Heavy Absorption and Powerful X-ray Luminosities

Figure 4.13 shows N_{H} versus intrinsic (i.e., absorption-corrected) X-ray luminosity for all SDSS-selected QSO2s that have been studied at low energies (< 10 keV) with *Chandra* and *XMM-Newton*, and have *direct* constraints from X-ray spectral analyses. The intrinsic
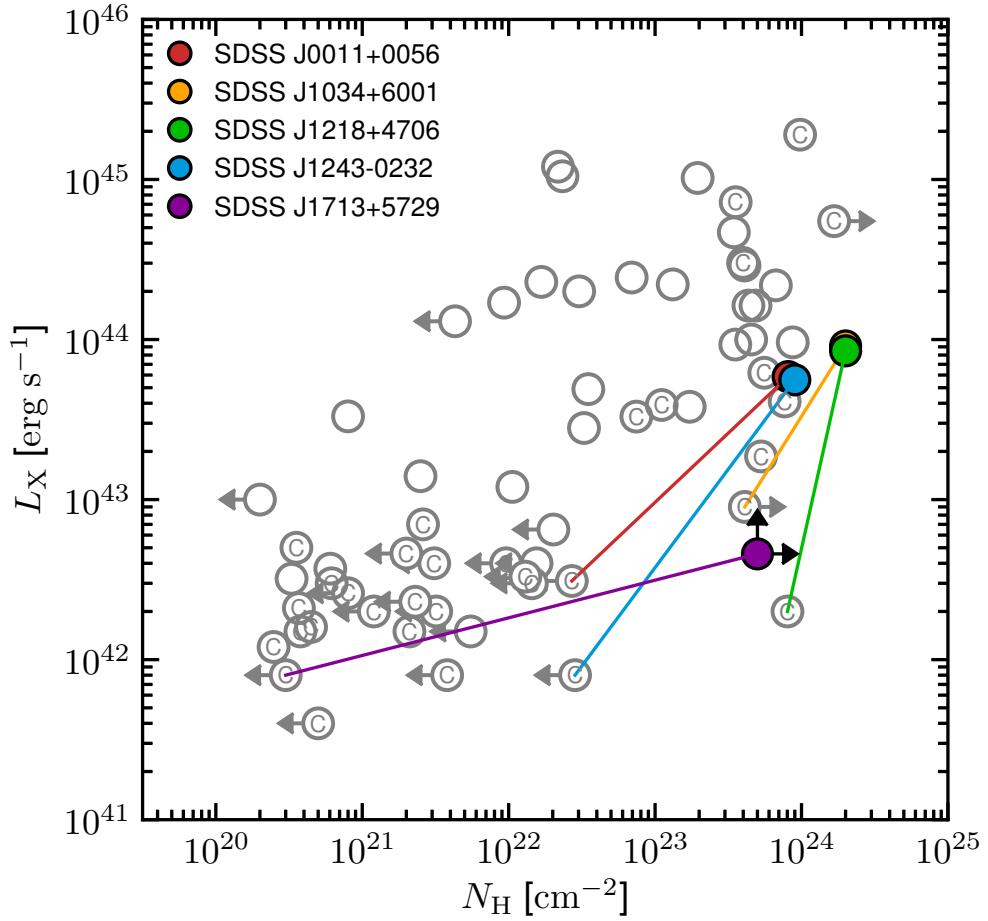
Figure 4.13: Intrinsic (i.e., absorption-corrected) rest-frame 2–10 keV luminosity ($L_{2-10 \text{ keV}}^{\text{in}}$, or L_X) versus N_H for SDSS-selected QSO2s, as measured from X-ray spectral analyses. The grey open circles show the constraints in the literature, all directly measured from X-ray spectral fitting at soft X-ray energies (< 10 keV; J13; LaMassa et al. 2014). Sources with evidence for being CT, primarily based on the indirect X-ray:[O III] luminosity ratio diagnostic, are marked with a "C". The coloured circles show our constraints for the five *NuSTAR*-observed candidate CTQSO2s detected at high energies (> 10 keV), from the broad-band *NuSTAR* plus soft X-ray spectral analyses presented in this study, Chapter 3 (L14), and G14. The coloured lines indicate the significant increase in both L_X and N_H for these five objects between the soft X-ray constraints in the literature and the *NuSTAR* plus soft X-ray studies. We note that for SDSS J1243–0232 the increase in L_X shown (blue line) may be an overestimate.[8]

X-ray luminosities shown are for the rest-frame 2–10 keV band ($L^{\mathrm{in}}_{2-10~\mathrm{keV}}$), and are here-after referred to as L_{X}. The data are compiled from J13 and LaMassa et al. (2014). Since these two studies have different approaches, with the former limiting the spectral analysis to absorbed power law models and the latter using physically motivated models, we adopt the LaMassa et al. (2014) values where multiple measurements exist. Overlaid are the five sources which have 8–24 keV detections with *NuSTAR*, for which it is therefore possible to remeasure N_{H} and L_{X} with the addition of the high-energy (> 10 keV) data. In each case, there is a range of column densities consistent with the data. To be conservative, we adopt measured values at the lower end of these ranges: e.g., for SDSS J1218+4706 we adopt the `Model M` results ($N_{\mathrm{H}} = 2.0 \times 10^{24}$ cm^{-2}; Section 4.4.1) and for SDSS J1243 –0232 we adopt the absorbed power law model results ($N_{\mathrm{H}} = 9 \times 10^{23}$ cm^{-2}; Section 4.4.1). The improvements made with *NuSTAR* are illustrated by the coloured lines, which connect the literature constraints prior to *NuSTAR* and the broad-band, *NuSTAR* plus soft X-ray constraints.

Our L_{X} and N_{H} measurements for these five objects are significantly higher than the constraints in the literature from spectral modelling of the soft X-ray (*Chandra* or *XMM-Newton*) data alone. For the fainter quasars which have net *Chandra* (0.5–8 keV) or *XMM-Newton* PN (0.5–10 keV) source counts of $S_{\mathrm{soft}} \lesssim 15$ (SDSS J0011+0056, 1243–0232 and 1713+5729) the soft X-ray constraints underpredict N_{H} by factors of $k_{N_{\mathrm{H}}} \approx 30$–1600, while for the brighter sources with $S_{\mathrm{soft}} \gtrsim 50$ (SDSS J1034+6001 and 1218+4706) N_{H} is underpredicted by factors of $k_{N_{\mathrm{H}}} \approx 2.5$–5. In general, the intrinsic X-ray luminosities (L_{X}) measured are ≈ 1–2 orders of magnitude higher with the addition of *NuSTAR* data, which is largely due to the increased absorption correction. These results have implications for X-ray studies of AGNs at $z < 1$ that lack sensitive high-energy (> 10 keV) coverage. For example, on the basis of our results we infer that X-ray data at < 10 keV may not reliably identify heavily obscured to CT ($N_{\mathrm{H}} \gtrsim 5 \times 10^{23}$ cm^{-2}) AGNs if the photon counts are low, and the intrinsic luminosities will be underestimated. A similar conclusion was reached by Wilkes et al. (2013), who used *Chandra* and multiwavelength data to investigate the intrinsic X-ray properties of quasars selected at low radio frequencies.

The intrinsic X-ray luminosities of our objects (close to $L_{\mathrm{X}} = 10^{44}$ erg s^{-1}, which

roughly agrees with the $L_{\mathrm{X},*}$ value for unobscured AGNs; e.g., Hasinger et al. 2005) makes them important for population synthesis models of the CXB, since $z \lesssim 1.5$ AGNs around this luminosity produce most of the CXB at its high energy peak (e.g., Treister & Urry, 2005).[9] It is thus useful to consider the N_{H} distribution and CT fraction for this class of optically selected QSO2s.

4.5.2 The N_{H} Distribution

In the left panel of Figure 4.14 we show the observed N_{H} distribution for SDSS-selected QSO2s that are detected with *Chandra* and *XMM-Newton*, and have *direct* constraints at < 10 keV from X-ray spectral fitting (J13; LaMassa et al. 2014). The 39 objects included have $z < 0.5$ and $L_{\mathrm{[O\ III]}} > 2.5 \times 10^8\ L_\odot$, and should therefore be broadly representative of the overall optically selected QSO2 population (for further details, see Section 4.2.2). The exclusion of QSO2s undetected by *Chandra* and *XMM-Newton* has a negligible impact since, for the adopted z and $L_{\mathrm{[O\ III]}}$ ranges, there are only three such objects. On the basis of these data, the column density distribution is relatively flat at $N_{\mathrm{H}} = 10^{21}$–10^{24} cm^{-2}, and there is only one object above $N_{\mathrm{H}} = 10^{24}$ cm^{-2}. The absorber for this object (SDSS J0939+3553) appears different in nature to those presented in this chapter, possibly taking the rare form of a geometrically thin toroidal ring (LaMassa et al., 2014).

In this work, we have demonstrated that soft X-ray (*Chandra* and *XMM-Newton*) studies can underpredict the N_{H} and L_{X} values of quasars with evidence for CT absorption based on multiwavelength diagnostics (CT candidates; see Section 4.5.1 and Figure 4.13). The severity of the N_{H} and L_{X} underpredictions is related to the observed soft X-ray source photon counts (S_{soft}), with the faintly detected sources suffering larger underpredictions than the more strongly detected sources. To understand the consequences of this for the true N_{H} distribution of QSO2s, our result for the *NuSTAR*-detected objects can be extrapolated to the remaining CT candidates in Figure 4.14, which were identified as

---

[9]While the *NuSTAR*-detected objects all satisfy the classical optical quasar luminosity definition (see Sections 4.2.1 and 4.2.2), based on Figure 4.13 they are just below the standard 'X-ray quasar' luminosity threshold ($L_{\mathrm{X}} > 10^{44}$ erg s^{-1}), although SDSS J1034+6001, 1218+4706 and 1243−0232 are consistent with lying above the threshold for some of the X-ray spectral model solutions.
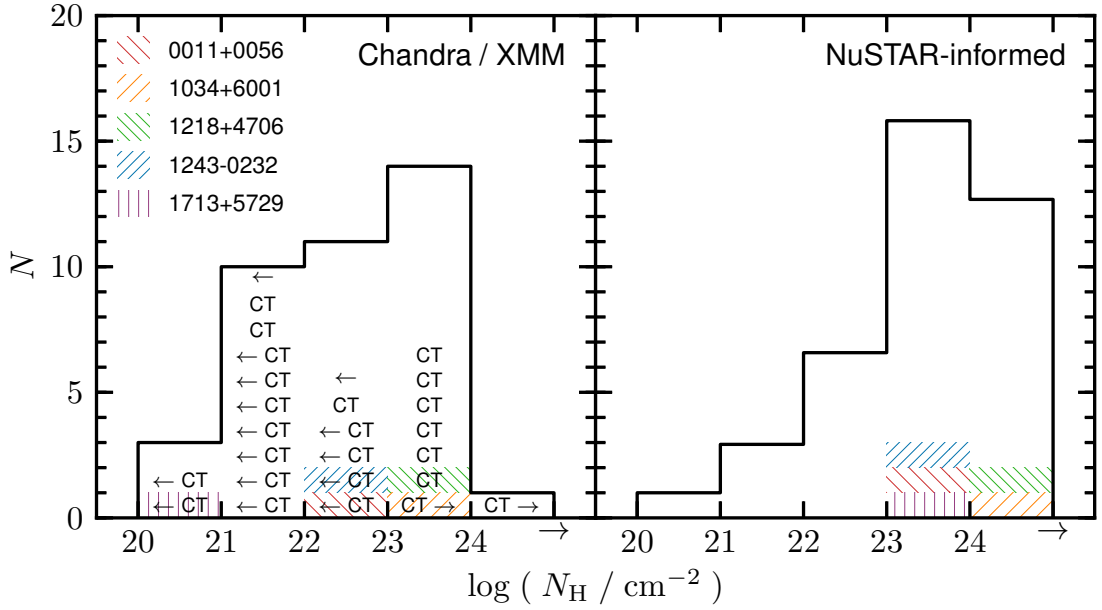
Figure 4.14: The N_H distribution of SDSS-selected QSO2s at $z < 0.5$, constructed using only direct constraints from X-ray spectral analyses. The five *NuSTAR*-observed objects with enough > 10 keV counts for X-ray spectral analyses are marked by the hatched regions. Left panel: a measurement of the N_H distribution from existing soft X-ray ($<$ 10 keV) *Chandra* and *XMM-Newton* constraints. CT candidates, identified as such in J13 and LaMassa et al. (2014) primarily using the indirect X-ray:[O III] luminosity ratio diagnostic, are labelled as "CT". Sources with upper/lower limits in N_H are marked with arrows. Right panel: Prediction for the true N_H distribution of SDSS-QSO2s, based on the results of this broad-band *NuSTAR* plus soft X-ray study; see Section 4.5.2.

such primarily based on the X-ray:[O III] luminosity ratio (J13; LaMassa et al. 2014). This extrapolation relies on assuming that the *NuSTAR*-detected subsample of five objects are representative of the remaining subsample of 19 CT candidates in terms of their absorption properties. This is a reasonable assumption; the $L_{\rm X}^{\rm obs}/L_{6\mu\rm m}$ distributions of the two subsamples are in agreement (KS test: $p = 0.70$), using the X-ray luminosities from J13 (except for SDSS J1243–0232, for which we use our measured luminosity; see footnote) and estimating the 6 μm luminosities from an interpolation between the *WISE* photometric bands.

To make a prediction for the true $N_{\rm H}$ distribution of optically selected QSO2s, we apply an $N_{\rm H}$ correction factor ($k_{N_{\rm H}}$) to each of the 19 CT candidates in Figure 4.14 not observed/detected with *NuSTAR*, informed by our *NuSTAR*-measured $k_{N_{\rm H}}$ values (Section 4.5.1). For sources with low ($S_{\rm soft} < 33$) and high ($S_{\rm soft} > 33$) soft X-ray source counts (using PN counts only in the case of *XMM-Newton* data) we draw correction factors at random from flat distributions between $1.5 < \log(k_{N_{\rm H}}) < 3.2$ and between $0.4 < \log(k_{N_{\rm H}}) < 0.7$, respectively. In determining these correction factors we assumed column densities which are at the lower end of the range that is consistent with the data (Section 4.5.1): for the three most strongly detected sources (SDSS J1034+6001, 1218+4706, 1243–0232), the lowest best-fit $N_{\rm H}$ values of $(0.9–2.0) \times 10^{24}$ cm^{-2} are adopted, although the sources are consistent with having much larger columns ($N_{\rm H} \gtrsim 5 \times 10^{24}$ cm^{-2}); and we assume the $N_{\rm H}$ lower limit for SDSS J1713+5729 ($N_{\rm H} = 5 \times 10^{23}$ cm^{-2}). As such, the $N_{\rm H}$ distribution prediction below may provide a lower limit on the CT fraction. However, this discussion is ultimately limited by the small number of sources detected above 10 keV with *NuSTAR*.

The predicted $N_{\rm H}$ distribution (averaged over many iterations) is shown in the right hand panel of Figure 4.14. This "*NuSTAR*-informed" $N_{\rm H}$ distribution for optically selected QSO2s is strongly skewed towards high columns of $N_{\rm H} > 10^{23}$ cm^{-2}. Our predicted CT fraction ($f_{\rm CT}$), defined here as the ratio of the number of objects with $N_{\rm H} > 10^{24}$ cm^{-2} to those with $N_{\rm H} > 10^{22}$ cm^{-2}, is $f_{\rm CT} = 36^{+14}_{-12}$ %, where the errors represent binomial uncertainties only. The full uncertainties are likely to be larger; considering extreme $k_{N_{\rm H}}$ distributions, where the $k_{N_{\rm H}}$ values assumed are all set equal to either the highest or lowest values of the ranges measured with *NuSTAR*, the uncertainties

on f_{CT} may be larger by a factor of ≈ 2.

The CT fraction is an important parameter in population synthesis models of the CXB. In many such models, f_{CT} is treated as a fixed, global quantity; the Treister et al. (2009) model assumes a relatively low value of 15%, while others assume 50% (Gilli et al. 2007, Ueda et al. 2014; the quoted fractions have been adjusted from the original published values to our adopted definition of f_{CT}). It is possible to estimate f_{CT} using this class of CXB synthesis model, although meaningful constraints are challenging to obtain due to degeneracies with other parameters (e.g., Akylas et al. 2012). Fixing the Compton-reflection strength parameter, Ueda et al. (2014) constrain $f_{CT} = 33$–62%, which is compatible with our result. In other CXB synthesis models, the CT fraction is dependent on physical properties of the AGN population; according to the Draper & Ballantyne (2010) model, high CT fractions are associated (beyond the local Universe) specifically with black holes accreting at a large fraction of their Eddington rate, in broad consistency with our findings.

With the N_H distribution in Figure 4.14 we have attempted to provide a prediction using only *directly* measured column densities since analysis of the X-ray spectrum should provide the "purest" measurement of the line-of-sight column density, without the need to make assumptions in comparing emission across very different wavelength regimes (i.e., using *indirect* absorption diagnostics such as the X-ray:mid-IR, X-ray:[O III] or X-ray:[Ne V] luminosity ratios). However, it is worthwhile considering an extreme scenario in which all of the candidate CTQSO2s in Figure 4.14 (labelled "CT") are truly CT; i.e., in which the indirect absorption diagnostics are assumed to be accurate. Applying this assumption, the predicted CT fraction is $f_{CT} = 65^{+11}_{-13}\,\%$. For comparison, Vignali et al. (2010) make similar assumptions using the X-ray:[O III] and X-ray:mid-IR luminosity ratios for a complete sample of 25 SDSS-selected QSO2s at $z \approx 0.5$, and determine $f_{CT} \approx 50\%$. Additionally, Vignali et al. (2014) utilize the X-ray:[Ne V] ratio for a sample of $z \approx 0.8$ type 2 AGNs and find $f_{CT} \approx 40\%$. In the case of Seyfert 2s in the local Universe, N_H distributions have been constructed for optically selected samples using indirect absorption diagnostics (primarily the X-ray:[O III] ratio), predicting a fraction of $f_{CT} \gtrsim 50\%$ for this lower luminosity AGN population (e.g., Bassani et al., 1999; Risaliti et al., 1999; LaMassa et al., 2011).

Indirect absorption diagnostics predict a larger CT fraction for $z < 0.5$ QSO2s than

our *NuSTAR*-informed N_H distribution. The apparent discrepancy may well be due to indirect diagnostics overpredicting the number of CT AGNs. Another reconciling factor could be that the quasars unobserved/undetected with *NuSTAR*, in general, suffer even heavier absorption than our detected objects. Deeper observations at both low (e.g., with *Athena*; Nandra et al. 2013) and high (e.g., with *NuSTAR* or *Astro-H*; Takahashi et al. 2012) X-ray energies are needed to reliably distinguish between the above scenarios, and thus achieve tighter constraints on f_CT for the quasar population.

4.6   Summary

Sensitive high-energy (> 10 keV) *NuSTAR* observations of five optically selected candidate CTQSO2s have been presented, along with broad-band X-ray spectral and multiwavelength analyses. Similar studies for a further four such objects have already been presented in the literature (Chapter 3 of this thesis; L14; G14). The overall sample of nine $z < 0.5$ candidate CTQSO2s was selected primarily on the basis of multiwavelength evidence for absorption by CT ($N_\mathrm{H} > 1.5 \times 10^{24}$ cm^{-2}) material along the line-of-sight (see Section 4.2.2). Our results are summarized as follows:

- Of the five recently observed objects, two are undetected by *NuSTAR* at 8–24 keV (SDSS J0758+3923 and 0840+3838), one is weakly detected (net source counts $S_{8-24\,\mathrm{keV}} = 38.1^{+19.6}_{-18.1}$; SDSS J1713+5729), and two are strongly detected ($S_{8-24\,\mathrm{keV}} \gtrsim 90$; SDSS J1218+4706 and 1243–0232). These represent the first detections of these sources at high X-ray energies; see Section 4.3.1.

- For the two strongly detected targets, spectral modelling of the *NuSTAR* plus archival soft X-ray data suggests that the primary transmitted AGN continua are suppressed by extreme levels of photoelectric absorption, with $N_\mathrm{H} \gtrsim 10^{24}$ cm^{-2}; see Section 4.4.1. For the brightest source, SDSS J1218+4706, the relatively high quality spectral analysis using physically motivated models provides strong evidence for CT absorption, with a contribution from Compton reflection; see Section 4.4.1.

- For SDSS J1713+5729, the *NuSTAR* detection likely represents the first identification of directly transmitted emission from the AGN; see Section 4.4.1. We charac-

terize the 3–24 keV spectrum using the *NuSTAR* band ratio ($\mathrm{BR_{Nu}}$) and estimate a high absorbing column density of $N_\mathrm{H} \gtrsim 5 \times 10^{23}$ cm^{-2}; see Section 4.4.2. Notably, the observed 10–40 keV luminosity appears to be extremely suppressed, by a factor of ≈ 35, with respect to the intrinsic luminosity, suggesting $N_\mathrm{H} \gg 10^{24}$ cm^{-2} if purely due to absorption; see Section 4.4.3.

- For the non detections, column densities of $N_\mathrm{H} \gtrsim 10^{24}$ cm^{-2} are inferred by comparing the upper limits in observed X-ray luminosity (at rest-frame 2–10 keV and 10–40 keV) with the intrinsic luminosities expected from the mid-IR emission. The majority of *NuSTAR*-observed candidate CTQSO2s have X-ray:mid-IR ratios suggesting CT absorption; see Section 4.4.3.

- For the five objects in the overall *NuSTAR*-observed candidate CTQSO2 sample that are detected at high energies, the column densities and intrinsic luminosities measured from spectral analyses are factors of ≈ 2.5–1600 and ≈ 10–70 higher, respectively, than soft X-ray constraints in the literature; see Section 4.5.1.

- Using direct constraints on absorption for 39 QSO2s studied at X-ray wavelengths, and assuming that the *NuSTAR*-detected QSO2s are representative of the larger sample with evidence for CT absorption, we make a prediction for the N_H distribution of optically selected QSO2s. The distribution is highly skewed toward large column densities ($N_\mathrm{H} > 10^{23}$ cm^{-2}) and the predicted CT fraction of $f_\mathrm{CT} = 36^{+14}_{-12}$ % is broadly consistent with CXB models. A higher fraction of up to 76% is possible if indirect absorption diagnostics are assumed to be accurate; see Section 4.5.2.

4.7 Additional Information for Individual Objects

Here we give further information on the individual *NuSTAR*-observed candidate CTQSO2s presented in this chapter, namely relevant multiwavelength properties and features which provide evidence for CT material. In the case of X-ray properties, this Section focuses on the low energy (< 10 keV) *Chandra* and *XMM-Newton* data which was available prior to the *NuSTAR* observations. For the broad-band X-ray constraints incorporating high energy (> 10 keV) *NuSTAR* data, which generally suggest extreme absorption, see Section

4.4.

4.7.1 SDSS J075820.98+392336.0 (z=0.216)

Fitting an unabsorbed power law model to the *XMM-Newton* 0.5–10 keV data, we measure a flat effective photon index of $\Gamma_{\rm eff} = 1.1 \pm 0.4$, indicative of photoelectric absorption in the X-ray spectrum. This source is not detected (above the 2.6σ confidence level) with *NuSTAR* at 8–24 keV; see Section 4.3.1.

4.7.2 SDSS J084041.08+383819.8 (z=0.313)

From *HST* WFPC2 (F814W) imaging (Villar-Martín et al., 2012), the host has a spiral morphology, with evidence for a tidal feature. Humphrey et al. (2010) included this object in their integral-field observations of six SDSS-QSO2s and found spatially extended [O III] and [O II] emission on scales of up to 27 kpc, consistent with being powered by AGN activity (e.g., via shocks or radiation). Using the available *XMM-Newton* 0.5–10 keV data for this object we measure $\Gamma_{\rm eff} = 0.7 \pm 0.1$, a low value suggestive of heavy absorption. This source is a non detection in the *NuSTAR* 8–24 keV data; see Section 4.3.1.

4.7.3 SDSS J121839.40+470627.7 (z=0.094)

The 0.5–10 keV *XMM-Newton* (obsID 0203270201) spectrum is modelled in J13 and LaMassa et al. (2012), who measure high column densities of $N_{\rm H} = 8.0^{+5.6}_{-4.1} \times 10^{23}$ cm^{-2} and $N_{\rm H} = (8.7^{+6.7}_{-3.4}) \times 10^{23}$ cm^{-2}, respectively. J13 measure a strong Fe Kα feature at $E_{\rm line} = 6.4 \pm 0.2$ keV with $\rm EW_{Fe\,K\alpha} = 1.7^{+2.4}_{-1.4}$ keV, consistent with CT absorption. This target is strongly detected with *NuSTAR* at 8–24 keV, allowing relatively detailed, broad-band spectral modelling which extends to high energies (> 10 keV); see Section 4.4.1.

4.7.4 SDSS J124337.34–023200.2 (z=0.281)

Using *HST* ACS imaging, Zakamska et al. (2006) find that the host galaxy light profile is well fit by a de Vaucouleurs profile, implying an elliptical morphology. The host mor-

phology is notably asymmetric. Zakamska et al. (2006) find no evidence for extinction in the host galaxy, suggesting that kpc-scale dust is not obscuring the AGN, and measure a blue excess in the nucleus which may be due to scattering or starburst emission.

Studying the existing *Chandra* data, we find an excess of emission at observed-frame ≈ 5 keV (i.e., rest-frame ≈ 6.4 keV). When fitting the continuum emission with a power law and the excess with a Gaussian component, we measure a rest-frame centroid energy compatible with Fe Kα ($E_{\text{line}} = 6.5^{+0.7}_{-0.2}$ keV), and a rest-frame equivalent width of $\text{EW}_{\text{Fe K}\alpha} = 2.5^{+4.2}_{-2.4}$ keV. Although the emission is consistent with $\text{EW}_{\text{Fe K}\alpha} \gtrsim 1$ keV, which would suggest the presence of CT material, there are too few photon counts to rule out low equivalent widths. The object appears to have an extremely flat spectrum, with $\Gamma_{\text{eff}} = -1.1^{+1.2}_{-1.6}$ for the 0.5–8 keV energy band, indicating strong photoelectric absorption. This target is strongly detected at 8–24 keV with *NuSTAR*, allowing broad-band X-ray spectral modelling; see Section 4.4.1.

4.7.5   SDSS J171350.32+572954.9 (z=0.113)

The mid-IR spectrum, as measured with *Spitzer*-IRS (Sargsyan et al., 2011), is AGN-dominated and has evidence for shallow silicate (Si) absorption at ≈ 10 μm. The low energy X-ray properties of this source are detailed in Section 4.4.1. To summarise, an extremely steep spectral shape at 0.5–10 keV ($\Gamma \approx 3$) suggests that the weak *NuSTAR* detection at 8–24 keV is the first identification of directly transmitted AGN emission from this system.

4.8   Near-ultraviolet to Mid-infrared Photometry

Here we provide the near-UV to mid-IR photometric data used in the SED modelling. In Table 4.5 we provide the near-UV to mid-IR photometric data set for the five *NuSTAR*-observed QSO2s presented in this work, and the one presented in G14 (SDSS J1034 +6001). This data set is adopted for the SED modelling in Section 4.3.3.

Table 4.5: Near-Ultraviolet to Mid-Infrared Source Properties

SDSS J	0758+3923	0840+3838	1034+6001	1218+4706	1243-0232	1713+5729
u (0.355 μm)^a	18.967 ± 0.025	20.349 ± 0.179	16.139 ± 0.008	18.727 ± 0.030	20.604 ± 0.116	18.721 ± 0.025
g (0.468 μm)^a	18.423 ± 0.008	19.166 ± 0.023	14.743 ± 0.002	17.562 ± 0.008	19.334 ± 0.018	17.480 ± 0.006
r (0.616 μm)^a	17.792 ± 0.007	18.021 ± 0.014	14.342 ± 0.002	16.843 ± 0.008	18.015 ± 0.010	16.629 ± 0.004
i (0.748 μm)^a	17.629 ± 0.008	17.627 ± 0.013	13.871 ± 0.002	16.386 ± 0.008	17.782 ± 0.012	16.133 ± 0.004
z (0.892 μm)^a	17.706 ± 0.019	17.171 ± 0.026	13.698 ± 0.004	16.180 ± 0.014	17.391 ± 0.029	16.093 ± 0.009
WISE (3.4 μm)^b	13.847 ± 0.028	14.322 ± 0.029	11.187 ± 0.024	12.592 ± 0.023	14.762 ± 0.040	12.466 ± 0.023
WISE (4.6 μm)^b	12.267 ± 0.024	13.549 ± 0.035	10.016 ± 0.021	11.448 ± 0.021	14.348 ± 0.063	11.060 ± 0.021
WISE (12 μm)^b	8.659 ± 0.022	10.013 ± 0.041	6.295 ± 0.014	8.242 ± 0.019	11.270 ± 0.155	7.242 ± 0.015
Spitzer (3.6 μm)^c	⋯	⋯	⋯	⋯	279.100 ± 3.333	⋯
Spitzer (4.5 μm)^c	⋯	⋯	⋯	⋯	258.600 ± 3.668	⋯
Spitzer (5.8 μm)^c	⋯	⋯	⋯	⋯	280.000 ± 10.640	⋯
Spitzer (8.0 μm)^c	⋯	⋯	⋯	⋯	535.300 ± 14.130	⋯

Notes.

^{a} SDSS DR7 model magnitudes in the AB sinh system, corrected for Galactic extinction.

^{b} WISE magnitudes in the Vega system. We use the gmag magnitude for SDSS J1713+5729, and profile-fit magnitudes for the remainder.

^{c} Spitzer 3.8″ diameter aperture flux densities in units of μJy.

Chapter 5

The *NuSTAR* serendipitous survey: the 40 month catalogue and the properties of the distant high energy X-ray source population

Abstract

We present the first full catalogue and science results for the *Nuclear Spectroscopic Telescope Array* (*NuSTAR*) serendipitous survey. The catalogue incorporates data taken during the first 40 months of *NuSTAR* operation, which provide ≈ 20 Ms of effective exposure time over 331 fields, with an areal coverage of 13 deg^2, and 497 sources detected in total over the 3–24 keV energy range. We have performed an extensive campaign of ground-based spectroscopic followup to obtain new source redshifts and classifications for 222 sources. Combining this with existing archival spectroscopy, there are 276 sources in total with spectroscopic identifications. We characterize the overall sample in terms of the X-ray, optical, and infrared (IR) source properties. The overall sample is primarily comprised of active galactic nuclei (AGNs), detected over a large range in redshift from $z = 0.002$ to 3.4 (median of $\langle z \rangle = 0.56$), but also includes 14 spectroscopically confirmed Galactic sources. There is a large range in X-ray flux, from $\log(f_{3-24\mathrm{keV}}/\mathrm{erg\ s^{-1}\ cm^{-2}}) \approx -14$ to -11, and in rest-frame 10–40 keV luminosity, from $\log(L_{10-40\mathrm{keV}}/\mathrm{erg\ s^{-1}}) \approx 39$ to 46, with a median of 44.1. Approximately 79%

of the *NuSTAR* sources have lower energy (< 10 keV) X-ray counterparts from *XMM-Newton*, *Chandra*, and *Swift* XRT. The mid-infrared (MIR) analysis, using *WISE* all-sky survey data, shows that MIR AGN colour-selections miss a large fraction of the *NuSTAR*-selected AGN population, from $\approx 20\%$ at the highest luminosities ($L_X > 10^{44}$ erg s^{-1}) to $\approx 80\%$ at the lowest luminosities ($L_X < 10^{43}$ erg s^{-1}). Our optical spectroscopic analysis finds that the observed fraction of optically obscured AGNs (i.e., the Type 2 fraction) is $F_{\text{Type 2}} = 53^{+14}_{-15}\%$, for a well-defined subset of the 8–24 keV selected sample. This is higher, albeit at a low significance level, than the Type 2 fraction measured for redshift- and luminosity-matched AGNs selected by < 10 keV X-ray missions.

5.1 Introduction

Since the late 1970s, which saw the advent of focusing X-ray observatories in space (e.g., Giacconi et al. 1979), X-ray surveys have provided fundamental advances in our understanding of growing supermassive black holes (e.g., Fabian & Barcons 1992; Brandt & Hasinger 2005; Alexander & Hickox 2012; Brandt & Alexander 2015). X-rays provide the most direct and efficient means of identifying active galactic nuclei (AGNs; the sites of rapid mass accretion onto supermassive black holes), since the effects of both line-of-sight absorption and dilution by host-galaxy light are comparatively low at X-ray energies. The collection of X-ray surveys over the last few decades have ranged from wide-area all-sky surveys to deep pencil-beam surveys, allowing the evolution of AGN obscuration and the X-ray luminosity function to be measured for a wide range in luminosity and redshift (up to $z \approx 5$; e.g., see Brandt & Alexander 2015 for a review). The deepest surveys with *Chandra* and *XMM-Newton* have directly resolved the majority (≈ 70–90%) of the $\lesssim 8$ keV cosmic X-ray background (CXB) into individual objects (e.g., Worsley et al. 2005; Hickox & Markevitch 2006; Xue et al. 2012).

Until very recently, the most sensitive X-ray surveys (e.g., with *Chandra* and *XMM-Newton*) have been limited to photon energies of < 10 keV, and are therefore biased against the identification of heavily obscured AGNs (for which the line-of-sight column density exceeds $N_H \sim$ a few $\times 10^{23}$ cm^{-2}). This bias is especially strong at $z \lesssim 1$, but becomes less so for higher redshifts where the spectral features of absorption, and

the penetrating higher energy X-rays, are shifted into the observed-frame X-ray energy window. The result is a complicated AGN selection function, which is challenging to correct for without a full knowledge of the prevalence of highly absorbed systems. These photon energies are also low compared to the peak of the CXB (at $\approx$ 20–30 keV), meaning that spectral extrapolations are required to characterize the AGN population responsible for the CXB peak. High energy (> 10 keV) X-ray surveys with non-focusing X-ray observatories (e.g., *Swift* BAT and *INTEGRAL*) have *directly* resolved $\approx$ 1–2% of the CXB peak into individual AGNs (Krivonos et al., 2007; Ajello et al., 2008; Bottacini et al., 2012). These surveys have been successful in characterizing the local high-energy emitting AGN population (e.g., Tueller et al., 2008; Burlon et al., 2011; Vasudevan et al., 2013; Ricci et al., 2015) but, being largely confined to $z \lesssim 0.1$, there is limited scope for evolutionary studies.

As described in Chapter 2 of this thesis, a great breakthrough in studying the high-energy X-ray emitting population is the *Nuclear Spectroscopic Telescope Array* (*NuSTAR*; Harrison et al. 2013). *NuSTAR* has opened up the possibility to study large, cleanly selected samples of high-energy emitting AGNs in the distant universe for the first time. The *NuSTAR* extragalactic survey program has provided the first measurements of the > 10 keV AGN luminosity functions at $z > 0.1$ (Aird et al., 2015b), and has directly resolved a large fraction ($35 \pm 5\%$) of the CXB at 8–24 keV (Harrison et al., 2016). In addition, both the survey program and targetted *NuSTAR* campaigns have demonstrated the importance of high-energy coverage for accurately constraining the intrinsic properties of distant AGNs (e.g., Del Moro et al., 2014; Luo et al., 2014; Civano et al., 2015; Lansbury et al., 2015; LaMassa et al., 2016), especially in the case of the most highly absorbed Compton-thick (CT) systems (where $N_{\mathrm{H}} > 1.5 \times 10^{24}$ cm^{-2}).

The *NuSTAR* extragalactic survey is the largest scientific program, in terms of time investment, undertaken with *NuSTAR* and is one of the highest priorities of the mission. There are two main "blind survey" components. Firstly, deep blank-field *NuSTAR* surveys have been performed in the following well-studied fields: the Extended *Chandra* Deep Field South (ECDFS; Lehmer et al. 2005), for which the total areal coverage with *NuSTAR* is ≈ 0.33 deg^2 (Mullaney et al. 2015, hereafter M15); the Cosmic Evolution Survey field (COSMOS; Scoville et al. 2007), which has ≈ 1.7 deg^2 of *NuSTAR* cov-

erage (Civano et al. 2015, hereafter C15); the Extended Groth Strip (EGS; Groth et al. 1994), with $\approx 0.25\ \mathrm{deg}^2$ of coverage (Aird et al., in prep.); the northern component of the Great Observatories Origins Deep Survey North (GOODS-N; Dickinson et al. 2003), with $\approx 0.07\ \mathrm{deg}^2$ of coverage (Del Moro et al., in prep.); and the Ultra Deep Survey field (UDS; Lawrence et al. 2007), with $\approx 0.4\ \mathrm{deg}^2$ of coverage (Masini et al., in prep.). Secondly, a wide-area "serendipitous survey" has been performed by searching the majority of *NuSTAR* pointings for chance background sources. An initial look at 10 serendipitous survey sources was presented in Alexander et al. (2013). Serendipitous surveys represent an efficient and economical way to sample wide sky areas, and provide substantial data sets with which to examine the X-ray emitting population and search for extreme populations. They have been undertaken with many X-ray missions over the last few decades (e.g., Gioia et al. 1990; Comastri et al. 2001; Fiore et al. 2001; Harrison et al. 2003; Nandra et al. 2003; Gandhi et al. 2004; Kim et al. 2004; Ueda et al. 2005; Watson et al. 2009; Evans et al. 2010, 2014).

In this chapter, we describe the *NuSTAR* serendipitous survey and present the first catalogue, compiled from data which span the first 40 months of *NuSTAR* operation. The serendipitous survey is a powerful component of the *NuSTAR* survey programme, with the largest overall sample size, the largest areal coverage ($\approx 13\ \mathrm{deg}^2$), and regions with comparable sensitivity to the other *NuSTAR* surveys in well-studied fields. Section 5.2 details the *NuSTAR* observations, data reduction, source detection, and photometry. We match to counterparts at lower X-ray energies (from *Chandra*, *XMM-Newton*, and *Swift* XRT; Section 5.3.1), and at optical and infrared (IR) wavelengths (Section 5.3.2). We have undertaken an extensive campaign of ground-based spectroscopic followup, crucial for obtaining source redshifts and classifications, which is described in Section 5.3.3. Our results for the X-ray, optical, and IR properties of the overall sample are presented in Sections 5.4.1, 5.4.2, and 5.4.3, respectively. We summarize the main results in Section 5.5. All uncertainties and limits are quoted at the 90% confidence level, unless otherwise stated. We assume the flat ΛCDM cosmology from WMAP7 (Komatsu et al., 2011).

5.2   The *NuSTAR* Data

Here we describe the observations, data reduction and data-analysis procedures used for the *NuSTAR* serendipitous survey: Section 5.2.1 describes the *NuSTAR* observations which have been incorporated as part of the survey; Section 5.2.2 details the data reduction procedures used to generate the *NuSTAR* science data; Section 5.2.3 provides details of the source detection approach; Section 5.2.4 outlines the photometric measurements for source counts, band ratios, fluxes and luminosities; and Section 5.2.5 describes the final source catalogue.

5.2.1   The serendipitous survey observations

The serendipitous survey is the largest area blind survey undertaken with *NuSTAR*. The survey is achieved by searching the background regions of almost every non-survey *NuSTAR* pointing for background sources unassociated with the original science target. The survey approach is well-suited to *NuSTAR* since there are generally large regions of uncontaminated background. We exclude from the survey *NuSTAR* fields with bright science targets, identified as fields with $> 10^6$ counts within $120''$ of the on-axis position. We also exclude the dedicated extragalactic (COSMOS, ECDFS, EGS, GOODS-N, UDS) and Galactic survey fields (the Galactic centre survey; Mori et al. 2015; Hong et al. 2016; and the Norma Arm survey; Fornasini et al., in prep.).

Over the period from 2012 July to 2015 November, which is the focus of the current study, there are 510 individual *NuSTAR* exposures which have been incorporated into the serendipitous survey. These exposures were performed over 331 unique fields (i.e., 331 individual sky regions, each with contiguous coverage comprised of one or more *NuSTAR* exposures), yielding a total sky area coverage of 13 deg^2. Table 5.1 lists the fields chronologically,[1] and provides the following details for each field: the name of the primary *NuSTAR* science target; the number of *NuSTAR* exposures; the individual *NuSTAR* observation ID(s); the observation date(s); the pointing coordinates; the exposure time(s); the number of serendipitous sources detected; and flags to indicate the *NuSTAR* fields

---

[1]In Table 5.1 we show the first ten fields as an example. The full table, which includes all 331 fields, is available online.

which were used in the Aird et al. (2015b) and Harrison et al. (2016) studies. Figure 5.1 shows an all-sky map of the serendipitous survey fields. The fields have a cumulative exposure time of 20.4 Ms. For comparison, the *NuSTAR* surveys of COSMOS and ECDFS have cumulative exposure times of 3.1 Ms and 1.5 Ms (C15 and M15, respectively). The serendipitous survey fields cover a wide range in individual exposure times (from ~ 10 ks to 1 Ms), and have a median exposure of 28 ks (these values correspond to a single *NuSTAR* FPM). For 76% of the fields there is a single *NuSTAR* exposure, and for the remainder there are multiple (from two to 15) exposures which are combined together for the science analyses (see Section 5.2.2).

An important contributor of fields to the *NuSTAR* serendipitous survey is the *NuSTAR* "snapshot survey" (Baloković et al. 2014; Baloković et al. 2016, in prep.), a dedicated *NuSTAR* program targetting *Swift* BAT-selected AGNs (the *Swift* BAT AGNs themselves are not included in the serendipitous survey, only the background regions of the *NuSTAR* observations). For this work we include 154 snapshot survey fields observed during the first 40 months of *NuSTAR* operation. These yield 21% of the total serendipitous survey source detections, and make up a large fraction of the survey area (accounting for 47% of the fields incorporated, in total).

5.2.2 Data processing

For data reduction, we use HEASoft v. 6.15, the *NuSTAR* Data Analysis Software (NuSTARDAS) v. 1.3.0, and CIAO v. 4.8. For each of the 510 obsIDs incorporated in the survey, the raw, unfiltered event files for FPMA and FPMB were processed using the NUPIPELINE program to yield calibrated, cleaned event files. For source detection and photometry (see Sections 5.2.3 and 5.2.4), we adopt the observed-frame energy bands which have been utilized for the *NuSTAR* extragalactic survey programme in general, and other recent *NuSTAR* studies: 3–8, 3–24, and 8–24 keV (hereafter referred to as the soft, full, and hard bands; e.g., Alexander et al., 2013; Luo et al., 2014; Aird et al., 2015b; Lansbury et al., 2015; Harrison et al., 2016). To produce individual energy band images from the *NuSTAR* event lists we used the CIAO program DMCOPY (Fruscione et al., 2006).

To produce exposure maps, which account for the natural dither of the observatory and regions of lower sensitivity (e.g., chip gaps), we follow the procedure outlined in detail

Table 5.1: Details of the individual *NuSTAR* observations which make up the serendipitous survey

Field ID (1)	Science Target (2)	N_{obs} (3)	Obs. ID (4)	Obs. Date (5)	R.A. (°) (6)	Decl. (°) (7)	t_{exp} (ks) (8)	$N_{serendips}$ (9)	A15 (10)	H16 (11)
1	2MASXJ05081967p1721483	1	60006011002	2012-07-23	77.08	17.36	16.6	0	0	0
2	Bkgd BII m11d2	1	10060003001	2012-07-24	71.11	28.38	8.9	0	0	0
3	2MASXJ04234080p0408017	2	...	...	...	...	12.3	2	1	1
3a		...	60006005002	2012-07-25	65.92	4.13	6.4	...	...	...
3b		...	60006005003	2012-07-25	65.92	4.13	5.9	...	...	...
4	IC4329A	1	60001045002	2012-08-12	207.33	-30.31	177.3	2	0	1
5	Mrk231	2	...	...	...	...	74.9	4	1	1
5a		...	60002025002	2012-08-26	194.06	56.87	44.3	...	...	...
5b		...	60002025004	2013-05-09	194.06	56.87	30.6	...	...	...
6	NGC7582	2	...	...	...	...	33.4	2	0	1
6a		...	60061318002	2012-08-31	349.60	-42.37	17.7	...	...	...
6b		...	60061318004	2012-09-14	349.60	-42.37	15.7	...	...	...
7	AE Aqr	4	...	...	...	...	134.2	2	1	1
7a		...	30001120002	2012-09-04	310.04	-0.87	7.2	...	...	...
7b		...	30001120003	2012-09-05	310.04	-0.87	40.5	...	...	...
7c		...	30001120004	2012-09-05	310.04	-0.87	76.6	...	...	...
7d		...	30001120005	2012-09-07	310.04	-0.87	9.8	...	...	...
8	NGC612	1	60061014002	2012-09-14	23.49	-36.49	17.9	0	0	1
9	3C382	1	60061286002	2012-09-18	278.76	32.70	18.0	1	0	0
10	PBCJ1630d5p3924	1	60061271002	2012-09-19	247.64	39.38	17.1	1	1	1
...	...	...	...	...	...	...	...	...	...	...

Notes. (1): ID assigned to each field. For fields with multiple *NuSTAR* exposures (i.e., $N_{obs} > 1$), each individual component exposure is listed with a letter suffixed to the field ID (e.g., 3a and 3b). (2): Object name for the primary science target of the *NuSTAR* observation(s). (3): The number of individual *NuSTAR* exposures for a given field (N_{obs}). (4): *NuSTAR* observation ID. (5): Observation start date. (6) and (7): Approximate R.A. and decl. (J2000) coordinates for the aim-point, in decimal degrees. (8): Exposure time ("ONTIME"; ks), for a single FPM (i.e., averaged over FPMA and FPMB). (9): The number of serendipitous *NuSTAR* sources detected in a given field. This table shows the first ten (out of 331) fields only. Machine readable versions the full table are available online. (10) and (11): Binary flags to highlight the serendipitous survey fields used for the Aird et al. (2015b) and Harrison et al. (2016) studies, respectively.
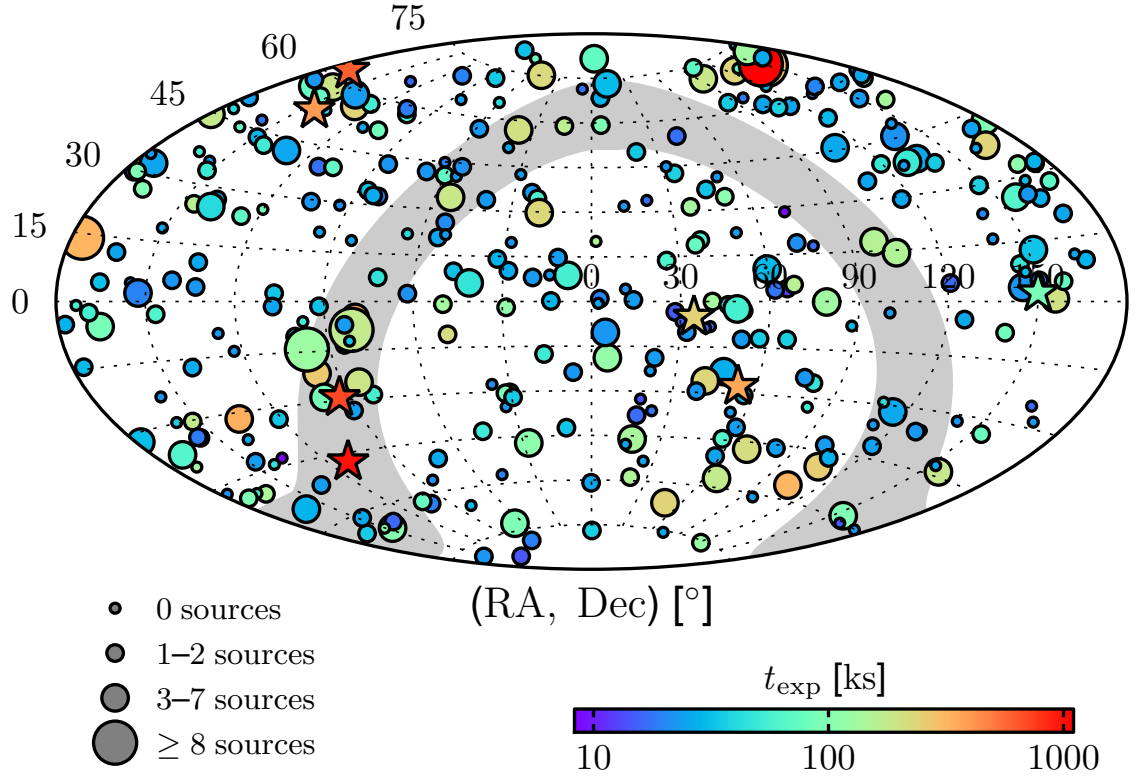
Figure 5.1: Aitoff projection showing the distribution of *NuSTAR* serendipitous survey fields on the sky, in equatorial coordinates (R.A., decl.). The circle sizes correspond to the number of sources detected in a given field, and the colours correspond to the cumulative exposure time (per FPM) for a given field. The locations of the dedicated *NuSTAR* surveys in well-studied fields (COSMOS, ECDFS, EGS, GOODS-N, UDS, the Galactic centre, and the Norma Arm), which are not included in the serendipitous survey, are marked with star symbols (with the colours representing the maximum unvignetted exposures). Also excluded from the serendipitous survey are *NuSTAR* fields containing bright targets (not shown on this figure; see Section 5.2.1). The gray area highlights the region $\pm 10°$ of the Galactic plane.

in Section 2.2.3 of M15. Vignetting in the optics results in a decrease in the effective exposure with increasing distance from the optical axis. We produce both vignetting-corrected and non-vignetting-corrected exposure maps. The former allow us to determine the effective exposure at source positions within the FoV and correctly determine count rates, while the latter are more appropriate for the scaling of background counts since the *NuSTAR* aperture background component dominates the background photon counts at $\lesssim 30$ keV (e.g., Wik et al., 2014).

In order to increase sensitivity, we perform source detection (see Section 5.2.3) and photometry (see Section 5.2.4) on the coadded FPMA+FPMB (hereafter "A+B") data, produced by combining the FPMA and FPMB science data with the HEASoft package XIMAGE. For fields with multiple obsIDs, we use XIMAGE to combine the data from individual observations, such that each field has a single mosaic on which source detection and photometry are performed.

5.2.3   Source detection

In general, the source-detection procedure follows that adopted in the dedicated blank-field surveys (e.g., see C15 and M15). A significant difference with the serendipitous survey, compared to the blank-field surveys, is the existence of a science target at the FoV aim-point. We account for the background contribution from such science targets by incorporating them in the background map generation, as described below. We also take two steps to exclude sources associated with the science target: (1) in cases where the target has an extended counterpart in the optical or IR bands (e.g., a low-redshift galaxy or galaxy cluster), we mask out custom-made regions which are conservatively defined to be larger than the extent of the counterpart in the optical imaging coverage (from the SDSS or DSS), accounting for spatial smearing of emission due to the *NuSTAR* PSF; (2) for all point-source detections with spectroscopic identifications, we assign an "associated" flag to those which have a velocity offset from the science target [$\Delta(cz)$] smaller than 5% of the total science target velocity.

Here we summarize the source detection procedure, which is applied separately for each of the individual *NuSTAR* energy bands (soft, full, and hard) before the individual band source lists are merged to form the final catalogue. For every pixel position across

the *NuSTAR* image, a "false probability" is calculated to quantify the chance that the counts measured in a source detection aperture around that position are solely due to a background fluctuation. In this calculation we adopt a circular source detection aperture of radius $20''$, which is justified by the tight core of the *NuSTAR* PSF (FWHM$= 18''$), and was also adopted for the dedicated blank-field surveys (e.g., C15; M15). To measure the background level at each pixel position, background counts are first measured from the *NuSTAR* image using an annular aperture of inner radius $45''$ and outer radius $90''$, centred on that position. These background counts are then re-scaled to the $20''$ source detection aperture according to the ratio of effective areas (as determined from non-vignetting-corrected exposure maps). This approach allows the local background to be sampled without significant contamination from source counts, and accounts for any contribution to the background from a bright science target. The Poisson false probability (P_{False}) is assessed at each pixel, using the source and scaled background counts (e.g., Lehmer et al., 2005; Nandra et al., 2005; Laird et al., 2009), to yield a P_{False} map. From this map we exclude areas within $30''$ of the low-exposure ($< 10\%$ of the maximum exposure) peripheral regions close to the FoV edge, where there is a steep drop-off in exposure and the background is poorly characterized.

We then perform source detection on the P_{False} map to identify sources. For a full, detailed description of this source detection procedure we refer the reader to Section 2.3 of M15. In brief, the SExtractor algorithm (Bertin & Arnouts, 1996) is used to identify regions of each P_{False} map which fall below a threshold of $\log(P_{\text{False}}) < -6$ (the approximate average of the thresholds adopted for the *NuSTAR*-COSMOS and *NuSTAR*-ECDFS surveys; C15; M15), producing source lists for each individual energy band. The coordinates for each detected source are measured at the local minimum in P_{False}. Finally, we merge the sources detected in the different energy bands to yield a final source list. To achieve this band-merging, the soft (3–8 keV) and hard (8–24 keV) band detected sources are matched to the full (3–24 keV) band source list using a matching radius of $35''$. The adopted *NuSTAR* source coordinates correspond to the position of the source in the full band, if there is a detection in this band. Otherwise the coordinates correspond to the soft band, if there is a detection in this band, or the hard band if there is no full or soft band detection. The analyses described below (e.g., photometry and multiwavelength counterpart

matching) are performed using these adopted source coordinates. After the above source detection has been performed, we exclude any sources within $90''$ of the central science target position (for comparison, the half-power diameter of the *NuSTAR* PSF is $58''$).

To determine the overall sky coverage of the survey as a function of flux sensitivity, we sum the sensitivity curves for the 331 individual fields. For each field the sensitivity curve is determined by calculating, for every point in the *NuSTAR* image (excluding the low-exposure peripheral regions), the flux limit corresponding to $\log(P_{\text{False}}) = -6$ (the detection threshold), given the background and exposure maps described above and the count-rate to flux conversion factors listed in Section 5.2.4. Figure 5.2 shows the total, summed sensitivity curves for the serendipitous survey, for the three main energy bands. Figure 5.3 shows the logarithmic version, compared to the other components of the *NuS-TAR* extragalactic surveys program. The serendipitous survey has the largest solid angle coverage for most fluxes, and a similar areal coverage to the deepest blank-field survey (the *NuSTAR*-EGS survey) at the lowest flux limits. In both Figure 5.2 and Figure 5.3 we also show the area curves for the subset of the serendipitous survey which lies outside of the Galactic plane ($|b| > 10°$) and is thus relatively free of Galactic sources. We note that the recent works of Aird et al. (2015b) and Harrison et al. (2016), which presented the source number counts and luminosity functions for the *NuSTAR* extragalactic survey program, only incorporated serendipitous survey fields at $\text{decl.} > -5°$ and $|b| > 20°$.

5.2.4 Photometry

For each source detected using the above procedure we measure the net counts, count rates and fluxes, and for sources with spectroscopic redshifts we calculate rest-frame luminosities. For the aperture photometry, we adopt a circular aperture of $30''$ radius to measure the gross (i.e., source plus background) counts (S). The scaled background counts (B_{src}) are determined using the same procedure as for the source detection (Section 5.2.3), and are subtracted from S to obtain the net source counts (S_{net}). The errors on S_{net} are computed as $1 + \sqrt{S + 0.75}$ (84% confidence level; e.g., Gehrels 1986). For sources undetected in a given band, 3σ upper limits for S_{net} are calculated as $3 \times \sqrt{S}$. To determine the net count rate, we divide S_{net} by the exposure time drawn from the vignetting-corrected exposure map (mean value within the $30''$ aperture).
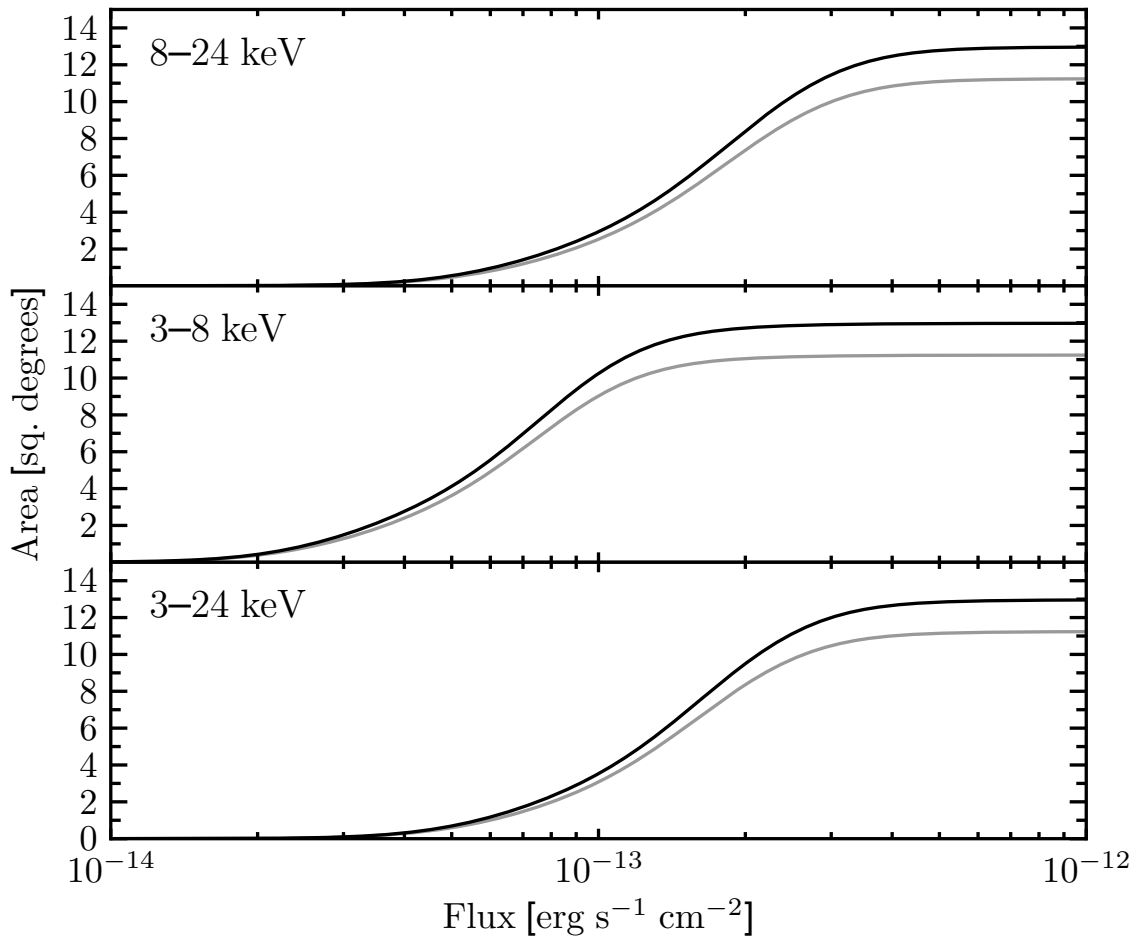
Figure 5.2: Sky coverage (solid angle) of the *NuSTAR* serendipitous survey as a function of (aperture-corrected) flux sensitivity, for the three main energy bands. The black line shows the area curve for the full survey, and the gray line shows that for the survey regions outside the Galactic plane ($|b| > 10°$).
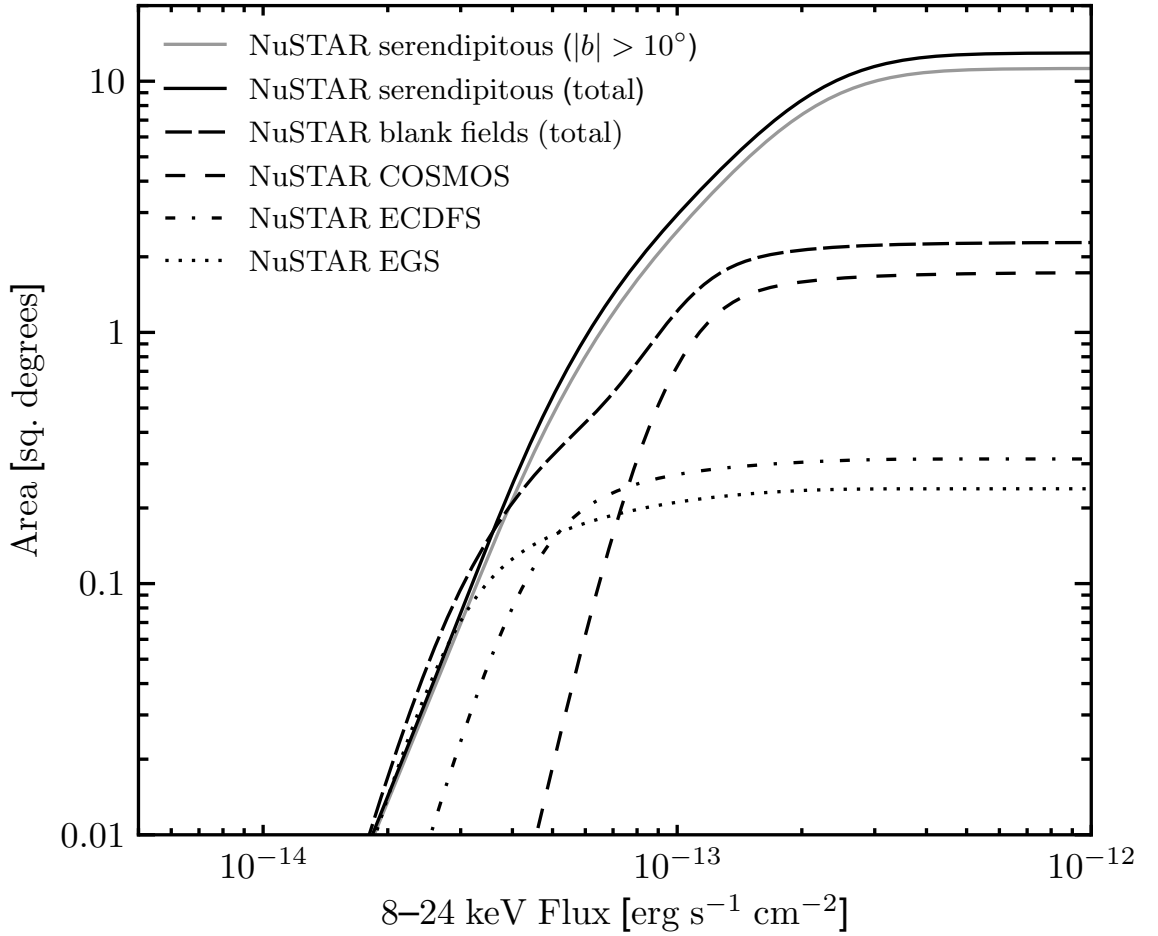
Figure 5.3: Sky coverage (solid angle) of the *NuSTAR* serendipitous survey as a function of flux sensitivity, for the hard (8–24 keV) energy band, at which *NuSTAR* is uniquely sensitive. I.e., the sky coverage for which sources above a given hard band flux will be detected in the hard band. The black and gray solid lines show the area curves for the overall and the $|b| > 10°$ serendipitous survey, respectively. We compare with the other completed components of the *NuSTAR* extragalactic surveys program, which include the following dedicated blank-field surveys: *NuSTAR*-COSMOS (dashed line; C15), *NuSTAR*-ECDFS (dash-dotted line; M15), and *NuSTAR*-EGS (dotted line; Aird et al., in prep.). The total area for these blank-field surveys (which are not included as part of the serendipitous survey) is shown as a long-dashed line.

Deblending is performed following the procedure outlined in detail in Section 2.3.2 of M15. In short, for a given source, the contributions from neighbouring detections (within a $90''$ radius) to the source aperture counts are accounted for using knowledge of their separation and brightness. The false probabilities and photometric quantities (e.g., counts, flux) are all recalculated post-deblending, and included in the catalogue in separate columns. Out of the total 498 sources in the source catalogue, only one is no longer significant (according to our detection threshold) post-deblending.

NuSTAR hard-to-soft band ratios ($\mathrm{BR_{Nu}}$) are calculated as the ratio of the 8–24 to 3–8 keV count rates. For sources with full band counts of $S_{\mathrm{net}} > 100$, and with a detection in at least one of the soft or hard bands, we derive an effective photon index (Γ_{eff}); i.e., the spectral slope of a power law spectrum that is required to produce a given band ratio.

To measure fluxes, we convert from the deblended $30''$ count rates using the following conversion factors: 6.7×10^{-11}, 9.4×10^{-11} and 13.9×10^{-11} erg cm^{-2} cts^{-1} for the soft, full and hard bands, respectively. These conversion factors were derived to account for the *NuSTAR* response, and assume an unabsorbed power-law with a photon index of $\Gamma_{\mathrm{eff}} = 1.8$ (typical of AGN detected by *NuSTAR*; e.g., Alexander et al. 2013). The conversion factors return aperture-corrected fluxes; i.e., they are corrected to the 100% encircled-energy fraction of the PSF. The general agreement between our *NuSTAR* fluxes and those from *Chandra* and *XMM-Newton* (see Section 5.3.1) indicates that the *NuSTAR* flux measurements are reliable. For sources with spectroscopic redshifts, we determine the rest-frame 10–40 keV luminosity by extrapolating from a measured observed-frame flux, assuming a photon index of $\Gamma_{\mathrm{eff}} = 1.8$. To ensure that the adopted observed-frame flux energy band corresponds to the rest-frame 10–40 keV energy band, we use the observed-frame 8–24 and 3–8 keV bands for sources with redshifts of $z < 1.35$ and $z \geq 1.35$, respectively. For cases with a non-detection in the relevant band (i.e., 8–24 or 3–8 keV), we instead extrapolate from the full band (3–24 keV).

5.2.5 The source catalogue

The serendipitous survey source catalogue is provided online in machine readable formats. In Section A.1 we give a detailed description of the 106 columns that are provided in the catalogue. In total, the catalogue contains 497 sources which are significantly detected

Table 5.2: Source statistics for the *NuSTAR* serendipitous survey

Band	N	N_z
(1)	(2)	(3)
Any band	497	276
F + S + H	104 (21%)	77
F + S	116 (23%)	82
F + H	35 (7%)	21
S + H	0 (0%)	0
F	165 (33%)	77
S	53 (11%)	16
H	24 (5%)	3

Notes. (1): F, S, and H refer to sources detected in the full (3–24 keV), soft (3–8 keV), and hard (8–24 keV) energy bands. E.g.: "F + H" refers to sources detected in the full and hard bands only, but not in the soft band; and "S" refers to sources detected exclusively in the soft band. (2): The number of sources detected post-deblending, for a given band or set of bands. (3): The number of sources with spectroscopic redshift measurements.

(according to the definition in Section 5.2.3) post-deblending, in at least one energy band. Table 5.2 provides source detection statistics, broken down for the different combinations of energy bands, and the number of sources with spectroscopic redshift measurements.

In addition to the primary source detection approach (Section 5.2.3), which has been used to generate the above main catalogue, in Section A.3 we provide a "secondary catalogue" containing sources that do not appear in the main catalogue (for reasons described therein). However, all analyses in this work are limited to the main catalogue only (the secondary catalogue is thus briefer in content).

5.3   The Multiwavelength Data

The positional accuracy of *NuSTAR* ranges from $\approx 8''$ to $\approx 20''$, depending on the source brightness (the latter is demonstrated in the following section). For matching to unique counterparts at other wavelengths (e.g., optical and IR), a higher astrometric accuracy is required, especially toward the Galactic plane where the sky density of sources increases dramatically. We therefore first match to soft X-ray (*Chandra*, *XMM-Newton*, and *Swift* XRT) counterparts, which have significantly higher positional accuracy (Sec-

tion 5.3.1), before proceeding to identify optical and IR counterparts (Section 5.3.2), and undertaking optical spectroscopy (Section 5.3.3)

5.3.1 Soft X-ray counterparts

The *NuSTAR* serendipitous survey is mostly composed of fields containing well-known extragalactic and Galactic targets. This means that the large majority of the serendipitous survey sources also have lower-energy (or "soft") X-ray coverage from *Chandra*, *XMM-Newton*, or *Swift* XRT, thanks to the relatively large FoVs of these observatories. In addition, short-exposure coordinated *Swift* XRT observations have been obtained for the majority of the *NuSTAR* observations. Overall, 81% $(401/497)$ of the *NuSTAR* detections have coverage with *Chandra* or *XMM-Newton*, and this increases to 99% $(493/497)$ if *Swift* XRT coverage is included. Only 1% $(4/497)$ lack any form of coverage from all of these three soft X-ray observatories.

We crossmatch with the third *XMM-Newton* serendipitous source catalogue (3XMM; Watson et al. 2009; Rosen et al. 2016) and the *Chandra* Source Catalogue (CSC; Evans et al. 2010) using a $30''$ search radius from each *NuSTAR* source position; the errors in the source matching are dominated by the *NuSTAR* positional uncertainty (as quantified below). Based on the sky density of X-ray sources with $f_{2-10\mathrm{keV}} \gtrsim 10^{-14}$ erg s^{-1} cm^{-2} found by Mateos et al. (2008; for $|b| > 20°$ sources in the *XMM-Newton* serendipitous survey), we estimate that the $30''$ radius matching results in a typical spurious match fraction of $\approx 7\%$ for this flux level and latitude range. Overall, we find multiple matches for $\approx 20\%$ of the cases where there is at least one match. In these multiple match cases we assume that the 3XMM or CSC source with the brightest hard-band (4.5–12 keV and 2–7 keV, respectively) flux is the correct counterpart.[2] We provide the positions and 3–8 keV fluxes (F_{soft}) for these soft X-ray counterparts in the source catalogue. In addition, for each *NuSTAR* source we provide the total combined flux of all 3XMM or

---

[2]For clarity, throughout the chapter we refer to the 3–8 keV band as the "soft" band, since it represents the lower (i.e., "softer") end of the energy range for which *NuSTAR* is sensitive. However, energies of 3–8 keV (and other similar bands; e.g., 2–7 keV) are commonly referred to as "hard" in the context of lower energy X-ray missions such as *Chandra* and *XMM-Newton*, for which these energies are at the upper end of the telescope sensitivity.

CSC sources contained within the $30''$ search aperture ($F_{\rm soft}^{30}$). For the 284 sources which are successfully matched to 3XMM or CSC, 29 (10%) have $F_{\rm soft}^{30}$ values which exceed $F_{\rm soft}$ by a factor of > 1.2, and there are only four cases where this factor is > 2. In other words, there are few cases where additional nearby X-ray sources appear to be contributing substantially to the *NuSTAR* detected emission.

In addition to the aforementioned catalogue matching, we identify archival *Chandra*, *XMM-Newton* and *Swift* XRT data that overlap in sky coverage with the *NuSTAR* data. Using these archival data sets, we manually identify and measure positions for soft X-ray counterparts which are not already included in the 3XMM and CSC catalogues. For *Chandra* we process the archival data using CHANDRA_REPRO,[3] for *XMM-Newton* we analyse data products from the Pipeline Processing System,[4] and for *Swift* XRT we use screened event files (as provided on HEASARC).[5] We perform source detection on the archival soft X-ray (≈ 0.5–8 keV) counts images using the CIAO source detection algorithm `wavdetect` (Freeman et al., 2002), which identifies 111 new soft X-ray counterparts. 88% of these have high detection significances (false probabilities of $< 10^{-6}$), and 12% have moderate detection significances (false probabilities of 10^{-6}–10^{-4}).

In total, soft X-ray counterparts are successfully identified for 79% ($395/497$) of the *NuSTAR* detections: 284 are existing counterparts in the 3XMM and CSC catalogues, with 269 and 82 counterparts from the individual 3XMM and CSC catalogues, respectively. Of the remaining 213 *NuSTAR* detections that lack 3XMM and CSC counterparts, we have manually identified soft X-ray counterparts in archival data (using `wavdetect` as described above) for 111 sources, of which 27, 60, and 24 are from *Chandra*, *Swift* XRT, and *XMM-Newton* data, respectively. In addition, we manually determine new *Chandra* positions for 12 sources which appear in 3XMM and not CSC, but have *Chandra* coverage, thus improving the X-ray position constraints for these sources. For four of these sources, the newly measured *Chandra* positions were obtained through our own *Chandra* observing program aimed at localizing the X-ray emission for Galactic-candidate *NuSTAR* serendipitous sources (Tomsick et al., in prep.). For the soft X-ray counterparts which are

---

[3]http://cxc.harvard.edu/ciao/ahelp/chandra_repro.html

[4]http://www.cosmos.esa.int/web/xmm-newton/pipeline

[5]http://heasarc.gsfc.nasa.gov

detected with multiple soft X-ray observatories, we adopt the position with the highest accuracy: for 31% ($121/395$) the adopted position is from *Chandra*, which has the best positional accuracy; for 54% ($214/395$) the adopted position is from *XMM-Newton*; and for 15% ($60/395$) the adopted counterpart is from *Swift* XRT.

Overall, 21% ($102/497$) of the *NuSTAR* detections lack soft X-ray counterparts. There are only four cases where this is due to zero coverage. The remainder can largely be explained as a result of insufficient-depth soft X-ray coverage. However, for the sources with sufficient-depth soft X-ray coverage the lack of a counterpart may indicate either a spurious *NuSTAR* detection, a transient detection, or the detection of an unidentified contaminating feature such as stray light (e.g., Mori et al. 2015). We estimate that there are 34 (out of 102) such sources, that lack a soft X-ray counterpart but have sufficiently deep soft X-ray data (from *Chandra* or *XMM-Newton*) that we would expect a detection (given the *NuSTAR* source flux in the overlapping 3–8 keV band). We retain these sources in the sample, but note that their inclusion (or exclusion) has a negligible impact on the results presented herein which are primarily based on the broader subsample with successful counterpart identifications and spectroscopic redshift measurements.

The upper panel of Figure 5.4 shows the distribution of positional offsets (in R.A. and decl.) for the *NuSTAR* sources relative to their soft X-ray (*Chandra*, *XMM-Newton*, and *Swift* XRT) counterparts. We find no evidence for systematic differences in the astrometry between observatories, since the mean positional offsets are all consistent with zero: the mean values of $\Delta\mathrm{RA}\cdot\cos(\mathrm{Dec})$ and $\Delta\mathrm{Dec}$ are $0.41\pm1.45''$ and $0.18\pm1.28''$ for *Chandra*, $-0.19\pm1.11''$ and $0.50\pm0.95''$ for *XMM-Newton*, and $-0.34\pm1.97''$ and $1.70\pm2.09''$ for *Swift* XRT.

The lower panel of Figure 5.4 shows the radial separation (in arcseconds) of *NuSTAR* sources from their well-localized soft X-ray counterparts (for those sources with *Chandra* or *XMM-Newton* counterparts) as a function of P_{False}, thus illustrating the positional accuracy of *NuSTAR* as a function of source-detection significance. To reliably assess the positional accuracy of *NuSTAR*, we limit this particular analysis to sources with unique matches at soft X-ray energies, and thus with higher likelihoods of being correctly matched. Assuming zero uncertainty on the *Chandra* and *XMM-Newton* positions, the 90% confidence limit on the *NuSTAR* positional uncertainty is $22''$ for the least-significant

detections, and $14''$ for the most-significant detections. If we instead only consider the *Chandra* positions, which are in general more tightly constrained (positional accuracy $\lesssim 1''$; e.g., see Section 5.3.2), then the inferred 90% positional accuracy of *NuSTAR* improves to $20''$ and $12''$ for the least-significant and most-significant sources, respectively.

Figure 5.5 compares the 3–8 keV fluxes, as measured by *NuSTAR*, with those measured by *Chandra* and *XMM-Newton* for the sources with 3XMM or CSC counterparts. The small flux corrections from the 3XMM and CSC energy bands (4.5–12 keV and 2–7 keV, respectively) to the 3–8 keV energy band are described in Section A.1. The majority of sources (92% and 89% for *Chandra* and *XMM-Newton*, respectively) are consistent with lying within a factor of three of the 1:1 relation, given the uncertainties, and thus show reasonable agreement between observatories. Given that the *NuSTAR* and the lower-energy X-ray observations are not contemporaneous, intrinsic source variability is expected to contribute to the observed scatter. A number of sources at the lowest X-ray fluxes lie above the relation, due to Eddington bias. This effect has been observed in the *NuSTAR*-ECDFS and *NuSTAR*-COSMOS surveys (M15; C15), and is predicted from simulations (C15).

Two relatively high-flux 3XMM sources lie significantly below the 1:1 relation, suggesting that they have experienced a large decrease in flux (by a factor of $\gtrsim 5$). The first, NuSTAR J183452-0845.6, is a known Galactic magnetar for which the *NuSTAR* (2015) flux is lower than the *XMM-Newton* (2005 and 2011 combined) flux by a factor of ≈ 15. This is broadly consistent with the known properties of the source, which varies in X-ray flux by orders of magnitude over multi-year timescales (e.g., Younes et al., 2012). The second outlying source is extragalactic in origin: NuSTAR J133311-3406.8 (hereafter J1333; $z = 0.091$; $L_{10-40\mathrm{keV}} = 8 \times 10^{42}$ erg s^{-1}). Our NTT (ESO New Technology Telescope) spectrum for J1333 reveals a NLAGN, with an apparently asymmetric, blue wing component to the Hα+[N II] complex, and our NTT R-band imaging shows a well-resolved, undisturbed host galaxy. Modelling the *XMM-Newton* (14 ks exposure; ≈ 1100 EPIC source counts at 0.5–10 keV) and *NuSTAR* (17 ks exposure; ≈ 75 source counts at 3–24 keV) spectra, the former of which precedes the latter by ≈ 9 years, the X-ray spectral flux has decreased by a factor of ≈ 5 in the energy band where the observatories overlap in sensitivity (3–10 keV). This variability is large compared to that
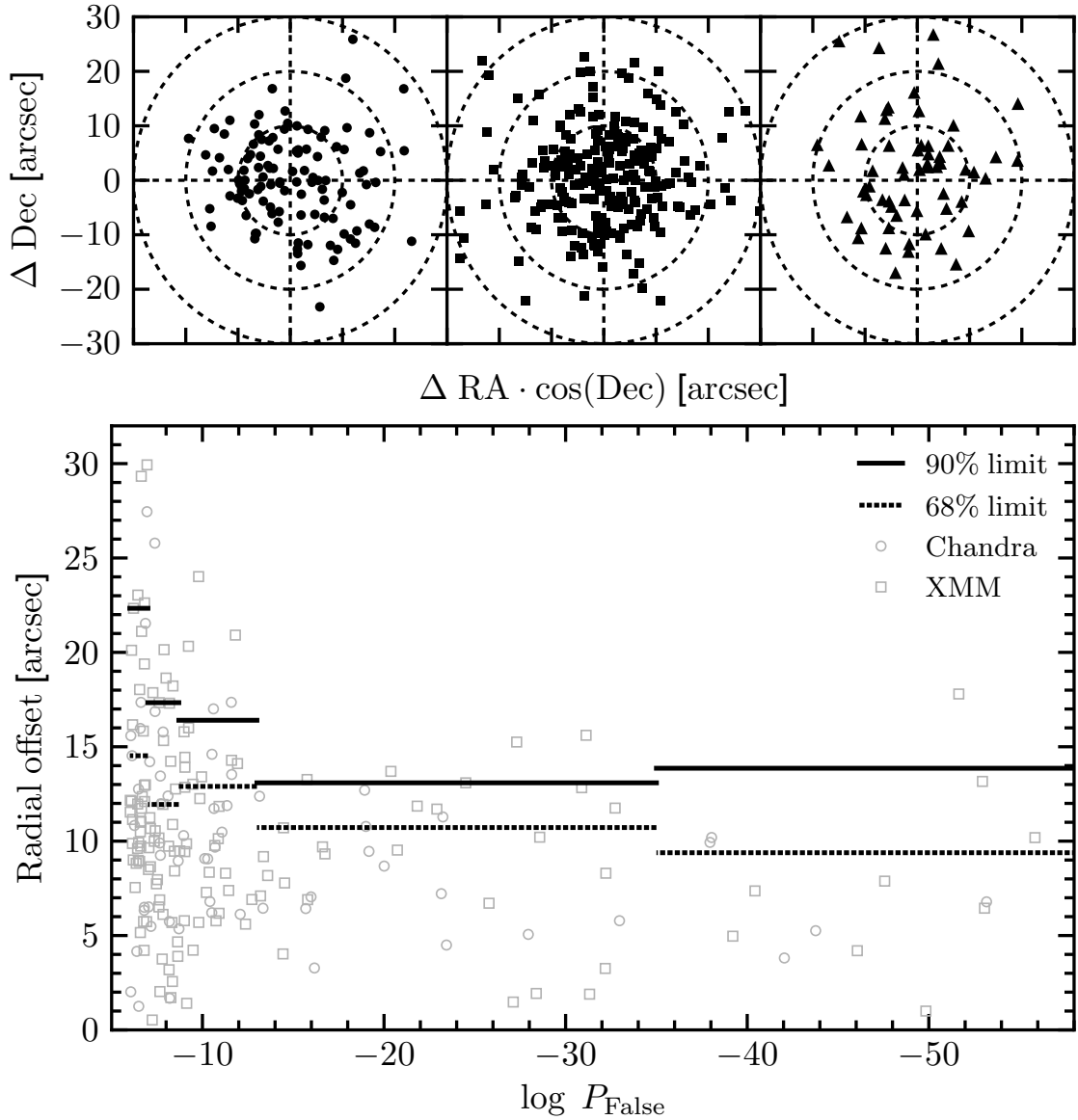
Figure 5.4: Upper panel: astrometric offsets between the *NuSTAR* coordinates and lower-energy X-ray counterpart coordinates as identified with *Chandra* (circles, left panel), *XMM-Newton* (squares, centre panel), and *Swift* XRT (triangles, right panel). Lower panel: the angular separation between *NuSTAR* and *Chandra/XMM-Newton* coordinates, as a function of P_{False} (source detection significance increases towards the right). The solid and dotted lines show the limits in angular offset enclosing 90% and 68% of sources, for bins in P_{False}. Each bin contains $\approx$ 40–50 sources, except the rightmost bin which contains 23 sources (and extends beyond the x-axis upper limit, including all sources with $P_{\text{False}} < -35$). This figure illustrates the positional accuracy of *NuSTAR* as a function of source significance.
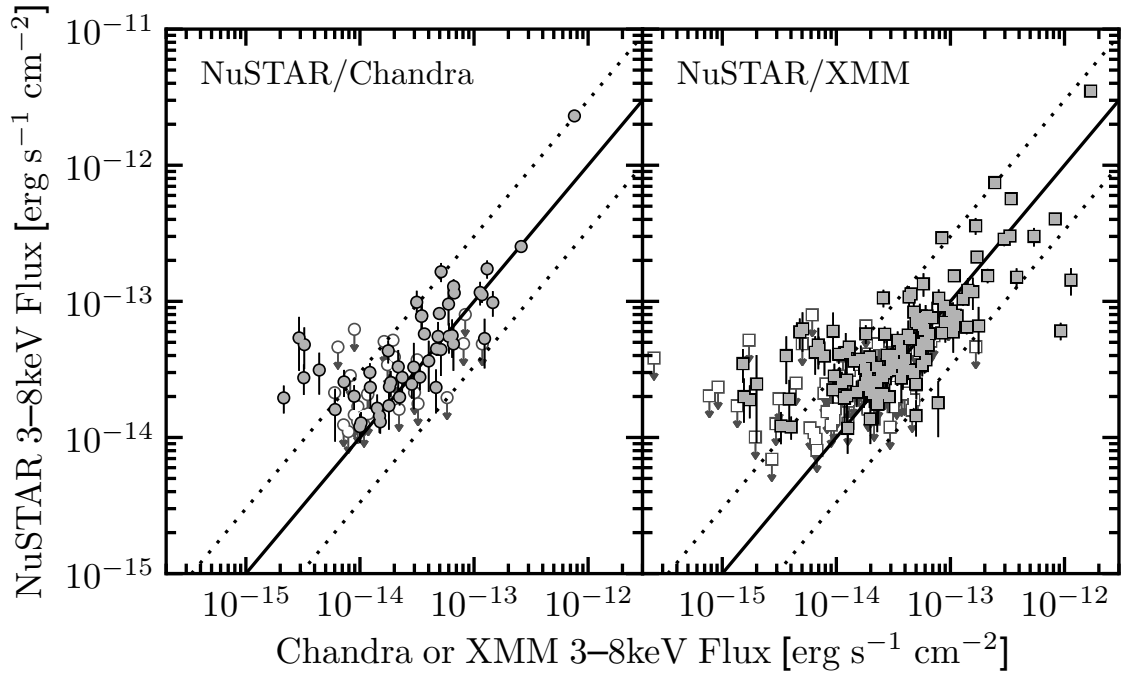
Figure 5.5: Comparison of the *NuSTAR* and soft X-ray mission flux (F_{soft}; from *Chandra* or *XMM-Newton*), at 3–8 keV, for those serendipitous survey sources with matched CSC or 3XMM counterparts. The empty symbols show upper limits. The 1:1 relation is shown by a solid line, and the dotted lines show values a factor of three from this relation.

typically observed for well-studied local NLAGNs (e.g., NGC 4945 and NGC 1068; see Puccetti et al. 2014; Bauer et al. 2015). While this is an outlier, it is not unexpected to observe one AGN with this level of variability, given the range of AGN variability observed on decade timescales in deep < 10 keV X-ray surveys such as CDFS (e.g., Yang et al., submitted). It is not possible to place informative constraints on spectral shape variability of J1333, since the *NuSTAR* spectral shape is poorly constrained at 3–10 keV ($\Gamma_{\text{eff}} = 1.2^{+1.3}_{-1.7}$). Deeper, simultaneous broad-band X-ray coverage would be required to determine whether a variation in spectral shape accompanies the relatively large variation in AGN flux. There is *Swift* XRT coverage contemporaneous with the 2014 *NuSTAR* data, but J1333 is undetected by *Swift* XRT. The *Swift* XRT flux upper limit is consistent with the *NuSTAR* flux, and is a factor of ≈ 4.2 lower than the *XMM-Newton* flux (and thus in agreement with a factor of ≈ 5 variation in the X-ray flux). This source represents the maximum variation in AGN flux identified in the survey.

5.3.2 IR and optical counterparts

Here we describe the procedure for matching between the 395 (out of 497) *NuSTAR* sources with soft X-ray counterparts (identified in Section 5.3.1), and counterparts at IR and optical wavelengths. The results from this matching are summarized in Table 5.3 (for the sources with Galactic latitudes of $|b| > 10°$). We adopt matching radii which are a compromise between maximizing completeness and minimizing spurious matches, and take into account the additional uncertainty (at the level of $1''$) between the X-ray and the optical/IR positions. For *Chandra* positions we use a matching radius of $2.5''$, which is well-motivated based on the known behaviour of the positional uncertainty as a function of off-axis angle (the majority of *NuSTAR* serendipitous sources lie significantly off-axis) and source counts (e.g., Alexander et al. 2003; Lehmer et al. 2005; Xue et al. 2011). For *Swift* XRT positions we use a matching radius of $6''$, justified by the typical positional uncertainty (statistical plus systematic) which is at the level of $\approx 5.5''$ (90% confidence level; e.g., Moretti et al. 2006; Evans et al. 2014). For *XMM-Newton* positions we use a matching radius of $5''$, which is motivated by the typical positional uncertainties of X-ray sources in the *XMM-Newton* serendipitous survey (e.g., $\approx 4''$ at the 90% confidence level for *XMM-Newton* bright serendipitous survey sources; Caccianiga et al. 2008).

Table 5.3: Summary of the optical and IR counterpart matching statistics and photometric magnitudes

Catalogue / Band	N	Fraction	$m_{\max}$	$m_{\min}$	$\bar{m}$	$\langle m \rangle$
(1)	(2)	(3)	(4)	(5)	(6)	(7)
Total optical + IR	290	87.9%	$\cdots$	$\cdots$	$\cdots$	$\cdots$
WISE (all)	252	76.4%	$\cdots$	$\cdots$	$\cdots$	$\cdots$
WISE / *W1*	249	75.5%	18.4	7.8	15.3	15.5
WISE / *W2*	248	75.2%	17.1	7.9	14.4	14.6
WISE / *W3*	194	58.8%	13.3	4.5	11.2	11.4
WISE / *W4*	131	39.7%	9.9	1.8	8.1	8.4
Optical (all)	249	75.5%	$\cdots$	$\cdots$	$\cdots$	$\cdots$
SDSS / r	121	36.7%[†]	24.5	11.7	19.6	19.9
		79.1%[††]				
USNOB1 / R	198	60.0%	20.9	10.5	18.5	19.1

Notes. Summary of the optical and IR counterpart matching for the 330 *NuSTAR* serendipitous survey sources with high Galactic latitudes ($|b| > 10°$) and soft X-ray telescope (*Chandra*, *Swift* XRT, or *XMM-Newton*) counterpart positions (see Section 5.3.2). (1): The catalogue and photometric band (where magnitude statistics are provided). (2): The number of the *NuSTAR* sources successfully matched to a counterpart in a given catalogue. For the *WISE* all-sky survey catalogue, this is broken down for the four photometric *WISE* bands. (3): The fraction of the *NuSTAR* sources which are matched. (4): The maximum (i.e., faintest) magnitude for the counterparts in a given catalogue and photometric band. (5): The minimum (i.e., brightest) magnitude. (6): The mean magnitude. (7): The median magnitude. [†]: The SDSS-matched fraction over the entire sky. [††]: The SDSS-matched fraction over the SDSS DR7 sky footprint.

To identify IR counterparts, we match to the *WISE* all-sky survey catalogue (Wright et al., 2010). Of the 395 sources with soft X-ray counterparts, 274 (69%) have *WISE* matches. In 100% of these cases there is a single unique *WISE* match (detected in at least one *WISE* band). To identify optical counterparts, we match to the SDSS DR7 catalogue (York et al., 2000) and the USNOB1 catalogue (Monet et al. 2003). If both contain matches, we adopt optical source properties from the former catalogue. Of the 395 sources with soft X-ray counterparts, 252 (64%) have a match in at least one of these optical catalogues. 121 sources have an SDSS match, 33 sources are covered by SDSS but do not have a match, and 241 sources are not covered by SDSS. Of the sources without SDSS matches, 131 have a USNOB1 match. In 77% (193/252) of cases there is a single optical (SDSS or USNOB1) match. In the case of multiple matches within the search radius we adopt the closest source. Figure 5.6 shows the distribution of astrometric offsets between the soft X-ray counterparts and the *WISE* and optical (SDSS and USNOB1) counterparts. For Galactic latitudes of $|b| > 10°$, which we focus on for the analysis of *NuSTAR* serendipitous survey source properties (Section 5.4), the spurious matching fractions are low ($\lesssim 10\%$; see Section 5.6).

For the 143 (out of 395) soft X-ray counterparts without SDSS and USNOB1 matches, we determine whether there are detections within the existing optical coverage, which is primarily photographic plate coverage (obtained through the DSS) but also includes dedicated R-band and multi-band imaging from our own programs with the ESO-NTT (EFOSC2) and ESO-2.2m (GROND), respectively. This identifies an additional 33 optical counterparts. For the 110 non-detections, we estimate R-band magnitude lower limits from the data (all cases have coverage, at least from photographic plate observations). These optical non-detections do not rule out follow-up spectroscopy; for 21 of them we have successfully performed optical spectroscopy, obtaining classifications and redshifts, either by identifying an optical counterpart in pre-imaging or by positioning the spectroscopic slit on a *WISE* source within the X-ray error circle. In Figure 5.7 we show histograms of the *WISE* and R-band magnitudes for the *NuSTAR* sources with soft X-ray counterparts.

For the 102 (out of 497) sources without soft X-ray counterparts, the X-ray positional error circle (from *NuSTAR*) is comparatively large (see Section 5.3.1), so unique coun-
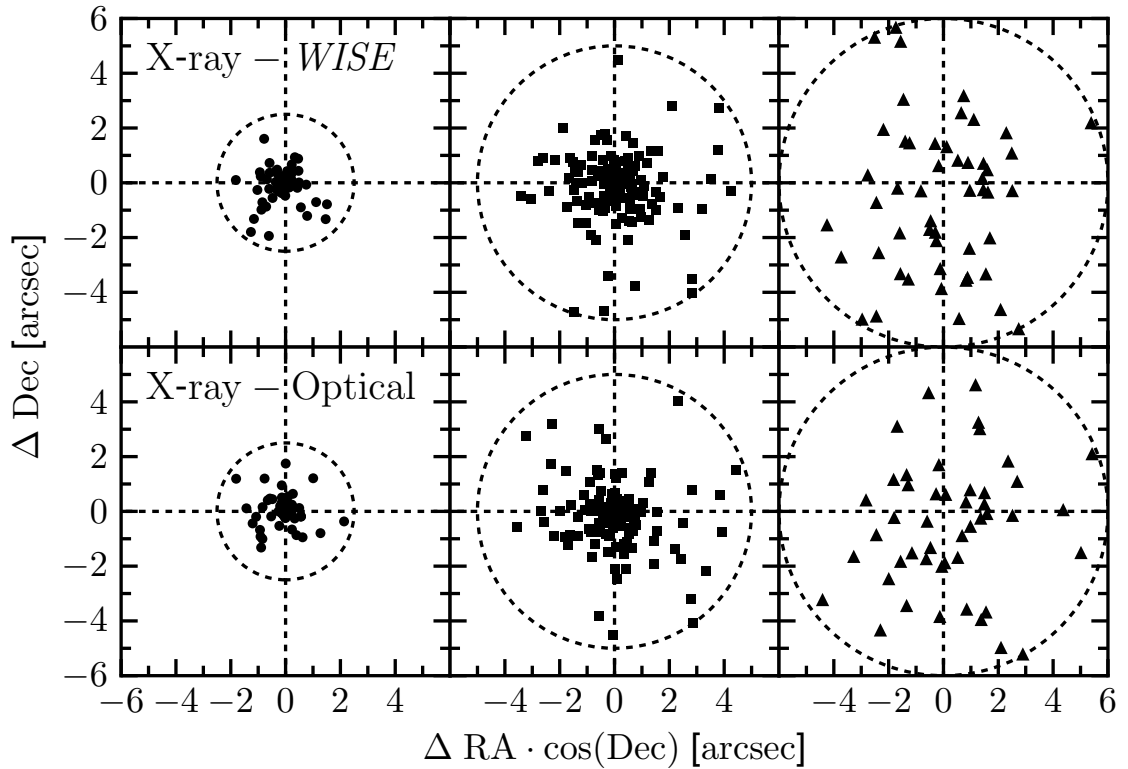
Figure 5.6: Astrometric offsets between the soft X-ray counterpart coordinates and the *WISE* (top row) and optical (bottom row) coordinates. The soft X-ray counterparts are from *Chandra* (left column), *XMM-Newton* (middle column) and *Swift* XRT (right column). The dashed circles correspond to the search radii for each telescope ($2.5''$, $5''$ and $6''$ for *Chandra*, *XMM-Newton* and *Swift* XRT, respectively).
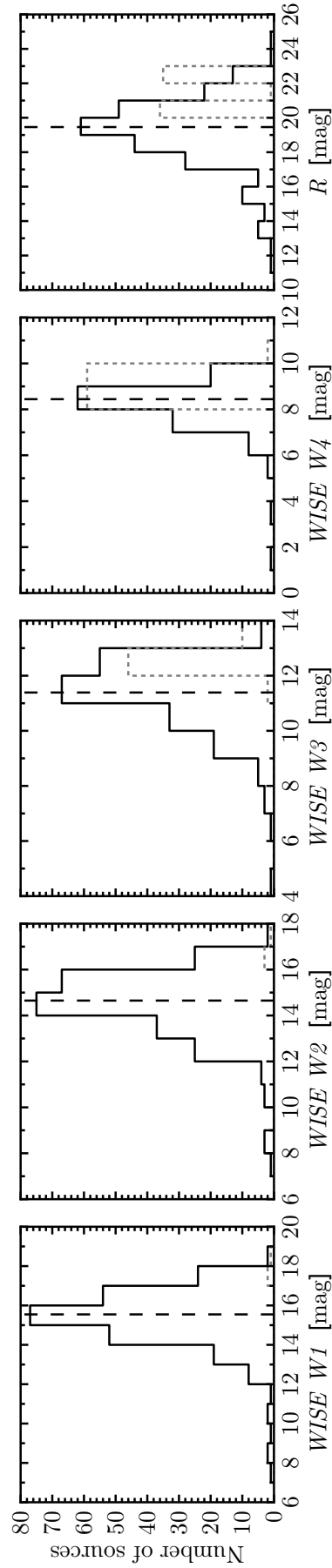
Figure 5.7: Distributions of the MIR and optical magnitudes for the *NuSTAR* serendipitous survey sources with high Galactic latitudes ($|b| > 10°$) and soft X-ray telescope (*Chandra*, *Swift* XRT, or *XMM-Newton*) counterparts. Left four panels: magnitude distributions for the four photometric *WISE* bands, for the sources with successful matches to the *WISE* all-sky survey catalogue. For each band, the solid line shows the magnitude distribution for detected sources, the dashed line marks the median magnitude of the detections, and the dotted line shows the distribution of magnitude lower limits for sources undetected in that band (but detected in other bands). Right panel: the *R*-band magnitudes (primarily from matching to the SDSS and USNOB1 catalogues) for all the sources.

terparts cannot be identified with high confidence. To identify possible counterparts for these sources, for the purposes of optical spectroscopic followup, we consider the properties of nearby *WISE* sources. Matching to the *WISE* all-sky survey, we identify AGN candidates within a $25''$ radius of the *NuSTAR* position, using the following two criteria: a *WISE* colour of $W1$–$W2 > 0.8$ (and $W2 < 15$; Stern et al. 2012) or a $W4$ band detection. The *WISE* $W1$, $W2$, $W3$, and $W4$ bands are are centred at $3.4~\mu$m, $4.6~\mu$m, $12~\mu$m, and $22~\mu$m, respectively. We limit this matching to the 85 (out of 102) sources at Galactic latitudes above $|b| = 10°$. Given the sky densities of *WISE* sources which satisfy these criteria, (≈ 46 deg^{-2} and ≈ 730 deg^{-2}, respectively, for $|b| > 10°$), the probabilities of chance matches are $\approx 1\%$ and $\approx 11\%$, respectively. Where multiple such *WISE* sources are identified, we prioritize those which satisfy both criteria, then those which satisfy the former criterion. For 24 (out of 102) of these sources there is a *WISE* AGN candidate within the *NuSTAR* error circle, the position of which we match to optical counterparts. The optical and IR counterparts identified in this manner (for *NuSTAR* sources without soft X-ray counterparts) are primarily used for the purposes of undertaking spectroscopic followup (Section 5.3.3), and we exclude them from our analysis of the IR properties of the *NuSTAR* serendipitous survey AGNs (Section 5.4.3), to avoid biasing the results. For the remaining 78 (out of 102) sources at $|b| < 10°$ or without matches to *WISE* AGN candidates, we use the available R-band information to obtain magnitude constraints: in cases where there is at least one optical source within the *NuSTAR* error circle, we adopt the lowest (i.e., brightest) R-band magnitude as a lower limit; and in cases with no optical source within the *NuSTAR* error circle, we adopt the magnitude limit of the imaging data.

For a large fraction of the sources discussed in this section, the spectroscopic followup (Section 5.3.3) shows evidence for an AGN, which provides additional strong support for correct counterpart identification (given the low sky density of AGNs). Furthermore, the optical and IR photometric properties of the *NuSTAR* serendipitous survey counterparts are in agreement with AGNs (see Sections 5.4.2 and 5.4.3).

5.3.3   Optical Spectroscopy

Optical identifications and source redshifts, obtained through spectroscopy, are a prerequisite to the measurement of intrinsic source properties such as luminosity and the amount

of obscuration. A small fraction ($\approx 11\%$; $57/497$) of the *NuSTAR* serendipitous survey sources have pre-existing spectroscopic coverage, primarily from the SDSS. However, the majority ($\approx 89\%$) of the serendipitous survey sources do not have pre-existing spectroscopy. For that reason, we have undertaken a campaign of dedicated spectroscopic followup in the optical–IR bands (Section 5.3.3), obtaining spectroscopic identifications for a large fraction (56%) of the total sample. For the high Galactic latitude ($|b| > 10°$) samples selected in individual bands, this has resulted in a spectroscopic completeness of $\approx 70\%$. The analysis of and classifications obtained from these new spectroscopic data, and those from pre-existing spectroscopy, are described in Section 5.3.3.

Dedicated followup campaign

Since *NuSTAR* performs science pointings across the whole sky, a successful ground-based followup campaign requires the use of observatories at a range of geographic latitudes, and preferably across a range of dates throughout the sidereal year. This has been achieved through observing programmes with, primarily, the following telescopes over a multi-year period: the Hale Telescope at Palomar Observatory (5.1 m; Decl. $> -21°$; PIs F. A. Harrison and D. Stern); Keck I and II at the W. M. Keck Observatory (10 m; $-35° <$ Decl. $< 75°$; PIs F. A. Harrison and D. Stern); the New Technology Telescope (NTT) at La Silla Observatory (3.6 m; Decl. $< 25°$; PI G. B. Lansbury);[6] and the Magellan I (Baade) and Magellan II (Clay) Telescopes at Las Campanas Observatory (6.5 m; Decl. $< 25°$; PIs E. Treister and F. E. Bauer).[7] Table 5.4 provides a list of the observing runs undertaken. In each case we provide the observing run starting date (UT), number of nights, telescope, instrument, and total number of spectroscopic redshifts obtained for *NuSTAR* serendipitous survey sources.

The total number of sources with spectroscopic redshift measurements and classifications is 276. The large majority of spectroscopic identifications in the northern hemisphere were obtained using a combination of Palomar and Keck, with the former being efficient for brighter targets and the latter for fainter targets. These account for 51% ($141/276$) of the spectroscopically identified sample. Similarly, for the southern hemi-

---

[6]Program IDs: 093.B-0881, 094.B-0891, 095.B-0951, and 096.B-0947.
[7]Program IDs: CN2013B-86, CN2014B-113, CN2015A-87, CN2016A-93.

Table 5.4: Chronological list of ground-based observing runs for spectroscopic followup of the *NuSTAR* serendipitous survey

Run ID (1)	UT start date (2)	Telescope (3)	Instrument (4)	Spectra (5)
1	2012 Oct 10	Palomar	DBSP	1
2	2012 Oct 13	Keck	DEIMOS	1
3	2012 Nov 09	Keck	LRIS	1
4	2012 Nov 20	Palomar	DBSP	2
5	2012 Dec 12	Gemini-South	GMOS	1
6	2013 Jan 10	Keck	LRIS	1
7	2013 Feb 12	Palomar	DBSP	2
8	2013 Mar 11	Palomar	DBSP	6
9	2013 Jul 07	Palomar	DBSP	2
10	2013 Oct 03	Keck	LRIS	9
11	2013 Dec 05	Magellan	MagE	2
12	2013 Dec 10	Keck	DEIMOS	6
13	2014 Feb 22	Palomar	DBSP	4
14	2014 Apr 22	Palomar	DBSP	6
15	2014 Jun 25	Keck	LRIS	12
16	2014 Jun 30	NTT	EFOSC2	8
17	2014 Jul 21	Palomar	DBSP	3
18	2014 Sep 25	Magellan	MagE	5
19	2014 Oct 20	Keck	LRIS	4
20	2014 Dec 23	Palomar	DBSP	4
21	2015 Feb 17	Palomar	DBSP	5
22	2015 Mar 14	NTT	EFOSC2	17
23	2015 Mar 18	Magellan	IMACS	6
24	2015 May 19	NTT	EFOSC2	14
25	2015 Jun 09	Palomar	DBSP	1
26	2015 Jun 15	Palomar	DBSP	1
27	2015 Jul 17	Keck	LRIS	3
28	2015 Jul 21	Palomar	DBSP	4
29	2015 Aug 09	Palomar	DBSP	6
30	2015 Aug 12	Keck	LRIS	6
31	2015 Dec 04	Keck	LRIS	28
32	2015 Dec 06	NTT	EFOSC2	25
33	2016 Jan 11	Palomar	DBSP	8
34	2016 Feb 05	Palomar	DBSP	2
35	2016 Feb 08	Magellan	MagE	6
36	2016 Feb 13	Keck	LRIS	17
37	2016 Jul 05	Keck	LRIS	10
38	2016 Jul 10	Palomar	DBSP	6

Notes. (1): ID assigned to each observing run. (2): Observing run start date. (3) and (4): The telescope and instrument used. (5): The number of spectra from a given observing run which have been adopted, in this work, as the analysed optical spectrum for a *NuSTAR* serendipitous survey source. These correspond to the individual sources listed in Table A.2 of Section A.2, and are primarily ($\approx 93\%$) sources with successful redshift measurements and spectroscopic classifications. These source numbers exclude the 33 sources in the secondary catalogue for which we have obtained new spectroscopic identifications (see Section A.3).

sphere the majority of spectroscopic identifications were obtained using the ESO NTT while complementary Magellan observations were used to identify the fainter optical sources. These account for 28% (76/276) of the overall spectroscopically identified sample.

Conventional procedures were followed for spectroscopic data reduction, using IRAF routines. Spectrophotometric standard star observations, from the same night as the science observations, were used to flux calibrate the spectra.

Spectral Classification and Analysis

All flux-calibrated optical spectra from this work are provided in Section A.2. For our instrument setups, the typical observed-frame wavelength range covered is $\lambda \approx 3500$–9000Å. At lower redshifts, for example $z = 0.3$, this results in coverage for the following emission lines common to AGNs and quasars: Mg II $\lambda2800$Å, [Ne V] $\lambda3346$Å and $\lambda3426$Å, [O II] $\lambda3728$Å, [Ne III] $\lambda3869$Å, Hδ $\lambda4102$Å, Hγ $\lambda4340$Å, Hβ $\lambda4861$Å, $\lambda4959$Å and [O III] $\lambda5007$Å, [O I] $\lambda6300$Å and $\lambda6364$Å, [N II] $\lambda6548$Å and $\lambda6584$Å, Hα $\lambda6563$Å, and [S II] $\lambda6716$Å and $\lambda6731$Å. At higher redshifts, for example $z = 2$, the lines covered are: Lyα $\lambda1216$Å, Si IV $\lambda1398$Å, C IV $\lambda1549$Å, He II $\lambda1640$Å, C III] $\lambda1909$Å, C II] $\lambda2326$Å, and Mg II $\lambda2800$Å.

To measure spectroscopic redshifts, we identify emission and absorption lines, and measure their observed-frame wavelengths using Gaussian profile fitting. To determine the redshift solution, we crossmatch the wavelength ratios of the identified lines with a look-up table of wavelength ratios based on the emission and absorption lines observed in AGN and galaxy spectra. The final, precise redshift measurement is then obtained from the Gaussian profile fit to the strongest line. For the large majority of cases there are multiple lines detected, and there is only one valid redshift solution. The lines identified for each individual *NuSTAR* source are tabulated in Section A.2. There are only five sources where the redshift is based on a single line identification (marked with "quality B" flags in Section A.2). For four of these, the single emission line detected is identified as Mg II $\lambda2800$Å. In all cases this is well justified: Mg II is a dominant broad line in quasar spectra, and there is a relatively large separation in wavelength between the next strong line bluewards of Mg II (C III] $\lambda1909$Å) and that redwards of Mg II (Hβ $\lambda4861$Å).

This means that Mg II can be observed in isolation for redshifts of $z \sim 0.8$ in cases where our wavelength coverage is slightly narrower than usual, or if the other lines (e.g., C III] and Hβ) are below the detection threshold. Mg II can also be clearly identifiable in higher S/N data due to the shape of the neighbouring Fe II pseudo-continuum.

We perform optical classifications visually, based on the spectral lines observed. For the extragalactic sources with available optical spectra and with identified lines (253 sources), emission lines are detected for all but one source (where multiple absorption lines are identified). Both permitted emission lines (e.g., the Balmer series and Mg II) and forbidden (e.g., [O III] and [N II]) emission lines are identified for 183 (out of 253) sources. For these sources, if any permitted line is broader than the forbidden lines we assign a BLAGN classification, otherwise we assign a NLAGN classification. There are 58 (out of 253) sources where only permitted (or semi-forbidden) emission lines are identified. For the majority of these (56 sources) the line profiles are visually broad, and we assign a BLAGN classification (these sources predominantly lie at higher redshifts, with 51 at $z \gtrsim 1$, and have quasar-like continuum-dominated spectra). For 24 sources where there is a level of ambiguity as to whether the permitted lines are broad or not, we append the optical classification (i.e., "NL" or "BL" in Table A.2) with a "?" symbol. For the remaining 11 sources (out of 253) with only forbidden line detections, and the single source with absorption line detections only, we assign NLAGN classifications.

In total we have spectroscopic classifications for 276 of the *NuSTAR* serendipitous survey sources, including the 253 extragalactic sources mentioned above, an additional BL Lac type object, 16 Galactic ($z = 0$) objects, and six additional (BLAGN and NLAGN) classifications from the literature. 222 of these classifications were assigned using data from the dedicated observing runs (Table 5.4), and 54 using existing data (primarily SDSS) or literature. Considering the total classified sample, the majority of the sources (162, or 58.7%) are BLAGNs, 97 (35.1%) are NLAGNs, one (0.4%) is a BL Lac type object, and the remaining 16 (5.8%) are Galactic objects (e.g., cataclysmic variables and high mass X-ray binaries). Tomsick et al. (in prep.) will present a detailed analysis of the Galactic subsample. The current spectroscopic completeness (i.e., the fraction of sources with successful spectroscopic identifications) is $\approx 70\%$ for the overall serendipitous survey (for the $|b| > 10°$ individual band-selected samples), although the completeness is a

function of X-ray flux (see Section 5.4.2).

In Table A.2 (see Section A.2) we provide the following for all *NuSTAR* serendipitous survey sources with optical spectra: the spectroscopic redshift, the optical classification, the identified emission and absorption lines, individual source notes, and the observing run ID (linking to Table 5.4).

5.4 Results and Discussion

Here we describe the properties of the *NuSTAR* serendipitous survey sources, with a focus on the high energy X-ray (Section 5.4.1), optical (Section 5.4.2) and infrared (Section 5.4.3) wavelength regimes. We compare and contrast with other relevant samples, including: the blank-field *NuSTAR* surveys in well-studied fields (COSMOS and ECDFS); non-survey samples of extreme objects targetted with *NuSTAR*; the *Swift* BAT all-sky survey, one of the most sensitive high energy X-ray surveys to precede *NuSTAR*; and lower energy (< 10 keV; e.g., *Chandra* and *XMM-Newton*) X-ray surveys.

5.4.1 X-ray properties

Basic NuSTAR properties

Overall there are 497 sources with significant detections (post-deblending) in at least one band. Section 5.2.5 details the source-detection statistics, broken down by energy band. In the 8–24 keV band, which is unique to *NuSTAR* amongst focusing X-ray observatories, there are 163 detections, i.e. 33% of the sample. The *NuSTAR*-COSMOS and *NuSTAR*-ECDFS surveys found very similar fractions of 8–24 keV detected sources: 35% ($32/91$ sources; C15) and 39% ($19/49$ sources post-deblending; M15), respectively.

The net (cleaned, vignetting-corrected) exposure times per source (t_{net}; for the combined FPMA+B data) have a large range, from 10–1500 ks, with a median of 60 ks. For the 3–8, 8–24, and 3–24 keV bands, the lowest net source counts (S_{net}) for sources with detections in these bands are 11, 17, and 19, respectively. The highest S_{net} values are 9900, 5859, and 15718, respectively, and correspond to one individual source NuSTAR J043727–4711.5, a BLAGN at $z = 0.051$. The median S_{net} values are 58, 63, and

79, respectively. The count rates range from 0.17–52, 0.15–36, and 0.14–94 ks^{-1}, respectively, and the median count rates are 0.80, 0.86, and 1.2 ks^{-1}, respectively.

Figure 5.8 shows the distribution of fluxes for the full sample, for each energy band. The distributions for detected and undetected sources (for a given band) are shown separately. For sources which are detected in the 3–8, 8–24, and 3–24 keV bands, the faintest fluxes measured are 1.17, 2.11, and 1.27×10^{-14} erg s^{-1} cm^{-2}, respectively. The brightest fluxes are 3.5, 5.0, and 8.9×10^{-12} erg s^{-1} cm^{-2}, respectively, and correspond to one individual source NuSTAR J075800+3920.4, a BLAGN at $z = 0.095$. The median fluxes are 5.4, 11.9, and 10.8×10^{-14} erg s^{-1} cm^{-2}, respectively. The dynamic range of the serendipitous survey exceeds the other *NuSTAR* extragalactic survey components. For comparison, the blank-field ECDFS and COSMOS components span 3–24 keV flux ranges of $\approx (2$–$10)$ and $(5$–$50) \times 10^{-14}$ erg s^{-1} cm^{-2}, respectively (C15 and M15). The serendipitous survey pushes to fluxes (both flux limits and median fluxes) $\sim$ two orders of magnitude fainter than those achieved by previous-generation hard X-ray observatories such as *Swift* BAT (e.g., Baumgartner et al., 2013) and *INTEGRAL* (e.g., Malizia et al., 2012).

Band ratios

Figure 5.9 shows the 8–24 to 3–8 keV band ratios ($\mathrm{BR_{Nu}}$) for the full sample of *NuSTAR* serendipitous survey sources, as a function of full-band (3–24 keV) count rate. In order to examine the results for extragalactic sources only, we remove sources which are spectroscopically confirmed as having $z = 0$ (see Section 5.3.3) and exclude sources with Galactic latitudes below $|b| = 10°$, for which there is significant contamination to the non-spectroscopically identified sample from Galactic sources. A large and statistically significant variation in $\mathrm{BR_{Nu}}$ is observed across the sample, with some sources exhibiting extreme spectral slopes ($\Gamma_{\mathrm{eff}} \approx 3$ at the softest values; $\Gamma_{\mathrm{eff}} \approx 0$ at the hardest values).

In Figure 5.9, we overlay mean band ratios and corresponding errors (in bins of full-band count rate, with an average of 13 sources per bin) for a subset of the extragalactic serendipitous sample with $\log(P_{\mathrm{False}}) < -14$ in the full band. This cut in source significance reduces the fraction of sources with upper or lower limits in $\mathrm{BR_{Nu}}$ to only 7%, allowing numerical means to be estimated. The results are consistent with a flat relation
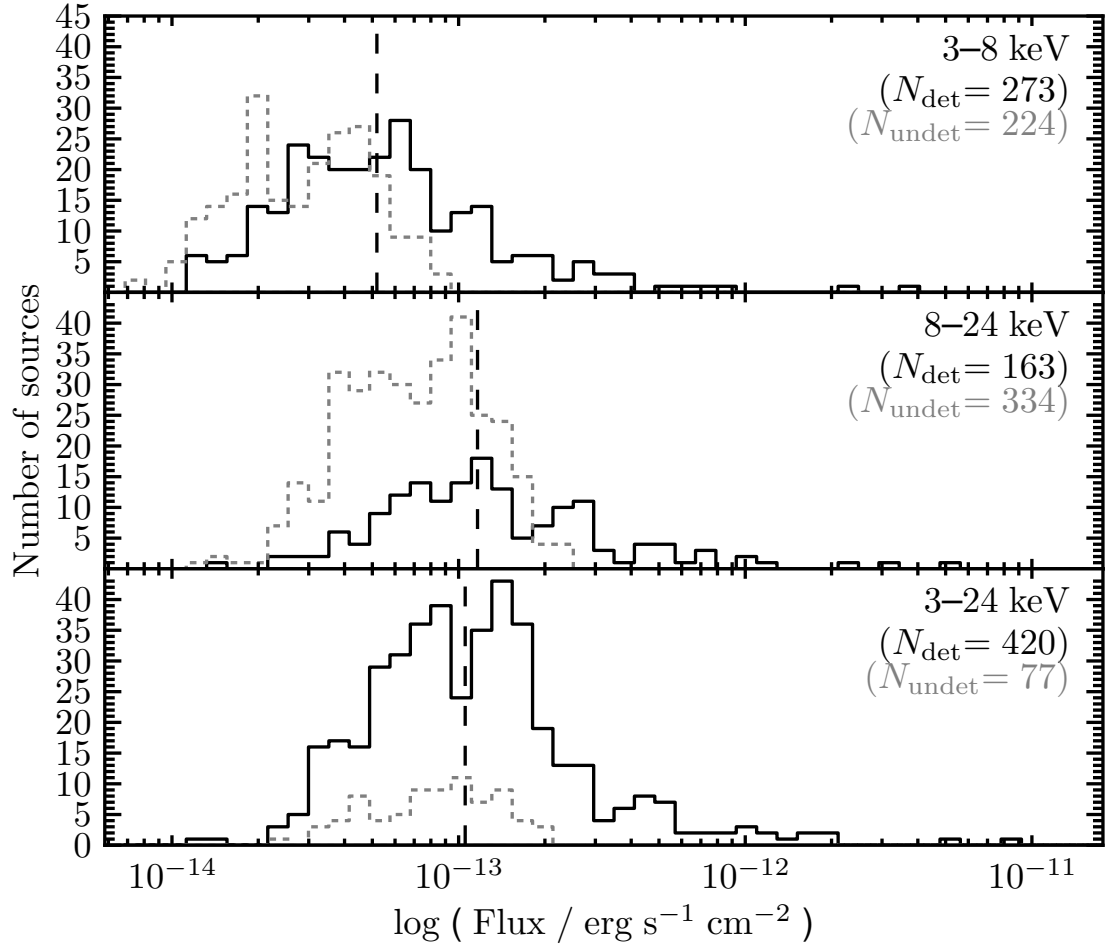
Figure 5.8: Flux distributions in the soft, hard, and full energy bands (top, middle, and bottom panels, respectively) for the *NuSTAR* serendipitous survey sample. For each band, the solid line shows the flux distribution for sources independently detected in that band (the number of these sources, N_{det}, is shown in black font), and the median flux of the detected sources is marked by a dashed line. For each band, the dotted line shows the distribution of flux upper limits for sources undetected in that band, but independently detected in at least one other band (the number of these sources, N_{undet}, is shown in grey font).
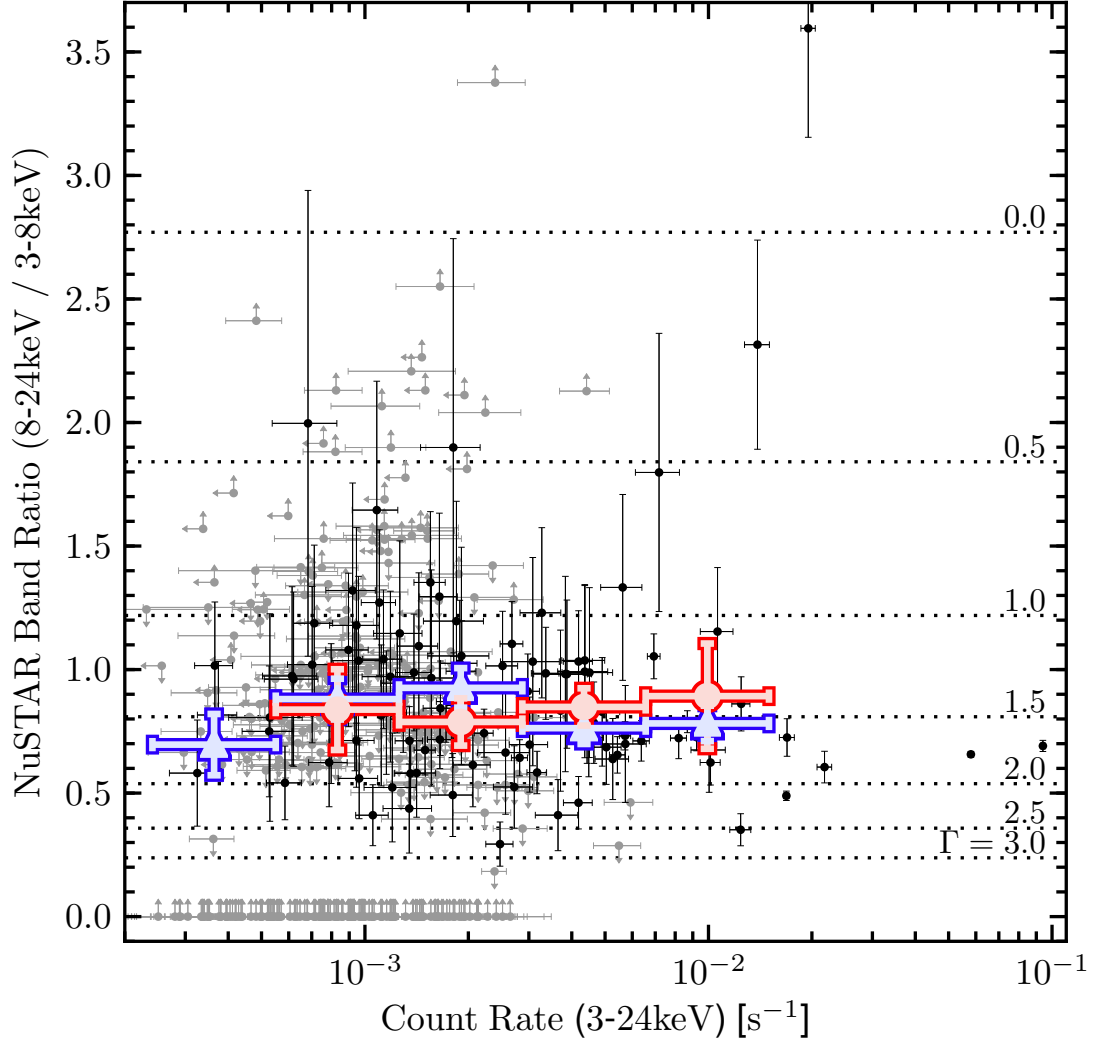
Figure 5.9: The *NuSTAR* 8–24 to 3–8 keV band ratio ($\mathrm{BR_{Nu}}$) versus full-band (3–24 keV) count rate for the full *NuSTAR* serendipitous survey sample. Constrained $\mathrm{BR_{Nu}}$ values are shown in black, and those with upper or lower limits are shown in gray. The dotted horizontal lines indicate spectral slopes (Γ_{eff}) to which the band ratios correspond. The overplotted red circles show numerical means (binning in full-band count rate), for a sub-set of extragalactic sources with $\log(P_{\mathrm{False}}) < -14$. The overplotted blue triangles show "stacked" means obtained from summing the net count-rates of all sources, including non-detections, and bootstrapping errors.

in the average band ratio versus count rate, and a constant average effective photon index of $\Gamma_{\mathrm{eff}} \approx 1.5$. This value is consistent with the average effective photon index found from spectral analyses of sources detected in the dedicated *NuSTAR* surveys of the ECDFS, EGS and COSMOS fields ($\Gamma_{\mathrm{eff}} = 1.59 \pm 0.14$; Del Moro et al. 2016, in prep). This hard average spectral slope suggests numerous obscured AGNs within the sample. The mean band ratios disfavor an increase toward lower count rates. This is in apparent disagreement with the recent results of M15 for the *NuSTAR*-ECDFS survey, which show an increase towards lower count rates, albeit for small source numbers with constrained band ratios. Deep surveys at lower X-ray energies have previously found an anticorrelation between band ratio and count rate for the 0.5–8 keV band (e.g., Della Ceca et al., 1999; Ueda et al., 1999; Mushotzky et al., 2000; Tozzi et al., 2001; Alexander et al., 2003), interpreted as being driven by an increase in the number of absorbed AGNs toward lower count rates. We find no evidence for such an anticorrelation in the higher energy 3–24 keV band. This may be understood partly as a result of the X-ray spectra of AGNs being less strongly affected by absorption in the high energy *NuSTAR* band.

To incorporate the full serendipitous sample, including weak and non-detections, we also calculate "stacked" means in $\mathrm{BR}_{\mathrm{Nu}}$ (also shown in Figure 5.9), by summing the net count-rates of all sources. The stacked means are also consistent with a flat trend in band ratio as function of count-rate.

While obscured AGNs can be crudely identified using $\mathrm{BR}_{\mathrm{Nu}}$ alone, an estimate of obscuring columns requires additional knowledge of the source redshifts, which shift key spectral features (e.g., the photoelectric absorption cut-off) across the observed energy bands. Here we use the combination of $\mathrm{BR}_{\mathrm{Nu}}$ and the source redshifts to identify potentially highly obscured objects. Figure 5.10 shows $\mathrm{BR}_{\mathrm{Nu}}$ versus z for the spectroscopically-identified serendipitous survey sample. We compare with the band ratios measured for CT, or near-CT, SDSS-selected Type 2 quasars observed with *NuSTAR* in a separate targetted program (Lansbury et al. 2014; Gandhi et al. 2014; Lansbury et al. 2015; see Chapters 3 and 4), and with tracks (gray region) predicted for CT absorption based on redshifting the best-fit spectra of local CT AGNs from the *NuSTAR* snapshot survey of *Swift* BAT AGNs (Baloković et al. 2014; Baloković et al. 2016, in prep.). A number of sources stand out as CT-candidates based on this analysis. While $\mathrm{BR}_{\mathrm{Nu}}$ can only provide a crude
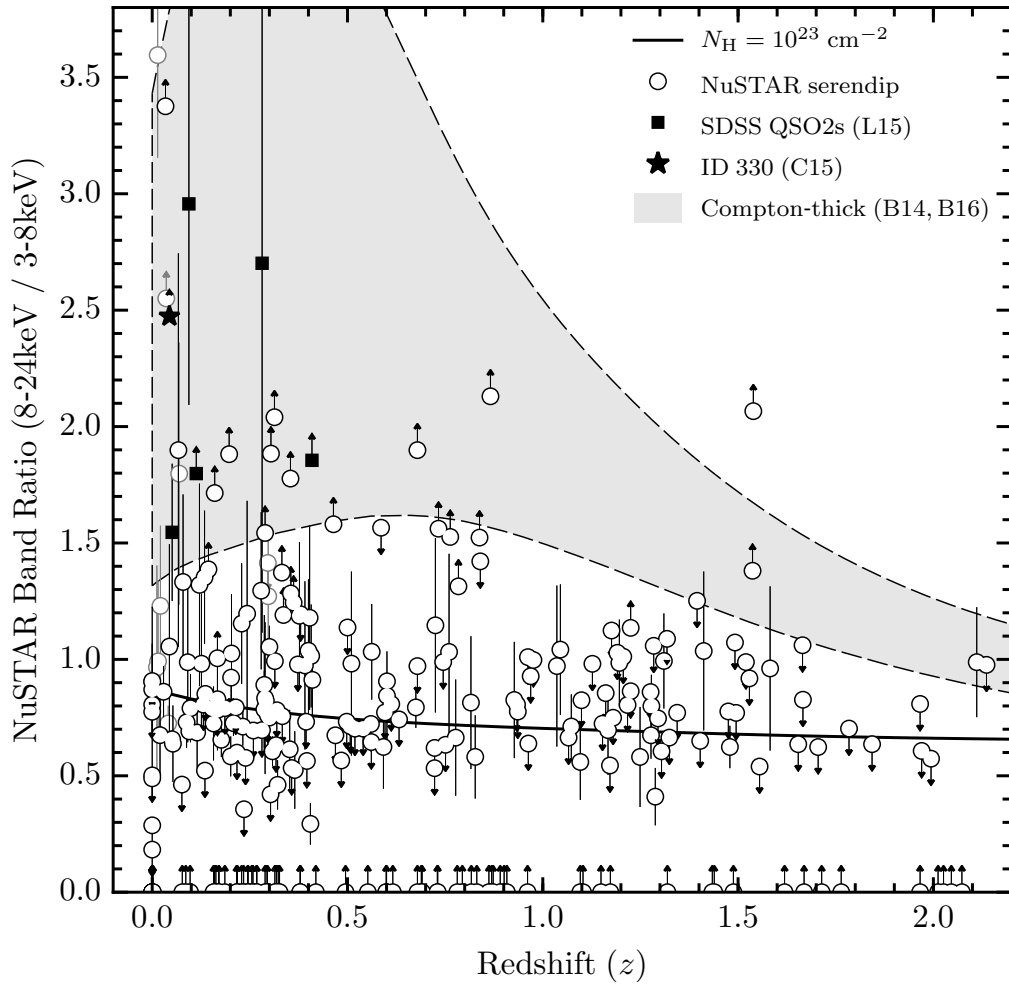
Figure 5.10: *NuSTAR* band ratio (BR_{Nu}) versus redshift (z) for the full *NuSTAR* serendipitous survey sample (black circles). Sources which are associated with the primary science targets of the *NuSTAR* observations (according to the $\Delta(cz)$ criterion in Section 5.2.3) are shown as lighter gray circles. We compare to other *NuSTAR*-observed sources targetted for other programs (i.e., not part of the serendipitous survey). The black star shows a CT AGN identified in the *NuSTAR*-COSMOS survey (C15). The black squares show heavily obscured SDSS-selected Type 2 quasars observed with *NuSTAR*, for which there is evidence for either CT or close to CT absorption (Chapters 3–4; Lansbury et al. 2014; Gandhi et al. 2014; Lansbury et al. 2015). The gray shaded region highlights the parameter space expected for CT (i.e., $N_H > 1.5 \times 10^{24}$ cm^{-2}) AGNs, considering all populations (including reflection- and transmission-dominated CT AGNs), based on results from the *NuSTAR* snapshot survey (Baloković et al. 2014; Baloković et al. 2016, in prep.). This gray region was obtained by redshifting the best-fit spectral models of local CT snapshot AGNs, for which the X-ray spectra are relatively well constrained. The upper and lower extents (dashed lines) represent the 68% percentiles (i.e., 84% of the CT snapshot AGNs lie above the lower dashed line). Serendipitous sources lying at BR_{Nu} values within or higher than this gray region are good candidates for being CT. The black track shows a MYTORUS model prediction for BR_{Nu} as a function of redshift, for a more moderate column density of $N_H = 10^{23}$ cm^{-2}.
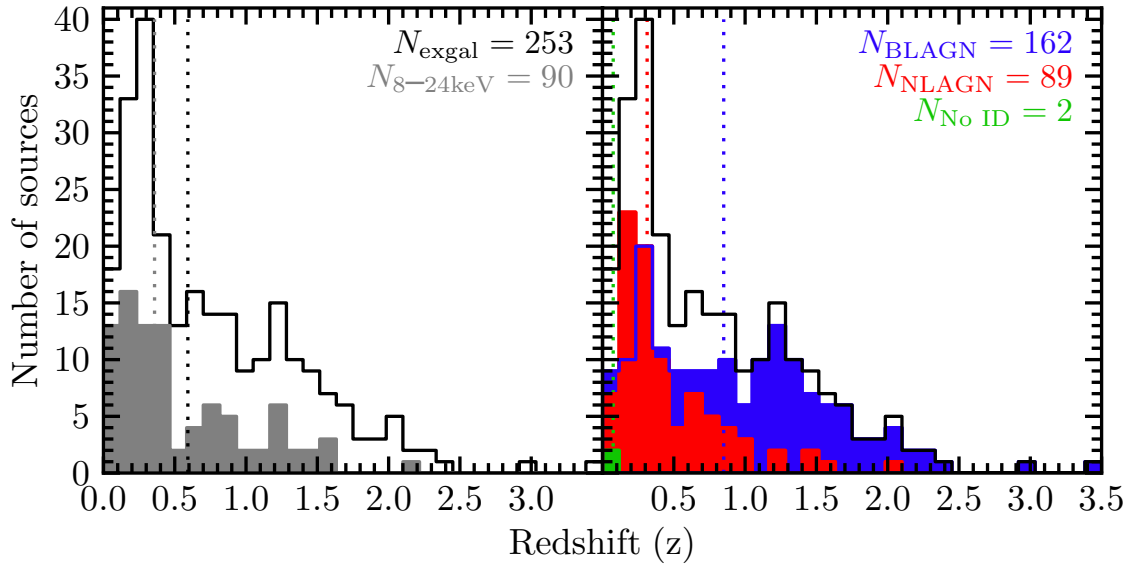
Figure 5.11: The distribution of spectroscopic redshifts for the spectroscopically identified *NuSTAR* serendipitous survey sample. Galactic ($z = 0$) sources have been excluded. In addition to the total distribution (black line), the left panel shows the distribution for the subset which are independently detected in the hard band (8–24 keV; gray filled histogram, left panel) and the right panel shows the distribution separated by optical classification: BLAGNs are shown in blue; NLAGNs are shown in red. The vertical lines mark the median redshifts.

estimate of the absorbing columns, a more detailed investigation of the *NuSTAR* spectra and multiwavelength properties of the CT-candidates can strengthen the interpretation of these high-BR_{Nu} sources as highly absorbed systems (Chapter 6).

Redshifts and Luminosities

Of the *NuSTAR* serendipitous survey sources with optical spectroscopic coverage and spectroscopic redshift measurements (described in Section 5.3.3), there are 262 identified as extragalactic. Figure 5.11 shows the redshift distribution for the extragalactic sources, excluding nine sources with evidence for being associated to the *NuSTAR* targets for their respective observations (see Section 5.2.3). The redshifts cover a large range, from $z = 0.002$ to 3.43, with a median of $\langle z \rangle = 0.56$. For the 90 extragalactic objects with independent detections in the high-energy band (8–24 keV), to which *NuSTAR* is uniquely sensitive, the median redshift is $\langle z \rangle = 0.34$. Roughly comparable numbers of

NLAGNs and BLAGNs are identified for lower redshifts ($z \lesssim 1$), but there is a significant bias towards BLAGNs at higher redshifts. This was also found for the *NuSTAR* surveys in well-studied fields (e.g., C15), and for surveys with sensitive lower energy (< 10 keV) X-ray observatories such as *Chandra* and *XMM-Newton* (e.g., Barger et al. 2003; Eckart et al. 2006; Barcons et al. 2007). This effect is largely due to selection biases against the detection of highly absorbed AGNs, and against the spectroscopic identification of the optically fainter NLAGNs (e.g., Treister et al. 2004).

Figure 5.12 shows the redshift–luminosity plane for the rest-frame 10–40 keV band. The luminosities are calculated from the observed frame *NuSTAR* fluxes, assuming an effective photon index of $\Gamma_{\mathrm{eff}} = 1.8$ (as detailed in Section 5.2.4). The *NuSTAR* serendipitous survey covers a large range in 10–40 keV luminosity; the large majority (99.6%; 238/239) of the unassociated sources lie in the range of $L_{10-40\mathrm{keV}} \approx 10^{42}$ to 10^{46} erg s^{-1}. The median luminosity of 1.2×10^{44} erg s^{-1} is just above the "X-ray quasar" threshold.[8] There is a single outlying source at very low luminosity and redshift, NuSTAR J115851+4243.2 (hereafter J1158; NLAGN; $z = 0.0023$; $L_{10-40\mathrm{keV}} = 1.0 \times 10^{39}$ erg s^{-1}), hosted by the galaxy IC750. In this case, the SDSS optical spectrum shows a narrow line AGN superimposed over the galaxy spectrum. The source is discussed in detail in a work focusing on the *NuSTAR*-selected AGNs with dwarf galaxy hosts (Chen et al., in prep.). At the other extreme end in luminosity is NuSTAR J052531-4557.8 (hereafter J0525; BLAGN; $z = 1.479$; $L_{10-40\mathrm{keV}} = 9.0 \times 10^{45}$ erg s^{-1}), also referred to as PKS 0524-460 in the literature.[9] J0525 has an effective *NuSTAR* photon index of $\Gamma_{\mathrm{eff}} = 1.9^{+0.3}_{-0.2}$, and a *Swift* XRT spectrum which is consistent with zero X-ray absorption. The optical spectrum of Stickel et al. (1993) shows a broad line quasar with strong He II, C III], and Mg II emission lines. The source is also radio-bright (e.g., $f_{1.4\mathrm{GHz}} = 1.7$ Jy; Tingay et al. 2003) and has been

---

[8]A threshold of 10^{44} erg s^{-1} is often adopted to define "X-ray quasars", since this roughly agrees with the classical optical quasar definition ($M_B \leq -23$; Schmidt & Green 1983) and the $L_{\mathrm{X},*}$ value for unobscured AGNs (e.g., Hasinger et al. 2005).

[9]We note that J0525 appears in the *Swift* BAT all-sky catalogue of Baumgartner et al. (2013) as a counterpart to the source SWIFTJ0525.3-4600. However, this appears to be a mismatch: an examination of the *Swift* BAT maps (following the procedures in Koss et al. 2013) and the *NuSTAR* data shows that J0525 is undetected by *Swift* BAT, and a nearby AGN in a foreground low redshift galaxy ESO 253-G003 ($z = 0.042$) instead dominates the SWIFTJ0525.3-4600 counts.
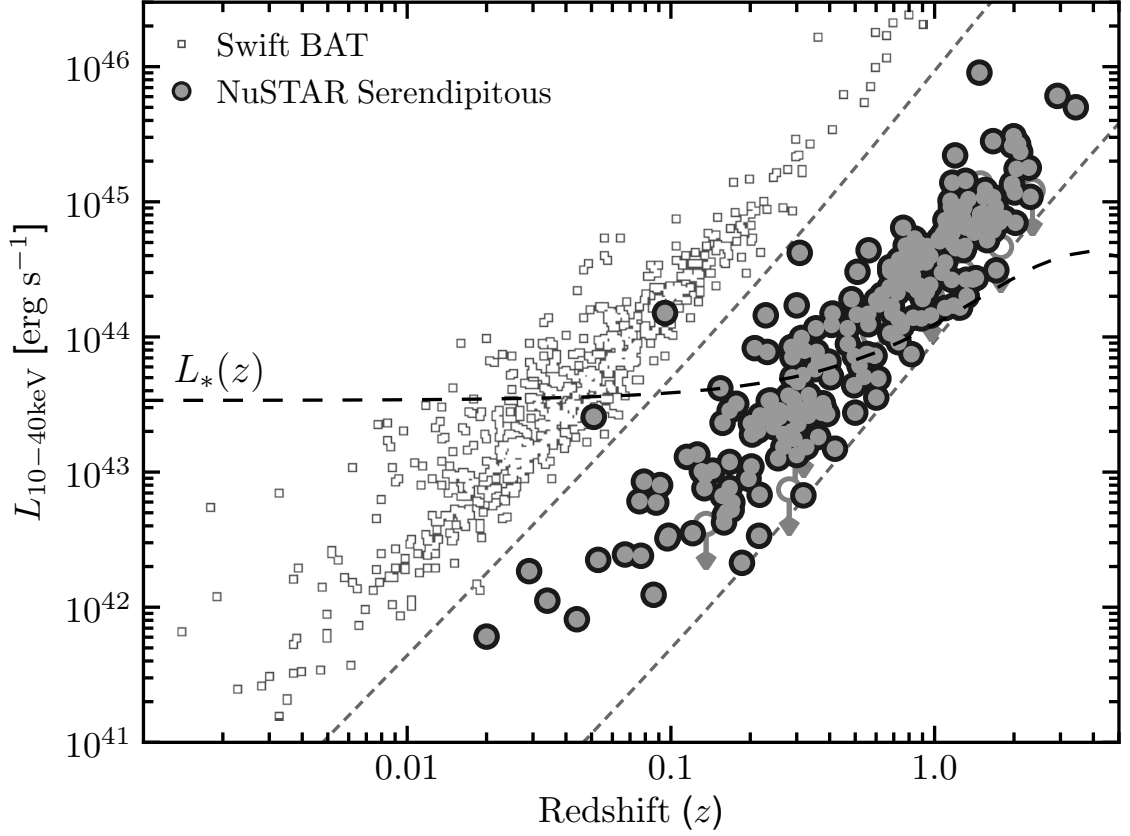
Figure 5.12: Rest-frame 10–40 keV luminosity ($L_{10-40\,\text{keV}}$) versus redshift. We compare the *NuSTAR* serendipitous survey sample (circles) with the *Swift* BAT 70-month all-sky survey catalogue (squares; Baumgartner et al. 2013; blazar and BL Lac types have been excluded). $L_{10-40\,\text{keV}}$ values for the *Swift* BAT sample are calculated from the 14–195 keV values, assuming $\Gamma_{\text{eff}} = 2.0$ for the K-correction factor (consistent with the median spectral slope for the *Swift* BAT sources shown). The gray short-dashed lines highlight an observed-frame X-ray flux range spanning two orders of magnitude, from 2×10^{-14} to 2×10^{-12} erg s^{-1} cm^{-2}. The black long-dashed line shows the evolution of the knee of the X-ray luminosity function (L_*) with redshift, as measured by Aird et al. (2015a). The *NuSTAR* serendipitous survey probes below L_* at $z \lesssim 1$.

classified as a blazar in the literature (e.g., Massaro et al. 2009).

The most distant source detected is an optically unobscured quasar, NuSTAR J232728+0849.3 (hereafter J2327; BLAGN; $z = 3.430$; $L_{10-40\text{keV}} = 5.0 \times 10^{45}$ erg s^{-1}), which represents the highest-redshift AGN identified in the *NuSTAR* survey program to-date. Our Keck optical spectrum for J2327 shows a quasar spectrum with strong Lyα, C IV, and C III] emission lines, and a well-detected Lyα forest. The source is consistent with having an observed X-ray spectral slope of $\Gamma_{\text{eff}} = 2$ for both the *NuSTAR* spectrum and the *XMM-Newton* counterpart spectrum, and is thus in agreement with being unobscured at X-ray energies. The most distant optically obscured quasar detected is NuS-TAR J125657+5644.6 (hereafter J1256; NLAGN; $z = 2.073$; $L_{10-40\text{keV}} = 2.7 \times 10^{45}$ erg s^{-1}). Our Keck optical spectrum for J1256 reveals strong narrow Lyα, C IV, He II, and C III] emission lines. Analysing the *NuSTAR* spectrum in combination with a deep archival *Chandra* spectrum (≈ 360 ks of exposure in total), we measure a moderately large line of sight column density of $N_{\text{H}} = (1.3 \pm 0.4) \times 10^{23}$ cm^{-2}. This distant quasar is thus obscured in both the optical and X-ray regimes.

In Figure 5.12 we compare with the 70-month *Swift* BAT all-sky survey (Baumgartner et al., 2013). The two surveys are highly complementary; the *Swift* BAT all-sky survey provides a statistical hard X-ray-selected sample of AGNs in the nearby universe (primarily $z < 0.1$), while the *NuSTAR* serendipitous survey provides an equivalent sample (with comparable source statistics) for the distant universe. We compare with the redshift evolution of the knee of the X-ray luminosity function ($L_{\star}$), as determined by Aird et al. (2015a). The *Swift* BAT all-sky survey samples the population below $L_{\star}$ for redshifts up to $z \approx 0.05$, while the *NuSTAR* serendipitous survey can achieve this up to $z \approx 1$. There is almost no overlap between the two surveys, which sample different regions of the parameter space. However, there are two *NuSTAR* sources, outlying in Figure 5.12, which have very high fluxes approaching the detection threshold of *Swift* BAT: NuSTAR J043727-4711.5 ($z = 0.051$; $L_{10-40\text{keV}} = 2.6 \times 10^{43}$ erg s^{-1}) and NuSTAR J075800+3920.4 ($z = 0.095$; $L_{10-40\text{keV}} = 1.5 \times 10^{44}$ erg s^{-1}). Both are BLAGNs (based on our Keck and NTT spectra), and are unobscured at X-ray energies ($\Gamma_{\text{eff}} \approx 1.9$). The former is detected in the 70 month *Swift* BAT catalogue of Baumgartner et al. (2013), and the latter is only detected with *Swift* BAT at the $\approx 2\sigma$ level, based on the direct examination of the 104

month BAT maps (following the procedures in Koss et al. 2013).

In Figure 5.13 we compare the luminosity–redshift source distribution with other *NuS-TAR* extragalactic survey samples: the *NuSTAR*-ECDFS survey (M15) and the *NuSTAR*-COSMOS survey (C15). Rest-frame luminosities are shown for the standard three *NuS-TAR* bands (3–8 keV, 3–24 keV, and 8–24 keV). The serendipitous survey fills out the broadest range of luminosities and redshifts, due to the nature of the coverage (a relatively large total area, but with deep sub-areas that push to faint flux limits).

5.4.2 Optical properties

The X-ray–optical flux plane

The X-ray–optical flux plane is a classic diagnostic diagram for sources detected in X-ray surveys (e.g., Maccacaro et al., 1988). This plane has recently been explored for the *NuSTAR*-COSMOS sample, using the i-band (C15). Here we investigate the plane using the optical R-band for the *NuSTAR* serendipitous survey, which provides a relatively large hard X-ray selected sample spanning a comparatively wide flux range. The X-ray-to-R-band flux ratio ($f_\mathrm{X}/f_\mathrm{opt}$) diagnostic has been widely applied in past *Chandra* and *XMM-Newton* surveys of well-known blank fields (e.g., Hornschemeier et al., 2001; Barger et al., 2003; Fiore et al., 2003; Xue et al., 2011). Figure 5.14 shows the optical R-band magnitude (R) against X-ray flux (f_X) for the *NuSTAR* serendipitous survey sources which are detected in the hard band (8–24 keV) and full band (3–24 keV). We exclude $|b| < 10°$ and $z = 0$ sources, thus minimizing contamination from Galactic sources. We subdivide the *NuSTAR* sample according to X-ray luminosity and optical spectroscopic classification: objects with successful identifications as either NLAGNs or BLAGNs; objects with redshift constraints, but no classification; and objects with no redshift constraint or classification. For $R > 20$, the sources shown with lower limits in R generally correspond to a non-detection in the optical coverage, within the X-ray positional error circle. For sources where it is not possible to obtain an R-band constraint (e.g., due to contamination from a nearby bright star), we plot lower limits at the lower end of the y-axis.

We compare with the range of X-ray to optical flux ratios typically observed for AGNs identified in soft X-ray surveys, $-1 < \log(f_\mathrm{X}/f_\mathrm{opt}) < 1$ (e.g., Schmidt et al., 1998;
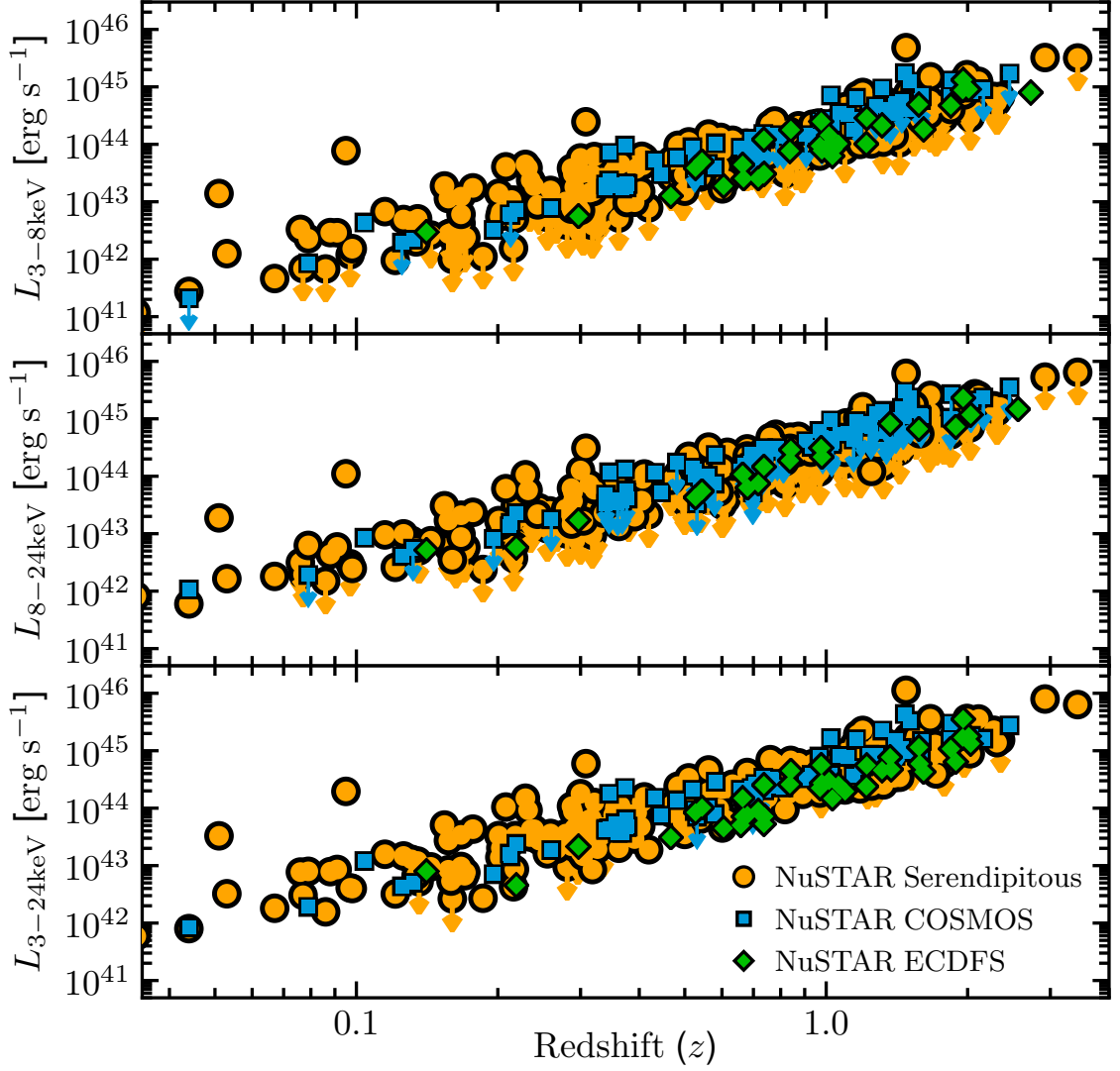
Figure 5.13: Luminosity versus redshift for the three *NuSTAR* energy bands: 3–8 (top), 8–24 (middle), and 3–24 keV (bottom). We compare the *NuSTAR* serendipitous survey sample (orange circles) with the blank-field *NuSTAR* surveys of COSMOS (blue squares; C15) and ECDFS (green diamonds; M15).
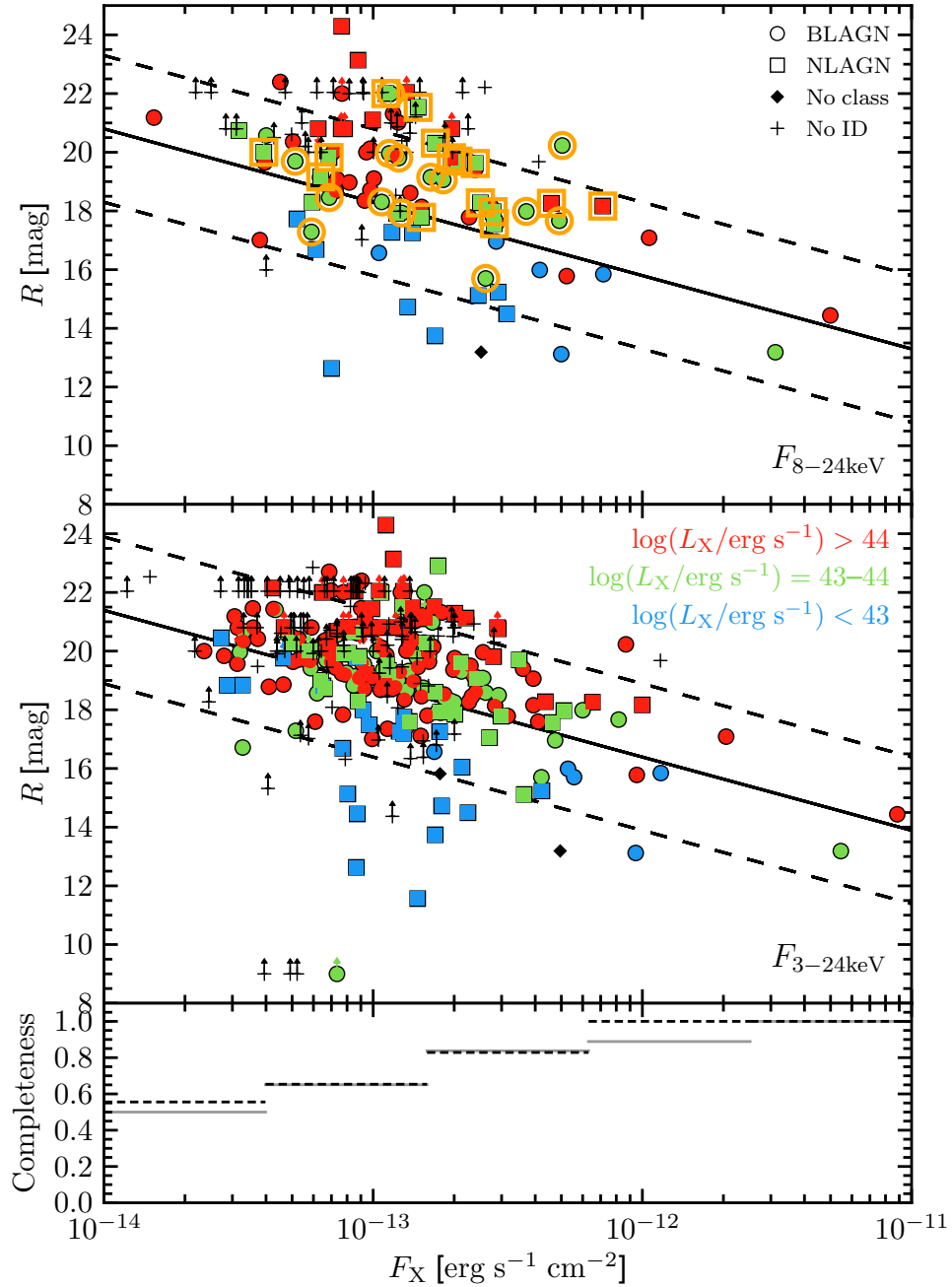
Figure 5.14: *R*-band optical magnitude (*R*) versus X-ray flux (f_X) for the hard band (8–24 keV; top panel) and full band (3–24 keV; middle panel) selected *NuSTAR* serendipitous survey samples. The blue, green, and red colours highlight three X-ray luminosity ranges, from low to high luminosity, respectively. The solid and dashed lines indicate constant X-ray-to-optical flux ratios of $\log(f_X/f_{opt}) = 0$ and ± 1, respectively. The hard band subsample for which we calculate a reliable Type 2 fraction (see Section 5.4.2) measurement is highlighted with orange outlines. In the bottom panel we show the optical spectroscopic completeness of both the 8–24 (dashed lines) and 3–24 keV (solid lines) samples as a function of f_X, calculated as the number of sources with successful optical spectroscopic classifications (see Section 5.3.3) divided by the total number of sources in a given f_X bin.
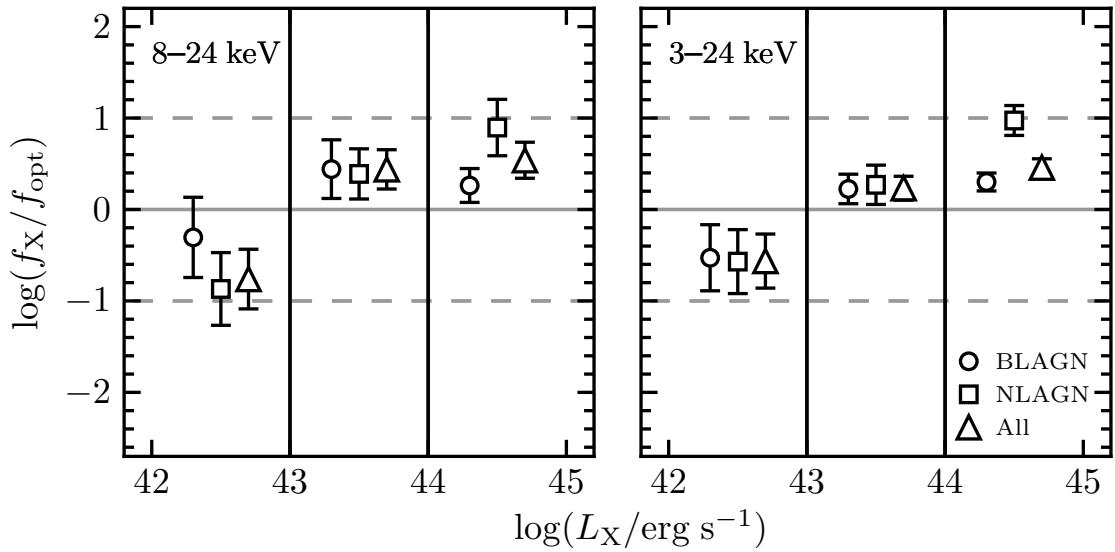
Figure 5.15: The X-ray-to-R-band flux ratio (f_X/f_{opt}), as a function of luminosity, for hard band (8–24 keV) selected sources (left); and full band (3–24 keV) selected sources (right). The luminosity bins follow those adopted in Figure 5.14. We show results for the overall spectroscopically identified population (triangles), BLAGN only (circles), and NLAGN only (squares). The solid and dashed horizontal gray lines indicate $\log(f_X/f_{opt}) = 0$ and ± 1, respectively. The horizontal offsets of the data points, within each luminosity bin, are arbitrary and for visualization purposes only.

Akiyama et al., 2000; Lehmann et al., 2001). To illustrate constant X-ray-to-optical flux ratios, we adopt the relation of McHardy et al. (2003) and correct to the *NuSTAR* energy bands assuming $\Gamma_{eff} = 1.8$. The large majority of sources lie at $\log(f_X/f_{opt}) > -1$, in agreement with them being AGNs. At least $\approx 25\%$ of the hard-band (8–24 keV) selected sources lie at $\log(f_X/f_{opt}) > 1$, in agreement with the findings for the lower energy selected X-ray sources detected in the *Chandra* and *XMM-Newton* surveys (e.g., Comastri et al., 2002; Fiore et al., 2003; Brandt & Hasinger, 2005). Such high f_X/f_{opt} values are interpreted as being driven by a combination of relatively high redshifts and obscuration (e.g., Alexander et al., 2001; Hornschemeier et al., 2001; Del Moro et al., 2008).

To demonstrate the dependence on X-ray luminosity and on spectral type, Figure 5.15 shows median f_X/f_{opt} values for bins of X-ray luminosity, and for the NLAGN and BLAGN subsamples separately. The low, medium, and high luminosity bins corre-

spond to $\log(L_{\mathrm{X}}/\mathrm{erg\ s}^{-1}) < 43$, $43 < \log(L_{\mathrm{X}}/\mathrm{erg\ s}^{-1}) < 44$, and $\log(L_{\mathrm{X}}/\mathrm{erg\ s}^{-1}) > 44$, respectively. The observed dependence on luminosity and on spectral type is consistent between the hard band and the full band selected samples (left and right panels of Figure 5.15, respectively). Overall, $f_{\mathrm{X}}/f_{\mathrm{opt}}$ increases with X-ray luminosity. The increase between the low and medium luminosity bins is highly significant; for the hard-band selected sample, the median $\log(f_{\mathrm{X}}/f_{\mathrm{opt}})$ value increases from ≈ -0.9 to ≈ 0.4. There is a marginally significant overall increase in $f_{\mathrm{X}}/f_{\mathrm{opt}}$ between the medium and high luminosity bins, which is driven by a significant increase in the $f_{\mathrm{X}}/f_{\mathrm{opt}}$ values of NLAGNs. A positive correlation between $f_{\mathrm{X}}/f_{\mathrm{opt}}$ and L_{X} has previously been identified for *Chandra* and *XMM-Newton* samples of optically obscured AGNs selected at < 10 keV, over the same luminosity range (Fiore et al. 2003). Here we have demonstrated a strong positive correlation for high energy ($\gtrsim 10$ keV) selected AGNs.

In general, the NLAGNs span a wider range in $f_{\mathrm{X}}/f_{\mathrm{opt}}$ than the BLAGNs, which mostly lie within the range expected for BLAGNs based on soft X-ray surveys, $-1 < \log(f_{\mathrm{X}}/f_{\mathrm{opt}}) < 1$. The most notable difference between the two classes is in the high-luminosity bin (which represents the "X-ray quasar" regime; $L_{\mathrm{X}} > 10^{44}$ erg s^{-1}), where the NLAGNs lie significantly higher than the BLAGNs, with a large fraction at $\log(f_{\mathrm{X}}/f_{\mathrm{opt}}) > 1$. This effect can be understood as a consequence of extinction of the nuclear AGN emission. For the BLAGNs the nuclear optical–UV emission contributes strongly to the R-band flux, while for the NLAGNs the nuclear optical emission is strongly suppressed by intervening dust (the corresponding absorption by gas at X-ray energies is comparatively weak). The effect is augmented for the high-luminosity bin, where the higher source redshifts ($\langle z \rangle \approx 0.9$) result in the observed-frame optical band sampling a more heavily extinguished part of the AGN spectrum, while the observed-frame X-ray band samples a less absorbed part of the spectrum (e.g., Del Moro et al. 2008). The other main difference between the two classes is seen for the lowest luminosity bin where, although the median flux ratios are consistent, the NLAGNs extend to lower values of $f_{\mathrm{X}}/f_{\mathrm{opt}}$ than the BLAGNs, with a handful of the NLAGNs lying at $\log(f_{\mathrm{X}}/f_{\mathrm{opt}}) < -1$.

The type 2 fraction

Here we investigate the relative numbers of the optically obscured (i.e., NLAGN) and optically unobscured (i.e., BLAGN) populations within the *NuSTAR* serendipitous survey sample. To provide meaningful constraints on the Type 2 fraction (i.e., the observed number of NLAGNs divided by the total number of NLAGNs+BLAGNs), it is important to understand the sample completeness. We therefore investigate a specific subset of the overall sample for which completeness is well understood: hard band (8–24 keV) selected sources with $0.1 < z < 0.5$, $2 \times 10^{43} < L_{10-40 \text{ keV}} < 2 \times 10^{44}$ erg s^{-1}, and $|b| > 10°$ (highlighted with orange outlines in the upper panel of Figure 5.14). The redshift limit ensures that the subsample has high spectroscopic completeness (i.e., the majority of sources have redshifts and classifications from optical spectroscopy; see below), and the luminosity limit ensures "X-ray completeness" (i.e., the AGN population within this L_X-z parameter space has fluxes which lie above the *NuSTAR* detection limit; e.g., see Figure 5.12). The luminosity range samples around the knee of the X-ray luminosity function (L_*) for these redshifts, $L_{10-40 \text{ keV}} \approx (4\text{--}7) \times 10^{43}$ erg s^{-1} (Aird et al. 2015a). In total, there are 30 spectroscopically identified sources (all NLAGNs or BLAGNs) within this subsample, which have a median redshift of $\langle z \rangle = 0.3$. Accounting for sources which are not spectroscopically identified, we estimate an effective spectroscopic completeness of 97–100% for this subsample (details are provided in Section 5.7).

The observed Type 2 fraction for the *NuSTAR* hard band-selected subsample described above is $F_{\text{Type 2}} = 53^{+14}_{-15}\%$ (binomial uncertainties). If we instead use the sources selected in the full band (3–24 keV), a similar fraction is obtained ($F_{\text{Type 2}} = 48 \pm 11\%$). In Figure 5.16 we compare with the Type 2 fraction for nearby ($z < 0.05$) AGNs similarly selected at high X-ray energies (> 10 keV). To obtain this data point we calculate the observed Type 2 fraction for the 70-month *Swift* BAT all-sky survey. Importantly, we use a luminosity-matched subsample of the *Swift* BAT survey ($2 \times 10^{43} < L_{10-40 \text{ keV}} < 2 \times 10^{44}$ erg s^{-1}, as for the *NuSTAR* subsample), since the Type 2 fraction likely varies with luminosity. We apply a redshift cut of $z < 0.05$ to ensure X-ray completeness (redshifts above this threshold push below the flux limit of *Swift* BAT for the adopted $L_{10-40 \text{ keV}}$ range; see Figure 5.12). For consistency with our approach for the *NuSTAR* sample, we class *Swift* BAT AGNs with intermediate types of 1.9 or below as BLAGNs,
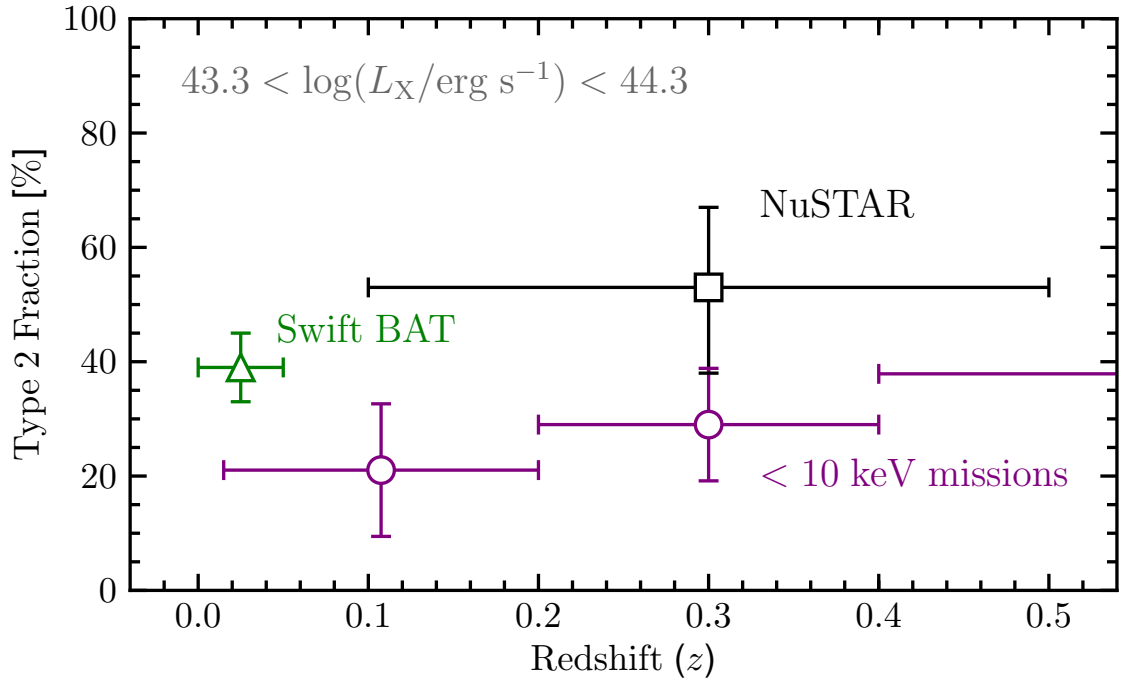
Figure 5.16: Observed Type 2 fraction versus redshift for various luminosity-matched $(2 \times 10^{43} < L_X < 2 \times 10^{44}$ erg s^{-1}), X-ray selected AGN samples: the black square shows a hard band (8–24 keV) selected subset of the *NuSTAR* serendipitous survey sample with $0.1 < z < 0.5$; the green triangle shows a subset of the 70-month *Swift* BAT all-sky survey sample ($z < 0.05$; Baumgartner et al. 2013); and the purple circles correspond to a < 10 keV selected AGN sample, compiled from multiple X-ray surveys (including *ASCA*, *Chandra* and *XMM-Newton* surveys; Hasinger 2008). The horizontal error bars show the redshift limits of each subsample.

those with NL Sy1 type spectra as BLAGNs, and those with galaxy type optical spectra as NLAGNs. The observed Type 2 fraction for this luminosity-matched *Swift* BAT sample at $z < 0.05$ is $F_{\text{Type 2}} = 37 \pm 6\%$, slightly lower than our *NuSTAR*-measured Type 2 fraction at $z \approx 0.3$, but consistent within the uncertainties. A caveat to this comparison is that the spectroscopic completeness of the *Swift* BAT subsample is unknown; overall there are ≈ 100 sources in the Baumgartner et al. (2013) catalogue which are consistent with being AGNs but lack an optical spectroscopic redshift and classification, some of which could potentially lie within the luminosity and redshift ranges adopted above. Making the extreme assumption that these ≈ 100 sources all lie in the above luminosity and redshift ranges, and are all NLAGNs, the maximum possible *Swift* BAT $F_{\text{Type 2}}$ value is 66% (which would still be in agreement with the *NuSTAR*-measured fraction). Depending on the full duration of the *NuSTAR* mission, the source numbers for the *NuSTAR* serendipitous survey may feasibly increase by a factor of two or more, which will reduce the uncertainties on the Type 2 fraction. However, to determine reliably whether there is evolution in the Type 2 fraction of high energy selected AGNs between $z < 0.05$ and $z > 0.1$, future studies should systematically apply the same optical spectroscopic classification methodologies to both samples. An early indication that the obscured fraction of AGN might increase with redshift was given by La Franca et al. (2005), and this has been further quantified in subsequent works (e.g., Ballantyne et al., 2006; Treister & Urry, 2006; Hasinger, 2008; Merloni et al., 2014). The slope of the increase with redshift is consistent with that found by Treister & Urry (2006).

The Type 2 fraction has been thoroughly investigated for the AGN population selected by lower energy (< 10 keV) X-ray missions such as *Chandra* and *XMM-Newton*. Hasinger (2008) presented a relatively complete 2–10 keV selected sample, compiled from a variety of surveys with < 10 keV missions (also see Merloni et al. 2014 for a more recent study of *XMM-Newton*-selected sources at $0.3 < z < 3.5$). We consider the $0.2 < z < 0.4$ subset of the Hasinger (2008) sample, in order to match to our *NuSTAR* subsample in redshift as closely as possible, and we limit to the luminosity range explored above ($2 \times 10^{43} < L_{10-40 \text{ keV}} < 2 \times 10^{44}$ erg s^{-1}; we assume a luminosity band correction of $L_{10-40 \text{ keV}}/L_{2-10 \text{ keV}} = 1$). The Type 2 fraction for this subset of the Hasinger (2008) sample is $F_{\text{Type 2}} = 29 \pm 10\%$, which is lower than our *NuSTAR*-measured Type 2 fraction

(see Figure 5.16), but only at a significance level of $\approx 2\sigma$. This could be explained as a result of the different selection functions of different X-ray missions, with the high energy (> 8 keV) selection of *NuSTAR* being less biased against obscured sources. Another factor to consider is the different classification methodologies applied. In addition to optical spectroscopic constraints, Hasinger (2008) use additional X-ray hardness information to classify ambiguous sources as NLAGNs or BLAGNs. Hasinger (2008) do assess the extent to which the Type 2 fraction measurements change if, instead, only the pure optical spectroscopic classification is adopted (i.e., a similar approach to our spectroscopic classification for the *NuSTAR* sources) and find that, for the redshift and luminosity ranges explored here, the Type 2 fraction would be somewhat higher but unlikely to increase by more than a factor of ≈ 1.2.

In Figure 5.16 we compare with additional luminosity-matched subsamples for the adjacent redshift bins studied by Hasinger (2008). The high-energy selected AGN samples (*NuSTAR* and *Swift* BAT) appear to lie systematically higher in Type 2 fraction than the luminosity-matched lower energy (< 10 keV) selected AGNs, for the redshift ranges covered. We note that the Type 2 fraction constraints of Merloni et al. (2014) for < 10 keV selected AGNs are broadly consistent with the values shown in Figure 5.16 (we primarily compare with the Hasinger 2008 sample since the source redshifts and luminosities sampled facilitate a direct comparison of results). The apparently small numbers of CT AGNs identified (e.g., see Figure 5.10) suggest that the offset in Type 2 fraction is not primarily driven by the uncovering of a new CT population, but more likely by the selection functions of *NuSTAR* and *Swift* BAT being generally less biased against significantly obscured AGNs.

5.4.3 Infrared properties

WISE **colour**

Mid-infrared (MIR; $\gtrsim 5$ μm) emission from AGNs is primary emission that has been reprocessed by circumnuclear dust, and suffers little extinction relative to other (e.g., optical and soft X-ray) wavelengths. Colour selections using the *WISE* telescope bands (e.g., Assef et al., 2010; Jarrett et al., 2011; Stern et al., 2012; Mateos et al., 2012, 2013;

Assef et al., 2013) can separate bright AGNs from host-galaxy light (from stars and the interstellar medium) through the identification of a red MIR spectral slope, and have thus become widely applied. These selections have the potential to identify large samples of AGNs with less bias against heavily obscured systems. However, their effectiveness worsens toward lower AGN luminosities, where identifying the AGN component of the MIR spectrum is more problematic. Here we investigate the MIR properties of our *NuS-TAR* serendipitous survey sample, and consider the results with respect to these AGN selection criteria. As mentioned in Section 5.3.2, we exclude from this analysis the few *NuSTAR* sources for which an infrared counterpart was assigned using prior knowledge of the *WISE* properties (due to the lack of a well-constrained X-ray position), to avoid biasing the results.

Figure 5.17 shows a *WISE* colour–colour diagram ($W1$–$W2$ versus $W2$–$W3$) for the *NuSTAR* serendipitous survey subsamples which are selected (i.e., independently detected) in the hard band (8–24 keV; upper panel) and full band (3–24 keV; lower panel). In general, the sources which lie at higher (i.e., redder) $W1$–$W2$ values have stronger AGN contributions to their MIR SEDs. We exclude low Galactic latitude sources ($|b| < 10°$), and sources which are spectroscopically confirmed as Galactic. In addition, we only consider sources with well constrained X-ray positions (i.e., with *Chandra*, *Swift* XRT, or *XMM-Newton* positions), and we limit the analysis to the fraction of these sources (70% and 61% for the hard and full band, respectively) with significant detections in all three of the relevant, shorter wavelength *WISE* bands ($W1$, $W2$, and $W3$; which are centred at 3.4 μm, 4.6 μm, and 12 μm, respectively). Figure 5.17 shows the sample subdivided according to X-ray luminosity and optical spectral classification. In Figure 5.18 we show the fraction (f_{wedge} hereafter) of sources which are selected as AGNs based on MIR colours alone, according to the selection "wedge" of Mateos et al. (2012), as a function of X-ray luminosity and optical classification.

For the *NuSTAR* AGNs selected in the full band (lower panel of Figure 5.17 and right panel of Figure 5.18) the overall fraction of sources identified as AGNs in the MIR is $f_{\mathrm{wedge}} = 64.6^{+5.9}_{-6.4}\%$ (104/161). Considering sources with optical spectroscopic classifications, the fractions for the overall BLAGN and NLAGN samples are $f_{\mathrm{wedge}} = 76.3^{+6.4}_{-7.9}\%$ (71/93) and $53.2^{+11.4}_{-11.8}\%$ (25/47), respectively. NLAGNs are therefore significantly less
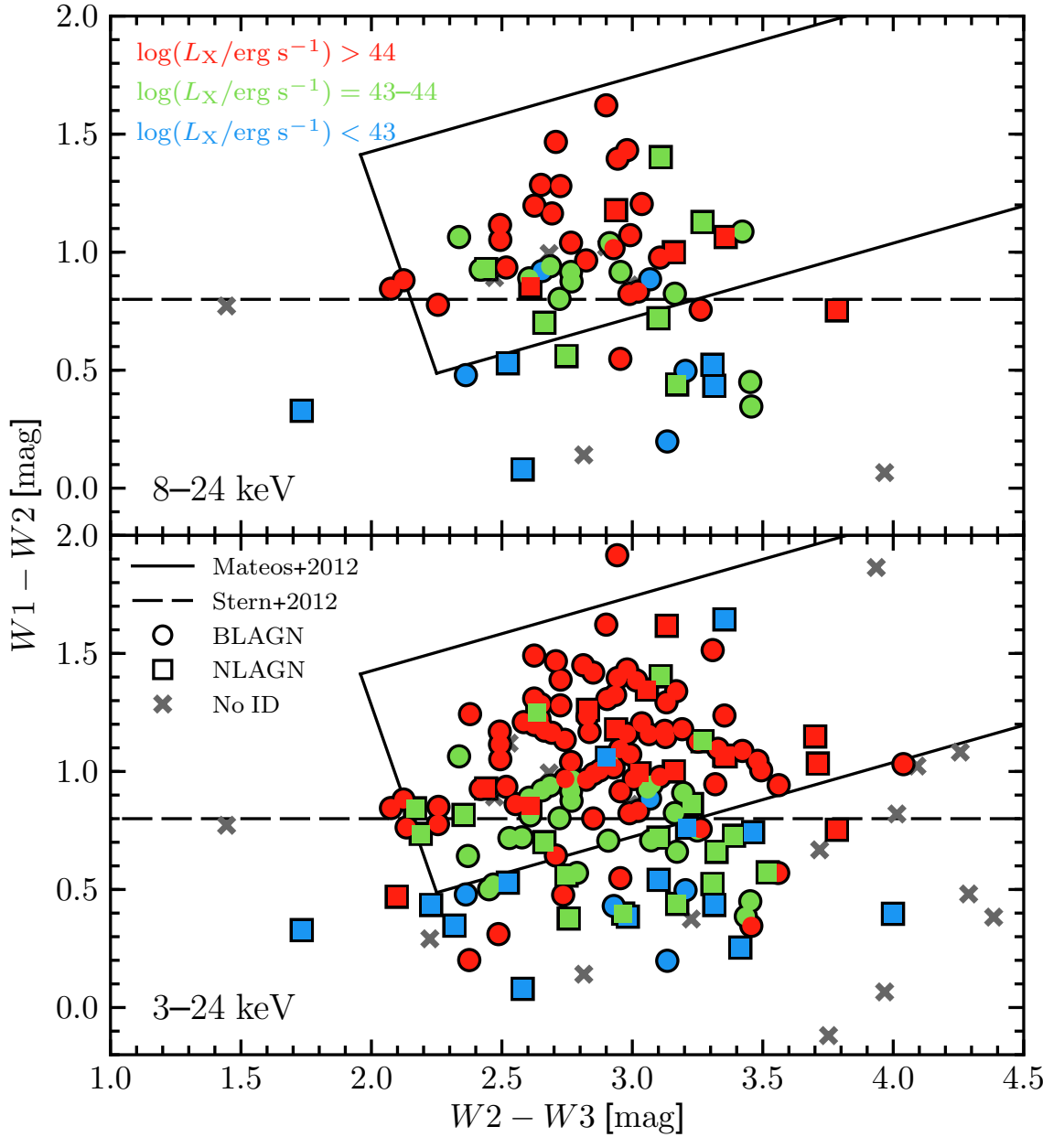
Figure 5.17: *WISE* colour–colour diagram of *NuSTAR* serendipitous survey AGNs as a function of X-ray luminosity (L_X) and source classification, for hard-band (8–24 keV) selected sources (top) and full-band (3–24 keV) selected sources (bottom). BLAGN and NLAGN are shown as circles and squares, respectively, while sources without a spectroscopic identification are shown as gray crosses. The blue, green, and red colours highlight three X-ray luminosity ranges, from low to high luminosity, respectively. The luminosities correspond to the selection bands used for this analysis (i.e., $L_{8-24\ \mathrm{keV}}$ and $L_{3-24\ \mathrm{keV}}$ for the upper and lower panels, respectively). We compare with the AGN 'wedge' of Mateos et al. (2012) and the AGN colour cut of Stern et al. (2012; $W1$–$W2 \geq 0.8$).
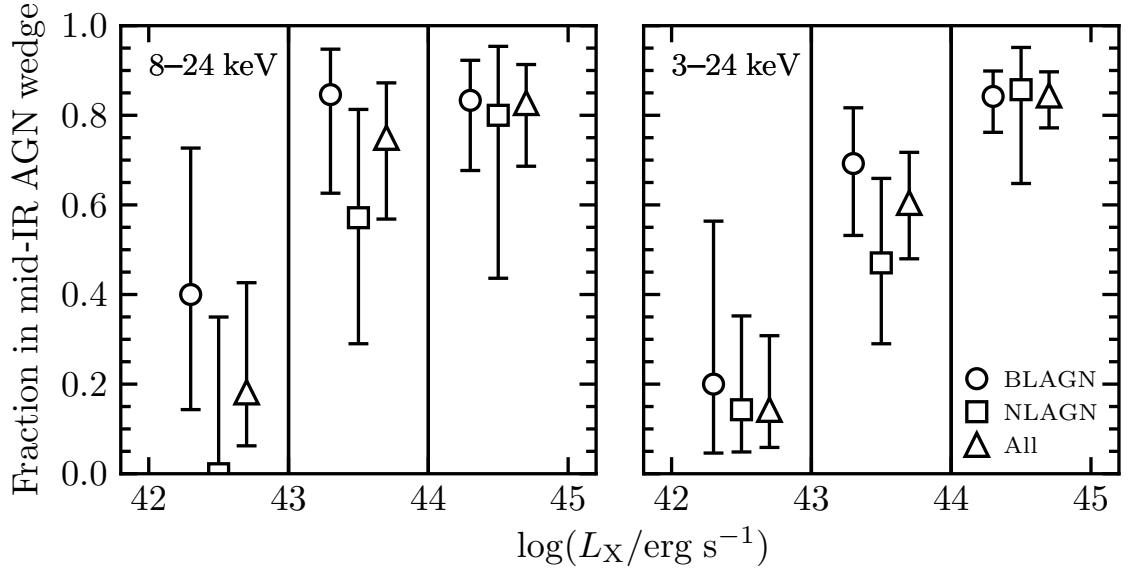
Figure 5.18: The fraction of extragalactic *NuSTAR* serendipitous survey sources which are selected as AGNs based on MIR colours alone (i.e., they lie in the *WISE* colour wedge of Mateos et al. 2012), as a function of luminosity, for hard-band (8–24 keV) selected sources (left) and full-band (3–24 keV) selected sources (right). The luminosity bins follow those adopted in Figure 5.17. We show results for the overall spectroscopically identified population (triangles), BLAGN only (circles), and NLAGN only (squares). The error bars show binomial uncertainties. The horizontal offsets of the data points, within each luminosity bin, are arbitrary and for visualization purposes only.

likely to be identified as AGNs based on MIR colours alone. This is largely driven by the lower luminosity, on average, of the NLAGNs (median of 4×10^{43} erg s^{-1}) compared to the BLAGNs (median of 3×10^{44} erg s^{-1}), in combination with the fact that f_{wedge} decreases toward lower luminosities (see Figure 5.18). Matching the NLAGNs and BLAGNs in luminosity, we do not find statistically significant differences in f_{wedge} between the two classes.

For the remainder of our overall sample which lack optical spectroscopic classifications (gray crosses in Figure 5.17), the *WISE* colours are informative of their likely properties. A low fraction of these sources lie within the wedge, $f_{\mathrm{wedge}} = 35.0^{+18.3}_{-14.7}$ (7/20). This suggests that, statistically, the unidentified sources are likely to be less luminous AGNs. In combination with the poor success rate for optical spectroscopy of these sources, we expect that they are likely to be dominated by optically obscured, low luminosity systems.

The results in Figure 5.18 show that MIR selections miss a significant fraction of the *NuSTAR*-selected AGN population, with the missed fraction increasing from $\approx 20\%$ at high luminosities, to $\approx 80\%$ at the lower luminosity end. The dependence of MIR selections on AGN luminosity has been identified for lower energy X-ray selected AGN samples (e.g., Cardamone et al. 2008; Eckart et al. 2010), and is likely primarily driven by a stronger contribution to the SED from the host galaxy for lower X-ray luminosities, which results in bluer MIR colours. The MIR AGN selection wedge of Mateos et al. (2012) was defined using the Bright Ultrahard *XMM-Newton* survey (BUXS) sample, selected at 4.5–10 keV, for comparable numbers of spectroscopically identified AGNs (114 BLAGNs and 81 NLAGNs) as the full-band selected *NuSTAR* serendipitous survey sources incorporated here (107 BLAGNs and 45 NLAGNs), and for a similar redshift and luminosity distribution. For the NLAGNs, our results for f_{wedge} as a function of X-ray luminosity and optical classification are consistent (given the uncertainties) with those found for the BUXS sample. Our BLAGNs have marginally lower f_{wedge} values than the BUXS BLAGNs. For instance, Mateos et al. (2012) find that the MIR selection is essentially complete for BLAGNs at $L_{\mathrm{X}} > 10^{43}$ erg s^{-1} (e.g., $f_{\mathrm{wedge}} = 100_{-6.6}\%$ and $96.1^{+3.00}_{-6.3}\%$ for $L_{2-10\mathrm{keV}} = 10^{43}$–$10^{44}$ and 10^{44}–10^{45} erg s^{-1}, respectively), while even at the highest luminosities ($L_{3-24\mathrm{keV}} > 10^{44}$ erg s^{-1}) we find $f_{\mathrm{wedge}} = 82.4^{+6.3}_{-8.8}\%$.

It is notable that the MIR selection fails for 12 (i.e., 17.6%) of the high luminosity

NuSTAR-selected BLAGNs, since MIR selections are typically expected to be close to complete for high luminosity, unobscured sources. To assess why these sources in particular are not MIR-selected, we compare their optical and X-ray source properties (e.g., *NuSTAR* detection significance, redshift, 10–40 keV luminosity, 2–10 keV luminosity, brightness, optical spectra) with the 59 (i.e., the 82.4%) high luminosity BLAGNs which are MIR-selected. There are no clear statistically significant differences, with a possible exception: the optical R-band magnitude distributions of the two subsets are different at a moderate significance level (KS-test p-value of $p = 0.037$), with the 12 MIR-unselected sources skewed to fainter R values (median of $\langle R \rangle = 19.9$) than their MIR-selected counterparts ($\langle R \rangle = 19.4$). This result increases in significance (to $p = 0.0075$) if we limit the comparison to the eight (out of 12) MIR-unselected sources which are additionally missed by the Stern et al. (2012) $W1$–$W2$ colour AGN selection. Comparing the distribution of f_X/f_{opt} versus $W1$–$W2$ for these eight sources with the overall serendipitous sample (see Figure 5.19), they overlap with lower luminosity AGNs where we expect that the relatively blue $W1$–$W2$ colours are driven by a stronger (relative) contribution to the MIR SED from the host galaxy. The latter could also be true for the eight MIR-unselected high-L_X BLAGNs if their MIR AGN luminosities are relatively low compared to the 59 MIR-selected counterparts (which are matched in X-ray luminosity). Estimating the rest-frame 6 μm luminosities ($L_{6\mu\mathrm{m}}$) by interpolating between the relevant observed-frame *WISE* band magnitudes,[10] we find that the eight MIR-unselected BLAGNs have a significantly different $L_{6\mu\mathrm{m}}$ distribution to the MIR-selected counterparts ($p = 0.046$), and are indeed skewed to lower MIR luminosities ($\langle L_{6\mu\mathrm{m}} \rangle = 3.4 \times 10^{44}$ erg s^{-1}) than the MIR-selected sources ($\langle L_{6\mu\mathrm{m}} \rangle = 1.3 \times 10^{45}$ erg s^{-1}). In summary, the incompleteness of MIR selections for unobscured high-L_X AGNs appears to be related to scatter in the intrinsic AGN properties (for matched z and L_X).

For the *NuSTAR* serendipitous survey sources selected in the hard band (upper panel of Figure 5.17 and left panel of Figure 5.18), for which *NuSTAR* is uniquely sensitive, the results are consistent with those for the full-band sample, but with greater uncertainties due to the smaller source numbers. For instance, $f_{\mathrm{wedge}} = 64.6^{+9.0}_{-10.1}\%$ (42/65) for the

---

[10]From the *WISE* all-sky survey catalogue, there are no indications of bad photometry (e.g., due to blending, contamination, or confusion) for these eight sources.
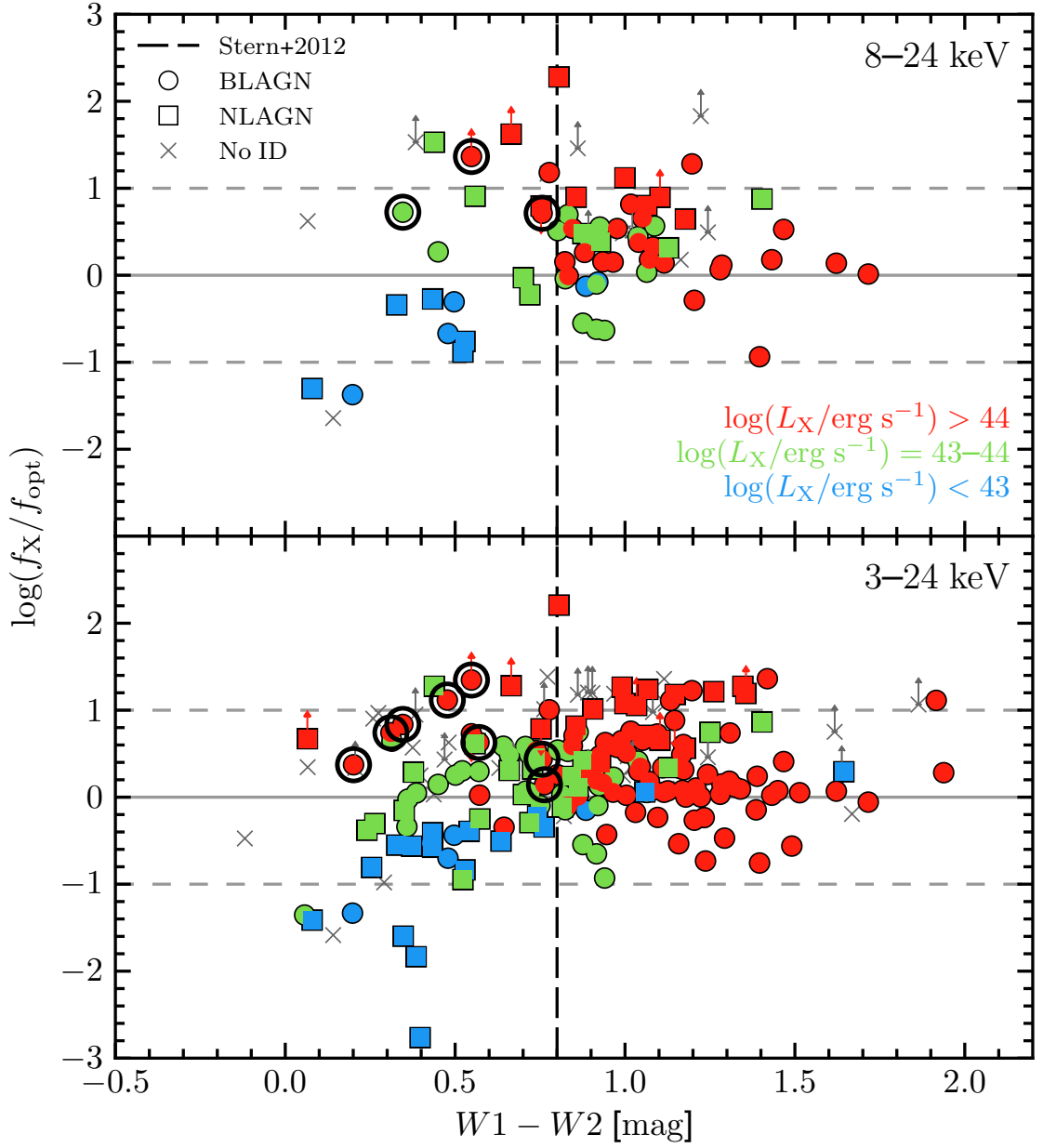
Figure 5.19: The X-ray-to-R-band flux ratio (f_X/f_{opt}) versus the *WISE* $W1$–$W2$ colour, for hard band (8–24 keV) selected sources (top); and full band (3–24 keV) selected sources (bottom). The luminosity bins and the marker labelling follow those adopted in Figures 5.14 and 5.17. Eight high luminosity BLAGNs which are not selected as AGNs in the MIR (see Section 5.4.3) are highlighted with large black circles.

overall hard band selected sample. We conclude that, while there are some differences, the MIR colour distribution of the *NuSTAR* serendipitous survey sample is largely consistent with that expected based on the results for lower-energy (< 10 keV) selected AGNs.

X-ray–MIR luminosity plane

There is a remarkably tight correlation between the X-ray luminosities and the MIR luminosities of unobscured AGNs, with both providing estimates of the intrinsic AGN power (e.g., Lutz et al., 2004; Fiore et al., 2009; Gandhi et al., 2009; Lanzuisi et al., 2009; Ichikawa et al., 2012; Matsuta et al., 2012; Asmus et al., 2015; Mateos et al., 2015; Stern, 2015). Low X-ray to MIR luminosity ratios are interpreted as being due to either X-ray absorption or intrinsic X-ray weakness.

In Figure 5.20 we show the observed (i.e., uncorrected for absorption) rest-frame X-ray luminosities ($L_{\mathrm{X}}^{\mathrm{obs}}$) versus the rest-frame 6 μm luminosities ($L_{6\mu\mathrm{m}}$, in νL_ν units) for *NuSTAR* serendipitous survey sources. We only include sources which are AGN-dominated at MIR wavelengths according to the *WISE* colours (based on either of the criteria in Section 5.4.3), and thus where we believe the rest-frame 6 μm flux to be dominated by the AGN rather than host-galaxy light. Additionally, we require the sources to be detected in the two observed-frame *WISE* bands which are interpolated between to estimate $L_{6\mu\mathrm{m}}$ (e.g., $W2$ and $W3$ for $z < 1$). For the high energy (10–40 keV) rest-frame X-ray band (bottom panel of Figure 5.20), the X-ray luminosities are from *NuSTAR* photometry (as described in Section 5.2.4). For the low energy (2–10 keV) rest-frame X-ray band (top panel of Figure 5.20), the X-ray luminosities are estimated from CSC or 3XMM counterpart fluxes (for the top panel, we only show sources with counterparts in these catalogues). We compare with other *NuSTAR*-observed samples, including a number of heavily obscured AGNs. To demonstrate the approximate X-ray to MIR luminosity ratios expected in the cases of zero absorption and high absorption, we show the intrinsic X-ray–MIR relation (as measured by multiple studies; Fiore et al. 2009; Gandhi et al. 2009; Stern 2015) and the same relation after absorption by $N_{\mathrm{H}} = 10^{24}$ cm^{-2} gas, respectively.

At 10–40 keV, the serendipitous survey sources are generally consistent with both the intrinsic and the highly absorbed X-ray–MIR relations (which are close together for these
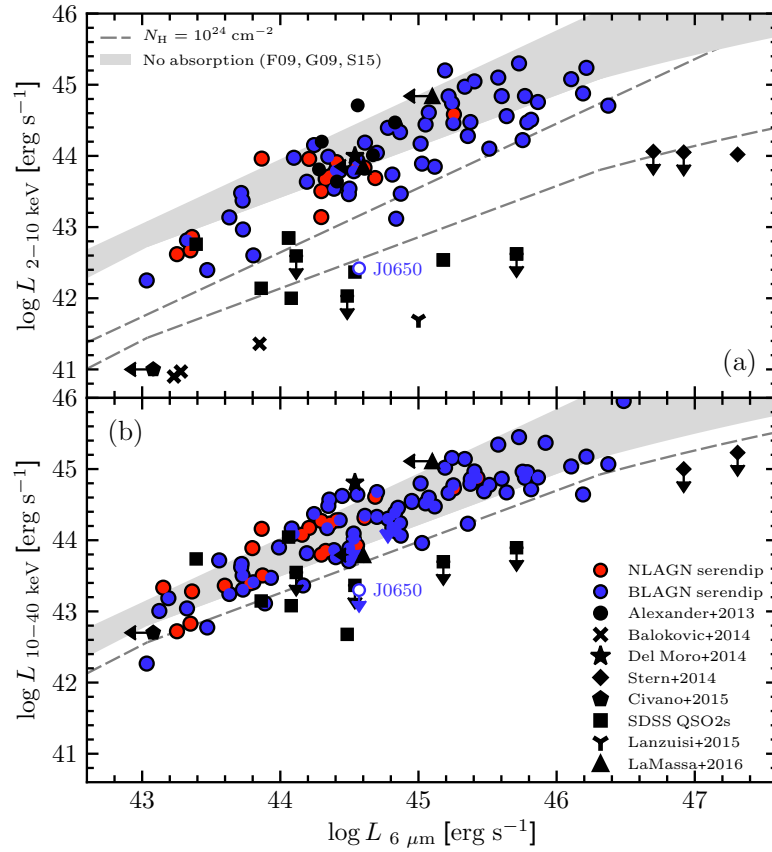
Figure 5.20: Observed (i.e., uncorrected for absorption) rest-frame 2–10 keV [$L_{2-10\ keV}$; (a)] and 10–40 keV X-ray luminosity [$L_{10-40\ keV}$; (b)] versus rest-frame 6 μm luminosity ($L_{6\mu m}$, in νL_ν units). Filled circles show the *NuSTAR* serendipitous survey sources. We only show sources that have detections in the *WISE* bands necessary to estimate $L_{6\mu m}$ (through interpolation), and which are AGN-dominated at MIR wavelengths according to their *WISE* colours (based on satisfying either the Mateos et al. 2012 or Stern et al. 2012 criteria), and thus where we believe $L_{6\mu m}$ to have minimal contamination from the host galaxy. The apparently X-ray weak source J0650 (see Section 5.4.3) is shown as an empty circle and labelled. We compare with other samples: *NuSTAR*-observed SDSS-selected heavily obscured Type 2 quasars (squares; $z = 0.05$–0.49; Lansbury et al. 2014; Gandhi et al. 2014; Lansbury et al. 2015); three CT Seyfert 2 AGNs from the *NuSTAR* snapshot survey ("×" symbols; $z \approx 0.01$; Baloković et al. 2014); luminous and heavily obscured *WISE*-selected AGNs targetted with *NuSTAR* (diamonds; $z \approx 2$; Stern et al., 2014); a heavily obscured quasar identified in the *NuSTAR*-ECDFS survey (star; $z \approx 2$; Del Moro et al., 2014); a CT AGN identified in the *NuSTAR*-COSMOS survey (pentagon; ID 330; $z = 0.044$; C15); a candidate heavily CT AGN identified in the COSMOS field (triangle; $z = 0.35$; Lanzuisi et al. 2015a); and *NuSTAR*-observed FIRST-2MASS red quasars (triangle; $z = 0.14$–0.41; LaMassa et al. 2016). All of the data are compared with the luminosity ratios expected in the case of zero line-of-sight absorption (gray region). This region shows the range of intrinsic luminosity ratios predicted by three different intrinsic relations in the literature: Gandhi et al. (2009), Fiore et al. (2009) and Stern (2015). The dashed lines illustrate the observed X-ray luminosity suppression expected if the zero absorption region is absorbed by gas with a column density of $N_H = 10^{24}\ cm^{-2}$.

energies). The most outlying source, J0650 (highlighted in Figure 5.20), has a very low upper limit in X-ray to MIR luminosity ratio. Notably, for this source the Keck optical spectroscopy reveals a narrow line Seyfert 1 (NL Sy1) spectrum, and we measure a very steep 0.5–10 keV X-ray spectrum ($\Gamma_{\mathrm{eff}} = 3.1$). Given these properties, we interpret the low X-ray to MIR ratio as likely being driven by intrinsic X-ray weakness (in combination with the steep X-ray spectrum), rather than being driven by extreme absorption levels. Intrinsic X-ray weakness has previously been identified for objects in the NL Sy1 class (e.g., Miniutti et al. 2012; Leighly et al. 2007b,a). A detailed discussion of J0650 is provided in Section 5.8.

At 2–10 keV, the sample shows evidence for significant downwards deviations from the intrinsic relations, although there is little overlap with the known heavily absorbed and CT sources which have been observed in targetted *NuSTAR* programs. We note however that this analysis is currently limited to a specific subset of the serendipitous survey (i.e., sources which are AGN-dominated at MIR wavelengths, and which are detected in the relevant *WISE* bands). Future SED modelling of the broader spectroscopically identified sample would allow reliable $L_{6\mu\mathrm{m}}$ measurements (disentangling AGN and host galaxy MIR emission) for a more complete subset of the serendipitous survey sample.

5.5   Summary

The high sensitivity of *NuSTAR* at $\gtrsim 10$ keV has provided access to large samples of high-energy X-ray emitting AGNs in the distant universe, whereas previous observatories were largely restricted to the local universe ($z \lesssim 0.1$). In this chapter we have presented the first full catalogue for the *NuSTAR* serendipitous survey, the largest survey undertaken with *NuSTAR*, which incorporates data from the first 40 months of telescope operation. The data include 331 unique fields, with a total areal coverage of 13 deg^2, and a cumulative exposure time of ≈ 20 Ms. We have characterized the *NuSTAR* detected AGNs in terms of their X-ray, optical, and IR properties. Below we summarize the main results:

- Overall, we detect 497 sources which are significant post-deblending (i.e., after accounting for contamination of the photon counts from nearby sources). Of these, 163 are independently detected in the hard (8–24 keV) energy band; see Section

5.2.5.

- The median vignetting-corrected exposure time per source (for the combined FPMA+FPMB data) is $\langle t_{\mathrm{net}} \rangle = 60$ ks, and the maximum is 1500 ks. The X-ray fluxes span from $f_{3-24\mathrm{keV}} \approx 10^{-14}$ to 10^{-11} erg s^{-1} cm^{-2}, with a median value of $\langle f_{3-24\mathrm{keV}} \rangle = 1.1 \times 10^{-13}$ erg s^{-1} cm^{-2}; see Section 5.4.1. The survey reaches flux depths similar to the *NuSTAR* surveys in well-studied fields (COSMOS, ECDFS, EGS, GOODS-N, and UDS) over comparable areas (see Section 5.2.3), and is $\approx$two orders of magnitude fainter than the *Swift* BAT surveys; e.g., see Section 5.4.1.

- There is a large range in the observed band ratios of AGNs at 3–24 keV, which imply a range of effective photon indices going from very soft ($\Gamma_{\mathrm{eff}} \approx 3$) to very hard ($\Gamma_{\mathrm{eff}} \approx 0$); see Section 5.4.1. We find no evidence for an anticorrelation between band ratio and count rate, as has previously been found for lower energy X-ray bands; see Section 5.4.1.

- A large fraction 79% $(395/497)$ of the sources have soft (< 10 keV) X-ray counterparts detected in surveys or archival data from *XMM-Newton*, *Chandra*, and *Swift* XRT. The *NuSTAR* fluxes and the soft X-ray counterpart fluxes show good agreement for the 3–8 keV energy band, and the maximum identified variation in AGN flux between the soft X-ray and *NuSTAR* observations is a factor of $\approx$five; see Section 5.3.1. The higher positional accuracies of the soft X-ray observatories relative to *NuSTAR* allow us to reliably match to optical and IR counterparts; see Section 5.3.2.

- Optical spectroscopic identifications (i.e., redshift measurements and source classifications) have been successfully obtained for 276 sources. For the large majority of the sample (222 sources) this was achieved through our extensive campaign of ground-based spectroscopic followup, using a range of observatories at multiple geographic latitudes; see Section 5.3.3. 16 sources are spectroscopically confirmed as Galactic. Of the 260 extragalactic sources (AGNs), 162 (62.3%) are classified as BLAGNs, 97 (37.3%) are NLAGNs, and one (0.4%) is a BL Lac; see Section 5.3.3. While similar numbers of NLAGNs and BLAGNs are identified at lower redshifts ($z \lesssim 1$) there is a bias towards detections of BLAGNs at higher redshifts;

this bias has been well established for other X-ray missions (e.g., *Chandra* and *XMM-Newton*); see Section 5.4.1.

- The serendipitous survey AGNs have redshifts covering a wide range, from $z = 0.002$ to 3.4, with a median of $\langle z \rangle = 0.56$. The rest-frame 10–40 keV luminosities also span a wide range, from $L_{10-40\text{keV}} \approx 10^{39}$ to 10^{46} erg s^{-1}, with a median value of $\langle L_{10-40\text{keV}} \rangle = 10^{44.1}$ erg s^{-1}. Previous X-ray missions with sensitivity at > 10 keV were able to sample the AGN population below the knee of the X-ray luminosity function ($L_\star$) for redshifts up to $z \approx 0.05$, and *NuSTAR* extends this to $z \approx 1$; see Section 5.4.1.

- We present the X-ray–optical flux plane for the optical R band, and the 8–24 keV and 3–24 keV *NuSTAR* bands. The majority of sources have f_X/f_{opt} values consistent with those expected for AGNs based on the findings of previous low energy (< 10 keV) X-ray observatories. We find a strong, positive correlation between f_X/f_{opt} and X-ray luminosity, in agreement with results at < 10 keV. We also find evidence for significant differences in f_X/f_{opt} between the BLAGNs and NLAGNs; see Section 5.4.2.

- We measure a Type 2 AGN fraction of $53^{+14}_{-15}\%$ for an effectively spectroscopically complete subset of the hard band (8–24 keV) selected sample at $0.1 < z < 0.5$ and with $2 \times 10^{43} < L_{10-40\text{keV}} < 2 \times 10^{44}$ erg s^{-1}. Comparing with luminosity-matched $z < 0.05$ AGNs selected by the *Swift* BAT survey, the *NuSTAR*-measured Type 2 fraction for distant AGNs is higher, but consistent within the uncertainties. However, the *NuSTAR*-measured and *Swift* BAT-measured Type 2 fractions appear to be systematically higher than those measured for redshift- and luminosity-matched AGNs selected by < 10 keV X-ray missions (e.g., *Chandra* and *XMM-Newton*); see Section 5.4.2.

- We compare the distribution of *WISE* $W1–W2$ and $W2–W3$ colours for *NuSTAR* AGNs with commonly applied MIR colour-selection techniques. The fraction of *NuSTAR* AGNs which would be selected as AGNs based on the MIR colours alone is a strong function of X-ray luminosity, in agreement with findings for low energy (< 10 keV) X-ray selected samples. The fraction of *NuSTAR* AGNs missed by

MIR colour-selections is large, ranging between $\approx 20\%$ and $\approx 80\%$ for the highest luminosities ($L_X > 10^{44}$ erg s^{-1}) and the lowest luminosities ($L_X < 10^{43}$ erg s^{-1}), respectively; see Section 5.4.3. It is notable that a number of luminous *NuSTAR*-selected BLAGNs are not selected in the MIR, and that this appears to be driven by the intrinsic AGN properties; see Section 5.4.3.

- We present the X-ray–MIR luminosity plane for sources which are AGN-dominated at MIR wavelengths. For both the rest-frame 2–10 keV and 10–40 keV bands the large majority of the sources are consistent with being scattered around the intrinsic L_X–$L_{6\mu m}$ relation; see Section 5.4.3. One source is highlighted as having an extremely low $L_{10-40\text{keV}}/L_{6\mu m}$ ratio (J0650; $z = 0.32$; $L_{6\mu m} \approx 4 \times 10^{44}$ erg s^{-1}; $L_{10-40\text{keV}} < 2 \times 10^{43}$ erg s^{-1}). A detailed investigation reveals a narrow-line Seyfert 1, likely to be intrinsically X-ray weak as opposed to heavily obscured; see Section 5.4.3.

5.6 Assessment of spurious optical and IR counterpart matches

Figure 5.21 shows histograms of the radial offsets between soft X-ray counterpart (*Chandra*, *Swift* XRT, and *XMM-Newton*) positions and the optical (SDSS and USNOB1) and IR (*WISE*) matches. We compare to the radial offset distributions expected for spurious matches, given the sky density of sources in the IR and optical surveys, in order to estimate spurious matching fractions.

5.7 Assessment of spectroscopic completeness for the Type 2 fraction subsample

Here we assess the effective spectroscopic completeness of the subset of the *NuSTAR* serendipitous survey sample used to measure the Type 2 fraction (see Section 5.4.2). The subset is limited to hard band (8–24 keV) selected sources at redshifts of $0.1 < z < 0.5$ and luminosities of $2 \times 10^{43} < L_{10-40\text{keV}} < 2 \times 10^{44}$ erg s^{-1}, and includes 29 spectro-
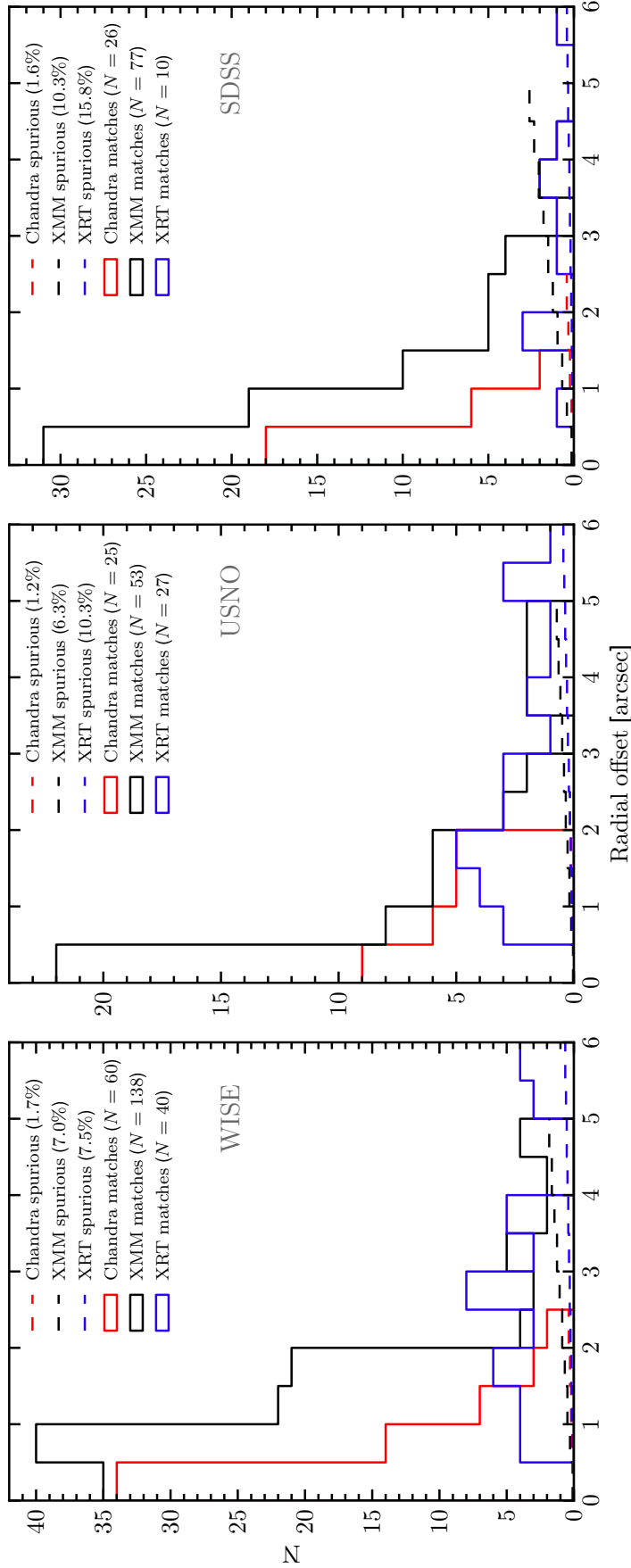
Figure 5.21: Histograms showing the distributions of positional offsets between the soft X-ray (*Chandra*, *XMM-Newton*, and *Swift* XRT; red, black, and blue solid lines, respectively) positions and the matched *WISE* (left panel), USNOB1 (middle panel), and SDSS (right panel) counterparts, for the *NuSTAR* serendipitous survey sources with $|b| > 10°$. The dashed lines show the distributions expected for spurious matches (i.e., assuming there are no true IR or optical counterparts to the X-ray sources); these are calculated using the IR and optical source densities, taking median values across the range of sky positions for the *NuSTAR* serendipitous survey sources: 3.2 arcmin^{-2} for *WISE*; 3.3 arcmin^{-2} for USNOB1; and 8.1 arcmin^{-2} for SDSS. The bracketed percentages show the inferred spurious fraction (i.e., the fraction of the X-ray sources with false IR or optical matches) for each subsample.

scopically identified sources (all NLAGNs or BLAGNs). To assess the completeness, we must also consider the unidentified sources which may or may not lie within these redshift and luminosity ranges (i.e., sources labelled as crosses in Figure 5.14), and their reasons for lacking successful spectroscopic followup. Since the majority of the spectroscopically identified sources in this subsample lie at $R < 20$, we consider all unidentified sources with $R < 20$ (we conservatively include sources with lower limits in R) as potentially lying within the redshift and luminosity ranges stated above. There are 11 such unidentified sources in total. This includes one likely BL Lac type object which we exclude due to the possibility of beaming. A further five of the unidentified sources can be safely excluded without biasing the Type 2 fraction measurement: two of these have unambiguous optical counterparts, and simply have not yet been targetted with ground-based facilities; two have not been targetted due to the lack of *Chandra* or *XMM-Newton* coverage, required to distinguish between multiple optical counterparts within the large *NuSTAR* positional error circle; and for one obtaining spectroscopy is problematic due to the close proximity of brighter optical sources. There are five remaining unidentified sources to consider, where followup has not been performed due to the lack of a detection in the available *Chandra* and/or *XMM-Newton* coverage (and therefore the lack of an accurate X-ray position). Four of these have high P_False values at 8–24 keV ($\log P_\mathrm{False} = -6.5$ to -6.0; i.e., close to our detection threshold of $\log P_\mathrm{False} = -6.0$) and comparably deep *Chandra* or *XMM-Newton* coverage, which indicates that they are likely to be spurious sources. The remaining single source is strongly detected at 8–24 keV ($\log P_\mathrm{False} = -9.6$), and has relatively low quality *Chandra* and *XMM-Newton* coverage, so is consistent with being a genuine astrophysical source. We therefore consider the effective spectroscopic completeness of this subsample to be 97–100% (i.e., 28/29 or 28/28, depending on whether the final source lies above or below $R = 20$, since there is only a lower limit in R).

5.8   J0650– A low $L_\mathrm{X}/L_\mathrm{MIR}$, likely X-ray weak NLSy1

Here we consider an outlier in X-ray to MIR luminosity ratio, NuSTAR J065003+6046.8 (hereafter J0650; $z = 0.319$). For this source, the upper limit of $L_{10-40\mathrm{keV}}/L_{6\mu\mathrm{m}} < 0.05$ lies below the CT AGN threshold (as shown in Figure 5.20). In other words, the hard

X-ray luminosity is very weak compared to that expected based on the MIR luminosity ($L_{6\mu\mathrm{m}} = 3.7 \times 10^{44}$ erg s^{-1}). The source is not detected in the full and hard *NuSTAR* bands, but is weakly detected in the soft band ($\log P_{\mathrm{False}} = -6.9$; ≈ 25 net source counts, for an effective exposure time of 16 ks), suggesting a relatively steep spectral slope. The properties of the counterparts at X-ray, IR, and optical wavelengths (see below) add confidence that the *NuSTAR* detection is not spurious. J0650 has a strongly detected *XMM-Newton* counterpart, the 0.5–10 keV spectrum of which has 107 net source counts (for an 8 ks exposure). A power law fit provides a statistically acceptable fit to the *XMM-Newton* spectrum ($C/n = 139/159$), and the photon index is constrained to be $\Gamma_{\mathrm{eff}} = 3.1 \pm 0.6$, which is very steep and above the typical range observed for AGNs. For the 3–10 keV band, where *NuSTAR* and *XMM-Newton* overlap in sensitivity, the source is undetected with *XMM-Newton*, with < 19.5 EPIC counts overall and a 3–8 keV flux upper limit of $< 1.5 \times 10^{-14}$ erg s^{-1} cm^{-2} (99% CL). This is significantly lower than our photometric *NuSTAR* flux of $4.8 \pm 1.6 \times 10^{-14}$ erg s^{-1} cm^{-2} in the 3–8 keV band. The disagreement could in part result from X-ray variability (between the 2003 *XMM-Newton* observation and the 2014 *NuSTAR* observation), which is especially likely in this case given the NLSy1 optical classification (see below). The *NuSTAR* flux is also likely boosted by the Eddington bias, which we have established to be significant at this low 3–8 keV flux level (see Figure 5.5, and C15).

The X-ray luminosities measured at high and low energies are $L_{10-40\ \mathrm{keV}}^{\mathrm{obs}} < 2.0 \times 10^{43}$ erg s^{-1} (from *NuSTAR* photometry) and $L_{2-10\ \mathrm{keV}}^{\mathrm{obs}} = 2.6 \times 10^{42}$ erg s^{-1} (from the *XMM-Newton* spectrum), respectively. Given the AGN 6 μm luminosity measured from *WISE* photometry ($L_{6\mu\mathrm{m}} = 3.7 \times 10^{44}$ erg s^{-1}; the source is AGN-dominated at this wavelength based on the *WISE* colours), these suggest comparatively low X-ray to MIR luminosity ratios, with the 2–10 keV and 10–40 keV X-ray luminosities potentially suppressed by factors of ≈ 50 and $\gtrsim 7$, respectively, with respect to the intrinsic relations for AGNs (see Figure 5.20). In the case of the 2–10 keV luminosity, the low value is in part due to the relatively steep soft X-ray spectral slope. If the apparent X-ray suppression were due to AGN absorption we would expect a flat X-ray spectral slope ($\Gamma_{\mathrm{eff}} < 1$), but the observed spectral slope is comparatively steep ($\Gamma_{\mathrm{eff}} \approx 3$). One possibility is that the source is an intrinsically X-ray weak, unobscured AGN. As described below, the source

shows the properties of a NLSy1 in the optical, and intrinsic X-ray weakness has been identified for some objects in this class (e.g., Miniutti et al. 2012; Leighly et al. 2007b,a).

Further evidence for the presence of an AGN in J0650 is given by the *WISE* colours, which place it firmly within the MIR AGN selection regions ($W1$–$W2$ = 1.2; $W2$–$W3$ = 3.2). The source is also comparatively bright in the longer wavelength *WISE* bands ($W3 = 9.50 \pm 0.03$ and $W4 = 7.24 \pm 0.07$). On the basis of our results for *WISE* colours as a function of X-ray luminosity (Section 5.4.3) J0650 is statistically highly likely to have an intrinsic X-ray luminosity of $L^{int}_{10-40 \text{ keV}} > 10^{44}$ erg s^{-1}. The fact that the observed X-ray luminosity is so much lower may be explained by a combination of intrinsic X-ray weakness and the steep spectral slope at low energies, the latter of which may result in a relative increase in the dust-heating photons which are reprocessed into the MIR waveband.

Key information for this object is provided by our Keck spectrum, which reveals a likely NLSy1 AGN. We detect multiple strong emission lines, from Mg II at the blue end to Hα and [N II] at the red end. The source satisfies the conventional NLSy1 definition, with a relatively narrow Hβ line (FWHM ≈ 1710 km s^{-1}), and a low [O III] $\lambda5007$/Hβ flux ratio (e.g., Goodrich, 1989). There are also multiple strong Fe II emission lines, another characteristic feature of NLSy1s (e.g., Zhou et al., 2006). Notably, the [O III] $\lambda5007$ line is contaminated by strong Fe emission. NLSy1s are associated with low black hole masses and high accretion rates (e.g., Pounds et al., 1995; Boller et al., 1996; Mathur, 2000), and typically have significantly steeper X-ray spectral slopes than normal unobscured AGNs (e.g., Boller et al., 1996; Brandt et al., 1997). The latter property is congruous with our measurement of an extremely steep X-ray photon index for J0650 ($\Gamma_{eff} \approx 3$).

Chapter 6

The *NuSTAR* serendipitous survey: hunting for the most extreme sources

Abstract

We identify extremely hard X-ray sources in the *NuSTAR* serendipitous survey, the largest survey undertaken with a focusing high energy (i.e., sensitive at $\gtrsim$ 10 keV) X-ray mission, in order to search for highly obscured AGNs. For the 10 identified extreme *NuSTAR* sources, we combine the *NuSTAR* data with the best available coverage from lower energy X-ray missions (*Chandra*, *Swift* XRT, and *XMM-Newton*) to characterize the broadband (0.5–24 keV) X-ray spectra. The majority (9 out of 10) of the sources are at least moderately obscured, with line-of-sight column densities ranging from $N_{\rm H} \approx 10^{23}$ to $> 10^{24}$ cm^{-2}. The X-ray classifications are all supported by the optical spectroscopic classifications. The intrinsic (i.e., absorption-corrected) rest-frame 10–40 keV luminosities of the sources cover a large range from $\approx 5 \times 10^{42}$ to 10^{45} erg s^{-1}. We find that the serendipitous survey has indeed unearthed some highly obscured systems, including three robust CT AGNs at low redshift ($z < 0.1$), and approximately two more at higher redshifts. Our estimates for the number counts of CT AGNs and for the CT fraction are in broad agreement with model expectations based on previous (primarily < 10 keV) X-ray surveys. The optical imaging coverage shows a remarkably high fraction of host galaxy mergers for the likely-CT AGNs (75%; i.e., $3/4$ of the optically resolved systems). Comparing to "normal" *NuSTAR* sources (matched in optical imaging data quality), we find tentative evidence for a connection between CT phases and the merger stage of galaxy

evolution.

6.1 Introduction

The majority of cosmic supermassive black hole growth has occured in an obscured phase (e.g., Fabian 1999; Gilli et al. 2007; Treister et al. 2009). Historically, the importance of obscured AGNs has been inferred from the shape of the extragalactic cosmic X-ray background (CXB), the high energy hump of which (peaking at $\approx$ 20–30 keV) requires significant populations of either highly obscured or reflection-dominated systems (e.g., Gilli et al. 2007). Large population studies have now quantified the relative abundance of obscured and unobscured black-hole growth phases (e.g., Aird et al. 2015a; Buchner et al. 2015), and have established that a large fraction occurs during the most obscured "Compton-thick" ("CT" hereafter) phases, where the absorbing column density exceeds the inverse of the Thomson scattering cross-section ($N_{\mathrm{H}} \gtrsim 1.5 \times 10^{24}$ cm^{-2}). However, the intrinsic absorption distribution of AGNs has proven difficult to constrain, especially at the highly obscured to CT end, where AGNs are particularly challenging to identify.

Besides completing the census on black hole growth, identifying the most heavily obscured AGNs is crucial to our understanding of the environment of supermassive black hole accretion. The unified model of AGNs (e.g., Antonucci 1993; Urry & Padovani 1995), which largely succeeds at describing AGNs in the local universe, posits that unobscured, obscured, and CT systems have intrinsically similar physical structures but are simply viewed from different inclination angles. In tension with this model (at least in its simplest form) are some observational studies which suggest that some fraction of obscured AGNs represent a specific evolutionary phase in the growth of the black hole. Possible evidence for a higher frequency of host galaxy mergers for CT AGNs (e.g., Kocevski et al. 2015; Koss et al. 2016a) may point towards some of the highly obscured systems representing a distinct phase in an evolutionary sequence of galaxy-AGN co-evolution (e.g., Sanders et al. 1988; Hopkins et al. 2008), potentially associated with a period of rapid black hole growth (e.g., Draper & Ballantyne 2010; Treister et al. 2010a).

The challenge in answering these questions is that most wavelength regimes are subject to strong biases against detecting highly obscured AGNs, due to a combination of: (i)

line-of-sight extinction and (ii) dilution by light from other (e.g., stellar) processes. Powerful selection methods exist which are relatively unhindered by (i), such as mid-infrared (MIR) colour selection (e.g., Lacy et al. 2004; Stern et al. 2005, 2012; Mateos et al. 2012) and optical spectroscopic selection based on high ionization emission lines (e.g., Zakamska et al. 2003; Reyes et al. 2008). However, these techniques both suffer from (ii), especially at sub-quasar luminosities, and both still require X-ray followup of the AGNs to provide informative measurements of the line-of-sight absorbing column densities (e.g., Vignali et al. 2006, 2010; Jia et al. 2013; LaMassa et al. 2014). Hard (> 10 keV) X-ray observations, on the other hand, have the advantage of effectively zero dilution from other processes, and are relatively unaffected by line-of-sight obscuring material up to the CT levels of absorption.

All-sky surveys with non-focusing hard X-ray missions (e.g., *Swift* BAT and *INTEGRAL*) have been important for the identification of highly obscured AGNs in the very local universe ($z < 0.05$; e.g., Burlon et al. 2011; Vasudevan et al. 2013; Ricci et al. 2015; Koss et al. 2016a). Now, with the first focusing hard X-ray mission (*NuSTAR*; Harrison et al. 2013) it is possible to study source populations that are approximately two orders of magnitude fainter, thus extending to lower luminosities and higher redshifts. The largest extragalactic survey being undertaken with *NuSTAR* is the serendipitous survey (the 40-month catalogue is presented in Chapter 5; Lansbury et al. submitted), which has covered ≈ 13 deg^2 and detected ≈ 500 sources, 276 of which have spectroscopic redshifts. The areal coverage and sample size are large compared to the dedicated *NuSTAR* extragalactic surveys (e.g., ECDFS and COSMOS; Mullaney et al. 2015; Civano et al. 2015), making the serendipitous survey well suited to the discovery of rare populations such as CT AGNs.

In this chapter, we search for the most highly obscured AGNs in the *NuSTAR* serendipitous survey sample. Firstly, we select the objects with the highest *NuSTAR* band ratios, implying very hard spectral slopes and hence the likely presence of absorption. Although band ratios only give a crude estimate of the amount of absorption, they are nevertheless an effective way to isolate the most extreme outliers. Secondly, we perform a detailed analysis of the X-ray and multiwavelength properties of these extreme objects, and discuss how their properties compare to the general AGN population. The chapter is struc-

tured as follows. Section 6.2 describes the selection of the 10 extreme objects from the
NuSTAR serendipitous survey sample. Section 6.3 details the data used and the X-ray
counterparts. In Section 6.4 we characterise the X-ray spectra of the sources (Section
6.4.1), and present the results for the X-ray spectral properties (Section 6.4.2). In Section
6.5 we investigate potential independent estimates of the source obscuration properties
through indirect techniques. Section 6.6 presents the optical properties of the sample,
including a summary of the optical spectral properties (Section 6.6.1) and host galaxy
imaging, with a focus on the frequency of galaxy mergers (Section 6.6.2). In Section 6.7
we discuss the likely CT AGNs and their implications for the prevalence of CT absorption
within the broader hard X-ray selected AGN population (Section 6.7). Finally, our main
results are summarized in Section 6.8.

All uncertainties and limits are quoted at the 90% confidence level, unless otherwise
stated. We assume the flat ΛCDM cosmology from WMAP7 throughout (Komatsu et al.,
2011).

6.2 Selection of Candidate Heavily Obscured AGNs from the *NuSTAR* Serendipitous Survey

To select sources with very hard X-ray spectra compared to the rest of the *NuSTAR*
serendipitous survey sample, we apply a cut in *NuSTAR* band ratio of $\mathrm{BR_{Nu}} > 1.7$
(see Figure 6.1). This cut is motivated by the $\mathrm{BR_{Nu}}$ values observed for CT AGNs
in other *NuSTAR* programs (e.g., Baloković et al. 2014; Gandhi et al. 2014; Civano
et al. 2015; Lansbury et al. 2015). We also limit the sample to sources with spectro-
scopic redshift measurements. Figure 6.1 shows $\mathrm{BR_{Nu}}$ versus redshift for the *NuSTAR*
serendipitous survey sample, excluding two sources with erroneously high band ratios:
NuSTARJ224225+2942.0, for which the photometry is affected by contamination from a
nearby bright target; and NuSTARJ172805-1420.9, for which the photometry is unreli-
able due to a high surface density of X-ray sources, with multiple *Chandra* sources likely
contributing to a blended *NuSTAR* detection (as determined using *Chandra* data obtained
through our followup program; PI J. A. Tomsick).

Overall, 11 sources have band ratios exceeding the selection threshold (all individ-
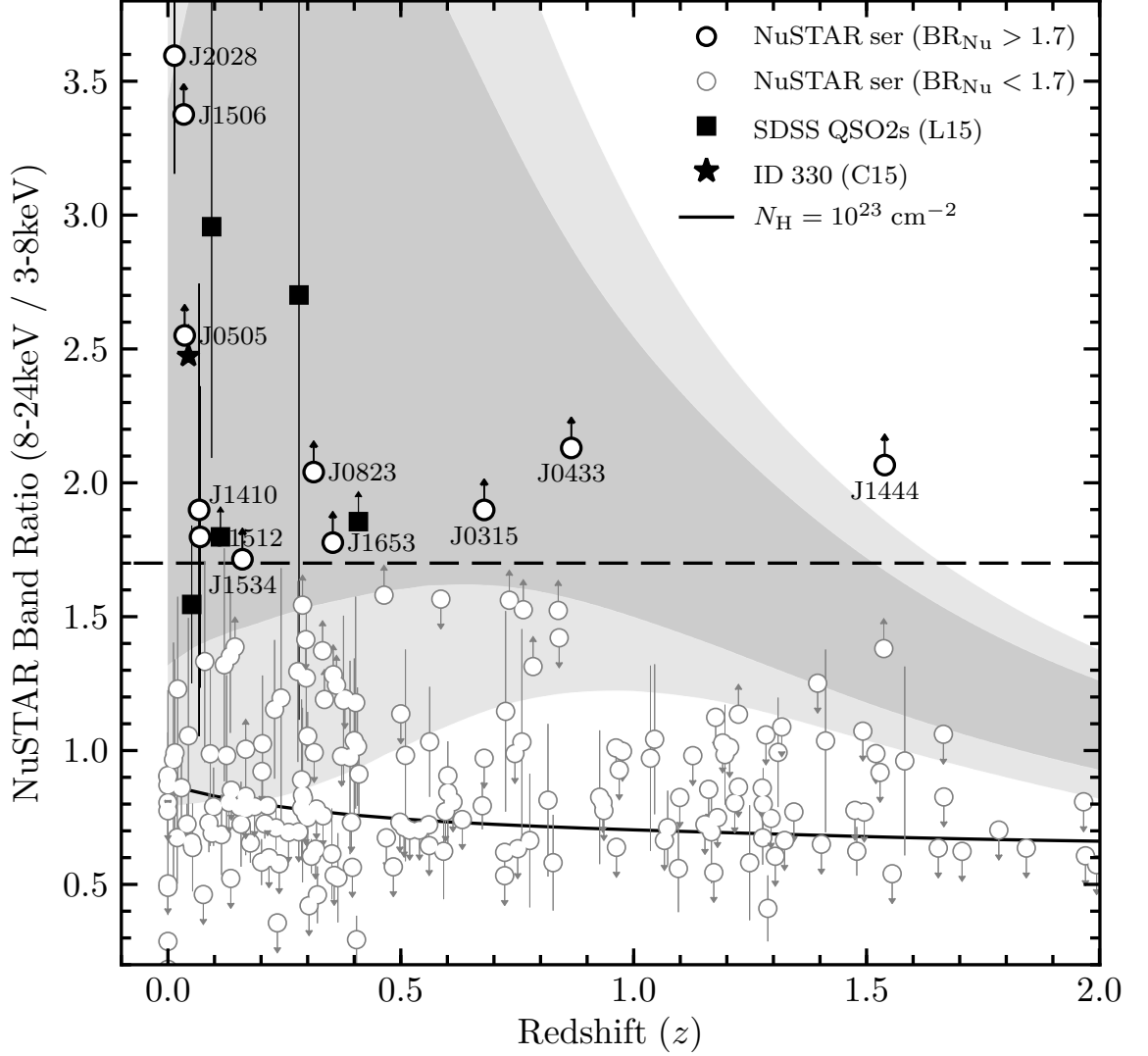
Figure 6.1: *NuSTAR* band ratio ($\mathrm{BR_{Nu}}$) as a function of redshift (z) for the extremely hard ($\mathrm{BR_{Nu}} > 1.7$) *NuSTAR* serendipitous survey AGNs (thick black open circles, individually labelled). "Normal" serendipitous survey sources at $\mathrm{BR_{Nu}} < 1.7$ are shown as thin gray circles. We compare to another extreme sample of optically (SDSS-) selected highly obscured Type 2 quasars observed with *NuSTAR* (black squares; Chapters 3–4; Lansbury et al. 2014; Gandhi et al. 2014; Lansbury et al. 2015), and to ID 330, the CT AGN identified in the *NuSTAR*-COSMOS survey (black star; Civano et al. 2015). Additionally we compare to the expected band ratios for CT AGNs based on the high quality X-ray spectral modelling of very local CT AGNs in the *NuSTAR* snapshot survey (68% percentiles in darker gray; 90% percentiles in lighter gray; Baloković et al. 2014; Baloković et al. 2016, in prep.).

ually labelled in Figure 6.1). Of these, three are flagged in the serendipitous survey catalogue as being narrowly offset in velocity (cz) from the science targets of their respective *NuSTAR* fields, and thus may be associated: NuSTAR J050559-2349.9 [hereafter J0505; $z = 0.036$; $\Delta(cz) \approx 0.03cz_{\text{target}}$], NuSTAR J151253-8124.3 [hereafter J1512; $z = 0.069$; $\Delta(cz) \approx 0.01cz_{\text{target}}$], and NuSTAR J202828+2543.4 [hereafter J2028; $z = 0.01447$; $\Delta(cz) \approx 0.04cz_{\text{target}}$]. We exclude J2028 (hosted by NGC 6921) from this work since it is unambiguously associated with the science target of the *NuSTAR* field (IGRJ20286+2544; projected separation of 26 kpc), and since the extreme obscuration properties of this system are the focus of a detailed study in Koss et al. (2016b). We include the other two sources (J0505 and J1512) in this work, since they represent *NuSTAR* discoveries, but exclude them when performing population analyses such as the measurement of the Compton-thick fraction (Section 6.7). There are thus 10 extreme *NuSTAR* sources in total which we incorporate into the analyses and discussion presented herein (listed in Table 6.1).

6.3 X-ray data and counterparts

Table 6.2 provides details of the *NuSTAR* and soft X-ray (i.e., *Chandra*, *Swift* XRT, and *XMM-Newton*) data sets adopted for this work. For each source we adopt the soft X-ray observatory which provides the most sensitive coverage at < 10 keV. In six cases we use the combined data set from multiple individual observations (as detailed in Table 6.2) to obtain the most precise X-ray constraints possible. The soft X-ray counterparts improve the X-ray positional accuracy and allow for accurate spectral constraints using the broadest energy band possible. Of the 10 very hard *NuSTAR* sources studied here, two lack soft X-ray counterparts (J1506 and J1410). In these cases there is no *Chandra* or *XMM-Newton* coverage, and the sources are undetected in the combined archival *Swift* XRT coverage (running `wavdetect` with a detection threshold of 10^{-4}). The other eight very hard *NuSTAR* sources have identified soft X-ray counterparts. For seven of these (J0505, J1512, J0823, J1653, J0315, J0433, and J1444) the soft X-ray counterparts are identified in Chapter 5. In Section 6.9 we give additional evidence to support the correct soft X-ray counterpart identifications for J0505 and J0433. For the remaining source (J1534), the

Table 6.1: The 10 extremely hard *NuSTAR* serendipitous survey sources

Object	R.A.	Decl.	z	$\mathrm{BR_{Nu}}$	Det.
(1)	(2)	(3)	(4)	(5)	(6)
NuSTARJ150645+0346.2	226.69040	3.77118	0.034	> 3.4	F H
NuSTARJ050559-2349.9	76.49839	-23.83169	0.036	> 2.6	F H
NuSTARJ141056-4230.0	212.73727	-42.50139	0.067	1.9	F S H
NuSTARJ151253-8124.3	228.22497	-81.40501	0.069	1.8	F S H
NuSTARJ153445+2331.5	233.68763	23.52593	0.160	> 1.7	H
NuSTARJ082303-0502.7	125.76385	-5.04650	0.313	> 2.0	F H
NuSTARJ165346+3953.7	253.44313	39.89639	0.354	> 1.8	H
NuSTARJ031548-0218.9	48.95153	-2.31640	0.679	> 1.9	F H
NuSTARJ043326+0517.1	68.35899	5.28514	0.866	> 2.1	F H
NuSTARJ144406+2506.3	221.02820	25.10515	1.539	> 2.1	F H

Notes. The sources are listed in order of increasing redshift. The entries in this table are drawn from the *NuSTAR* serendipitous survey source catalogue (Chapter 5 of this thesis; Lansbury et al. 2016, submitted). (1): *NuSTAR* source name. (2) and (3): Right ascension and declination J2000 coordinates in decimal degrees. (4): Source spectroscopic redshift. (5): *NuSTAR* photometric band ratio. I.e., the ratio of the hard band to soft band count rates. (6): The *NuSTAR* energy bands for which the source is independently detected. F, S, and H correspond to the full (3–24 keV), soft (3–8 keV), and hard (8–24 keV) bands, respectively.

Table 6.2: Summary of the X-ray data adopted for the spectroscopic and photometric X-ray analyses

	NuSTAR Observations						Soft X-ray Observations				
Object	Observation ID	UT Date	t	S_{net}	B	Observatory	Observation ID	UT Date	t	S_{net}	B
(1)	(2)	(3)	(4)	(5)	(6)	(7)	(8)	(9)	(10)	(11)	(12)
J1506	60061261002	2014-09-08	21.3	81	122	Swift XRT	00036622001	2007-12-19	9.4	...	...
							00036622002	2007-12-21	8.7	...	...
							00080144001	2014-09-08	6.1	...	...
J0505	60061056002	2013-08-21	21.1	66	53	XMM-Newton	0605090101^c	2009-08-06	29.4	70	46
J1410	60160571002	2015-05-14	22.2	153	125	Swift XRT	00040973002	2010-09-27	5.0	...	...
							00040973003	2011-03-10	5.0	...	...
							00081157002	2015-04-30	5.8	...	...
							00081157003	2015-05-14	5.6	...	...

Notes. Table continued on the next page. (1): The abbreviated NuSTAR source name. (2) and (3): The NuSTAR observation ID and start date (YYYY-MM-DD). (4), (5), and (6): The net exposure time (ks), net source counts, and scaled background counts, respectively, for the extracted 3–24 keV (or 8–24 keV for J1534 and J1653) NuSTAR spectrum. (7): The soft X-ray observatory with the best (or in some cases, the only) coverage, which we adopt for the analyses. (8) and (9): the adopted soft X-ray observation ID(s) and their corresponding start date(s) (YYYY-MM-DD), respectively. (10), (11), and (12): The exposure time (ks), net source counts, and scaled background counts, respectively. For J0505, J1512, J1653, J0315, and J1444, the soft X-ray spectrum has sufficient quality to be included in the X-ray spectral analysis, and these columns thus correspond to the extracted spectrum (0.5–10 keV and 0.6–10 keV for XMM-Newton and Swift XRT, respectively). The remaining five sources (J1506, J1410, J1534, J0823, and J0433) are non-detections or weak detections in the soft X-ray coverage, and the soft X-ray information tabulated here is thus used for source detection and obtaining photometric constraints (see Section 6.3). ^{a}: In these cases we limit the NuSTAR spectral analysis to the 8–24 keV band, since the sources are undetected in the soft (3–8 keV) and full (3–24 keV) NuSTAR bands, indicating no significant source emission at < 8 keV. ^{b}: Here we use the NuSTAR FPMB data only (i.e., excluding the FPMA data). ^{c}: In these cases we use the combined MOS1+MOS2 data only. ^{d}: Here we use the MOS2 data only.

Table 6.3: Continued: Summary of the X-ray data adopted for the spectroscopic and photometric X-ray analyses

	NuSTAR Observations					Soft X-ray Observations					
Object	Observation ID	UT Date	t	S_net	B	Observatory	Observation ID	UT Date	t	S_net	B
(1)	(2)	(3)	(4)	(5)	(6)	(7)	(8)	(9)	(10)	(11)	(12)
J1512	60061263002	2013-08-06	13.3	153	74	*Swift* XRT	00036623001	2007-06-07	6.2	11	...
							00036623002	2007-06-09	5.3	7	...
							00080146001	2013-08-06	6.8	11	...
J1534	60002026002[a]	2013-08-13	66.7	42	133	*Chandra*	16092	2014-04-30	171.5	...	...
J0823	60061080002[b]	2014-01-10	24.3	41	67	*XMM-Newton*	0501210501	2007-10-14	11.9	...	...
J1653	60002024002[a]	2013-04-13	18.3	14	16	*XMM-Newton*	0652570101[c]	2010-09-08	43.7	73	47
							0652570201[c]	2010-09-10	44.0	82	42
J0315	60101048002	2015-07-19	51.4	55	118	*XMM-Newton*	0693520101[d]	2012-07-23	117.8	263	47

Notes. Table continued on next page.

Table 6.4: Continued: Summary of the X-ray data adopted for the spectroscopic and photometric X-ray analyses

	NuSTAR Observations					Soft X-ray Observations					
Object	Observation ID	UT Date	t	S_{net}	B	Observatory	Observation ID	UT Date	t	S_{net}	B
(1)	(2)	(3)	(4)	(5)	(6)	(7)	(8)	(9)	(10)	(11)	(12)
J0433	60001042003	2013-02-06	127.7	118	404	Swift XRT	00036369001	2007-03-28	6.4	…	…
							00036369002	2007-07-30	4.3	…	…
							00036369003	2008-08-10	20.1	…	…
							00037594001	2008-07-18	6.2	…	…
							00037594002	2010-02-25	1.5	…	…
							00037594003	2010-02-25	2.3	…	…
							00080334001	2013-02-06	1.9	…	…
							00091444001	2012-04-02	2.0	…	…
							00091444002	2012-04-06	2.1	…	…
							00091444003	2012-04-10	2.4	…	…
							00091444004	2012-12-15	2.2	…	…
							00091444005	2012-12-20	2.0	…	…
							00091444006	2012-12-30	2.5	…	…
							00091444007	2013-01-04	2.0	…	…
							00091444008	2013-01-09	2.1	…	…
							00091444009	2013-01-14	1.9	…	…
							00091444010	2013-01-19	2.4	…	…
							00091444012	2013-01-29	1.8	…	…
							00091444013	2013-02-03	2.4	…	…
							00091444014	2013-02-08	1.9	…	…
							00091444015	2013-02-13	2.0	…	…
							00091444016	2013-02-16	2.0	…	…
							00091444017	2013-02-23	2.0	…	…
							00091444018	2013-02-28	2.3	…	…
							00091444019	2013-03-05	2.5	…	…
							00091444020	2013-03-10	2.0	…	…
							00091444021	2013-03-15	1.9	…	…
							00091444022	2013-03-20	2.5	…	…
							00091444023	2013-03-25	1.8	…	…
							00092352002	2016-04-07	0.1	…	…

Notes. Table continued on next page.

Table 6.5: Continued: Summary of the X-ray data adopted for the spectroscopic and photometric X-ray analyses

Object	*NuSTAR* Observations						Soft X-ray Observations					
	Observation ID	UT Date	t	S_{net}	B	Observatory	Observation ID	UT Date	t	S_{net}	B
(1)	(2)	(3)	(4)	(5)	(6)	(7)	(8)	(9)	(10)	(11)	(12)
J1444	90101004002	2015-04-25	38.2	62	153	*Swift* XRT	00033768001	2015-05-13	3.1	⋯	⋯
							00033768002	2015-05-18	3.0	⋯	⋯
							00033768003	2015-06-01	4.1	⋯	⋯
							00033768004	2015-09-04	4.0	⋯	⋯
							00033768005	2016-04-13	4.0	⋯	⋯
							00033768006	2016-04-17	1.4	⋯	⋯
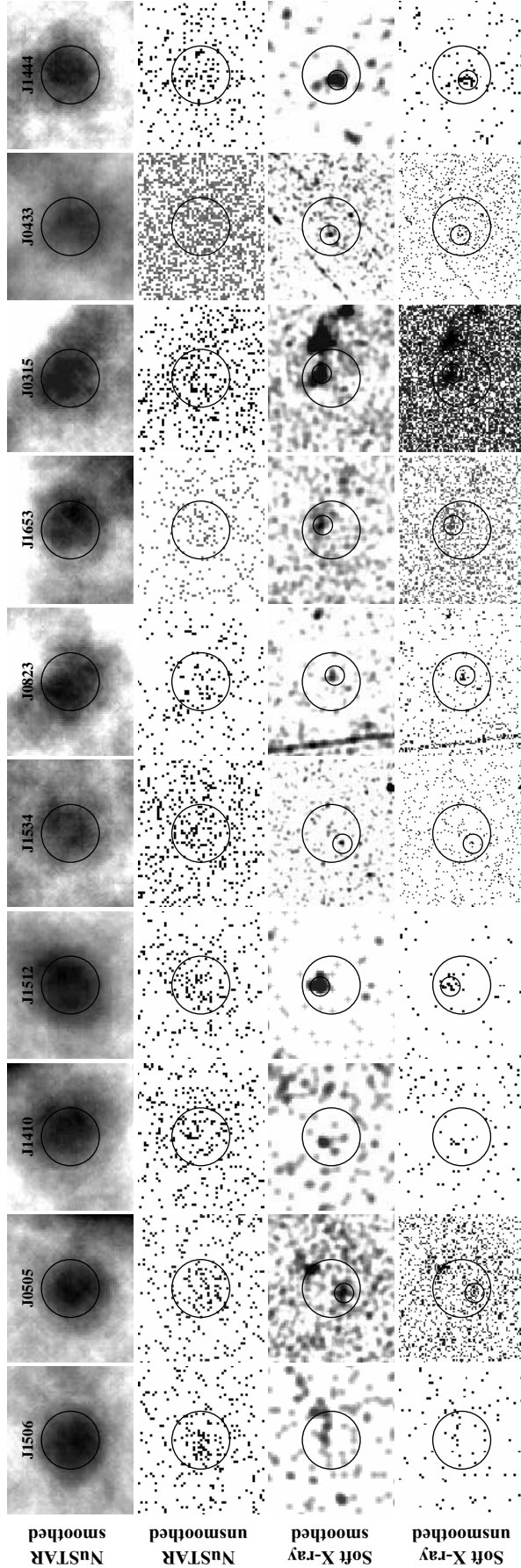
Figure 6.2: X-ray images for the 10 extreme *NuSTAR* serendipitous survey sources. Each column corresponds to an individual *NuSTAR* source (the abbreviated source names are shown). The columns are ordered by source redshift, increasing from left to right. 30″ circular apertures are shown for each source, centred on the *NuSTAR* position. Upper two rows: *NuSTAR* hard (8–24 keV) band images, both smoothed (with a top hat function of radius 14 pixels; first row) and unsmoothed (second row). Lower two rows: soft X-ray images from *Chandra* (the 0.5–2 and 0.5–7 keV bands are shown for J1534 and J0433, respectively), *XMM-Newton* (the full energy band is shown for J0505, J0823, J1653, and J0315), and *Swift* XRT (the full energy band is shown for J1506, J1410, J1512, and J1444). The data are shown both smoothed (with a gaussian function of radius 3 pixels; third row) and unsmoothed (fourth row). The soft X-ray counterpart positions are marked by smaller (10″ radius) circular apertures, for all of the sources except J1506 and J1410 (which are undetected in the available *Swift* XRT coverage; see Section 6.4).

counterpart is faint and did not satisfy the detection criteria in Chapter 5. Below we detail the identification of this specific counterpart.

For J1534, the deepest soft X-ray coverage is from a 170 ks *Chandra* observation (obsID 16092). Running `wavdetect` for the broad *Chandra* energy band of 0.5–7 keV there are no sources detected with false-probabilities (i.e., `sigthresh` values) of $P_{\text{False}} \leq 10^{-4}$ within the *NuSTAR* error circle. However, running the source detection for multiple energy bands, there is one significant detection for the 0.5–2 keV energy band, with $P_{\text{False}} \approx 10^{-6}$. Adding further confidence to this counterpart, SDSS coverage reveals a prominent $z = 0.160$ galaxy within the *NuSTAR* error circle (SDSS J153445.80+233121.2), which agrees closely with the *Chandra* position ($0.6''$ offset). For an independent assessment of the source significance in the *Chandra* data, we perform aperture photometry ($2''$ source radius; large background annulus) at the SDSS position. For the 0.5–2 keV band, the source is indeed detected at the 4.0σ level (according to the binomial false probability). The source is not significantly detected with *Chandra* above 2 keV, implying a steep spectral slope of $\Gamma_{\text{eff}} \approx 3$–$4$, uncharacteristic of AGN emission, and more likely resulting from other processes in the host galaxy.

6.4 X-ray properties

6.4.1 X-ray spectral modelling

We perform X-ray spectral modelling using XSPEC (version 12.8.1j; Arnaud 1996), with the `statistic cstat` setting. This applies the W statistic (Wachter et al., 1979) for modelling, which is more appropriate than χ^2 in the low-counts regime (e.g., Nousek & Shue, 1989). We group the data from *NuSTAR* and from other X-ray missions by a minimum of 3 counts and 1 count per bin, respectively. In all cases, we fit a simple unabsorbed power law model in order to constrain the effective photon index (Γ_{eff}), and thus obtain a basic measure of the overall X-ray spectral slope. Figure 6.3 shows the *NuSTAR* plus soft X-ray (*Chandra*, *Swift* XRT, or *XMM-Newton*) spectra for the 10 extreme *NuSTAR* serendipitous survey sources, with power law model fits to each. Flat Γ_{eff} values (e.g., $\lesssim 0.5$) give empirical evidence for heavy or CT absorption. Further empirical evidence for CT absorption can be obtained from the detection of a strong fluorescent Fe Kα emis-
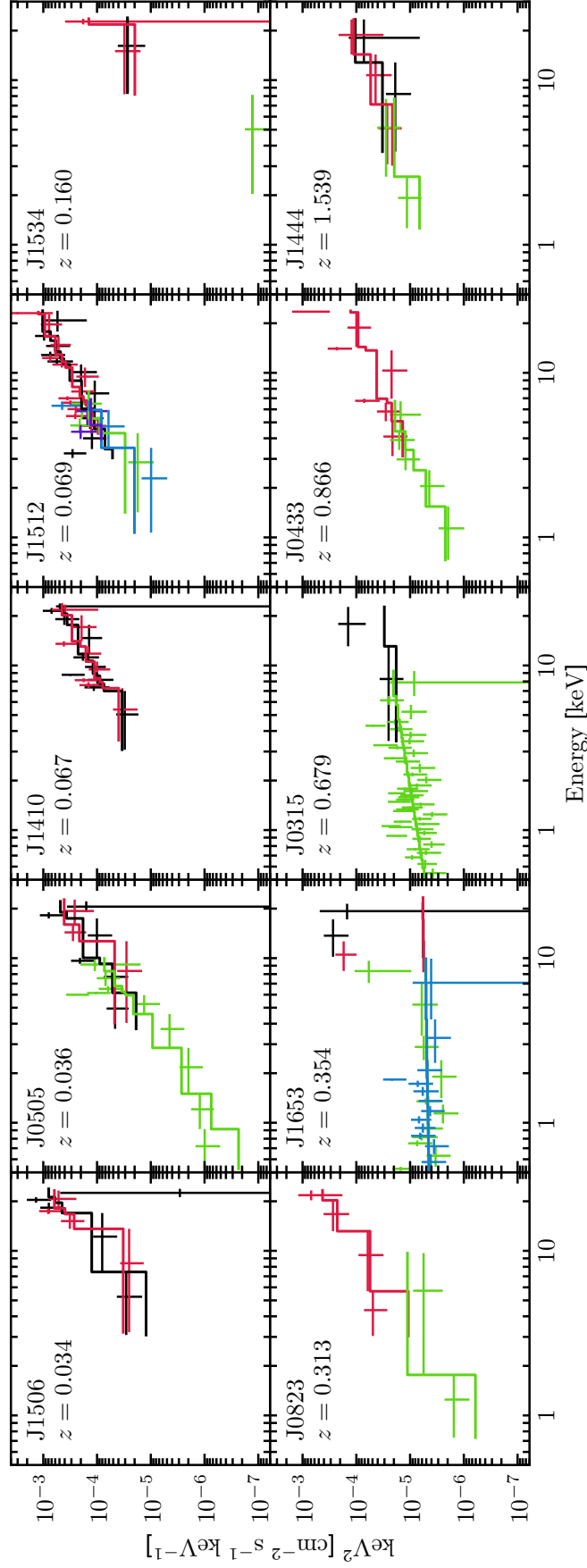
Figure 6.3: X-ray spectra, in EF_E units, for the 10 very hard *NuSTAR* sources (Section 6.4). Black and red correspond to FPMA and FPMB. The green, blue and purple spectra are from the available *Chandra*, *Swift* XRT and *XMM-Newton* data. The data are binned to a mimimum significance of 2σ per bin for visual purposes. Best-fit power law models are shown, binned to match the data (solid lines). The power law photon index constraints are provided in Table 6.6.

sion line at ≈ 6.4 keV (with an equivalent width of $\mathrm{EW_{Fe\ K\alpha}} > 1$ keV, although lower values do not necessarily rule out CT absorption; e.g., Della Ceca et al. 2008; Gandhi et al. 2016). This reflection feature becomes more prominent with increasing levels of absorption (e.g., Risaliti, 2002). To place constraints on $\mathrm{EW_{Fe\ K\alpha}}$ for our sources, we model the continuum over the rest-frame ≈ 4–9 keV energy range as a power law, and add an additional redshifted gaussian component at $E = 6.4$ keV (we unfix this energy centroid parameter for the two cases with well-detected lines). For the majority of sources, the emission line is not significantly detected, and we can therefore only place high upper limits on $\mathrm{EW_{Fe\ K\alpha}}$. In Table 6.6 we provide the basic observed X-ray spectral properties for the sample: effective photon indices, Fe Kα line equivalent widths, and observed (i.e., uncorrected for absorption) luminosities in the rest-frame 2–10 keV and 10–40 keV bands.

Where the photon statistics permit, we test three more spectral models in order to constrain source properties such as the intrinsic absorbing column density (N_{H}), the intrinsic photon index (Γ), and the X-ray luminosity. Firstly, we fit a transmission-only model (the `transmission` model, hereafter): a power law attenuated by redshifted photoelectric absorption and Compton scattering of photons out of the line of sight (`CABS · ZWABS · POW`, in XSPEC formalism). This model represents one extreme of obscured AGN spectra, where the X-ray spectrum is dominated by the primary AGN continuum transmitted directly along the line of sight. Secondly, we fit a reflection-only model (the `reflection` model, hereafter), which represents a power law spectrum reflected by circumnuclear material. For this we use the `PEXRAV` model (Magdziarz & Zdziarski, 1995) with the reflection scaling factor set to -1 to yield a pure reflection spectrum, and with the other parameters set to default values. This model represents the other extreme of obscured AGN spectra, where the X-ray spectrum is dominated by the reflected AGN continuum, which (in combination with strong Fe line emission) implies very high column densities ($N_{\mathrm{H}} \gg 10^{24}$ cm^{-2}). At high column densities, X-ray spectra are typically more complex than the `transmission` and `reflection` models above, and ideally any absorbed continuum, reflected continuum, and fluorescent line emission should be modelled in a self-consistent way and assuming a well-motivated geometry. We therefore perform an additional third test using the BNTORUS model (the `torus` model, hereafter; Brightman & Nandra 2011), which

Table 6.6: Basic X-ray spectral parameters

Object	$\Gamma_{\mathrm{eff}}^{\mathrm{NuSTAR}}$	$\Gamma_{\mathrm{eff}}^{\mathrm{soft}}$	$\mathrm{EW}_{\mathrm{FeK}\alpha}$	L_{2-10}^{obs}	L_{10-40}^{obs}
(1)	(2)	(3)	(4)	(5)	(6)
J1506	$-0.7^{+0.9}_{-1.6}$	$\cdots$	< 3.4	39.9	42.6
J0505	$-0.1^{+0.7}_{-0.8}$	$-0.9^{+0.8}_{-1.4}$	$1.4^{+1.4}_{-0.9}$	41.3	42.3
J1410	0.3 ± 0.4	$\cdots$	< 1.6	42.0	42.7
J1512	$0.9^{+0.4}_{-0.5}$	$-0.6^{+0.7}_{-0.9}$	$0.76^{+1.04}_{-0.56}$	42.4	43.2
J1534	$< -0.9^{\,\dagger}$	$3.3^{+5.9}_{-2.4}$	$\cdots$	39.8	42.7
J0823	$0.3^{+1.1}_{-1.3}$	$1.2^{+1.2}_{-0.9}$	$\cdots$	42.5	44.4
J1653	$-0.5^{+0.9\,\dagger}_{-0.6}$	2.0 ± 0.3	$\cdots$	42.7	44.3
J0315	$1.5^{+1.4\,\dagger}_{-0.9}$	1.5 ± 0.2	$\cdots$	43.8	44.7
J0433	$0.7^{+1.0}_{-1.1}$	0.7 ± 0.7	$\cdots$	43.9	44.6
J1444	$-0.3^{+0.9}_{-1.2}$	0.7 ± 1.1	$\cdots$	44.7	45.1

Notes. (1): Abbreviated *NuSTAR* source name. (2): The *NuSTAR* effective photon index; i.e., the photon index obtained from approximating the *NuSTAR* 3–24 keV spectrum as a simple power law. For the sources marked †, the constraint was obtained using a combination of *NuSTAR* and soft X-ray (*XMM-Newton* or *Swift* XRT) data, due to weak *NuSTAR*-only constraints. (3): The "soft" effective photon index, measured using the available soft X-ray spectra from *Chandra*, *Swift* XRT, or *XMM-Newton* (over the full energy range for the relevant observatory; ≈ 0.5–10 keV). (4): Constraint on the Fe Kα line equivalent width ($\mathrm{EW}_{\mathrm{FeK}\alpha}$). Units: keV. (5) and (6): Logarithm of the observed (i.e., uncorrected for absorption) X-ray luminosities in the rest-frame 2–10 keV and 10–40 keV bands, respectively. Units: $\mathrm{erg\ s^{-1}}$.

was produced using simulations of X-ray radiative transfer through a toroidal distribution of gas. We set the model to an edge-on torus configuration (with $\theta_{\text{inclination}}$ and θ_{torus} set to $87°$ and $60°$, respectively). In this form, the `torus` model has the same number of free parameters as the `transmission` and `reflection` models, and is therefore no less suited to the statistical quality of the data. For every model fit, we account for Galactic absorption with a `PHABS` multiplicative component, fixed to column density values from Kalberla et al. (2005). In Table 6.7 we show the best-fit parameters obtained by applying the three models described above: intrinsic photon indices, column densities, fit statistics, and intrinsic (i.e., absorption-corrected) luminosities.

In one case (J1653) we find that an additional soft model component is necessary to obtain an acceptable fit to the data. For J1653 all three models provide a poor fit to the *XMM-Newton* plus *NuSTAR* spectrum ($C/n = 352/200$, $311/202$, and $335/201$ for the `transmission`, `reflection`, and `torus` models, respectively) and leave strong positive residuals at high energies ($\gtrsim 8$ keV). This is due to an apparently sudden change in the spectral shape, with the low energies ($\lesssim 4$ keV) dominated by a steep ($\Gamma \approx 2$) component and the higher energies ($\gtrsim 4$ keV) dominated by a flatter component ($\Gamma \approx -0.5$). One reasonable way to interpret this is a scattered AGN power law at lower energies, and a primary AGN continuum coming through at higher energies. The relatively high luminosity ($L_{0.5-4 \text{ keV}} \approx 7 \times 10^{42}$ erg s^{-1}) justifies the scattered AGN power law interpretation rather than, e.g., thermal emission associated with star formation. For J1653 we therefore add an unobscured power law component to the three spectral models, with the spectral slope tied to that of the intrinsic AGN power law continuum. This results in statistically improved fits (see Table X), and reasonable scattered power law fraction constraints ($f_{\text{scatt}} \approx 0.04$–5%). The source J1534 also shows evidence for a steep soft component at $\lesssim 2$ keV in the *Chandra* spectrum (see Section 6.3). In this case, there are two few counts to model the soft component, so we simply exclude the < 2 keV photons when applying the `transmission`, `reflection`, and `torus` models.

For the sources where we model the *NuSTAR* data simultaneously with soft X-ray (*Chandra*, *Swift* XRT, or *XMM-Newton*) data, there is a general caveat that the soft X-ray observations are not contemporaneous with the *NuSTAR* data, and AGN variability could thus affect the interpretations (although observed variability is generally less likely

Table 6.7: Best-fit parameters for the X-ray spectral modelling

| Object (1) | E range (2) | transmission | | | reflection | | torus | | | $L^{\rm int}_{2-10}$ (11) | $L^{\rm int}_{10-40}$ (12) |
		Γ (3)	$N_{\rm H}$ (4)	C/n (5)	Γ (6)	C/n (7)	Γ (8)	$N_{\rm H}$ (9)	C/n (10)		
J1506	3–24	[1.9]	$5.0^{+3.6}_{-3.7}$	82/64	[1.9]	79/65	$1.5^{+1.2}_{-\rm u}$	$4.1^{+\rm u}_{-2.3}$	70/63	$\cdots$	43.3
J0505	0.5–24	[1.9]	$0.87^{+0.37}_{-0.27}$	159/139	1.3 ± 0.4	148/139	$2.5^{+0.4}_{-0.8}$	$1.5^{+4.7}_{-0.5}$	148/142	43.1	42.7
J1410	3–24	[1.9]	$0.74^{+0.31}_{-0.25}$	78/87	1.8 ± 0.4	82/87	[1.9]	$0.63^{+0.31}_{-0.24}$ *	80/87	$\cdots$	43.1
J1512	0.6–24	[1.9]	$0.13^{+0.22}_{-0.06}$	142/98	$2.1^{+0.2}_{-0.3}$	112/98	$2.8^{+\rm u}_{-0.8}$ **	$2.9^{+\rm u}_{-1.2}$	112/97	44.6	44.0
J1534	2–24	[1.9]	$2.4^{+\rm u}_{-1.1}$	66/62	[1.9]	73/63	[1.9]	$1.6^{+\rm u}_{-1.2}$	69/62	43.8	43.8
J0823†	0.5–24	[1.9]	$0.73^{+1.51}_{-0.61}$	45/33††	$2.6^{+1.0}_{-0.7}$	71/53	[1.9]	$12.6^{+\rm u}_{-12.0}$	41/33††	44.4	44.4
J1653	0.5–24	$2.3^{+0.5}_{-0.4}$	$2.4^{+1.3}_{-0.9}$	165/192	$2.4^{+0.8}_{-0.5}$	179/193	$2.3^{+0.6}_{-0.5}$	$1.6^{+1.5}_{-1.1}$	175/192	45.4	45.2
J0315	0.5–24	$1.7^{+0.4}_{-0.3}$	<0.005	189/192	[1.9]	484/194	1.8 ± 0.3	<0.003	190/192	43.8	44.0
J0433	0.6–24	[1.9]	$0.11^{+0.13}_{-0.07}$	114/112	[1.9]	110/113	[1.9]	$0.09^{+0.16}_{-0.06}$ *	113/112	44.3	44.3
J1444	0.6–24	[1.9]	$0.21^{+0.28}_{-0.17}$	104/75	$2.1^{+0.7}_{-0.6}$	102/75	[1.9]	$0.21^{+0.28}_{-0.17}$ *	103/75	45.1	45.1

Notes. (1): Abbreviated *NuSTAR* source name. (2): Energy range modelled. (3)–(10): Best-fit results for the transmission, reflection, and torus models, respectively. These include the intrinsic photon index (Γ), the column density ($N_{\rm H}$; units of 10^{24} cm^{-2}), and the fit statistic (C/n, where C is the C-statistic and n is the number of degrees of freedom). (11) and (12): Logarithm of the intrinsic (i.e., absorption-corrected) X-ray luminosities in the rest-frame 2–10 keV and 10–40 keV bands, respectively. Units: erg s^{-1}. *For three sources (J1410, J0433, and J1444) we show the conservative low-$N_{\rm H}$ torus model solution in this Table, but in each case there is also a second similarly valid solution at very high column densities (for J1410, $N_{\rm H} > 6\times10^{24}$ cm^{-2} and $C/n = 92/87$; for J0433, $N_{\rm H} > 7\times10^{24}$ cm^{-2} and $C/n = 110/112$; and for J1444, $N_{\rm H} > 6 \times 10^{24}$ cm^{-2} and $C/n = 102/75$). †As mentioned in Section 6.4.1, the *XMM-Newton:NuSTAR* cross-normalisation constant is left free in even higher-$N_{\rm H}$ solutions (e.g., a lower limit of $N_{\rm H} > 8.0 \times 10^{24}$ cm^{-2} for $\Gamma = 1.9$). **For J1512, fixing Γ to more typical values results in this case, and has a best-fit value of $0.12^{+0.19}_{-0.08}$ for the reflection model shown here. For J0823, the reflection model is the only basic model that does a reasonable job (i.e., low C/n) at simultaneously fitting the *XMM-Newton* plus *NuSTAR* spectrum, without the cross-normalization constant converging at extreme values (≈ 0.01). For this reason, we limit the transmission and torus model fits for J0823 to the *NuSTAR* data only (††).

to be significant in the case of heavy to CT absorption). While there is generally no evidence for significant variability (e.g., see Figure 6.3), the spectral uncertainties are generally too large to rule out low-level (e.g., factors of $\lesssim 2$) variability. We thus fix the cross-normalization constants to standard values: 1.0 for *Chandra*:*NuSTAR*; 1.0 for *Swift* XRT:*NuSTAR*; and 0.93 for *XMM-Newton*:*NuSTAR* (Madsen et al., 2015). There is one exception, J0823, where there is evidence for X-ray variability between the 2007 *XMM-Newton* observation and the 2014 *NuSTAR* observation (see the spectral energy range where *XMM-Newton* and *NuSTAR* overlap in Figure 6.3). The consequence for the spectral modelling is that the *XMM-Newton*:*NuSTAR* cross-normalisation parameter must be left free to obtain statistically acceptable solutions. We do not draw strong conclusions from the broad-band spectral modelling in this case.

For J0823, we limit the modelling to FPMB, since the source is only fully within the *NuSTAR* FoV for FPMB. For J0315, we limit to FPMA for the same reason. For J0433 we only fit the FPMB data, since the source is only weakly detected in FPMA; the spatial distribution of the background noise is different for the two FPMs of *NuSTAR*, meaning that a source can lie in a region of relatively high background for one FPM, and relatively low background for the other (e.g., Wik et al. 2014).

6.4.2 Results for the X-ray source properties

Here we summarize the measured X-ray properties. Figure 6.4 shows the effective photon indices (i.e., the observed spectral slopes) of the sources as a function of X-ray luminosity (uncorrected for absorption). The extreme *NuSTAR* sources cover a broad range in luminosity. The *NuSTAR*-measured effective photon indices (right panel of Figure 6.4) are generally very low (average value of $\Gamma_{\mathrm{eff}} \approx 0.2$ at 3–24 keV), giving empirical evidence for very high absorption levels. We compare with another sample of extreme systems: heavily obscured SDSS-selected Type 2 quasars targetted with *NuSTAR* (Chapters 3–4 of this thesis; Gandhi et al. 2014; Lansbury et al. 2014, 2015). The two extreme samples cover a similar range of spectral slopes, and lie at significantly harder values (i.e. lower Γ_{eff} values) than the general population of "normal" *NuSTAR* serendipitous survey sources (also shown in Figure 6.4, for sources with constrained Γ_{eff} values; Chapter 5 of this thesis; Lansbury et al. 2016, submitted). The spectral slopes measured at soft ener-
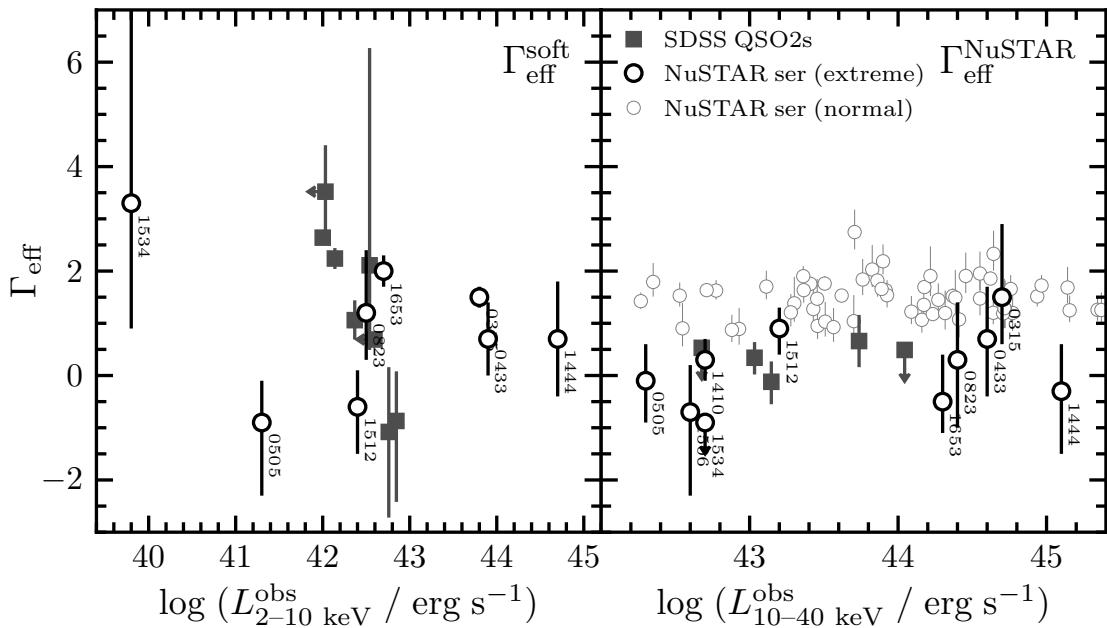
Figure 6.4: Observed X-ray properties: effective photon index (i.e., spectral slope) versus rest-frame X-ray luminosity (uncorrected for absorption). The left panel shows the properties measured at soft X-ray energies (with *Chandra*, *Swift* XRT, or *XMM-Newton*), and the right panel shows the properties measured at harder X-ray energies with *NuSTAR*. $\Gamma_{\text{eff}}^{\text{soft}}$ and $\Gamma_{\text{eff}}^{\text{NuSTAR}}$ are measured for the observed-frame ≈ 0.5–10 keV and 3–24 keV bands, respectively. We compare the extreme *NuSTAR* serendipitous survey sources (black circles, individually labelled) to "normal" serendipitous survey sources (smaller grey circles) and to highly obscured and CT Type 2 quasars which were optically selected and followed up with *NuSTAR* observations (filled gray squares; Chapters 3–4; Gandhi et al. 2014; Lansbury et al. 2014, 2015).
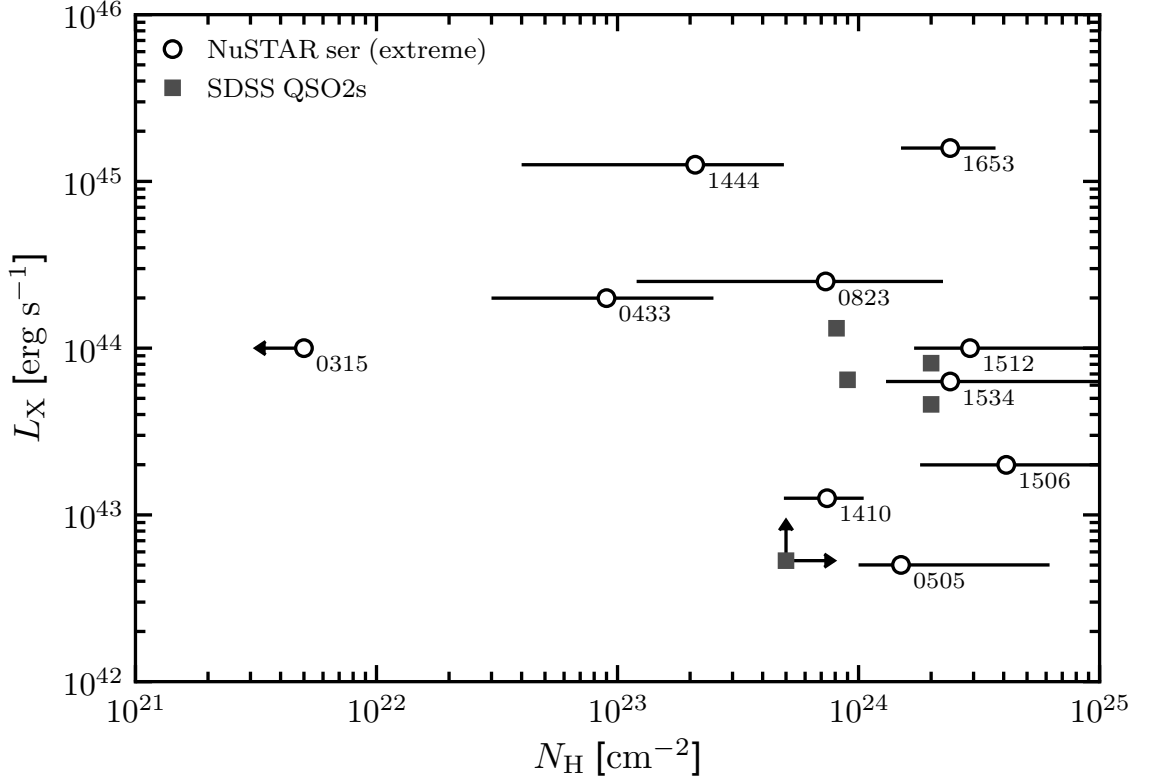
Figure 6.5: Rest-frame intrinsic (i.e., absorption-corrected) 10–40 keV X-ray luminosity (L_X) versus column density (N_H), from spectral fitting of the X-ray data (Section 6.4.1).

gies ($\approx$ 0.5–10 keV) are more strongly scattered, partly due to an increased contribution at these lower X-ray energies from radiative processes unrelated to the direct AGN emission (e.g., AGN emission scattered from distant warm gas), as was found to be the case for the *NuSTAR*-observed SDSS Type 2 quasars.

For the purposes of comparing N_H constraints and estimating intrinsic luminosities (L_X), for each source we adopt either the `transmission` or the `torus` solution, depending on which yields the lowest C/n (see Table 6.7). We adopt the `torus` solutions for J1506, J0505, J1512, J0433, and J1444, and the `transmission` solutions for J1410, J1534, J0823, J1653, and J0315. The adopted best-fitting N_H and L_X values are shown in Figure 6.5. Based on these intrinsic luminosity constraints, the more distant AGNs ($z > 0.2$) are at "X-ray quasar" luminosities ($L_X \gtrsim 10^{44}$ erg s^{-1}), and the less distant AGNs ($z < 0.2$) range from relatively low luminosities up to the quasar threshold ($L_X \approx 10^{42.7}$–10^{44} erg s^{-1}). The N_H constraints shown may be conservative for sources where the `reflection` model gives a valid fit to the X-ray spectrum (indicat-

ing consistency with $N_{\rm H} \gg 10^{24}$ cm^{-2}). For a similar reason, the Compton-thin constraints shown for J1410, J0433, and J1444 are possibly conservative since the `torus` modelling also finds valid reflection-dominated model solutions at very high column densities ($N_{\rm H} > 6 \times 10^{24}$ cm^{-2}) in these cases.

Considering all of the X-ray spectral constraints together, there are three sources with strong evidence for being CT AGNs (J1506, J0505, and J1512; the latter two objects have supporting evidence from high equivalent width Fe Kα emission, as shown in Table 6.6), two highly likely CT AGNs (J1534 and J1653), one highly obscured Compton thin AGN (J1410), one uncertain but likely highly obscured AGN (J0823), two likely moderately absorbed AGNs (J0433 and J1444), and one source consistent with being an unobscured AGN (J0315).

Prior to this work, one other AGN has been identified in the *NuSTAR* extragalactic surveys with strong evidence for CT absorption: ID 330 in the *NuSTAR*-COSMOS survey (Civano et al. 2015). Like the robust CT AGNs presented here (J1506, J0505, and J1512), ID 330 lies at low redshift ($z = 0.044$), and has a high *NuSTAR* band ratio (see Figure 6.1). Assuming a BNTORUS-based model to fit the X-ray spectrum, the column density of ID 330 is $N_{\rm H} = (1.2^{+0.3}_{-0.1}) \times 10^{24}$ cm^{-2} (Civano et al. 2015), similar to J0505 and slightly lower than J1506 and J1512.

6.5   Indirect Absorption Diagnostics

The intrinsic X-ray luminosities and the MIR luminosities of AGNs are tightly correlated (e.g., Lutz et al., 2004; Fiore et al., 2009; Gandhi et al., 2009; Lanzuisi et al., 2009; Ichikawa et al., 2012; Matsuta et al., 2012; Asmus et al., 2015; Mateos et al., 2015; Stern, 2015). The observed X-ray to MIR luminosity ratio of a source can therefore give an independent, albeit indirect, assessment of the degree of obscuration; the *observed* X-ray luminosity for any significantly absorbed AGN will be suppressed with respect to the *intrinsic* luminosity, causing it to deviate from the intrinsic X-ray to MIR relation. This diagnostic has been utilized for other *NuSTAR* studies of obscured AGNs (e.g., Baloković et al., 2014; Lansbury et al., 2014; Stern et al., 2014; Annuar et al., 2015; Lansbury et al., 2015; Gandhi et al., 2016; LaMassa et al., 2016).
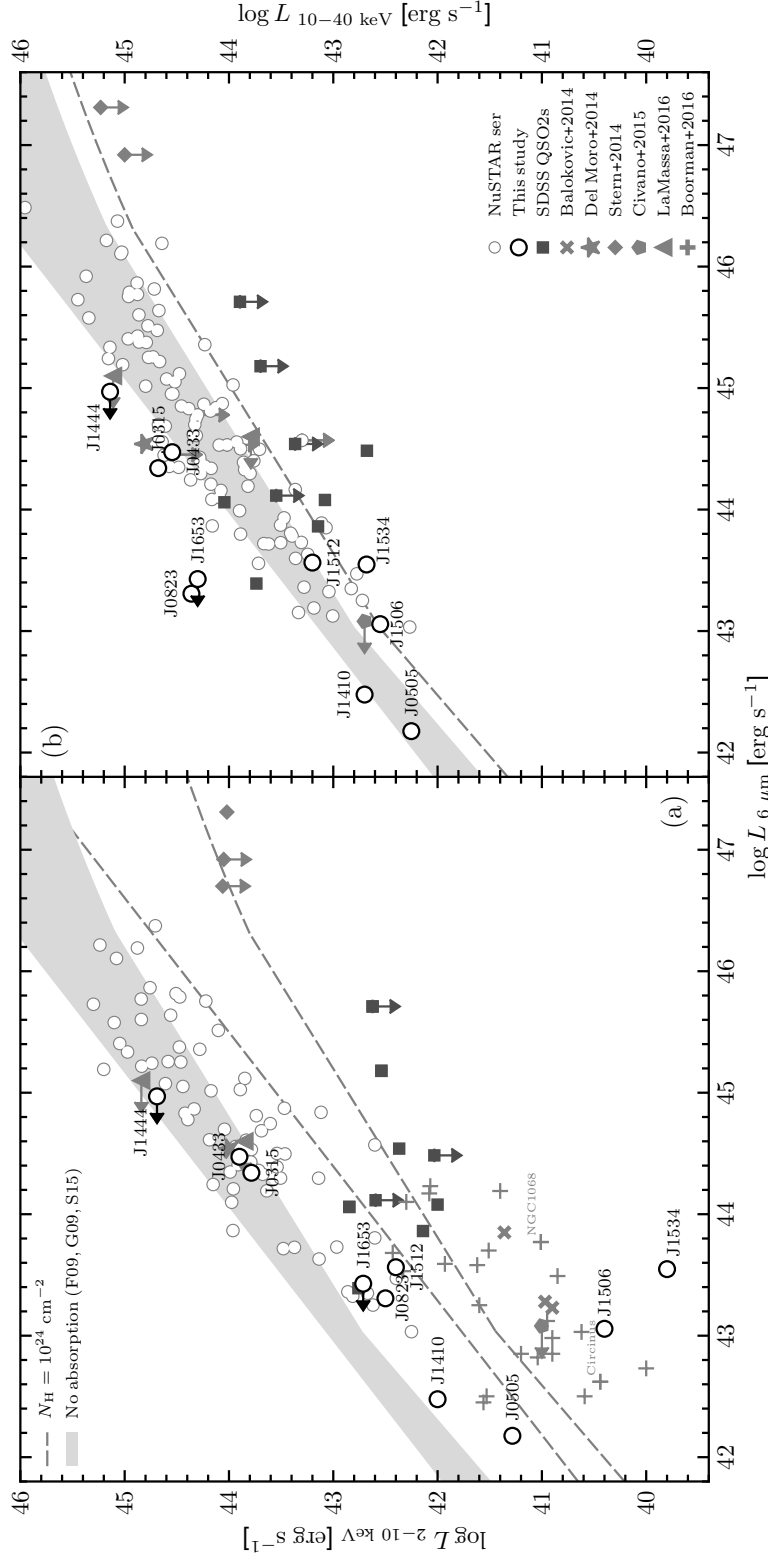
Figure 6.6: X-ray luminosities (at rest-frame 2–10 keV and 10–40 keV) versus rest-frame 6 μm luminosity in νL_ν units. For the data points, we show observed X-ray luminosities (i.e., uncorrected for line-of-sight absorption of the X-rays). The extreme *NuSTAR* serendipitous survey sources are highlighted as thick black circles, and are individually labelled. We compare to "normal" *NuSTAR* serendipitous survey sources (smaller gray circles; Chapter 5 of this thesis; Lansbury et al. 2016, submitted) and to other *NuSTAR*-observed samples of obscured to CT AGNs (see figure legend). We also compare with known "bona fide" CT AGNs in the local universe ("+" symbols; distance $\lesssim$ 100 Mpc; data compiled in Boorman et al. 2016, in prep.), including NGC 1068 and Circinus. The grey regions highlight the range of luminosity ratios expected in the case of zero X-ray absorption (based on Gandhi et al. 2009; Fiore et al. 2009; Stern 2015), and the dashed lines show the approximate X-ray suppression expected for absorption by $N_{\rm H} = 10^{24}$ cm^{-2} gas.

Figure 6.6 shows the observed X-ray versus intrinsic 6 μm luminosities for the 10 very hard *NuSTAR* serendipitous survey sources. Using the methodology of Assef et al. (2008, 2010, 2013), the AGN $L_{6\mu\mathrm{m}}$ values have been determined using SED modelling of the SDSS and *WISE* photometry available, allowing host galaxy flux contributions to be subtracted (the same approach was applied in Chapters 3–4). In Figure 6.6 we compare with "normal" *NuSTAR* serendipitous survey sources (Chapter 5 of this thesis; Lansbury et al. 2016, submitted) and with other *NuSTAR*-observed highly obscured AGNs, including: nearby CT AGNs identified in the *NuSTAR* snapshot survey ($z \approx 0.01$; Baloković et al. 2014); candidate CT Type 2 quasars selected by SDSS ($z = 0.05$–0.49; Chapters 3–4 of this thesis; Lansbury et al. 2014; Gandhi et al. 2014; Lansbury et al. 2015); a heavily obscured quasar identified in the *NuSTAR*-ECDFS survey ($z \approx 2$; Del Moro et al. 2014); and the CT AGN identified in the *NuSTAR*-COSMOS survey ($z = 0.044$; C15). Also plotted are "bona fide" CT AGNs in the local universe ($\mathrm{distance} \lesssim 100$ Mpc; data compiled in Boorman et al. 2016, in prep.). We compare all sources with the intrinsic X-ray–MIR relation for unobscured AGNs (Fiore et al., 2009; Gandhi et al., 2009; Stern, 2015), and to demonstrate the expected deviation from the relation for heavily obscured AGNs, we also show the modified relation for X-ray luminosities suppressed by $N_{\mathrm{H}} = 10^{24}$ cm^{-2} gas. The latter results in a more extreme suppression of the X-ray luminosity for the 2–10 keV band (L_{X} is decreased by a factor of ≈ 20) than for the 10–40 keV band (a factor of ≈ 2 decrease), where the higher energy photons are less affected by absorption.

For the 10 extreme *NuSTAR* serendipitous survey sources, the X-ray to MIR luminosity ratios are in broad agreement with the X-ray spectral modelling results, in that the sources with X-ray spectroscopic evidence for being CT are further offset from the intrinsic L_{X}–L_{MIR} relations than the less obscured AGNs. This is especially apparent for J1506, J0505, J1512, and J1534 at 2–10 keV, where these likely CT sources overlap well with the X-ray to MIR luminosity ratios of local "bona fide" CT AGNs, as well as luminous heavily obscured and CT Type 2 quasars. The L_{X}–L_{MIR} ratios are very low in the cases of J1506 and J1534, which appear to lie even lower than local bona fide CT AGNs (including Circinus and NGC 1068), and have observed X-ray luminosities which are suppressed by multiple orders of magnitude. The exception is J1653, which lies relatively high with respect to the other likely CT sources (at both 2–10 keV and 10–40 keV) and

with respect to the $L_{\mathrm{X}}-L_{\mathrm{MIR}}$ relations, suggesting a low column density which is in tension with the high value measured in Section 6.4. Overall, this indirect analysis does not highlight any additional likely-CT which were not already identified by the X-ray spectral analysis.

6.6   Optical Properties

6.6.1   Optical spectra

For eight of the ten extreme *NuSTAR* sources studied here, the optical spectra are presented in Chapter 5, and were obtained from our dedicated followup program with Keck, Palomar, NTT and Magellan (for J1512, J0823, J1653, J0315, J0433, and J1444) and the SDSS (for J1506 and J1534). For the remaining two extreme *NuSTAR* sources (J0505 and J1410) the spectroscopic redshifts and spectra are from the 6dF survey (Jones et al. 2004, 2009) and the Anglo-Australian Telescope (AAT) observations of Radburn-Smith et al. (2006), respectively. The spectroscopic redshifts (see Table 6.1) are all robust (having been determined using 4–18 detected emission/absorption lines for each source; median of 9 detected lines per source), except in the case of J1444 where the redshift solution is based on two weakly detected emission lines detected (most likely C IV and C III] at $z = 1.539$).

Nine of the ten optical spectra (i.e., all sources except J0315) show narrow emission lines, with AGN-like emission-line ratios. All nine appear consistent with having continua dominated by the host galaxy, and in five cases (J1506, J0505, J1410, J1534, and J1653) this is confirmed by the identification of galactic absorption lines. These optical spectra all support the interpretation of these sources as obscured or CT AGNs, in agreement with the X-ray constraints. We note that many of these nine narrow line AGNs would unlikely be identified by typical optical selection techniques (e.g., Zakamska et al. 2003; Reyes et al. 2008), due to: less luminous high ionization lines; low signal-to-noise; non-detection of key lines such as Hβ (in the majority of cases) and [O III] (in two cases) due to dilution by galaxy light. The remaining source (J0315) has the one optical spectrum that is not in agreement with a narrow line AGN, since it shows broad Balmer lines. This is in agreement with our X-ray results for J0315, which that it is likely unobscured or

weakly obscured (see Section 6.4.2).

6.6.2 Host galaxies

The five lowest redshift ($z < 0.2$) of the extreme *NuSTAR* sources (J1506, J0505, J1410, J1512, and J1534) have well resolved host galaxies at optical wavelengths, while the higher redshift sources are consistent with point source emission (see Figure 6.7). Four of these are likely CT systems based on the X-ray analyses, and also have relatively high quality optical coverage from either the SDSS, Pan-STARRS, or our own ESO-NTT imaging. The other source (J1410), on the other hand, is likely Compton-thin, and is limited to photographic plate coverage (precluding visual analyses, such as disturbance classifications). Here we focus on the host galaxies of the four well resolved, likely CT systems (image cutouts for these are shown in Figure 6.7). Since three of these (J1506, J0505, and J1534) appear to be hosted by merging systems, we also comment on their companion galaxies.

J1506 The optical counterpart is UGC 09710, a close to edge-on Sb spiral galaxy belonging to a close spiral-spiral galaxy pair in a major merger (see Figure 6.7), and separated from its similar mass partner galaxy (IC 1087; $z = 0.035$; S0-a type) by ≈ 16 kpc (Yuan et al., 2012). We do not necessarily expect the edge-on inclination of UGC 09710 to be related to the CT absorption of J1506, since the orientations of local CT AGN host galaxies trace those expected for randomly oriented galaxies (Annuar et al., in prep.; but see also Koss et al. 2016a). However, physical disturbances resulting from the major merger could potentially be related to an increase in the central gas content (e.g., Kocevski et al. 2015; Koss et al. 2016a). In Section 6.9 we present a Palomar (Hale Telescope) optical spectrum for the companion galaxy (IC 1087), which shows a possible AGN (also consistent with a LINER classification) with a dominant galaxy continuum. [O III] and Hβ are undetected (presumably due to host galaxy dilution), and the [N II]:Hα line strength ratio is very high, but is likely affected by stellar absorption. For this companion galaxy, there is no additional evidence from the *WISE* colours for an AGN.
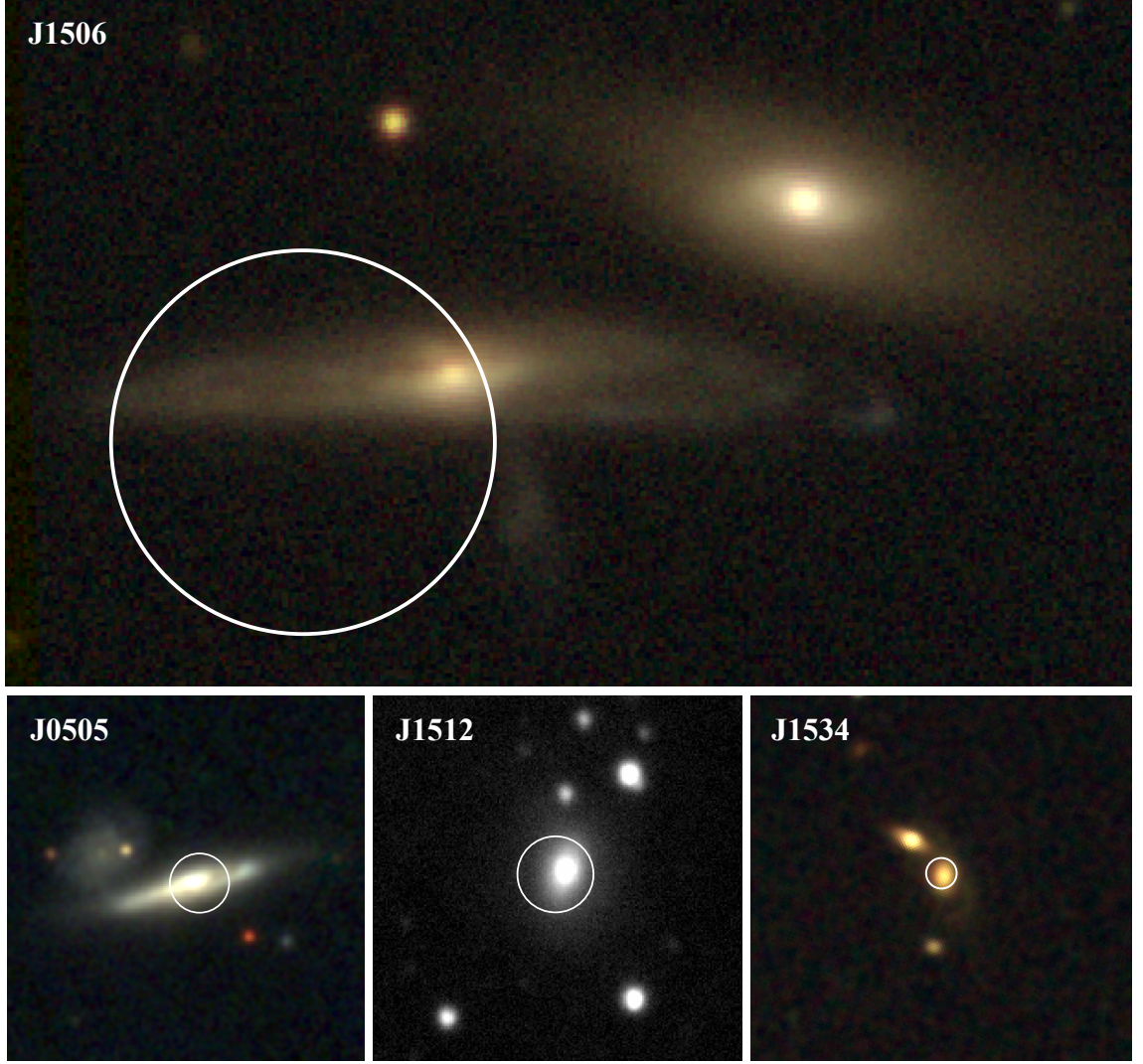
Figure 6.7: Optical images for the extreme *NuSTAR* sources which are both likely CT, and have well resolved host galaxies in the optical imaging. For J1506 (first panel; $z = 0.034$) and J1534 (fourth panel; $z = 0.160$) we use SDSS (g, r, and i band) colour composites. For J0505 (second panel; $z = 0.036$) we use a Pan-STARRS (g, r, and i band) colour composite. For J1512 (third panel; $z = 0.069$) we use NTT R-band imaging from our followup program. The white circles mark the X-ray positions: for J1506 we show the *NuSTAR* positional error circle ($16''$ radius) while for J0505, J1512, and J1534 the circles mark the *XMM-Newton*, *Swift* XRT, and *Chandra* positions, respectively ($5''$, $5''$, and $2.5''$ radii shown, respectively). North is up and east is to the left. Two of these *NuSTAR*-identified likely-CT AGNs (J1506 and J1534) belong to galaxy major mergers, with tidal features visible in both cases, and a third AGN (J0505) also shows evidence for a significant merger.

J0505 The Pan-STARRS coverage shows a highly inclined disk galaxy counterpart, with a nearby ($\approx 12''$ offset, or a projected separation of ≈ 9 kpc) galaxy. A spectroscopic redshift is not available for this companion galaxy, so it is currently difficult to rule out this being a chance alignment along the line-of-sight.

J1512 We have obtained R-band imaging with the ESO-NTT, which is in visual agreement with the host being a relatively undisturbed early type galaxy.

J1534 The SDSS imaging (Figure 6.7) shows evidence that the optical host galaxy (SDSS J153445.80+233121.2; $z = 0.160$) is undergoing a major merger with a narrowly offset companion galaxy (SDSS J153446.19+233127.1; no spec-z); the respective galaxy nuclei are separated by $\approx 8''$ (or ~ 20 kpc), and extended tidal features are visible. We present Palomar (Hale Telescope) spectroscopic followup for the companion galaxy in Section 6.9, although there are no significantly detected emission or absorption features.

A high fraction of galaxy mergers for the Compton-thick AGNs?

It is notable that three of the four lower-redshift ($z < 0.2$) likely CT AGNs (J1506, J0505, J1512, and J1534) are hosted by significant galaxy mergers (see Figure 6.7). The result is of interest given recent findings at higher redshifts. For instance, Kocevski et al. (2015) find evidence that heavily obscured AGNs ($N_{\mathrm{H}} \gtrsim 3 \times 10^{23}$ cm^{-2}) at $z \sim 1$ have a higher frequency of merger/interaction morphologies relative to less obscured AGNs matched in redshift and luminosity, albeit at a relatively low statistical significance. These results may suggest a departure from simple orientation-based unified models of AGN obscuration, and indicate an evolutionary scenario where heavily obscured phases of black hole growth can be associated with a merger-driven increase in the circumnuclear gas content (e.g., Sanders et al. 1988; Draper & Ballantyne 2010; Treister et al. 2010a).

To assess the statistical significance of this apparently high merger fraction for the extreme *NuSTAR* serendipitous survey AGNs (3/4, or $f_{\mathrm{merger}} = 75.0^{+19.2}_{-39.3}\%$), we can search for similar merging systems in the remaining sample of non-extreme (or "normal") serendipitous survey AGNs. To this end, from the overall serendipitous survey sample, we apply a cut of $\mathrm{BR}_{\mathrm{Nu}} < 1.7$, thus limiting to those sources which do not have very hard
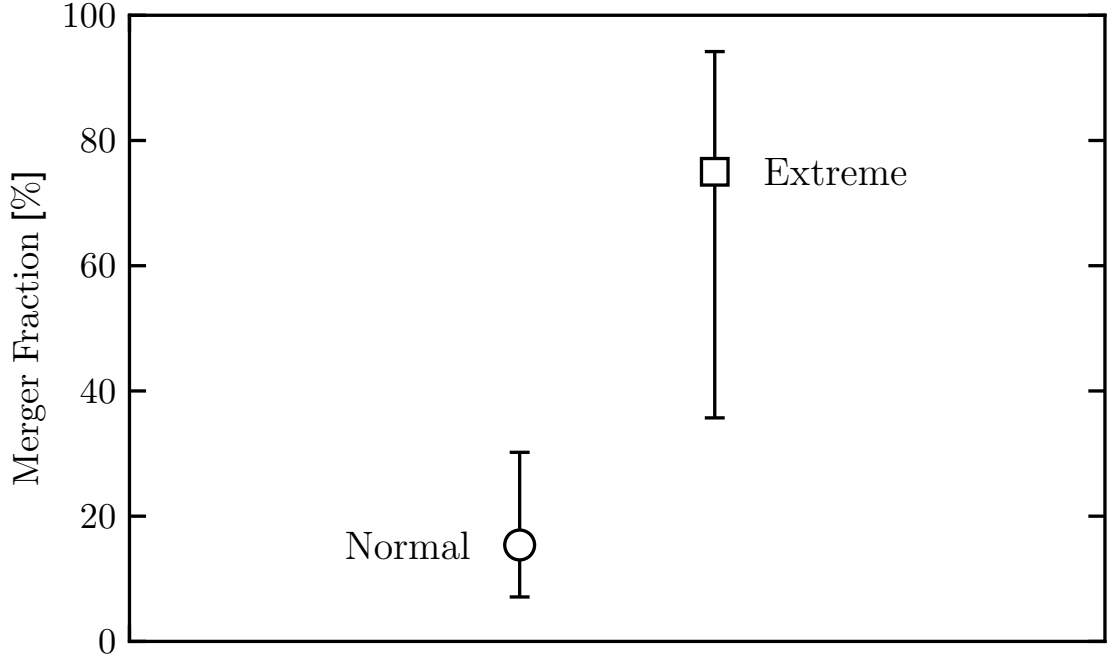
Figure 6.8: The fraction of host galaxies showing evidence for significant mergers, for *NuSTAR* serendipitous survey sources at $z < 0.2$. The fraction is shown for two subsets of the serendipitous survey: (1) the extreme sources (square) with very hard X-ray spectra and evidence for CT obscuration (J1506, J0505, J1512, and J1534; i.e., those discussed in this work) and (2) the remaining "normal" sources (circle) which do not satisfy the high band ratio criterion in Section 6.2 of this work (i.e., they do not have very hard *NuSTAR* spectra).

NuSTAR spectra (based on the BR_{Nu} threshold on Section 6.2). We limit the sample to source redshifts of $0.01 < z < 0.2$, thus matching to the range of the four extreme sources. We also exclude two sources from the sample which are likely strongly associated with the science targets of their *NuSTAR* observations (similar to the exclusion of J2028 from the extreme sample; see Section 6.2). These cuts leave 36 normal *NuSTAR* sources. Finally, we limit the sample to the 26 (out of 36) sources which are covered by either SDSS or Pan-STARRS observations, and therefore have optical coverage which is of comparable quality to the four extreme *NuSTAR* sources. As a result, the comparison of visual merger classifications between the two different samples is unlikely to be significantly affected by variations in optical imaging sensitivity.

Of the 26 normal *NuSTAR* AGNs, we identify 3–4 systems which have similar ev-

idence for galaxy major mergers (i.e., a narrowly offset companion galaxy and/or very strong tidal features) as the extreme *NuSTAR* AGNs. Our estimate for the merger fraction of normal *NuSTAR* AGNs is therefore $f_{\mathrm{merger}} = 15.4^{+14.8}_{-8.3}\%$. This is in agreement with the typical major-merger fraction observed for X-ray detected AGNs overall ($\approx 20\%$; see Brandt & Alexander 2015). Figure 6.8 compares the two merger fractions. At a significance level of $\approx 2\sigma$, the extreme (very hard, likely CT) *NuSTAR* AGNs have a higher merger fraction than the normal *NuSTAR* AGNs. In other words, we find tentative evidence that CT phases of black hole growth at $z < 0.2$ are more strongly linked (than less-obscured phases) to the merger stage of the galaxy evolutionary sequence.

6.7   The prevalence of Compton-thick absorption

We have taken advantage of the relatively large sample size of the *NuSTAR* serendipitous survey to identify elusive highly obscured AGNs. While most of the 10 extreme sources investigated are consistent with being highly obscured, five in particular are likely CT (J1506, J0505, J1512, J1534, and J1653), and three of these are suitable for number counts measurements (J1506, J1534, and J1653; see Section 6.2), as presented below. Although this is a very small number of sources, combining this information with the overall number counts for the serendipitous survey sample still provides informative constraints on the prevalence of CT AGNs. We note that this could be a lower limit to the total number of CT AGNs within the *NuSTAR* serendipitous survey as there are additional sources, not included in this work, which have band-ratio limits consistent with a large range in column density (see Figure 6.1). Also, from detailed studies in the nearby Universe, CT AGNs are established to have complex spectra, and the simple band-ratio selection we apply here could potentially miss some CT sources. Detailed X-ray spectral studies of the general hard-band selected *NuSTAR* serendipitous survey sample (e.g., L. Zappacosta et al., in prep.) thus have the potential to identify additional CT AGNs.

Here we assess whether the observed number of CT AGNs in the *NuSTAR* serendipitous survey agrees with the number expected based on the results from previous (primarily < 10 keV) X-ray missions. We consider the hard band (8–24 keV) selected serendipitous survey sample, since this is the energy band in which *NuSTAR* is uniquely sensitive, and

Galactic latitudes of $|b| > 10°$ (i.e., out of the Galactic plane). The top panel of Figure 6.9 shows the observed (cumulative) number of CT sources as a function of limiting flux. We compare to model predictions for the observed numbers of CT AGNs and all AGNs. For these predictions (shown in the top panel of Figure 6.9), we fold the area sensitivity curve of the serendipitous survey through models for the evolution of the X-ray luminosity function (XLF) and the $N_{\rm H}$ distribution of AGNs, assuming an AGN X-ray spectral model. We consider two different XLF/$N_{\rm H}$ models: that of Ueda et al. (2014) (hereafter U14), which is based on < 10 keV surveys with MAXI, *ASCA*, *XMM-Newton*, *Chandra*, and *ROSAT*, in addition to > 10 keV *Swift* BAT data for the very local universe; and that of Aird et al. (2015a) (hereafter A15), based on < 10 keV surveys with *Chandra*, *ASCA*, and *ROSAT*. In both cases we assume the AGN X-ray spectral model in Section 3.1 of A15, and in the case of the U14 model predictions we fix the reflection scaling factor to 2, since this is required to best reproduce the shape of the *NuSTAR* XLF (see Aird et al. 2015b). We additionally show, in the middle and lower panels of Figure 6.9, the "intrinsic" cumulative number densities [$N(> S)$, in units of $\deg^{-2}$] and the implied CT fractions, respectively, as a function of flux. The cumulative CT number counts observed for the serendipitous survey are broadly consistent with both of the model predictions, but agree more closely with the U14-based predictions.

Integrating over all luminosities and redshifts ($0.01 < z < 5$), the predicted numbers of hard-band detected CT AGNs are $N_{\rm CT}^{\rm mod} = 1.5$ and 5.6 for the A15 and U14 models, respectively. Since our identification of CT sources requires redshift information, we must also account for the spectroscopic completeness of the survey. We assume 60% spectroscopic completeness for CT AGNs (based on Chapter 5), which yields modified number predictions of $N_{\rm CT}^{\rm mod} = 0.9$ and 3.3 for the A15 and U14 models, respectively. Our observed number of CT AGNs, $N_{\rm CT}^{\rm obs} = 3$, is thus in good agreement with the $N_{\rm CT}^{\rm mod}$ prediction based on the U14 model. There is a mild disagreement with the A15 model, at a low significance level, possibly suggesting that the CT fraction is underestimated by this model. In summary, our present identifications of CT AGNs within the *NuSTAR* serendipitous survey are broadly harmonious with the current constraints on the prevalence of CT absorption throughout the AGN population, based on lower energy (< 10 keV) X-ray surveys. However, if more CT AGNs are identified within the serendipitous survey, using
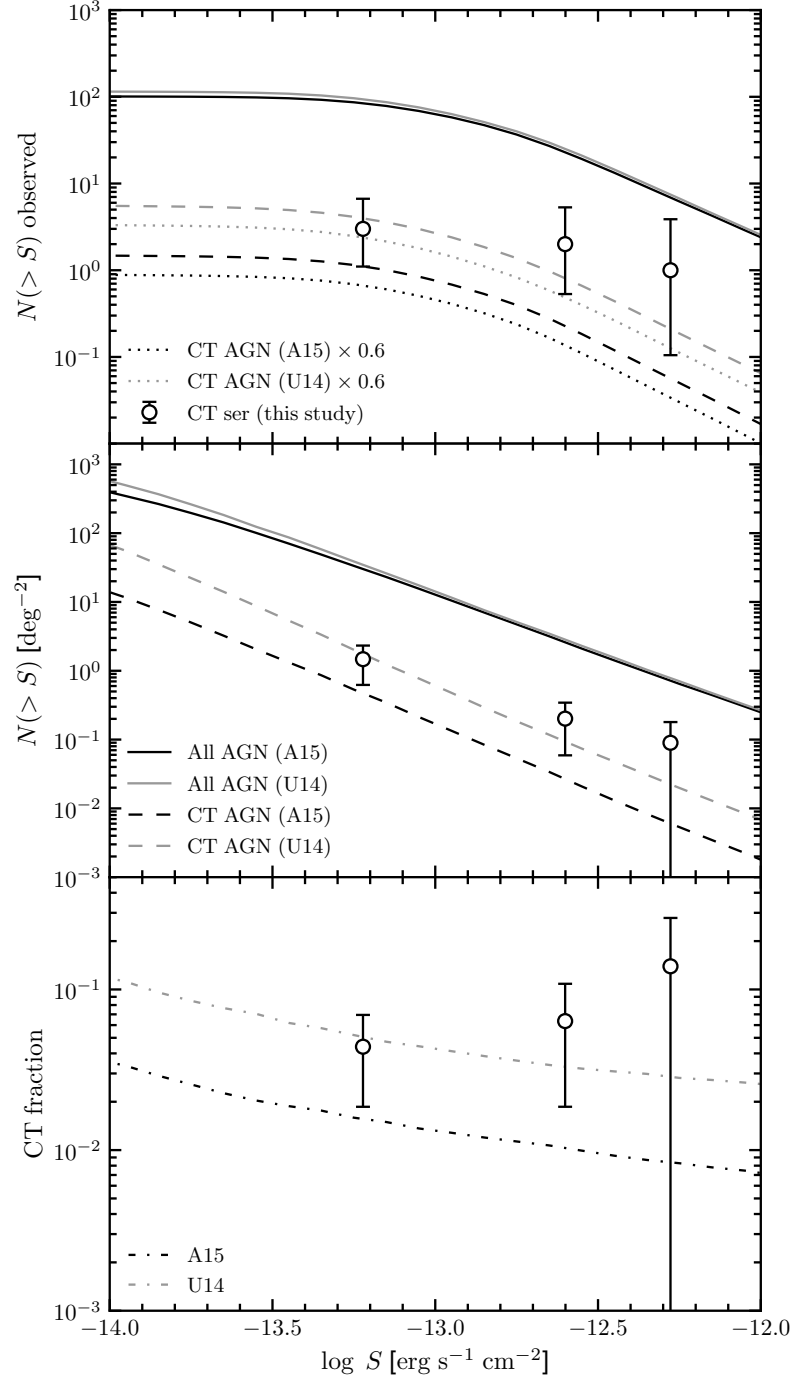
Figure 6.9: Top panel: observed cumulative number counts (and 90% CL uncertainties), as a function of 8–24 keV flux (S), for the likely CT AGNs identified in the *NuSTAR* serendipitous survey (circles). We compare to predicted tracks for CT AGNs (dashed lines) and all AGNs (solid lines) based on the models of A15 and U14 (fixing $R = 2$ for the latter). The dotted lines show modifications of the CT model tracks to account for the spectroscopic incompleteness of the serendipitous survey. Middle panel: "intrinsic" cumulative number density, as a function of flux. Lower panel: CT fraction (relative to all AGNs), as a function of flux. For the middle and lower panels, the error bars represent 68% CL uncertainties.

alternative approaches for their identification (e.g., detailed X-ray spectral analyses of the entire sample), this would possibly indicate a tension with the < 10 keV constraints.

6.8 Summary

In this chapter we have searched for the most extreme outliers in the *NuSTAR* serendipitous survey, in terms of having very hard 3–24 keV spectral slopes ($\mathrm{BR_{Nu}} \geq 1.7$). The 10 selected sources are all candidates for being highly obscured AGNs. A detailed look at the broad-band (0.5–24 keV) X-ray data available, and the multiwavelength properties of these sources has yielded the following main results:

- The X-ray spectral analyses find that three of the sources are newly identified robust CT AGNs at low redshift ($z < 0.1$). Two (J1506 and J1512) have higher best-fit column densities than, and one (J0505) has a similar best-fit column density to, the single other robust CT AGN identified in the *NuSTAR* extragalactic survey program to-date (ID 330; Civano et al. 2015). Two other sources at higher redshift are likely CT. Most of the likely CT AGNs would not be identified as highly absorbed systems based on the low energy (< 10 keV) X-ray coverage alone; see Section 6.4.2.

- As a notable example, the search has uncovered a new unambiguous CT AGN in the nearby universe (J1506; $z = 0.034$; $N_{\mathrm{H}} \gtrsim 2 \times 10^{24}$ cm^{-2}; $L_{\mathrm{X}} \approx 2 \times 10^{43}$ erg s^{-1}), hosted by a previously known galaxy major merger; see Sections 6.4.2 and 6.6.2.

- For all 9 (out of 10) extreme sources which are at least moderately absorbed ($N_{\mathrm{H}} \approx 10^{23}$ cm^{-2}) based on the X-ray constraints, the optical spectra show evidence for narrow line AGNs or galaxy-dominated spectra, supporting the X-ray classifications; see Section 6.6.1.

- A large fraction of the $z < 0.2$ likely CT AGNs are hosted by significant galaxy mergers ($f_{\mathrm{merger}} \approx 75\%$; i.e., 3/4). This is higher than the merger fraction for "normal" *NuSTAR* serendipitous survey sources ($f_{\mathrm{merger}} \approx 15\%$), at a significance level of $\approx 2\sigma$; see Section 6.6.2.
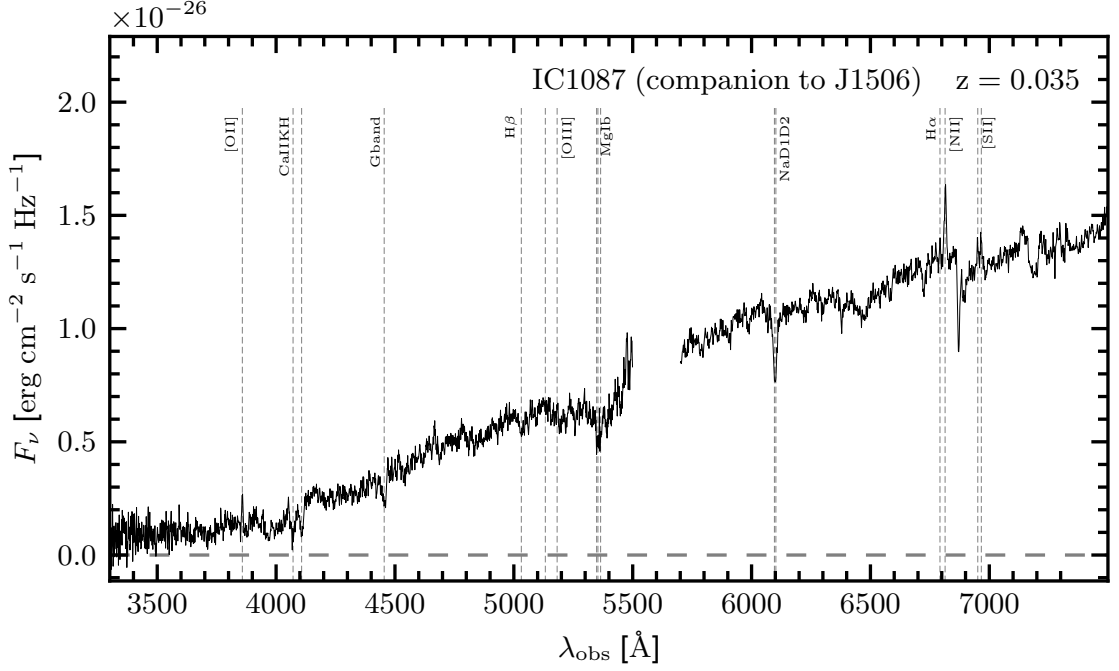
Figure 6.10: Palomar optical spectrum for IC 1087, the merging companion galaxy to UGC 09710 (the host galaxy for our lowest redshift extreme *NuSTAR* source, J1506). Multiple emission and absorption lines are identified, and labelled here.

- For the hard band (8–24 keV) selected serendipitous survey sample at $|b| > 10°$, the number of currently identified CT AGNs is in broad agreement with the expectations based on results from previous (primarily < 10 keV) X-ray missions. This assumes knowledge of the X-ray luminosity function, the N_{H} distribution, and the X-ray spectra of AGNs; see Section 6.7.

6.9   Additional information for individual objects

6.9.1   J1506

As described in the main text, J1506 belongs to one of two galaxies in a major merger. With the Palomar Observatory Hale Telescope we performed optical spectroscopy for the companion galaxy (known as IC 1087). The resulting spectrum is shown in Figure 6.10.

6.9.2 J0505

For J0505 there are two potential counterparts in the 3XMM catalogue, one at $14''$ offset from the *NuSTAR* position (R.A. $= 76.49983°$, decl. $= -23.83536°$; hereafter "XMM1") and one brighter source at $27''$ offset (R.A. $= 76.49296°$ decl. $= -23.82597°$; hereafter "XMM2"). For XMM1 we use the combined MOS data only since the source lies on a chip gap for PN. The 0.5–10 keV spectrum for XMM1 is extremely flat ($\Gamma_{\rm eff} = -0.9^{+0.8}_{-1.4}$) and there is a line detection consistent with Fe Kα ($E = 6.3 \pm 0.1$ keV). The Fe Kα line has a high equivalent width of $\rm EW_{FeK\alpha} = 1.4^{+1.4}_{-0.9}$ keV, suggesting a heavily absorbed, possibly CT AGN. For XMM2, the 0.5–10 keV (PN plus MOS) spectrum is steeper ($\Gamma_{\rm eff} = 1.4 \pm 0.2$). Although, XMM2 is brighter than XMM1 over the full energy band, XMM1 is significantly brighter for the energies at which *NuSTAR* is sensitive: for the 3–10 keV energy band, XMM1 and XMM2 have fluxes of 8.9×10^{-14} erg s^{-1} cm^{-2} and 1.8×10^{-14} erg s^{-1} cm^{-2}, respectively. Given these fluxes and the relative spectral slopes of XMM1 and XMM2 (with the former sharply increasing, and the latter decreasing, towards higher X-ray energies), and the fact that the majority of *NuSTAR* source counts (79%) lie at high energies (> 8 keV), we expect XMM1 to dominate the *NuSTAR* detected emission. We therefore adopt XMM1 as the counterpart to J0505.

6.9.3 J1534

As described in the main text, J1534 (hosted by galaxy J153445.80+233121.2) appears to be undergoing a major merger with a neighbouring galaxy (SDSS J153446.19+233127.1). Since no spectroscopic redshift is available for the latter galaxy, we performed optical spectroscopy with the Palomar Observatory Hale Telescope, the spectrum from which is shown in Figure 6.11. Since no clear emission or absorption features are detected, this companion requires deeper spectroscopic observations in the future to reliably determine the redshift.

6.9.4 J0433

The counterpart for J0433 presented in Chapter 5 is from *Chandra*, and was obtained by combining the event lists for the two longest exposure *Chandra* observations with
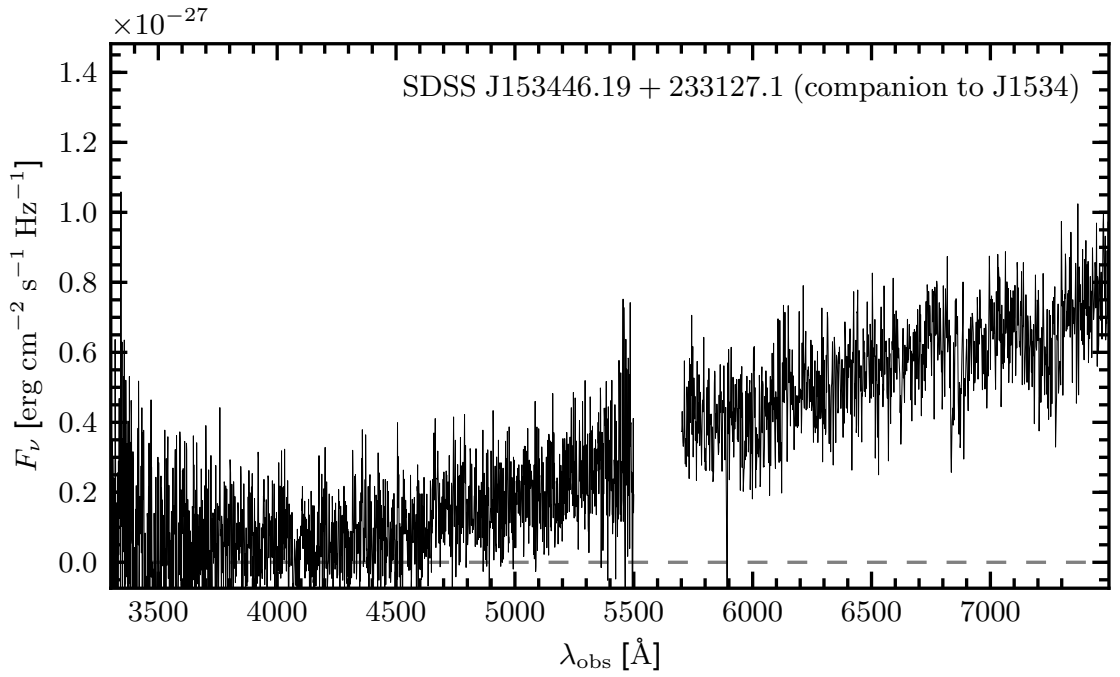
Figure 6.11: Palomar optical spectrum for SDSS J153446.19+233127.1, the merging companion galaxy to SDSS J153445.80+233121.2 (the host galaxy for J1534). The continuum is detected, although no clear emission or absorption lines are identified, precluding a spectroscopic redshift measurement.

uncontaminated coverage of J0433 (obsIDs 3015 and 17576) which were both taken in the HETG grating mode (combined exposure at source position of 110.7 ks), resulting in a $\approx 4\sigma$ detection. We have more recently obtained a more robust detection of the same soft X-ray counterpart by combining 30 archival short-exposure *Swift* XRT observations (the *Swift* XRT data are adopted for this study; see Table 6.2).

Chapter 7

Summary and future work

NuSTAR is the first X-ray observatory able to focus high energy (i.e., hard; $\gtrsim 10$ keV) X-ray photons, resulting in large improvements in sensitivity and angular resolution compared to previous generation hard X-ray missions. In this thesis, I have used *NuSTAR* to study the distant hard X-ray emitting AGN population. Here I summarise the main results and conclusions of this research (Section 7.1), and discuss additional work which can potentially extend the research into the future (Section 7.2).

7.1 Summary of the presented work

7.1.1 Highly obscured Type 2 quasars observed with *NuSTAR*

In Chapters 3–4 I presented a program of targetted *NuSTAR* observations of SDSS-selected $z \lesssim 0.5$ candidate CTQSO2s. All nine of the observed quasars were selected based on indirect evidence for CT ($N_{\rm H} > 1.5 \times 10^{24}$ cm^{-2}) material along the line-of-sight. The quasars have observed [O III] luminosities in the range $8.4 < \log(L_{\rm [O\,III]}/L_\odot) < 9.6$. Broad-band X-ray spectral and multiwavelength analyses have been performed to characterise these extreme sources, and assess how *NuSTAR* affects their interpretation. Overall, five of the sources are detected, and four are undetected, with *NuSTAR*. The sources are generally too faint to have been detected by previous generation hard X-ray observatories. Three (of the five) detected sources have sufficient photon counts for relatively detailed X-ray spectral modelling, which reveals suppressed primary continua and ev-

idence for dominant Compton reflection components, indicating CT column densities ($N_{\rm H} \gtrsim 10^{24}$ cm^{-2}). One of the weaker *NuSTAR* detections (SDSS J1713+5729) is particularly interesting. For this source, I find that *NuSTAR* has provided the first detection of the directly transmitted AGN X-ray emission, and the extremely low X-ray–mid-IR luminosity ratio suggests that this is a deeply buried AGN ($N_{\rm H} \gg 10^{24}$ cm^{-2}). Likewise, most of the *NuSTAR*-undetected quasars have very low X-ray–mid-IR luminosity ratios, suggesting CT absorption. The *NuSTAR* data of the detected quasars allow column densities and intrinsic luminosities to be constrained which are up to orders of magnitude higher (factors of ≈ 2.5–1600 and ≈ 10–70 higher, respectively) than previous soft (< 10 keV) X-ray constraints. I discuss the implications of these higher values for the $N_{\rm H}$ distribution of optically selected Type 2 quasars. The results imply an $N_{\rm H}$ distribution which is skewed towards large column densities ($N_{\rm H} > 10^{23}$ cm^{-2}) and has a CT fraction of $f_{\rm CT} = 36^{+14}_{-12}$ %. This predicted distribution is broadly consistent with CXB models.

7.1.2 The *NuSTAR* serendipitous survey: the 40 month catalogue and the properties of the distant high energy X-ray source population

In Chapter 5 I presented the first full catalogue for the *NuSTAR* serendipitous survey. This is the largest survey undertaken with *NuSTAR*, incorporating ≈ 20 Ms of data from the first 40 months of telescope operation. The survey reaches flux depths similar to the *NuSTAR* surveys in the well-studied blank-field regions (e.g., COSMOS and ECDFS) over comparable areas, and is approximately two orders of magnitude fainter than the *Swift* BAT surveys. A total of 497 *NuSTAR* sources are detected over a sky area of $13 \deg^2$, and 163 of these sources are independently detected in the hard (8–24 keV) energy band. I find that the spectral slopes are varied, ranging from very soft ($\Gamma_{\rm eff} \approx 3$) to very hard ($\Gamma_{\rm eff} \approx 0$). A large fraction (79%) of the *NuSTAR* sources are successfully matched to soft (< 10 keV) X-ray counterparts detected in surveys or archival data from *XMM-Newton*, *Chandra*, and *Swift* XRT. The higher positional accuracy of the soft X-ray counterparts facilitates optical and infrared counterpart matching. I have presented the results from an extensive campaign of ground-based spectroscopic followup, using a range of obser-

vatories at multiple geographical latitudes. Spectroscopic redshifts now exist for 276 of the *NuSTAR* serendipitous survey sources (i.e., 56% of the full sample; the spectroscopic completeness is $\approx 70\%$ for the $|b| > 10°$ individual band-selected samples), largely due to this followup campaign. The AGNs cover a wide range in redshift, from $z = 0.002$ to 3.4 (with a median of $\langle z \rangle = 0.56$), and in luminosity, from $L_{10-40\mathrm{keV}} \approx 10^{39}$ to 10^{46} erg s^{-1} (with a median of $\langle L_{10-40\mathrm{keV}} \rangle = 10^{44.1}$ erg s^{-1}). Similar numbers of Type 1 and Type 2 AGNs are identified at lower redshifts ($z \lesssim 1$), and there is a bias towards detections of Type 1 AGNs at higher redshifts. The latter is likely due to a bias against the detection of highly obscured AGNs, and against the spectroscopic identification of fainter AGNs. The X-ray–optical flux plane for *NuSTAR* serendipitous survey sources suggests source properties which are broadly consistent with those previously found for AGNs selected at lower X-ray energies. However, I find tentative evidence that the Type 2 AGN fraction for *NuSTAR* (and *Swift* BAT) AGNs is higher than than for redshift- and luminosity-matched AGNs selected by lower energy X-ray missions (e.g., *Chandra* and *XMM-Newton*). Studying the *WISE* colours of the *NuSTAR* sources, the fraction of MIR-selected AGNs is found to be a strong function of luminosity, as was previously known. However, I also find that commonly applied MIR-selection techniques still miss a fraction of AGNs ($\approx 20\%$) at the high luminosity end ($L_{\mathrm{X}} > 10^{44}$ erg s^{-1}), where these selections are often assumed to be highly complete.

7.1.3 The *NuSTAR* serendipitous survey: hunting for the most extreme sources

In Chapter 6 I aimed to identify CT AGNs in the *NuSTAR* serendipitous survey which are akin to the candidate CTQSO2s studied in Chapters 3–4 in terms of their extreme obscuration. Since the serendipitous survey is relatively unbiased at X-ray energies (see Chapter 5), this approach provides insights into the prevalence of extreme, CT systems in the general AGN population. To this end, I identified the ten most extreme outliers in the *NuSTAR* serendipitous survey, which have extremely hard X-ray spectral slopes indicating high absorption levels. X-ray spectral analyses applied to all of the extreme sources revealed three newly identified robust CT AGNs at low redshift ($z < 0.1$), quadrupling

the number of robust CT AGNs identified in the *NuSTAR* extragalactic survey program to-date. A further two extreme sources at higher redshifts are likely CT, although deeper data is required for confirmation of this. An important point is that most of these sources would not have been identified as highly obscured AGNs based on the low energy (< 10 keV) X-ray coverage alone. Additionally, these extreme *NuSTAR* sources show variety in their optical spectra, and would not necessarily be identified using commonly applied optical selection techniques (e.g., like those used to identify the candidate CTQSO2s in Chapters 3–4). I find that, for the hard band (8–24 keV) selected serendipitous survey sample, the number counts for CT AGNs are currently in broad consistency with model expectations. With improved source statistics in the future, it may be possible rule out certain AGN population models. Finally, an unexpected result was that a large fraction of the $z < 0.2$ likely CT AGNs are hosted by significant galaxy mergers ($f_{\mathrm{merger}} \approx 75\%$; i.e., 3/4). The fraction is higher than that for "normal" *NuSTAR* serendipitous survey sources ($f_{\mathrm{merger}} \approx 15\%$), at a low significance level ($\approx 2\sigma$), possibly indicating a connection between CT phases of black hole growth and the merger stage of galaxy evolution.

7.2 Looking to the future

The *NuSTAR* serendipitous survey presented in this thesis is, thus far, the largest sample of distant AGNs selected with a focusing high energy ($\gtrsim 10$ keV) X-ray observatory (see Chapter 5). The data incorporated in the survey are from the first 40 months of *NuSTAR* telescope operations. As the *NuSTAR* science operations continue into the future, the serendipitous survey will continue to grow at a similar rate. *NuSTAR* operations are expected to continue for another two to four years, and the serendipitous survey is therefore likely to eventually achieve a sample size on the order of $\gtrsim 1000$ sources. This may even be a conservative estimate, since *NuSTAR* is likely to be in orbit for over 10 years. A future continuation of the serendipitous survey presented herein will improve statistical constraints on the overall properties of the hard X-ray emitting source population, and will facilitate the discovery of rare and extreme sources (e.g., see Chapter 6) which are not sampled as effectively by the smaller-area dedicated *NuSTAR* surveys (e.g., in the COSMOS, ECDFS, EGS, GOODS-N, and UDS fields). However, a large program of fol-

lowup observations, preferably with both 8m-class and 4m-class optical telescopes will be necessary to maximize the effectiveness of the serendipitous survey. In addition to the continued serendipitous survey, an extragalactic legacy survey program is to be undertaken with *NuSTAR*, aiming to fill out the regions of L_X–z parameter space which are less well-sampled by the existing *NuSTAR* and *Swift* BAT surveys (e.g., see Figures 5.12 and 5.13). This may involve either, or some combination of: an extremely deep dedicated survey in a well-known field, exceeding the depths of *NuSTAR*-ECDFS and *NuSTAR*-EGS; a shallow wide-area survey in a region of sky with good multiwavelength coverage; or targetted observations of a well-defined AGN sample (similar to the snapshot survey of *Swift* BAT AGNs; Baloković et al. 2014).

Observations and theory suggest a close link between AGN activity and galaxies. Although this thesis has primarily focused on the AGNs themselves, the *NuSTAR* extragalactic survey samples have the potential to address questions related to the AGN host galaxies. Studies of the distant universe ($z \gtrsim 1$) find broadly similar host galaxy morphologies for AGNs and non-AGNs, and possibly some subtle differences at $z \lesssim 1$, but recent results show that stark differences appear at $z < 0.05$ (e.g., Koss et al. 2011; Rosario et al. 2015; Brandt & Alexander 2015). In addition, the characteristic stellar mass of AGN host galaxies shows no strong evolution towards $z \approx 0.2$, but there appears to be a significantly lower characteristic mass by the present day (e.g., see Brandt & Alexander 2015). These studies suggest an evolution over a remarkably narrow redshift range, but it is currently unclear why these changes emerge and whether the evolution is real or an effect of different methodologies or sample biases (e.g., different sample luminosities). A key limitation in current analyses is that no study has measured the AGN and host properties in a uniform and self-consistent manner for both the local ($z < 0.05$) and distant ($z > 0.2$) universe. Future studies can potentially achieve this using a combination of the *NuSTAR* and *Swift* BAT AGN samples. The *Swift* BAT all-sky survey is a statistical, unbiased, hard X-ray selected sample of local ($z \lesssim 0.05$) AGNs. Now, thanks to the *NuSTAR* surveys (e.g., Chapter 5 of this thesis), we also have such a sample for the distant Universe ($z \approx 0.1$–2). AGNs can be selected from the *Swift* BAT sample using specific energy channels (e.g., ≈ 14–41 keV) which precisely match the rest-frame energy selection for the higher redshift ($z \sim 0.7$) *NuSTAR* AGNs (e.g., selected at observed-frame

8–24 keV), thus eliminating the possibility of selection effects related to the observed energy window. Consistent methodologies should be applied across both samples, to solve the problem of systematic differences between studies. For instance, a UV–mid-IR SED modelling approach can be applied to both samples where stellar masses are accurately determined through the reliable subtraction of the AGN SED component (e.g., see Chapters 3 and 4). To illustrate the stellar mass results that can be achieved using the current sample of $\gtrsim 500$ spectroscopically identified *NuSTAR* sources, Figure 7.1 shows preliminary results for eight sources which hint toward a significant mass evolution. These observational stellar mass constraints, along with model comparisons (e.g., with Aird et al. 2012), can be used to determine whether the findings for $z > 0.2$ (e.g., that the AGN incidence and accretion rate distributions are independent of stellar mass) hold or break down for the local universe. Similarly, open questions regarding the morphological evolution of AGN host galaxies (e.g., Koss et al. 2011; Cotini et al. 2013; Rosario et al. 2015) can be addressed using the combination of the *NuSTAR* and *Swift* BAT surveys.

As a final note, a new generation of astronomical observatories are arriving over the next ≈ 5 years: the *James Webb Space Telescope* (*JWST*) will act as a successor to *Hubble* in the near-IR to mid-IR wavelength regime, advancing host morphology studies and IR diagnostics (both photometric and spectroscopic) for AGNs; in the radio regime, the square kilometer array (SKA) will provide an unbiased radio view of AGNs as far back as the early Universe, with an extremely high resolution for identifying the AGN core and host galaxy star formation; the Large Synoptic Survey Telescope (LSST), with its rapid scanning of the entire observable sky, will provide deep optical imaging coverage and huge advances in the understanding of AGN variability; and at X-ray energies (0.3–10 keV), the *eROSITA* observatory will achieve survey depths that compete with the shallow *XMM-Newton* surveys, but over a sky area which is larger by multiple orders of magnitude (i.e., the entire sky). These next-generation observatories are likely to significantly improve the cosmic census of black hole growth, and provide important breakthroughs for AGN research in general.
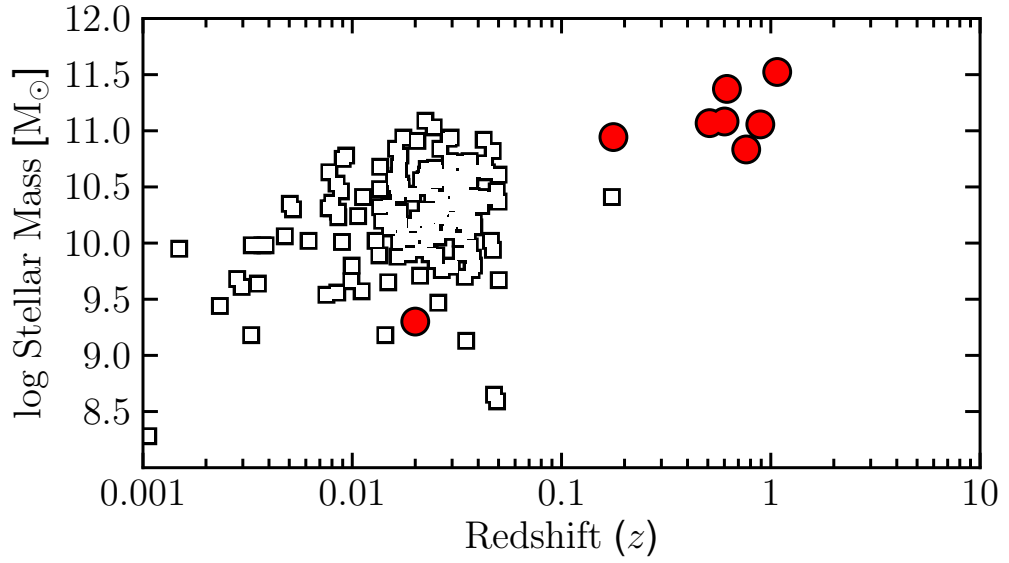
Figure 7.1: Stellar mass versus redshift. The stellar masses for the preliminary sample of eight *NuSTAR* serendipitous survey sources (red circles) are roughly a factor of five times higher than the average stellar mass of local high energy selected *Swift* BAT AGNs (squares). Incorporating the full spectroscopically-identified serendipitous survey sample (≈ 276 sources to-date; this number will continue to increase with time) and those from the deep *NuSTAR* surveys of ECDFS, COSMOS, EGS and GOODS-N (≈ 200 sources in total), it will be possible to validate or repudiate a cosmic evolution of the AGN host galaxy stellar masses.

Bibliography

Abazajian, K. N., Adelman-McCarthy, J. K., Agüeros, M. A., et al. 2009, ApJS, 182, 543

Abbott, B. P., Abbott, R., Abbott, T. D., et al. 2016, Physical Review Letters, 116, 241103

Agüeros, M. A., Anderson, S. F., Covey, K. R., et al. 2009, ApJS, 181, 444

Aird, J., Coil, A. L., Georgakakis, A., et al. 2015a, MNRAS, 451, 1892 (abbreviated to "A15" in the thesis text)

Aird, J., Alexander, D. M., Ballantyne, D. R., et al. 2015b, ApJ, 815, 66

Ajello, M., Greiner, J., Kanbach, G., et al. 2008, ApJ, 678, 102

Akiyama, M., Ohta, K., Yamada, T., et al. 2000, ApJ, 532, 700

Akylas, A., Georgakakis, A., Georgantopoulos, I., Brightman, M., & Nandra, K. 2012, A&A, 546, A98

Alexander, D. M., Bauer, F. E., Chapman, S. C., et al. 2005a, ApJ, 632, 736

Alexander, D. M., Brandt, W. N., Hornschemeier, A. E., et al. 2001, AJ, 122, 2156

Alexander, D. M., Chartas, G., Bauer, F. E., et al. 2005b, MNRAS, 357, L16

Alexander, D. M., & Hickox, R. C. 2012, NewAR, 56, 93

Alexander, D. M., Bauer, F. E., Brandt, W. N., et al. 2003, AJ, 126, 539

Alexander, D. M., Chary, R.-R., Pope, A., et al. 2008, ApJ, 687, 835

Alexander, D. M., Stern, D., Del Moro, A., et al. 2013, ApJ, 773, 125

Annuar, A., Gandhi, P., Alexander, D. M., et al. 2015, ApJ, 815, 36

Antonucci, R. 1993, ARA&A, 31, 473

Antonucci, R. R. J. 1982, Nature, 299, 605

Antonucci, R. R. J., & Miller, J. S. 1985, ApJ, 297, 621

Armus, L., Bernard-Salas, J., Spoon, H. W. W., et al. 2006, ApJ, 640, 204

Arnaud, K. A. 1996, in Astronomical Society of the Pacific Conference Series, Vol. 101, Astronomical Data Analysis Software and Systems V, ed. G. H. Jacoby & J. Barnes, 17

Asmus, D., Gandhi, P., Hönig, S. F., Smette, A., & Duschl, W. J. 2015, MNRAS, 454, 766

Assef, R. J., Kochanek, C. S., Brodwin, M., et al. 2008, ApJ, 676, 286

—. 2010, ApJ, 713, 970

Assef, R. J., Stern, D., Kochanek, C. S., et al. 2013, ApJ, 772, 26

Assef, R. J., Eisenhardt, P. R. M., Stern, D., et al. 2015, ApJ, 804, 27

Awaki, H., Koyama, K., Inoue, H., & Halpern, J. P. 1991, PASJ, 43, 195

Baade, W., & Minkowski, R. 1954, ApJ, 119, 215

Bachetti, M., Harrison, F. A., Cook, R., et al. 2015, ApJ, 800, 109

Baldwin, J. A., Phillips, M. M., & Terlevich, R. 1981, PASP, 93, 5

Ballantyne, D. R., Everett, J. E., & Murray, N. 2006, ApJ, 639, 740

Baloković, M., Comastri, A., Harrison, F. A., et al. 2014, ApJ, 794, 111 (abbreviated to "B14" in the thesis text)

Barcons, X., Carrera, F. J., Ceballos, M. T., et al. 2007, A&A, 476, 1191

Barger, A. J., Cowie, L. L., Capak, P., et al. 2003, AJ, 126, 632

Bassani, L., Dadina, M., Maiolino, R., et al. 1999, ApJS, 121, 473

Bauer, F. E., Alexander, D. M., Brandt, W. N., et al. 2004, AJ, 128, 2048

Bauer, F. E., Yan, L., Sajina, A., & Alexander, D. M. 2010, ApJ, 710, 212

Bauer, F. E., Arévalo, P., Walton, D. J., et al. 2015, ApJ, 812, 116

Baumgartner, W. H., Tueller, J., Markwardt, C. B., et al. 2013, ApJS, 207, 19

Becker, R. H., White, R. L., & Helfand, D. J. 1995, ApJ, 450, 559

Bertin, E., & Arnouts, S. 1996, A&AS, 117, 393

Blustin, A. J., Page, M. J., Fuerst, S. V., Branduardi-Raymont, G., & Ashton, C. E. 2005, A&A, 431, 111

Boller, T., Brandt, W. N., & Fink, H. 1996, A&A, 305, 53

Bottacini, E., Ajello, M., & Greiner, J. 2012, ApJS, 201, 34

Bower, R. G., Benson, A. J., Malbon, R., et al. 2006, MNRAS, 370, 645

Boyle, B. J., Fong, R., Shanks, T., & Peterson, B. A. 1990, MNRAS, 243, 1

Brandt, W. N., & Alexander, D. M. 2015, A&A Rev., 23, 1

Brandt, W. N., & Hasinger, G. 2005, ARA&A, 43, 827

Brandt, W. N., Mathur, S., & Elvis, M. 1997, MNRAS, 285, L25

Brandt, W. N., Alexander, D. M., Hornschemeier, A. E., et al. 2001, AJ, 122, 2810

Brightman, M., & Nandra, K. 2011, MNRAS, 413, 1206

Brightman, M., Nandra, K., Salvato, M., et al. 2014, MNRAS, 443, 1999

Buchner, J., Georgakakis, A., Nandra, K., et al. 2015, ApJ, 802, 89

Burbridge, G. R. 1963, Radiotekhnika, 168

Burlon, D., Ajello, M., Greiner, J., et al. 2011, ApJ, 728, 58

Burtscher, L., Meisenheimer, K., Tristram, K. R. W., et al. 2013, A&A, 558, A149

Caccianiga, A., Severgnini, P., Braito, V., et al. 2004, A&A, 416, 901

Caccianiga, A., Severgnini, P., Della Ceca, R., et al. 2008, A&A, 477, 735

Cappi, M., Panessa, F., Bassani, L., et al. 2006, A&A, 446, 459

Cardamone, C. N., Urry, C. M., Damen, M., et al. 2008, ApJ, 680, 130

Cash, W. 1979, ApJ, 228, 939

Christensen, F. E., Jakobsen, A. C., Brejnholt, N. F., et al. 2011, in Proc. SPIE, Vol. 8147, Society of Photo-Optical Instrumentation Engineers (SPIE) Conference Series, 81470U

Civano, F., Hickox, R. C., Puccetti, S., et al. 2015, ApJ, 808, 185 (abbreviated to "C15" in the thesis text)

Collinson, J. S., Ward, M. J., Done, C., et al. 2015, MNRAS, 449, 2174

Comastri, A. 2004, in Astrophysics and Space Science Library, Vol. 308, Supermassive Black Holes in the Distant Universe, ed. A. J. Barger, 245

Comastri, A., Fiore, F., Vignali, C., et al. 2001, MNRAS, 327, 781

Comastri, A., Setti, G., Zamorani, G., & Hasinger, G. 1995, A&A, 296, 1

Comastri, A., Vignali, C., Brusa, M., Hellas, & Hellas2XMM Consortia. 2002, in Astronomical Society of the Pacific Conference Series, Vol. 284, IAU Colloq. 184: AGN Surveys, ed. R. F. Green, E. Y. Khachikian, & D. B. Sanders, 235

Comastri, A., Ranalli, P., Iwasawa, K., et al. 2011, A&A, 526, L9

Condon, J. J. 1992, ARA&A, 30, 575

Condon, J. J., Cotton, W. D., Greisen, E. W., et al. 1998, AJ, 115, 1693

Corral, A., Della Ceca, R., Caccianiga, A., et al. 2011, A&A, 530, A42

Cotini, S., Ripamonti, E., Caccianiga, A., et al. 2013, MNRAS, 431, 2661

Craig, W. W., An, H., Blaedel, K. L., et al. 2011, in Proc. SPIE, Vol. 8147, Society of Photo-Optical Instrumentation Engineers (SPIE) Conference Series, 81470H

Curtis, H. D. 1917, PASP, 29, 206

de Carvalho, R. R., Ribeiro, A. L. B., Capelato, H. V., & Zepf, S. E. 1997, ApJS, 110, 1

Del Moro, A., Mateos, S., Watson, M. G., & Akiyama, M. 2008, in 8th National Conference on AGN, ed. L. Lanteri, C. M. Raiteri, A. Capetti, & P. Rossi

Del Moro, A., Alexander, D. M., Mullaney, J. R., et al. 2013, A&A, 549, A59

Del Moro, A., Mullaney, J. R., Alexander, D. M., et al. 2014, ApJ, 786, 16

Della Ceca, R., Castelli, G., Braito, V., Cagnoni, I., & Maccacaro, T. 1999, ApJ, 524, 674

Della Ceca, R., Severgnini, P., Caccianiga, A., et al. 2008, Mem. Soc. Astron. Italiana, 79, 65

Dickinson, M., Giavalisco, M., & GOODS Team. 2003, in The Mass of Galaxies at Low and High Redshift, ed. R. Bender & A. Renzini, 324

Done, C., Davis, S. W., Jin, C., Blaes, O., & Ward, M. 2012, MNRAS, 420, 1848

Donley, J. L., Rieke, G. H., Pérez-González, P. G., & Barro, G. 2008, ApJ, 687, 111

Donley, J. L., Koekemoer, A. M., Brusa, M., et al. 2012, ApJ, 748, 142

Donoso, E., Yan, L., Stern, D., & Assef, R. J. 2014, ApJ, 789, 44

Draper, A. R., & Ballantyne, D. R. 2010, ApJ, 715, L99

Eckart, M. E., McGreer, I. D., Stern, D., Harrison, F. A., & Helfand, D. J. 2010, ApJ, 708, 584

Eckart, M. E., Stern, D., Helfand, D. J., et al. 2006, ApJS, 165, 19

Edge, A. C., & Stewart, G. C. 1991, MNRAS, 252, 414

Edge, D. O., Shakeshaft, J. R., McAdam, W. B., Baldwin, J. E., & Archer, S. 1959, MmRAS, 68, 37

Einstein, A. 1916, Annalen der Physik, 354, 769

Ekers, J. A. 1969, Australian Journal of Physics Astrophysical Supplement, 7

Elitzur, M. 2008, NewAR, 52, 274

Elvis, M., Maccacaro, T., Wilson, A. S., et al. 1978, MNRAS, 183, 129

Elvis, M., Wilkes, B. J., McDowell, J. C., et al. 1994, ApJS, 95, 1

Evans, I. N., Primini, F. A., Glotfelty, K. J., et al. 2010, ApJS, 189, 37

Evans, P. A., Osborne, J. P., Beardmore, A. P., et al. 2014, ApJS, 210, 8

Fabian, A. C. 1999, MNRAS, 308, L39

Fabian, A. C., & Barcons, X. 1992, ARA&A, 30, 429

Fabian, A. C., Vasudevan, R. V., & Gandhi, P. 2008, MNRAS, 385, L43

Fabian, A. C., Vasudevan, R. V., Mushotzky, R. F., Winter, L. M., & Reynolds, C. S. 2009, MNRAS, 394, L89

Ferrarese, L., & Merritt, D. 2000, ApJ, 539, L9

Fiore, F., Giommi, P., Vignali, C., et al. 2001, MNRAS, 327, 771

Fiore, F., Brusa, M., Cocchia, F., et al. 2003, A&A, 409, 79

Fiore, F., Puccetti, S., Brusa, M., et al. 2009, ApJ, 693, 447

Freeman, P. E., Kashyap, V., Rosner, R., & Lamb, D. Q. 2002, ApJS, 138, 185

Fruscione, A., McDowell, J. C., Allen, G. E., et al. 2006, in Society of Photo-Optical Instrumentation Engineers (SPIE) Conference Series, Vol. 6270, Society of Photo-Optical Instrumentation Engineers (SPIE) Conference Series

Gallagher, S. C., Brandt, W. N., Laor, A., et al. 2001, ApJ, 546, 795

Gandhi, P., Crawford, C. S., Fabian, A. C., & Johnstone, R. M. 2004, MNRAS, 348, 529

Gandhi, P., Horst, H., Smette, A., et al. 2009, A&A, 502, 457

Gandhi, P., Yamada, S., Ricci, C., et al. 2015, MNRAS, 449, 1845

Gandhi, P., Lansbury, G. B., Alexander, D. M., et al. 2014, ApJ, 792, 117 (abbreviated to "G14" in the thesis text)

Gandhi, P., Annuar, A., Lansbury, G. B., et al. 2016, ArXiv e-prints, arXiv:1605.08041

Gebhardt, K., Bender, R., Bower, G., et al. 2000, ApJ, 539, L13

Gehrels, N. 1986, ApJ, 303, 336

Georgantopoulos, I., Rovilos, E., Akylas, A., et al. 2011a, A&A, 534, A23

Georgantopoulos, I., Dasyra, K. M., Rovilos, E., et al. 2011b, A&A, 531, A116

George, I. M., & Fabian, A. C. 1991, MNRAS, 249, 352

Ghisellini, G., Haardt, F., & Fabian, A. C. 1993, MNRAS, 263, L9

Ghisellini, G., Haardt, F., & Matt, G. 1994, MNRAS, 267, 743

Giacconi, R., Gursky, H., Paolini, F. R., & Rossi, B. B. 1962, Physical Review Letters, 9, 439

Giacconi, R., Murray, S., Gursky, H., et al. 1974, ApJS, 27, 37

Giacconi, R., Bechtold, J., Branduardi, G., et al. 1979, ApJ, 234, L1

Giacconi, R., Zirm, A., Wang, J., et al. 2002, ApJS, 139, 369

Gilli, R., Comastri, A., & Hasinger, G. 2007, A&A, 463, 79

Gilli, R., Vignali, C., Mignoli, M., et al. 2010, A&A, 519, A92

Gilli, R., Su, J., Norman, C., et al. 2011, ApJ, 730, L28

Gioia, I. M., Maccacaro, T., Schild, R. E., et al. 1990, ApJS, 72, 567

Goodrich, R. W. 1989, ApJ, 342, 224

Goulding, A. D., & Alexander, D. M. 2009, MNRAS, 398, 1165

Goulding, A. D., Alexander, D. M., Bauer, F. E., et al. 2012, ApJ, 755, 5

Goulding, A. D., Alexander, D. M., Mullaney, J. R., et al. 2011, MNRAS, 411, 1231

Groth, E. J., Kristian, J. A., Lynds, R., et al. 1994, in Bulletin of the American Astronomical Society, Vol. 26, American Astronomical Society Meeting Abstracts, 1403

Hailey, C. J., An, H., Blaedel, K. L., et al. 2010, in Proc. SPIE, Vol. 7732, Space Telescopes and Instrumentation 2010: Ultraviolet to Gamma Ray, 77320T

Hainline, K. N., Hickox, R., Greene, J. E., Myers, A. D., & Zakamska, N. L. 2013, ApJ, 774, 145

Harp, D. I., Liebe, C. C., Craig, W., et al. 2010, in Proc. SPIE, Vol. 7738, Modeling, Systems Engineering, and Project Management for Astronomy IV, 77380Z

Harrison, F. A., Eckart, M. E., Mao, P. H., Helfand, D. J., & Stern, D. 2003, ApJ, 596, 944

Harrison, F. A., Christensen, F. E., Craig, W., et al. 2005, Experimental Astronomy, 20, 131

Harrison, F. A., Craig, W. W., Christensen, F. E., et al. 2013, ApJ, 770, 103

Harrison, F. A., Aird, J., Civano, F., et al. 2016, ApJ, 831, 185

Hasinger, G. 2004, Nuclear Physics B Proceedings Supplements, 132, 86

—. 2008, A&A, 490, 905

Hasinger, G., Miyaji, T., & Schmidt, M. 2005, A&A, 441, 417

Hazard, C., Mackey, M. B., & Shimmins, A. J. 1963, Nature, 197, 1037

Heckman, T. M., & Best, P. N. 2014, ARA&A, 52, 589

Heckman, T. M., Ptak, A., Hornschemeier, A., & Kauffmann, G. 2005, ApJ, 634, 161

Herschel, W. 1786, Philosophical Transactions of the Royal Society of London Series I, 76, 457

Hickox, R. C., & Markevitch, M. 2006, ApJ, 645, 95

Hickox, R. C., Jones, C., Forman, W. R., et al. 2007, ApJ, 671, 1365

Hong, J., Mori, K., Hailey, C. J., et al. 2016, ApJ, 825, 132

Hopkins, P. F., Hernquist, L., Cox, T. J., & Kereš, D. 2008, ApJS, 175, 356

Hornschemeier, A. E., Brandt, W. N., Garmire, G. P., et al. 2001, ApJ, 554, 742

Hoyle, F., & Fowler, W. A. 1963, MNRAS, 125, 169

Hubble, E. 1929a, Proceedings of the National Academy of Science, 15, 168

Hubble, E. P. 1926, ApJ, 64, doi:10.1086/143018

—. 1929b, ApJ, 69, doi:10.1086/143167

Huchra, J. P., Macri, L. M., Masters, K. L., et al. 2012, ApJS, 199, 26

Huggins, W., & Miller, W. A. 1864, Philosophical Transactions of the Royal Society of
    London Series I, 154, 437

Humphrey, A., Villar-Martín, M., Sánchez, S. F., et al. 2010, MNRAS, 408, L1

Ichikawa, K., Ueda, Y., Terashima, Y., et al. 2012, ApJ, 754, 45

Iwasawa, K., Koyama, K., Awaki, H., et al. 1993, ApJ, 409, 155

Iwasawa, K., Gilli, R., Vignali, C., et al. 2012, A&A, 546, A84

Jarrett, T. H., Cohen, M., Masci, F., et al. 2011, ApJ, 735, 112

Jia, J., Ptak, A., Heckman, T., & Zakamska, N. L. 2013, ApJ, 777, 27 (abbreviated to
    "J13" in the thesis text)

Jones, D. H., Saunders, W., Colless, M., et al. 2004, MNRAS, 355, 747

Jones, D. H., Read, M. A., Saunders, W., et al. 2009, MNRAS, 399, 683

Kalberla, P. M. W., Burton, W. B., Hartmann, D., et al. 2005, A&A, 440, 775

Kallman, T., & Mushotzky, R. 1985, ApJ, 292, 49

Kant, I. 1755, Allgemeine Naturgeschichte und Theorie des Himmels

Katz, J. I. 1976, ApJ, 206, 910

Kellermann, K. I., Sramek, R., Schmidt, M., Shaffer, D. B., & Green, R. 1989, AJ, 98, 1195

Khachikian, E. E., & Weedman, D. W. 1971, Astrofizika, 7, 389

Kim, D.-W., Cameron, R. A., Drake, J. J., et al. 2004, ApJS, 150, 19

Kirkpatrick, A., Pope, A., Charmandaris, V., et al. 2013, ApJ, 763, 123

Kitaguchi, T., Grefenstette, B. W., Harrison, F. A., et al. 2011, in Proc. SPIE, Vol. 8145, Society of Photo-Optical Instrumentation Engineers (SPIE) Conference Series, 814507

Kitaguchi, T., Bhalerao, V., Cook, W. R., et al. 2014, in Proc. SPIE, Vol. 9144, Space Telescopes and Instrumentation 2014: Ultraviolet to Gamma Ray, 91441R

Kocevski, D. D., Brightman, M., Nandra, K., et al. 2015, ApJ, 814, 104

Koglin, J. E., An, H., Blaedel, K. L., et al. 2009, in Proc. SPIE, Vol. 7437, Optics for EUV, X-Ray, and Gamma-Ray Astronomy IV, 74370C

Komatsu, E., Smith, K. M., Dunkley, J., et al. 2011, ApJS, 192, 18

Kormendy, J., & Ho, L. C. 2013, ARA&A, 51, 511

Kormendy, J., & Richstone, D. 1995, ARA&A, 33, 581

Koss, M., Mushotzky, R., Baumgartner, W., et al. 2013, ApJ, 765, L26

Koss, M., Mushotzky, R., Veilleux, S., et al. 2011, ApJ, 739, 57

Koss, M. J., Assef, R., Baloković, M., et al. 2016a, ApJ, 825, 85

Koss, M. J., Glidden, A., Baloković, M., et al. 2016b, ApJ, 824, L4

Kraft, R. P., Burrows, D. N., & Nousek, J. A. 1991, ApJ, 374, 344

Krivonos, R., Revnivtsev, M., Lutovinov, A., et al. 2007, A&A, 475, 775

Krivonos, R. A., Tsygankov, S. S., Lutovinov, A. A., et al. 2015, ApJ, 809, 140

Krolik, J. H., & Begelman, M. C. 1988, ApJ, 329, 702

Krolik, J. H., & Kriss, G. A. 1995, ApJ, 447, 512

La Franca, F., Fiore, F., Comastri, A., et al. 2005, ApJ, 635, 864

Lacy, M., Ridgway, S. E., Sajina, A., et al. 2015, ApJ, 802, 102

Lacy, M., Storrie-Lombardi, L. J., Sajina, A., et al. 2004, ApJS, 154, 166

Laing, R. A., Riley, J. M., & Longair, M. S. 1983, MNRAS, 204, 151

Laird, E. S., Nandra, K., Georgakakis, A., et al. 2009, ApJS, 180, 102

LaMassa, S. M., Heckman, T. M., & Ptak, A. 2012, ApJ, 758, 82

LaMassa, S. M., Heckman, T. M., Ptak, A., et al. 2009, ApJ, 705, 568

—. 2010, ApJ, 720, 786

—. 2011, ApJ, 729, 52

LaMassa, S. M., Yaqoob, T., Ptak, A. F., et al. 2014, ApJ, 787, 61

LaMassa, S. M., Ricarte, A., Glikman, E., et al. 2016, ApJ, 820, 70

Lansbury, G. B., Alexander, D. M., Del Moro, A., et al. 2014, ApJ, 785, 17 (abbreviated to "L14" in the thesis text)

Lansbury, G. B., Gandhi, P., Alexander, D. M., et al. 2015, ApJ, 809, 115 (abbreviated to "L15" in the thesis text)

Lanzuisi, G., Piconcelli, E., Fiore, F., et al. 2009, A&A, 498, 67

Lanzuisi, G., Ranalli, P., Georgantopoulos, I., et al. 2015a, A&A, 573, A137

Lanzuisi, G., Perna, M., Delvecchio, I., et al. 2015b, A&A, 578, A120

Laor, A., & Behar, E. 2008, MNRAS, 390, 847

Lawrence, A. 1991, MNRAS, 252, 586

Lawrence, A., Warren, S. J., Almaini, O., et al. 2007, MNRAS, 379, 1599

Lehmann, I., Hasinger, G., Schmidt, M., et al. 2001, A&A, 371, 833

Lehmer, B. D., Brandt, W. N., Alexander, D. M., et al. 2005, ApJS, 161, 21

Lehmer, B. D., Xue, Y. Q., Brandt, W. N., et al. 2012, ApJ, 752, 46

Leighly, K. M., Halpern, J. P., Jenkins, E. B., & Casebeer, D. 2007a, ApJS, 173, 1

Leighly, K. M., Halpern, J. P., Jenkins, E. B., et al. 2007b, ApJ, 663, 103

Levenson, N. A., Krolik, J. H., Życki, P. T., et al. 2002, ApJ, 573, L81

Liebe, C. C., Craig, W., Kim, Y., et al. 2012, Optical Engineering, 51, 043605

Lonsdale Persson, C. J., & Helou, G. 1987, ApJ, 314, 513

Luo, B., Brandt, W. N., Alexander, D. M., et al. 2013, ApJ, 772, 153

—. 2014, ApJ, 794, 70

Lusso, E., Hennawi, J. F., Comastri, A., et al. 2013, ApJ, 777, 86

Lutz, D., Maiolino, R., Spoon, H. W. W., & Moorwood, A. F. M. 2004, A&A, 418, 465

Lynden-Bell, D. 1969, Nature, 223, 690

Maccacaro, T., Gioia, I. M., Wolter, A., Zamorani, G., & Stocke, J. T. 1988, ApJ, 326, 680

Madsen, K. K., Harrison, F. A., Mao, P. H., et al. 2009, in Proc. SPIE, Vol. 7437, Optics for EUV, X-Ray, and Gamma-Ray Astronomy IV, 743716

Madsen, K. K., Harrison, F. A., Markwardt, C. B., et al. 2015, ApJS, 220, 8

Magdziarz, P., & Zdziarski, A. A. 1995, MNRAS, 273, 837

Magorrian, J., Tremaine, S., Richstone, D., et al. 1998, AJ, 115, 2285

Maiolino, R., & Rieke, G. H. 1995, ApJ, 454, 95

Maiolino, R., & Risaliti, G. 2007, in Astronomical Society of the Pacific Conference
    Series, Vol. 373, The Central Engine of Active Galactic Nuclei, ed. L. C. Ho & J.-W.
    Wang, 447

Maiolino, R., Salvati, M., Bassani, L., et al. 1998, A&A, 338, 781

Maiolino, R., Shemmer, O., Imanishi, M., et al. 2007, A&A, 468, 979

Malizia, A., Bassani, L., Bazzano, A., et al. 2012, MNRAS, 426, 1750

Marconi, A., & Hunt, L. K. 2003, ApJ, 589, L21

Markowitz, A. G., Krumpe, M., & Nikutta, R. 2014, MNRAS, 439, 1403

Massaro, E., Giommi, P., Leto, C., et al. 2009, A&A, 495, 691

Mateos, S., Alonso-Herrero, A., Carrera, F. J., et al. 2013, MNRAS, 434, 941

Mateos, S., Warwick, R. S., Carrera, F. J., et al. 2008, A&A, 492, 51

Mateos, S., Carrera, F. J., Page, M. J., et al. 2010, A&A, 510, A35

Mateos, S., Alonso-Herrero, A., Carrera, F. J., et al. 2012, MNRAS, 426, 3271

Mateos, S., Carrera, F. J., Alonso-Herrero, A., et al. 2015, MNRAS, 449, 1422

Mathur, S. 2000, MNRAS, 314, L17

Matsuta, K., Gandhi, P., Dotani, T., et al. 2012, ApJ, 753, 104

Matthews, T. A., & Sandage, A. R. 1963, ApJ, 138, 30

Mayo, J. H., & Lawrence, A. 2013, MNRAS, 434, 1593

McCarthy, P. J. 1993, ARA&A, 31, 639

McHardy, I. M., Gunn, K. F., Newsam, A. M., et al. 2003, MNRAS, 342, 802

Meléndez, M., Kraemer, S. B., Armentrout, B. K., et al. 2008, ApJ, 682, 94

Merloni, A., Bongiorno, A., Brusa, M., et al. 2014, MNRAS, 437, 3550

Messier, C. 1781, Catalogue des Nébuleuses & des amas d'Étoiles (Catalog of Nebulae and Star Clusters), Tech. rep.

Miley, G., & De Breuck, C. 2008, A&A Rev., 15, 67

Miniutti, G., Brandt, W. N., Schneider, D. P., et al. 2012, MNRAS, 425, 1718

Minkowski, R. 1960, ApJ, 132, 908

Monet, D. G., Levine, S. E., Canzian, B., et al. 2003, AJ, 125, 984

Moretti, A., Perri, M., Capalbi, M., et al. 2006, A&A, 448, L9

Mori, K., Hailey, C. J., Krivonos, R., et al. 2015, ApJ, 814, 94

Morris, S. L., Stocke, J. T., Gioia, I. M., et al. 1991, ApJ, 380, 49

Mortlock, D. J., Warren, S. J., Venemans, B. P., et al. 2011, Nature, 474, 616

Moustakas, J., & Kennicutt, Jr., R. C. 2006, ApJS, 164, 81

Mulchaey, J. S., Koratkar, A., Ward, M. J., et al. 1994, ApJ, 436, 586

Mullaney, J. R., Alexander, D. M., Goulding, A. D., & Hickox, R. C. 2011, MNRAS, 414, 1082

Mullaney, J. R., Del-Moro, A., Aird, J., et al. 2015, ApJ, 808, 184 (abbreviated to "M15" in the thesis text)

Murphy, K. D., & Yaqoob, T. 2009, MNRAS, 397, 1549

Mushotzky, R. F., Cowie, L. L., Barger, A. J., & Arnaud, K. A. 2000, Nature, 404, 459

Nandra, K., Georgantopoulos, I., Ptak, A., & Turner, T. J. 2003, ApJ, 582, 615

Nandra, K., & Pounds, K. A. 1994, MNRAS, 268, 405

Nandra, K., Laird, E. S., Adelberger, K., et al. 2005, MNRAS, 356, 568

Nandra, K., Barret, D., Barcons, X., et al. 2013, ArXiv e-prints, arXiv:1306.2307

Nenkova, M., Sirocky, M. M., Ivezić, Ž., & Elitzur, M. 2008a, ApJ, 685, 147

Nenkova, M., Sirocky, M. M., Nikutta, R., Ivezić, Ž., & Elitzur, M. 2008b, ApJ, 685, 160

Netzer, H. 2015, ARA&A, 53, 365

Netzer, H., Mainieri, V., Rosati, P., & Trakhtenbrot, B. 2006, A&A, 453, 525

Norman, C., Hasinger, G., Giacconi, R., et al. 2002, ApJ, 571, 218

Norman, C., Ptak, A., Hornschemeier, A., et al. 2004, ApJ, 607, 721

Nousek, J. A., & Shue, D. R. 1989, ApJ, 342, 1207

Opik, E. 1922, ApJ, 55, doi:10.1086/142680

Oppenheimer, J. R., & Volkoff, G. M. 1939, Physical Review, 55, 374

Orr, M. J. L., & Browne, I. W. A. 1982, MNRAS, 200, 1067

Osterbrock, D. E. 1981, ApJ, 249, 462

Panessa, F., & Bassani, L. 2002, A&A, 394, 435

Panessa, F., Bassani, L., Cappi, M., et al. 2006, A&A, 455, 173

Pâris, I., Petitjean, P., Aubourg, É., et al. 2012, A&A, 548, A66

Pâris, I., Petitjean, P., Ross, N. P., et al. 2016, ArXiv e-prints, arXiv:1608.06483

Perola, G. C., Puccetti, S., Fiore, F., et al. 2004, A&A, 421, 491

Petre, R., & Serlemitsos, P. J. 1985, Appl. Opt., 24, 1833

Pier, E. A., & Krolik, J. H. 1992, ApJ, 401, 99

Pietsch, W., Bischoff, K., Boller, T., et al. 1998, A&A, 333, 48

Pounds, K. A., Done, C., & Osborne, J. P. 1995, MNRAS, 277, L5

Prieto, M. A., Meisenheimer, K., Marco, O., et al. 2004, ApJ, 614, 135

Pringle, J. E., & Rees, M. J. 1972, A&A, 21, 1

Ptak, A., Serlemitsos, P., Yaqoob, T., & Mushotzky, R. 1999, ApJS, 120, 179

Ptak, A., Zakamska, N. L., Strauss, M. A., et al. 2006, ApJ, 637, 147

Puccetti, S., Comastri, A., Fiore, F., et al. 2014, ApJ, 793, 26

Radburn-Smith, D. J., Lucey, J. R., Woudt, P. A., Kraan-Korteweg, R. C., & Watson, F. G. 2006, MNRAS, 369, 1131

Ramsey, B. D., Alexander, C. D., Apple, J. A., et al. 2002, ApJ, 568, 432

Reichert, G. A., Mushotzky, R. F., Holt, S. S., & Petre, R. 1985, ApJ, 296, 69

Reyes, R., Zakamska, N. L., Strauss, M. A., et al. 2008, AJ, 136, 2373

Ricci, C., Ueda, Y., Koss, M. J., et al. 2015, ApJ, 815, L13

Richards, G. T., Fan, X., Schneider, D. P., et al. 2001, AJ, 121, 2308

Richards, G. T., Lacy, M., Storrie-Lombardi, L. J., et al. 2006, ApJS, 166, 470

Richards, G. T., Myers, A. D., Gray, A. G., et al. 2009, ApJS, 180, 67

Risaliti, G. 2002, A&A, 386, 379

Risaliti, G., & Elvis, M. 2004, in Astrophysics and Space Science Library, Vol. 308, Supermassive Black Holes in the Distant Universe, ed. A. J. Barger, 187

Risaliti, G., Elvis, M., Fabbiano, G., Baldi, A., & Zezas, A. 2005, ApJ, 623, L93

Risaliti, G., Elvis, M., Fabbiano, G., et al. 2007, ApJ, 659, L111

Risaliti, G., Elvis, M., & Nicastro, F. 2002, ApJ, 571, 234

Risaliti, G., Maiolino, R., & Salvati, M. 1999, ApJ, 522, 157

Roberts, B., Bester, M., Dumlao, R., et al. 2014, in Proc. SPIE, Vol. 9149, Observatory Operations: Strategies, Processes, and Systems V, 91490T

Rosario, D. J., McIntosh, D. H., van der Wel, A., et al. 2015, A&A, 573, A85

Rosati, P., Tozzi, P., Giacconi, R., et al. 2002, ApJ, 566, 667

Roseboom, I. G., Lawrence, A., Elvis, M., et al. 2013, MNRAS, 429, 1494

Rosen, S. R., Webb, N. A., Watson, M. G., et al. 2016, A&A, 590, A1

Rosse, T. E. O. 1850, Philosophical Transactions of the Royal Society of London Series I, 140, 499

Salpeter, E. E. 1964, ApJ, 140, 796

Sanders, D. B. 1999, in IAU Symposium, Vol. 194, Activity in Galaxies and Related Phenomena, ed. Y. Terzian, E. Khachikian, & D. Weedman, 25

Sanders, D. B., Soifer, B. T., Elias, J. H., et al. 1988, ApJ, 325, 74

Sargsyan, L., Weedman, D., Lebouteiller, V., et al. 2011, ApJ, 730, 19

Scheiner, J. 1899, ApJ, 9, doi:10.1086/140564

Schmidt, M. 1963a, Nature, 197, 1040

—. 1963b, Nature, 197, 1040

Schmidt, M., & Green, R. F. 1983, ApJ, 269, 352

Schmidt, M., Hasinger, G., Gunn, J., et al. 1998, A&A, 329, 495

Schwarzschild, K. 1916, Abh. Konigl. Preuss. Akad. Wissenschaften Jahre 1906,92, Berlin,1907, 1916

Scott, A. E., Stewart, G. C., Mateos, S., et al. 2011, MNRAS, 417, 992

Scoville, N., Aussel, H., Brusa, M., et al. 2007, ApJS, 172, 1

Setti, G., & Woltjer, L. 1989, A&A, 224, L21

Seyfert, C. K. 1943, ApJ, 97, 28

Shakura, N. I., & Sunyaev, R. A. 1973, A&A, 24, 337

Sharples, R., Bender, R., Agudo Berbel, A., et al. 2013, The Messenger, 151, 21

Shi, Y., Rieke, G. H., Hines, D. C., et al. 2006, ApJ, 653, 127

Silva, L., Granato, G. L., Bressan, A., & Danese, L. 1998, ApJ, 509, 103

Simpson, C. 2005, MNRAS, 360, 565

Slipher, V. M. 1913, Lowell Observatory Bulletin, 2, 56

—. 1915, Popular Astronomy, 23, 21

Smith, R. K., Brickhouse, N. S., Liedahl, D. A., & Raymond, J. C. 2001, ApJ, 556, L91

Soltan, A. 1982, MNRAS, 200, 115

Steffen, A. T., Strateva, I., Brandt, W. N., et al. 2006, AJ, 131, 2826

Steidel, C. C., Hunt, M. P., Shapley, A. E., et al. 2002, ApJ, 576, 653

Stern, D. 2015, ApJ, 807, 129

Stern, D., Moran, E. C., Coil, A. L., et al. 2002, ApJ, 568, 71

Stern, D., Eisenhardt, P., Gorjian, V., et al. 2005, ApJ, 631, 163

Stern, D., Assef, R. J., Benford, D. J., et al. 2012, ApJ, 753, 30

Stern, D., Lansbury, G. B., Assef, R. J., et al. 2014, ApJ, 794, 102

Stickel, M., Kuehr, H., & Fried, J. W. 1993, A&AS, 97, 483

Takahashi, T., Mitsuda, K., Kelley, R., et al. 2012, in Society of Photo-Optical Instrumentation Engineers (SPIE) Conference Series, Vol. 8443, Society of Photo-Optical Instrumentation Engineers (SPIE) Conference Series, 1

Teng, S. H., Brandt, W. N., Harrison, F. A., et al. 2014, ApJ, 785, 19

Thorne, K. S. 1974, ApJ, 191, 507

Tingay, S. J., Jauncey, D. L., King, E. A., et al. 2003, PASJ, 55, 351

Tozzi, P., Rosati, P., Nonino, M., et al. 2001, ApJ, 562, 42

Tozzi, P., Gilli, R., Mainieri, V., et al. 2006, A&A, 451, 457

Treister, E., Natarajan, P., Sanders, D. B., et al. 2010a, Science, 328, 600

Treister, E., & Urry, C. M. 2005, ApJ, 630, 115

—. 2006, ApJ, 652, L79

—. 2012, Advances in Astronomy, 2012, 516193

Treister, E., Urry, C. M., Schawinski, K., Cardamone, C. N., & Sanders, D. B. 2010b, ApJ, 722, L238

Treister, E., Urry, C. M., & Virani, S. 2009, ApJ, 696, 110

Treister, E., Urry, C. M., Chatzichristou, E., et al. 2004, ApJ, 616, 123

Tueller, J., Mushotzky, R. F., Barthelmy, S., et al. 2008, ApJ, 681, 113

Tueller, J., Krimm, H. A., Okajima, T., et al. 2005, Experimental Astronomy, 20, 121

Turner, T. J., George, I. M., Nandra, K., & Mushotzky, R. F. 1997, ApJ, 488, 164

Turner, T. J., & Pounds, K. A. 1989, MNRAS, 240, 833

Ueda, Y., Akiyama, M., Hasinger, G., Miyaji, T., & Watson, M. G. 2014, ApJ, 786, 104 (abbreviated to "U14" in the thesis text)

Ueda, Y., Akiyama, M., Ohta, K., & Miyaji, T. 2003, ApJ, 598, 886

Ueda, Y., Ishisaki, Y., Takahashi, T., Makishima, K., & Ohashi, T. 2005, ApJS, 161, 185

Ueda, Y., Takahashi, T., Inoue, H., et al. 1999, ApJ, 518, 656

Urry, C. M., & Padovani, P. 1995, PASP, 107, 803

Vanden Berk, D. E., Richards, G. T., Bauer, A., et al. 2001, AJ, 122, 549

Vasudevan, R. V., Brandt, W. N., Mushotzky, R. F., et al. 2013, ApJ, 763, 111

Véron-Cetty, M.-P., & Véron, P. 2010, A&A, 518, A10

Vignali, C., Alexander, D. M., & Comastri, A. 2006, MNRAS, 373, 321

Vignali, C., Alexander, D. M., Gilli, R., & Pozzi, F. 2010, MNRAS, 404, 48

Vignali, C., Comastri, A., Stirpe, G. M., et al. 1998, A&A, 333, 411

Vignali, C., Mignoli, M., Gilli, R., et al. 2014, A&A, 571, A34

Villar-Martín, M., Cabrera Lavers, A., Bessiere, P., et al. 2012, MNRAS, 423, 80

Voges, W., Aschenbach, B., Boller, T., et al. 1999, A&A, 349, 389

—. 2000, VizieR Online Data Catalog, 9029

Wachter, K., Leach, R., & Kellogg, E. 1979, ApJ, 230, 274

Wall, J. V., & Peacock, J. A. 1985, MNRAS, 216, 173

Watson, M. G., Auguères, J.-L., Ballet, J., et al. 2001, A&A, 365, L51

Watson, M. G., Schröder, A. C., Fyfe, D., et al. 2009, A&A, 493, 339

Weedman, D. W. 1970, ApJ, 159, 405

Weisskopf, M. C., Wu, K., Trimble, V., et al. 2007, ApJ, 657, 1026

Werner, M. W., Roellig, T. L., Low, F. J., et al. 2004, ApJS, 154, 1

Wik, D. R., Hornstrup, A., Molendi, S., et al. 2014, ApJ, 792, 48

Wilkes, B. J., Kuraszkiewicz, J., Haas, M., et al. 2013, ApJ, 773, 15

Wolter, H. 1952, Mirror systems with grazing incidence as image-forming optics for X-rays, Tech. rep.

Woltjer, L. 1959, ApJ, 130, 38

Wong, D. S., Chornock, R., & Filippenko, A. V. 2008, PASP, 120, 266

Worsley, M. A., Fabian, A. C., Bauer, F. E., et al. 2005, MNRAS, 357, 1281

Wright, E. L., Eisenhardt, P. R. M., Mainzer, A. K., et al. 2010, AJ, 140, 1868

Wright, T. 1750, An original theory or new hypothesis of the universe ..., doi:10.3931/e-rara-28672

Wu, J., Brandt, W. N., Hall, P. B., et al. 2011, ApJ, 736, 28

Xue, Y. Q., Luo, B., Brandt, W. N., et al. 2011, ApJS, 195, 10

Xue, Y. Q., Wang, S. X., Brandt, W. N., et al. 2012, ApJ, 758, 129

Yaqoob, T. 1997, ApJ, 479, 184

Yaqoob, T., & Murphy, K. D. 2011, MNRAS, 412, 835

York, D. G., Adelman, J., Anderson, Jr., J. E., et al. 2000, AJ, 120, 1579

Younes, G., Kouveliotou, C., Kargaltsev, O., et al. 2012, ApJ, 757, 39

Yuan, F.-T., Takeuchi, T. T., Matsuoka, Y., et al. 2012, A&A, 548, A117

Zakamska, N. L., Gómez, L., Strauss, M. A., & Krolik, J. H. 2008, AJ, 136, 1607

Zakamska, N. L., Strauss, M. A., Heckman, T. M., Ivezić, Ž., & Krolik, J. H. 2004, AJ, 128, 1002

Zakamska, N. L., Strauss, M. A., Krolik, J. H., et al. 2003, AJ, 126, 2125

—. 2006, AJ, 132, 1496

Zhang, W. W. 2009, in Proc. SPIE, Vol. 7437, Optics for EUV, X-Ray, and Gamma-Ray Astronomy IV, 74370N

Zhou, H., Wang, T., Yuan, W., et al. 2006, ApJS, 166, 128

Appendix A

Additional material for Chapter 5

A.1 Description of the *NuSTAR* Serendipitous Survey Source Catalogue

The *NuSTAR* serendipitous survey source catalogue, containing 497 sources in total, is provided in electronic format. Here we describe the columns of the catalogue, which are summarized in Table A.1.

Column 1: the unique source identification numbers (ID), in order of increasing right ascension (R.A.).

Column 2: the unique *NuSTAR* source names, following the IAU-approved format: NuSTAR JHHMMSS±DDMM.m, where m is the truncated fraction of one arcminute for the arcseconds component of the declination (decl.).

Columns 3, 4: the *NuSTAR* R.A. and decl. coordinates (J2000), as described in Section 5.2.3.

Columns 5–7: a binary flag indicating whether the source is detected with a false probability lower than our threshold of $\log(P_{\text{False}}) = -6$, for the soft (3–8 keV), hard (8–24 keV), and full (3–24 keV) bands. These three bands are abbreviated as SB, HB, and FB, respectively, throughout the source catalogue.

Columns 8–10: the same as columns 5–7, after deblending has been performed to account for contamination of the source counts from very nearby sources (see Section 5.2.4 of this chapter, and Section 2.3.2 of M15. Deblending only affects a very small

261

Table A.1: Column Descriptions for the Primary *NuSTAR* Serendipitous Source Catalogue

Column number	Description
1	Unique source identification number (ID).
2	Unique *NuSTAR* source name.
3, 4	Right ascension (R.A.) and declination (decl.).
5–7	Flags indicating the energy bands for which the source is detected.
8–10	Same as columns 5–7, post-deblending.
11–13	Logarithm of the false probabilities for the three standard energy bands.
14–16	Same as columns 11–13, post-deblending.
17	Flag indicating whether the source is significant post-deblending, for at least one energy band.
18–32	Total, background, and net source counts for the three standard energy bands, and associated errors.
33–44	Same as columns 18–32, post-deblending.
45–47	Net vignetting-corrected exposure times at the source position, for the combined A+B data.
48–62	Total, background, and net source count rates for the three standard energy bands, and associated errors.
63–68	Deblended net source count rates for the three standard energy bands, and associated errors.
69–71	Band ratio and upper and lower errors.
72–74	Effective photon index and upper and lower errors.
75–80	Deblended fluxes in the three standard bands and associated errors.
81	Reference for the adopted lower-energy X-ray (*Chandra*, *XMM-Newton* or *Swift* XRT) counterpart.
82, 83	R.A. and decl. of the lower-energy X-ray counterpart.
84	Angular separation between the *NuSTAR* and lower-energy X-ray counterpart positions.
85	3–8 keV (3XMM or CSC) flux of the lower-energy X-ray counterpart.
86	Total 3–8 keV flux of all (3XMM or CSC) sources within 30″ of the *NuSTAR* position.
87, 88	R.A. and decl. of the adopted *WISE* counterpart.
89	Angular separation between the *NuSTAR* and *WISE* counterpart positions.
90–97	*WISE* magnitudes in the four standard bands and associated errors.
98	Reference for the adopted optical counterpart.
99, 100	R.A. and decl. of the optical counterpart.
101	Angular separation between the *NuSTAR* and optical counterpart positions.
102	*R*-band magnitude for the optical counterpart.
103	Spectroscopic redshift.
104	Non-absorption-corrected, rest-frame 10–40 keV luminosity.
105	Binary flag to indicate sources associated with the primary science targets of their respective *NuSTAR* fields.
106	Binary flag to indicate the sources used for the Aird et al. (2015b) study.

Notes. Machine readable versions of the full table are available online.

fraction of the overall sample (e.g., see Section 5.2.4).

Columns 11–13: the logarithm of the false probabilities (P_{False}) of the *NuSTAR* detected sources, for the three standard energy bands (see Section 5.2.3).

Columns 14–16: the same as columns 11–13, after deblending has been performed.

Column 17: a binary flag indicating whether the *NuSTAR* detected source remains significant after deblending, in at least one of the three standard energy bands.

Columns 18–32: photometric quantities, calculated at the source coordinates in columns 3 and 4, and using a source aperture of $30''$ radius (see Section 5.2.4). The values are non-aperture-corrected; i.e., they correspond to the $30''$ values, and have not been corrected to the full PSF values. We provide the total counts (i.e., all counts within the source aperture) and associated errors (84% CL), the background counts scaled to the source aperture, and the net source counts (i.e., total minus background) and associated errors. For the latter, we give 3σ upper limits for sources not detected in a given band. Throughout the table, upper limits are flagged with a -99 value in the error column.

Columns 33–44: the same as columns 18–32, after deblending has been performed.

Columns 45–47: the average net, vignetting-corrected exposure time at the source coordinates (columns 3 and 4), for each energy band. These correspond to the A+B data, so should be divided by two to obtain the average exposure per FPM. Units: s.

Columns 48–62: the non-aperture-corrected total, background, and net count rates (and associated errors; $84\%CL$) determined from the photometric values in columns 18–32, and the exposure times in columns 45–47. Units: s^{-1}.

Columns 63–68: the deblended net count rates, and associated errors, determined from the photometric values in columns 33–44, and the exposure times in columns 45–47. Units: s^{-1}.

Columns 69–71: the *NuSTAR* band ratio (BR_{Nu}) and associated errors, as described in Section 5.2.4. Upper limits, lower limits, and sources with no constraints are flagged with -99, -88, and -77 values, respectively, in the error columns.

Columns 72–74: the effective photon index (Γ_{eff}), and associated errors, estimated from the band ratio values in columns 69–71 (see Section 5.2.4).

Columns 75–80: the observed-frame fluxes and associated errors ($84\%CL$) for the three standard energy bands, after deblending has been performed. These are aperture

corrected values (i.e., they correspond to the full *NuSTAR* PSF), and are calculated from the count rates in columns 63–68 using the conversion factors listed in Section 5.2.4. Units: $\mathrm{erg\ s^{-1}\ cm^{-2}}$.

Column 81: an abbreviated code indicating the origin of the adopted soft (i.e., low energy; < 10 keV) X-ray counterpart. CXO_CSC indicates counterparts from the *Chandra* Source Catalogue (CSC; Evans et al. 2010). XMM_3XMM indicates counterparts from the third *XMM-Newton* serendipitous source catalogue (3XMM; Watson et al. 2009; Rosen et al. 2016). CXO_MAN, XMM_MAN, and XRT_MAN indicate sources manually identified using archival *Chandra*, *XMM-Newton*, and *Swift* XRT data, respectively. Section 5.3.1 details the counterpart matching.

Columns 82, 83: the R.A. and decl. coordinates (J2000) of the soft X-ray counterpart.

Column 84: the angular offset between the *NuSTAR* position (columns 3 and 4) and the soft X-ray counterpart position (columns 82 and 83). Units: arcsec.

Column 85: the observed-frame 3–8 keV flux of the soft X-ray counterpart, for sources with counterparts in the CSC and 3XMM catalogues. For CSC sources we convert to the 3–8 keV flux from the 2–7 keV flux using a conversion factor of 0.83, and for the 3XMM sources we convert from the 4.5–12 keV flux using a conversion factor of 0.92. Units: $\mathrm{erg\ s^{-1}\ cm^{-2}}$.

Column 86: the total combined 3–8 keV flux of all (3XMM or CSC) sources within $30''$ of the *NuSTAR* position. Units: $\mathrm{erg\ s^{-1}\ cm^{-2}}$.

Columns 87, 88: the R.A. and decl. coordinates (J2000) of the *WISE* counterpart, if there is a match in the *WISE* all-sky survey catalogue (Wright et al., 2010). Section 5.3.2 details the *WISE* counterpart matching.

Column 89: the angular offset between the *NuSTAR* position (columns 3 and 4) and the *WISE* counterpart position (columns 87 and 88). Units: arcsec.

Columns 90–97: the *WISE* profile-fit magnitudes (and associated errors), for the four standard *WISE* bands: $W1$ ($\lambda \approx 3.4\ \mu$m), $W2$ ($\approx 4.6\ \mu$m), $W3$ ($\approx 12\ \mu$m), and $W4$ ($\approx 22\ \mu$m). Units: Vega mag.

Column 98: an abbreviated code indicating the origin of the adopted optical counterpart to the *NuSTAR* source. The code SDSS indicates sources with soft X-ray counterparts and successful matches in the SDSS DR7 catalogue (York et al., 2000). The code USNO

indicates sources with soft X-ray counterparts and successful matches in the USNOB1 catalogue (Monet et al., 2003). MAN indicates sources where the optical counterpart is manually identified in the available optical coverage. SDSS_WISE and USNO_WISE indicate the cases where there is no soft X-ray counterpart to the *NuSTAR* position, but a *WISE* AGN is identified within the *NuSTAR* error circle and successfully matched to the SDSS DR7 or USNOB1 catalogue. We give a detailed description of the procedure used to identify optical counterparts in Section 5.3.2.

Columns 99, 100: the R.A. and decl. coordinates (J2000) of the optical counterpart, for the sources with SDSS DR7 and USNOB1 matches.

Column 101: the angular offset between the *NuSTAR* position (columns 3 and 4) and the optical counterpart position (columns 99 and 100). Units: arcsec.

Column 102: the R-band magnitude of the optical counterpart. For the SDSS DR7 matches, this is calculated as $R = r - 0.16$. For the USNOB1 matches, this is taken as the mean of the two independent photographic plate measurements, R1mag and R2mag. For the manual identifications, the magnitude is taken from another optical catalogue or manually determined from the imaging data. Units: Vega mag.

Column 103: the spectroscopic redshift of the *NuSTAR* source. The large majority of the redshifts were obtained through our own campaign of ground-based spectroscopic followup of *NuSTAR* serendipitous survey sources (see Section 5.3.3).

Column 104: the rest-frame 10–40 keV luminosity, estimated from the fluxes in columns 75–80, following the procedure outlined in Section 5.2.4. Negative values indicate upper limits. The luminosities are observed values, uncorrected for any absorption along the line of sight. The intrinsic luminosities may therefore be higher, for highly absorbed AGNs. Units: $\mathrm{erg\ s^{-1}}$.

Column 105: a binary flag indicating the few sources which show evidence for being associated with the primary science targets of their respective *NuSTAR* observations, according to the definition in Section 5.2.3 [$\Delta(cz) < 0.05cz$].

Column 106: a binary flag highlighting the sources used in the Aird et al. (2015b) study.

A.2 Optical spectroscopic properties of individual objects

Here we provide details of the optical spectroscopic properties of individual sources from the *NuSTAR* serendipitous survey. As described in Section 5.3.3, these largely result from our dedicated followup campaign using the Keck, Magellan, NTT, and Palomar facilities, and also from existing publically available spectroscopy (primarily SDSS spectroscopy). Individual source spectra (F_ν versus λ) are shown in Figure A.1, and details for individual sources are tabulated in Table A.2, the columns of which are as follows: columns 1 and 2 give the unique source identification number and the unique *NuSTAR* source name, as listed in source catalogue; columns 3 and 4 give the source redshift and classification (see Section 5.3.3); column 5 lists the emission or absorption lines identified (the latter are marked with † symbols), which are additionally highlighted in Figure A.1; column 6 gives individual object notes, including references for literature spectra; and column 7 gives the unique observing run identification number, as defined in Table 5.4 ("S" and "L" mark spectra obtained from the SDSS and from elsewhere in the literature, respectively). In Figure A.1, we show (in the upper right corner of each subplot) the unique *NuSTAR* source name, the unique source ID, the source redshift, and the observing run identification number (corresponding to Tables 5.4 and A.2; with "S" again indicating SDSS spectra).

Table A.2: Summary of the optical spectroscopy for the *NuSTAR* serendipitous survey sources. The columns are described in Section A.2.

ID (1)	*NuSTAR* Name (2)	z (3)	Type (4)	Lines (5)	Notes (6)	Run (7)
1	NuSTARJ000011-7652.5	0.053	...	...	Jones et al. (2004, 2009)	L
2	NuSTARJ001130+0057.8	1.492	BL	C IV He II C III] Mg II [O II] [Ne III] Hδ	...	S
3	NuSTARJ001442+8131.9	0.365	BL	Mg II [Ne V] [O II] Hβ [O III] Hα [N II]	...	28
4	NuSTARJ001542+8134.4	...	...	...	Continuum detected	33
6	NuSTARJ001852-1026.1	0.332	BL	[Ne V] [O II] [Ne III] Hδ Hγ Hβ [O III] Hα [N II] [S II]	...	31
7	NuSTARJ001858-1022.7	1.172	NL	C III] Mg II [Ne V] [O II] [Ne III] Hδ Hγ	...	31
13	NuSTARJ002227-1854.7	0.287	NL	Mg II [Ne V] [O II] [Ne III] Hδ Hβ [O III] Hα [N II]	...	29
14	NuSTARJ002544+6818.8	0.012	NL	[O III] Hα [N II] [S II]	...	17
16	NuSTARJ005332+7304.0	1.403	NL	[Ne V] [O II] [Ne III]	...	38
17	NuSTARJ005408+7303.2	0.321	BL	Mg II [O II] [Ne III] Hδ Hγ Hβ [O III] Hα [N II]	...	31
21	NuSTARJ011042-4604.3	1.073	BL	C III] Mg II	...	5
23	NuSTARJ011103-4602.7	0.495	NL	Ca$^†_{H,K}$ Hγ Hβ [O III]	...	11
25	NuSTARJ012215+5002.2	0.021	...	...	Huchra et al. (2012)	L
28	NuSTARJ012809-1851.6	0.303	BL	Mg II [Ne V] [O II] Hβ [O III] Hα [N II]	...	29
32	NuSTARJ020932-1011.7	0.144	NL	[O II] [Ne III] Ca$^†_{H,K}$ G-band† Hβ [O III] Mg 1b† Na$^†_{D1,D2}$ [O I]	...	32
35	NuSTARJ022454+1842.4	0.380	NL	[O II] Hβ [O III] Hα [N II] [S II]	...	29
36	NuSTARJ022744+3121.2	1.488	NL	[O II]	Quality B	36
37	NuSTARJ023229+2023.7	0.029	BL	[Ne V] [O II] [Ne III] Hβ [O III] [O I] Hα [N II] [S II] [Ar III] CaT†	...	10
38	NuSTARJ023454-2934.5	0.679	BL	...	Pietsch et al. (1998)	L
39	NuSTARJ023536-2938.6	...	...	...	Continuum detected	32
40	NuSTARJ024219-0004.7	...	...	...	Continuum detected	31
41	NuSTARJ024259-0003.9	2.351	BL	Lyα Si IV C IV He II C III] C II] Mg II	...	S
42	NuSTARJ024429-2604.7	1.395	BL	C IV C III] Mg II [Ne V] [O II] [Ne III]	...	31
43	NuSTARJ024434-2612.9	...	...	...	Continuum detected	31

Table A.2 – continued from previous page

ID	NuSTAR Name	z	Type	Lines	Notes	Run
45	NuSTARJ024459-2603.6	0.519	BL?	Hβ Hα	Hα affected by strong cosmic ray	20
47	NuSTARJ024507-2605.7	0.751	NL	[O II] Hβ [O III]	...	18
48	NuSTARJ025031+5432.6	0.218	BL	Mg II [Ne V] [O II] [Ne III] Hδ Hγ Hβ [O III] Hα [N II]	...	36
50	NuSTARJ030356-0109.1	1.520	BL	C IV He II C III] C II] Mg II	...	S
51	NuSTARJ030749-2255.0	...	...	...	Continuum detected; tentative [O II] detection at $z = 0.601$	12
53	NuSTARJ030828-2253.6	0.394	BL	Mg II [O II] Hβ [O III] Hα	...	10
54	NuSTARJ031548-0218.9	0.679	BL	Mg II [O II] [Ne III] Hγ Hβ [O III]	...	34
55	NuSTARJ031558-0227.9	0.255	BL?	[Ne V] [O II] G-band† Hγ Hβ [O III] Mg 1b† Hα [N II] [S II]	...	32
56	NuSTARJ031602-0224.1	0.730	BL	Mg II [Ne V] [O II] [Ne III] Hγ Hβ [O III]	...	31
57	NuSTARJ031611-0224.8	1.066	BL	C III] Mg II [Ne V] [O II] [Ne III] Hδ Hγ Hβ	...	31
58	NuSTARJ031901-6629.7	1.180	BL	Mg II	Quality B	11
59	NuSTARJ031924-6629.9	0.391	NL	[O III] Hα	...	18
60	NuSTARJ031925-6635.0	0.281	NL	[O II] [Ne III] Ca$^\dagger_{H,K}$ Hδ G-band† Hγ Hβ [O III] He I [O I] Hα [N II] [S II]	...	32
64	NuSTARJ032459-0256.2	0.020	BL	Hβ [O III] [O I] Hα [N II] [S II]	...	10
65	NuSTARJ034404-4439.7	0.561	BL	Mg II [Ne V] [O II] [Ne III] Hδ Hγ Hβ [O III]	...	32
66	NuSTARJ034439-4433.3	1.217	BL	C III] C II] Mg II [O II] [Ne III]	...	32
67	NuSTARJ034632-3026.8	0.239	BL	[O II] [Ne III] Hβ [O III] Hα [N II] [S II]	...	10
68	NuSTARJ034646-3026.9	0.267	BL	Mg II [Ne V] [O II] [Ne III] Hδ Hγ Hβ [O III] Hα [N II]	...	31
69	NuSTARJ034912-1158.1	0.314	BL?	[O II] [Ne III] Hγ Hβ [O III] Hα [N II] [S II]	...	32
71	NuSTARJ035002-5014.5	0.794	BL	Mg II [O II] Hγ Hβ [O III]	...	32
72	NuSTARJ035009-5018.5	1.344	BL	C IV He II O III] C III] Mg II	...	32
74	NuSTARJ035636-4041.7	0.869	BL	Mg II [O II] G-band† Hβ	...	32
75	NuSTARJ035829+1030.4	...	...	...	Continuum detected	36
77	NuSTARJ035911+1031.4	0.167	NL	[O II] Hα [N II] [S II]	...	19
82	NuSTARJ042538-5714.5	0.000	Gal	Hδ Hγ Hβ Hα	...	32
83	NuSTARJ042612-5715.0	0.098	BL	[Ne V] [O II] Ca$^\dagger_{H,K}$ G-band† Hβ [O III] Mg 1b† Fe$_{IE2}^\dagger$ Na$^\dagger_{D1,D2}$ Hα	...	32

Continued on next page

Table A.2 – continued from previous page

ID	NuSTAR Name	z	Type	Lines	Notes	Run
84	NuSTARJ042711-1202.4	0.838	BL	Mg II [Ne V] Hγ Hβ [O III]	...	32
85	NuSTARJ042723-1207.0	0.289	NL	[O II] Ca$^\dagger_{H,K}$ G-band† Hβ [O III] Mg 1b† Fe I$_{E2}^\dagger$ [O I] [N II]	...	32
86	NuSTARJ043326+0517.1	0.866	NL?	Mg II [O II] Hβ [O III]	...	10
88	NuSTARJ043705-4713.7	...	...	...	Continuum detected	35
90	NuSTARJ043727-4711.5	0.051	BL	Hδ Hγ Hβ [O III] [Fe VII] Hα [S II]	...	22
91	NuSTARJ043734-4716.7	0.362	NL	Hγ Hβ [O III] Hα	...	22
92	NuSTARJ043750-4715.0	0.731	NL	Hγ Hβ [O III]	...	35
94	NuSTARJ050559-2349.9	0.036	NL	Ca$^\dagger_{H,K}$ G-band† Hβ [O III] Mg 1b† Na$^\dagger_{D1,D2}$ Hα [N II] [S II]	Jones et al. (2004, 2009)	L
95	NuSTARJ050608-2348.3	0.333	BL?	[O II] Hβ [O III] Hα [N II]	...	19
96	NuSTARJ051556-0012.6	0.927	BL	C III] Mg II	...	8
97	NuSTARJ051617-0013.7	0.201	NL	[O II] [O III] Hα	...	8
98	NuSTARJ051626-0012.2	0.000	Gal	Hβ Hα	...	8
99	NuSTARJ052100-2528.8	1.666	BL	C IV C III] Mg II	...	8
100	NuSTARJ052109-2519.1	1.196	BL	C IV C III] Mg II	...	8
101	NuSTARJ052531-4557.8	1.479	BL	...	Stickel et al. (1993)	L
102	NuSTARJ054259+6309.0	0.079	BL	[Ne V] [O II] [Ne III] Hδ Hγ Hβ [O III] [O I] Hα [N II] [S II]	...	31
103	NuSTARJ061452+7105.0	1.714	BL	C IV C III] Mg II	...	21
106	NuSTARJ061607+7106.8	1.705	BL	Lyα C IV C III] Mg II	...	20
107	NuSTARJ061639+7108.2	0.203	NL	[O II] Ca$^\dagger_{H,K}$ Hα [N II] [S II]	...	20
110	NuSTARJ063358+1742.4	0.891	NL	[O II] Ca$^\dagger_{H,K}$	...	6
113	NuSTARJ065003+6046.8	0.319	BL	Mg II [Ne V] [O II] [Ne III] Hδ Hγ Hβ [O III] Hα [N II]	...	31
114	NuSTARJ065010+6048.6	0.396	BL	Mg II [O II] Hα [N II]	...	14
116	NuSTARJ065318+7424.8	0.170	NL	[Ne V] [O II] [O III] Hα [N II]	...	31
117	NuSTARJ065751-5559.0	1.537	BL	C IV C III] Mg II	...	22
118	NuSTARJ065759-5550.2	2.310	BL	Lyα Si IV C IV C III]	...	22
119	NuSTARJ065805-5601.2	0.296	NL?	[Ne V] [O II] [Ne III] G-band† [O III] Mg 1b† Hα [N II] [S II]	...	32
120	NuSTARJ065843-5550.2	0.297	NL	[O III] Hα	...	18
124	NuSTARJ065947+1412.6	0.500	NL?	[Ne V] [O III] Hα [N II]	...	31

Table A.2 – continued from previous page

ID	NuSTAR Name	z	Type	Lines	Notes	Run
125	NuSTARJ070004+1414.6	0.134	NL	[O II] [Ne III] G-band† Hγ He II Hβ [O III] Mg 1b† Na†$_{\text{D1,D2}}$ [O I] Hα [N II]	...	32
127	NuSTARJ070014+1416.8	0.000	Gal	Ca†$_{\text{H,K}}$ Hδ G-band† Hγ He II Hβ Mg 1b† Fe$_{\text{I E2}}$† Na†$_{\text{D1,D2}}$ Hα	...	32
129	NuSTARJ070810-4933.2	0.186	NL	[O II] Ca†$_{\text{H,K}}$ G-band† Mg 1b† Na†$_{\text{D1,D2}}$ Hα	...	32
130	NuSTARJ070825-4937.8	1.654	BL	C IV C III] Mg II	...	22
131	NuSTARJ070829-4645.4	1.176	BL	C III] Mg II [Ne V] Hδ	...	32
133	NuSTARJ070859-4937.9	1.412	BL	C III] Mg II	...	18
134	NuSTARJ071109+5907.4	1.966	BL	Mg II	Quality B	36
135	NuSTARJ071345+4542.1	0.126	NL	[Ne V] [O II] [Ne III] Hδ† Hβ Hα [N II] [S II]	...	31
136	NuSTARJ071404+4541.0	0.167	NL	[Ne V] [O II] [Ne III] [O III] Hα [N II] [S II]	Hα affected by A-band telluric feature	31
137	NuSTARJ071422+3523.9	0.015	NL	[O II] [O III] Hα [N II]	...	13
138	NuSTARJ071422+4538.4	0.157	BL	[Ne V] [O II] [Ne III] Hδ Hγ [O III] Hα [N II] [S II]	Hα affected by A-band telluric feature	31
139	NuSTARJ071430+4540.2	0.159	NL	[Ne V] [O II] [Ne III] [O III]	Hα lost to A-band telluric feature	31
140	NuSTARJ071432+3515.0	0.596	NL	Mg II [O II] [Ne III] Hγ Hβ [O III]	...	13
141	NuSTARJ073730+5846.1	0.357	NL?	[O II] [Ne III] Hβ [O III] Hα [N II] [S II]	...	12
142	NuSTARJ073938-3146.4	...	...	...	Continuum detected; tentative Hα detection at $z \approx 0$	32
144	NuSTARJ073959-3147.8	0.000	Gal	Ca†$_{\text{H,K}}$ Hδ Hγ Hβ Mg 1b† Fe$_{\text{I E2}}$† Na†$_{\text{D1,D2}}$ Hα He I	...	24
146	NuSTARJ075611-4133.9	0.000	Gal	Ca†$_{\text{H,K}}$ G-band† Hβ Mg 1b† Na†$_{\text{D1,D2}}$ Hα CaT†	...	24
148	NuSTARJ075800+3920.4	0.095	BL	He I [Fe VII] [O I] Hα [N II] [S II] [Ar III]	...	19
149	NuSTARJ080359+0513.0	0.167	NL	Ca†$_{\text{H,K}}$ Mg 1b†	...	22
150	NuSTARJ080421+0504.9	0.000	Gal	Hδ Hγ Hβ Mg 1b† Na†$_{\text{D1,D2}}$ Hα	Counterpart uncertainty	35
152	NuSTARJ081003-7527.2	...	BL Lac?	...	...	22
153	NuSTARJ081900+7037.2	1.276	BL?	C IV C III] Mg II [Ne V] [O II] [Ne III] Hδ	...	31
154	NuSTARJ081910+7039.3	1.278	NL	Mg II [O II] [Ne III]	...	31

Table A.2 – continued from previous page

ID	*NuSTAR* Name	z	Type	Lines	Notes	Run
155	NuSTARJ082004+7037.2	1.319	BL	C IV C III] Mg II [Ne V] [O II] [Ne III] Hδ	...	31
157	NuSTARJ082031+7038.3	0.419	BL	Mg II [Ne V] [O II] [Ne III] Hδ Hγ Hβ [O III] Hα [N II]	...	31
158	NuSTARJ082303-0502.7	0.313	NL	[O II] [O III] Hα [N II]	...	23
160	NuSTARJ084034+3834.7	0.217	NL	Mg II [O II] Hβ [O III] Hα [N II] [S II]	...	19
163	NuSTARJ090016+3902.8	0.862	BL	C II] Mg II [O II] [Ne III] Hγ Hβ [O III]	...	S
164	NuSTARJ090028+3901.7	0.963	BL	Mg II Hγ	...	S
165	NuSTARJ090053+3856.3	0.229	NL	[O II] [Ne III] Hδ Hγ Hβ [O III] [O I] Hα [N II] [S II] [Ar III]	...	S
166	NuSTARJ091058+4532.3	0.245	NL	[O II] Hβ Hα [N II]	...	33
167	NuSTARJ091104+4528.0	0.295	BL	[O II] [Ne III] Hδ Hγ Hβ [O III] He I [O I] Hα [N II] [S II]	...	S
169	NuSTARJ092018+3706.4	0.235	NL	[O II] Ca$^{\dagger}_{H,K}$ G-band† Hβ [O III] Mg 1b† Na$^{\dagger}_{D1,D2}$ [O I] Hα [N II] [S II]	...	S
170	NuSTARJ092042-0808.9	1.495	BL	C IV C III] Mg II	...	20
171	NuSTARJ093534+6119.3	0.202	BL	[O II] [Ne III] Ca$^{\dagger}_{H,K}$ G-band† Hβ [O III] Mg 1b† Na$^{\dagger}_{D1,D2}$ [O I] Hα [N II] [S II]	...	S
173	NuSTARJ094010+0330.6	0.616	BL	[Ne IV] Mg II [Ne V] [O II] Hδ Hγ Hβ [O III]	...	S
174	NuSTARJ094031+0331.4	...	...	...	Continuum detected	36
175	NuSTARJ094052+0331.6	0.552	NL	C II] Mg II [O II] [Ne III] Hδ Hγ Hβ [O III] He I [O I] Hα [N II]	...	S
182	NuSTARJ095503+6944.7	1.249	BL	C IV C III] Mg II	...	21
183	NuSTARJ095507+6935.8	1.324	BL	C IV C III] Mg II	...	31
184	NuSTARJ095512+6947.6	0.675	BL	Mg II Hβ [O III]	...	14
190	NuSTARJ095735+6900.0	0.612	BL	Mg II [O II] Hβ [O III]	...	13
194	NuSTARJ095838+6909.2	0.000	Gal	Mg 1b† CaT†	...	13
195	NuSTARJ095848+6905.7	1.288	BL	C III] C III] Mg II	...	S
199	NuSTARJ100153+0300.7	0.044	NL?	[O II] Ca$^{\dagger}_{H,K}$ G-band† [O III] Mg 1b† Na$^{\dagger}_{D1,D2}$ [O I] Hα [N II] [S II] CaT†	...	S
200	NuSTARJ100206+5542.9	1.153	BL	C III] C II] Mg II [O II] [Ne III] Hδ	...	S
201	NuSTARJ100417+0517.4	0.268	NL	[O II] Ca$^{\dagger}_{H,K}$ G-band† Mg 1b†	...	22
203	NuSTARJ100714+1253.7	0.586	BL	Mg II [O II] [Ne III] Ca$^{\dagger}_{H,K}$ Hγ Hβ [O III] He I [O I] Hα [N II]	...	S
204	NuSTARJ100717+1245.7	1.284	BL	C IV He II C III] Mg II [O II] [Ne III] Ca$^{\dagger}_{H,K}$ Hδ Hγ	...	S

Table A.2 – continued from previous page

ID	NuSTAR Name	z	Type	Lines	Notes	Run
205	NuSTARJ100751+1245.5	0.214	BL	[O II] [Ne III] $Ca^{\dagger}_{H,K}$ G-band† Hγ Hβ [O III] Mg Ib† $Na^{\dagger}_{D1,D2}$ [O I]	...	S
206	NuSTARJ101609-3328.9	0.562	BL	Hα [N II] [S II] Mg II [Ne V] [O II] [Ne III] Hγ [O III]	...	22
211	NuSTARJ102318+0036.5	0.000	Gal	Hβ Fe I$_{E2}$† $Na^{\dagger}_{D1,D2}$ Hα	Counterpart uncertainty	35
213	NuSTARJ102345+0044.1	0.300	NL	[O II] $Ca^{\dagger}_{H,K}$ G-band† Hβ† [O III] Mg Ib† $Na^{\dagger}_{D1,D2}$ [O I] Hα [N II]	...	S
214	NuSTARJ102622+2545.2	0.326	BL?	[S II] Mg II [Ne V] [O II] [Ne III] $Ca^{\dagger}_{H,K}$ [O III] Hα	...	7
215	NuSTARJ102628+2544.2	0.827	BL	C III] Mg II [Ne V] [O II] [Ne III] Hγ	...	7
217	NuSTARJ102710-4352.5	0.498	BL	[O II] Hβ [O III] Hα [N II]	...	23
218	NuSTARJ102735-4351.0	1.096	BL	C III] Mg II	...	24
219	NuSTARJ102802-4351.0	1.784	BL	Si IV C IV C III] Mg II	...	32
220	NuSTARJ103410+6006.7	0.258	BL	[O II] [Ne III] Hβ [O III] Hα	...	12
222	NuSTARJ103813+5331.3	1.225	BL	C IV C III] Mg II	...	21
224	NuSTARJ104339+7025.5	0.086	NL	[O II] Hα [N II]	...	33
227	NuSTARJ105931+2429.8	0.908	BL	C II] Mg II [O II] [Ne III] Hδ Hγ Hβ	...	S
228	NuSTARJ110403+3813.8	1.096	BL	C III] Mg II	...	8
229	NuSTARJ110414+3807.2	0.725	NL	[O II] $Ca^{\dagger}_{H,K}$ [O III]	...	12
230	NuSTARJ110418+3820.8	2.046	BL	Lyα C IV C III] Mg II	...	31
234	NuSTARJ110728+7228.7	0.403	NL?	Hα [N II]	...	21
235	NuSTARJ110740+7232.5	2.111	BL	Lyα C IV C III] Mg II	...	34
236	NuSTARJ110752+7230.7	0.901	BL	C III] Mg II [Ne V] [O II] [Ne III] Hγ Hβ [O III]	...	36
237	NuSTARJ111320+0934.7	1.103	BL	Mg II	Quality B	22
239	NuSTARJ111417+3242.8	0.208	BL	[Ne V] [O II] $Ca^{\dagger}_{H,K}$ G-band† Hβ† [O III] Mg Ib† $Na^{\dagger}_{D1,D2}$ [O I] Hα	...	S
243	NuSTARJ112829+5831.8	0.410	NL	[N II] [S II] [O II] Hβ [O III] Hα	...	12
244	NuSTARJ113202+2744.0	0.171	NL	[Ne V] $Ca^{\dagger}_{H,K}$ Hδ† G-band† Hγ† Hβ† [O III] Mg Ib† $Na^{\dagger}_{D1,D2}$ [O I]	...	S
245	NuSTARJ113235+2735.6	0.691	NL	[N II] Mg II [O II] [Ne III] Hδ Hγ Hβ [O III]	...	36

Table A.2 – continued from previous page

ID	NuSTAR Name	z	Type	Lines	Notes	Run
246	NuSTARJ113900+5913.8	0.115	BL	[O II] [Ne III] Hδ Hγ Hβ [O III] He I [O I] Hα [N II] [S II] [Ar III]	...	S
247	NuSTARJ114004+3147.3	0.781	NL	Mg II [Ne V] [O II] [Ne III] Hβ [O III]	...	31
249	NuSTARJ115745+6005.0	2.923	BL?	Lyα C III]	...	4
250	NuSTARJ115833+4237.7	1.036	NL	[O II] [Ne III] Hδ	...	27
252	NuSTARJ115851+4243.2	0.002	NL	$Ca^\dagger_{H,K}$ G-band† Hβ [O III] Mg 1b† $Na^\dagger_{D1,D2}$ [O I] Hα [N II] [S II]	...	S
254	NuSTARJ115912+4232.7	0.177	NL	CaT† [Ne V] [O II] [O III] Hα	...	4
256	NuSTARJ120242+4437.2	0.296	NL?	Mg II [O II] Hβ [O III] Hα [N II]	...	33
257	NuSTARJ120308+4437.0	0.679	NL	[O II] Hγ Hβ [O III]	...	33
258	NuSTARJ120331+4431.4	1.669	BL	C IV Mg II	...	14
259	NuSTARJ120348+4428.0	1.994	BL	C IV Mg II	...	12
260	NuSTARJ120610-3157.1	0.234	NL?	[Ne V] [O II] [Ne III] Hδ Hγ Hβ [O III] Hα [N II] [S II]	...	36
261	NuSTARJ120613+4957.2	0.784	BL	C II] Mg II [O II] Hδ Hγ Hβ [O III]	...	S
263	NuSTARJ120647-3154.4	1.665	BL	C IV C III] Mg II	...	36
265	NuSTARJ121355+1404.4	0.154	BL	[O II] [Ne III] $Ca^\dagger_{H,K}$ G-band† Hγ Hβ [O III] Mg 1b† He I $Na^\dagger_{D1,D2}$	...	S
266	NuSTARJ121357+1407.3	0.245	NL	[O I] Hα [N II] [S II] $Ca^\dagger_{H,K}$ [O III] Hα [N II]	...	35
267	NuSTARJ121358+2936.1	0.131	BL	[O II] [Ne III] $Ca^\dagger_{H,K}$ Hδ G-band† Hγ Hβ [O III] He I [O I] Hα [N II]	...	S
268	NuSTARJ121405+1407.0	1.843	BL	[S II] [Ar III] Lyα C IV C III] Mg II	...	15
269	NuSTARJ121407+1409.5	0.300	BL	Mg II [O II] [Ne III] $Ca^\dagger_{H,K}$ Hδ G-band† Hγ Hβ [O III] Mg 1b†	...	S
270	NuSTARJ121411+1359.0	0.377	BL	$Na^\dagger_{D1,D2}$ [O I] Hα [N II] [S II] Mg II [O II] Hβ [O III] Hα [N II] [S II]	...	15
272	NuSTARJ121415+1408.1	0.318	NL	[O II] Hβ [O III] Hα [N II]	...	33
273	NuSTARJ121425+2936.1	0.308	BL	[O II] [Ne III] Hδ Hγ Hβ [O III] He I [O I] Hα [N II] [S II]	...	S
274	NuSTARJ121426-1405.9	...	...	...	Continuum detected	36
275	NuSTARJ121426+1403.1	1.277	BL	C III] C II] Mg II [O II] [Ne III] $Ca^\dagger_{H,K}$	...	S

Table A.2 – continued from previous page

ID	*NuSTAR* Name	z	Type	Lines	Notes	Run
276	NuSTARJ121427+1410.8	...	...	[O II] Ca$^\dagger_{H,K}$ G-band† Hβ [O III] Mg 1b† Na$^\dagger_{D1,D2}$ Hα [N II] [S II]	Counterpart uncertainty	S
277	NuSTARJ121430+1406.4	0.216	NL	[Ar III] [O II] Ca$^\dagger_{H,K}$ G-band† Hβ [O III] Mg 1b† Na$^\dagger_{D1,D2}$ H$\alpha^\dagger$ [N II] [S II]	...	S
278	NuSTARJ121435+1404.5	...	...	[Ar III] ...	Possible Balmer lines at $z = 0$; counterpart uncertainty	35
280	NuSTARJ121849+2945.9	1.318	BL	C IV C III] Mg II	...	36
281	NuSTARJ121849+2954.6	0.962	BL	C II] Mg II [O II] Ca$^\dagger_{H,K}$	...	S
284	NuSTARJ122733+3210.7	0.961	NL	C III] Mg II [Ne V] [O II] Hγ Hβ [O III]	...	38
285	NuSTARJ122751+3212.2	0.733	BL	Mg II [Ne V] [O II] [Ne III] Hδ Hγ Hβ [O III]	...	27
287	NuSTARJ123041+5752.9	0.745	BL	[O II] Hγ Hβ [O III]	...	38
288	NuSTARJ124043-3645.5	1.475	BL	C IV C III] Mg II	...	22
292	NuSTARJ124347-0228.9	1.206	BL	C III] Mg II [Ne V]	...	22
293	NuSTARJ124946+2629.0	0.407	BL	Mg II [Ne V] [O II] [Ne III] Hγ Hβ [O III] Hα [N II]	...	33
294	NuSTARJ124954+2633.1	0.831	BL	C III] Mg II [Ne V] [O II] [Ne III] Hγ Hβ [O III]	...	33
295	NuSTARJ125609+5649.0	1.161	BL	C III] C II] Mg II [O II] [Ne III] Hδ Hγ [O III]	...	S
296	NuSTARJ125617-0543.8	1.764	BL	Lyα C IV C III] Mg II	...	36
297	NuSTARJ125623-0545.6	0.934	BL	C III] Mg II	...	14
298	NuSTARJ125631+5652.1	2.275	BL	Lyα C IV He II C III] C II] Mg II	...	S
299	NuSTARJ125636-0543.7	1.439	BL	C IV C III] Mg II [O II]	...	15
300	NuSTARJ125644+5647.4	1.966	BL	C IV He II C III] C II] Mg II	...	S
302	NuSTARJ125657+5644.6	2.073	BL	Lyα C IV He II C III]	...	15
305	NuSTARJ130906+1133.3	0.840	NL	Mg II [Ne V] [O II] [Ne III] Hδ Hβ [O III]	...	22
306	NuSTARJ130915+1140.5	0.324	NL	[O II] Hβ [O III] Hα	...	22
308	NuSTARJ131513-5513.2	...	...	...	Continuum detected; likely line at ≈ 4870Å	16
309	NuSTARJ131539-5512.6	0.136	NL	Ca$^\dagger_{H,K}$ G-band† [O III] Mg 1b† Hα [N II]	...	24
310	NuSTARJ132903+5827.0	2.026	BL	Lyα C IV C III] Mg II	...	36

Table A.2 – continued from previous page

ID	NuSTAR Name	z	Type	Lines	Notes	Run
311	NuSTARJ132916+5827.8	0.817	BL?	Mg II [O II] [Ne III] Hβ	...	9
312	NuSTARJ132934+5828.7	0.592	BL	Mg II [O II] [Ne III] Hβ [O III]	...	9
313	NuSTARJ133311-3406.8	0.091	NL?	Hβ [O III] Hα [N II] [S II]	...	22
316	NuSTARJ133628-3414.1	0.000	Gal	...	...	16
317	NuSTARJ134447+5546.8	0.936	BL	Mg II [O II] [Ne III] Hδ Hγ [O III]	...	S
318	NuSTARJ134513+5547.8	1.167	BL	C III] C II] Mg II [O II] [Ne III] Hδ	...	S
319	NuSTARJ134906-3023.1	1.304	BL	C III] Mg II	...	16
320	NuSTARJ134934-3025.5	0.163	NL	[O II] $Ca^\dagger_{H,K}$ G-band† Mg 1b†	...	22
321	NuSTARJ134937+0208.8	0.317	BL	Mg II Hδ Hγ Hβ [O III] Hα [N II]	...	24
324	NuSTARJ135358+3328.1	0.077	NL	[O II] $Ca^\dagger_{H,K}$ G-band† Hγ Hβ [O III] Mg 1b† $Na^\dagger_{D1,D2}$ [O I] Hα [N II]	...	S
325	NuSTARJ140515+4326.4	0.135	BL	[S II] [O II] $Ca^\dagger_{H,K}$ G-band† [O III] Mg 1b† He I $Na^\dagger_{D1,D2}$ [O I] Hα [N II]	...	S
328	NuSTARJ141056-4230.0	0.067	NL	[S II] [O II] $Ca^\dagger_{H,K}$ G-band† [O III] $Na^\dagger_{D1,D2}$ Hα [N II]	Radburn-Smith et al. (2006)	L
333	NuSTARJ141338-6524.8	0.088	BL?	Hδ Hγ Hβ [O III] Hα	...	24
334	NuSTARJ141809+2500.7	0.723	BL?	Mg II [O II] Hβ [O III]	...	14
335	NuSTARJ143026+4159.9	0.352	BL	[O II] [Ne III] Hδ Hγ Hβ [O III] He I Hα [N II]	...	S
336	NuSTARJ143035+4159.9	1.529	BL	C IV C III] Mg II [Ne V] [O II] [Ne III]	...	27
338	NuSTARJ143543+5846.9	0.632	NL	Mg II [O II] [Ne III] Hδ Hγ Hβ [O III]	...	36
339	NuSTARJ143602+5850.9	0.379	NL?	[Ne V] [O II] [Ne III] Hγ Hβ [O III] Hα [N II] [S II]	...	36
340	NuSTARJ143636+5843.0	0.000	Gal	...	Agüeros et al. (2009)	L
341	NuSTARJ144238-1709.8	...	...	...	Continuum detected	15
342	NuSTARJ144336+2459.1	2.136	BL	Lyα C IV C III] Mg II	...	37
343	NuSTARJ144405+2500.2	0.600	NL	[O II] $Ca^\dagger_{H,K}$ Hδ† Hγ† Hβ† [O III]	...	37
344	NuSTARJ144406+2506.3	1.539	NL?	C IV C III]	...	30
345	NuSTARJ144528+2702.2	0.469	BL	Mg II Hγ Hβ [O III] Hα [N II]	...	14
346	NuSTARJ144618-6415.0	0.355	BL	Hβ [O III] Hα	...	16
347	NuSTARJ145439-5135.3	0.186	NL	Hβ [O III] Hα [N II] [S II]	...	35
349	NuSTARJ145824-3143.5	1.434	BL	C IV He II C III] Mg II	...	24

Table A.2 – continued from previous page

ID	NuSTAR Name	z	Type	Lines	Notes	Run
351	NuSTARJ145836-3142.1	0.601	BL	Mg II [O II]	...	24
353	NuSTARJ145857-3135.5	1.045	BL	...	Caccianiga et al. (2008)	L
354	NuSTARJ150333+1024.5	1.127	BL	C IV C III] Mg II [O II] Hγ	...	38
355	NuSTARJ150645+0346.2	0.034	NL	[O II] Ca$^\dagger_{\rm H,K}$ G-band† H$\beta^\dagger$ [O III] Mg 1b† Na$^\dagger_{\rm D1,D2}$ Hα [N II] [S II]	...	S
356	NuSTARJ151253-8124.3	0.069	NL	CaT† [O III] Hα [N II]	...	16
358	NuSTARJ151440+4200.5	0.373	NL	Mg II [O II] [Ne III] Hα [N II]	...	26
359	NuSTARJ151508+4208.6	0.289	NL	Mg II [Ne V] [O II] [Ne III] Hβ [O III] [O I] Hα [N II] [S II]	...	15
360	NuSTARJ151549+5610.4	0.294	BL	Mg II [O III] Hα [N II]	...	29
361	NuSTARJ151610+5613.7	0.969	NL	C III] [Ne V] [O II] Ca$^\dagger_{\rm H,K}$ [O III]	...	15
362	NuSTARJ151627+5612.9	0.540	BL	Mg II [O II] Hβ [O III]	...	15
363	NuSTARJ151654+5617.6	1.310	BL	C III] Mg II [O II] [Ne III]	...	15
364	NuSTARJ153443+2323.7	...	...	Ca$^\dagger_{\rm H,K}$ G-band† Mg 1b† Na$^\dagger_{\rm D1,D2}$ [O I] Hα [N II]	Continuum detected	30
365	NuSTARJ153445+2331.5	0.160	NL	Mg II [O II] [Ne III] Ca$^\dagger_{\rm H,K}$ G-band† Hβ [O III] Mg 1b† Na$^\dagger_{\rm D1,D2}$ [O I]	...	S
366	NuSTARJ153548+5747.0	0.314	NL?	Hα [N II] [S II]	...	S
367	NuSTARJ153638+5750.2	0.336	NL	[O II] [O III] Hα [N II]	...	15
369	NuSTARJ162055+8108.1	1.149	BL	C IV C III] Mg II	...	29
370	NuSTARJ163017+3920.7	1.191	BL	C III] C II] Mg II [O II]	...	S
371	NuSTARJ164327+7034.0	0.560	BL	Mg II [Ne V] [O II] Hβ [O III]	...	10
372	NuSTARJ165105-0129.4	0.041	NL	[O II] Ca$^\dagger_{\rm H,K}$ Hδ G-band† Hβ [O III] Mg 1b† Na$^\dagger_{\rm D1,D2}$ Hα [N II] [S II]	...	24
374	NuSTARJ165312+0224.4	1.970	BL	Si IV C IV He II C III] Mg II	...	22
375	NuSTARJ165346+3953.7	0.354	NL	Mg II [O II] Ca$^\dagger_{\rm H,K}$ H$\beta^\dagger$ [O III] Hα [N II]	...	37
376	NuSTARJ165351+3938.5	0.000	Gal	CaT†	...	36
379	NuSTARJ170114+2927.8	0.259	BL	[Ne V] [O II] [Ne III] Hδ Hγ Hβ [O III] Hα [N II]	...	25
380	NuSTARJ170132+5144.5	2.012	BL	Lyα C IV C III] Mg II	...	36
382	NuSTARJ171309+5734.3	0.243	BL	[O II] [Ne III] Ca$^\dagger_{\rm H,K}$ G-band† Hγ Hβ [O III] Mg 1b† He I [O I] Hα [N II] [S II] [Ar III]	...	S

Table A.2 – continued from previous page

ID	NuSTAR Name	z	Type	Lines	Notes	Run
387	NuSTARJ172326-2836.4	...	...	CaT†	Counterpart uncertainty	37
388	NuSTARJ172750-1414.8	0.279	BL	Hβ Hα	...	16
390	NuSTARJ172803-1423.0	1.555	BL	C III] Mg II	...	23
391	NuSTARJ172805-1416.5	1.582	BL	C IV C III] Mg II	...	15
392	NuSTARJ172805-1420.9	0.197	NL	[O III] Hα [N II]	...	23
394	NuSTARJ172807-1418.2	...	...	...	Possibly two sources contributing to NuSTAR detection	23
399	NuSTARJ175323-0132.5	0.760	NL	Hδ Hγ Hβ [O III]	...	30
400	NuSTARJ175538-3314.9	...	...	...	Two spectra obtained, both showing CaT absorption at $z =$ 0	37
401	NuSTARJ181429+3410.8	0.763	BL	C III] C II] Mg II	...	3
408	NuSTARJ182604-0707.9	0.000	Gal	Hα	...	30
409	NuSTARJ182615+7209.7	1.225	BL	C III] Mg II	...	21
417	NuSTARJ183443+3237.8	0.510	BL	Mg II [Ne V] [O II] [Ne III] Hβ [O III]	...	1
421	NuSTARJ183639-2851.2	...	...	H$\alpha^\dagger$ CaT†	Counterpart uncertainty	37
428	NuSTARJ184135-0502.3	...	...	...	Extremely red continuum; likely Galactic	38
429	NuSTARJ185900-7828.1	0.076	BL	Hβ [O III] Hα [N II]	...	16
431	NuSTARJ191311-5008.0	0.157	NL	[O II] H$\delta^\dagger$ G-band† H$\gamma^\dagger$ [O III] Hα	Hα affected by telluric absorption	24
432	NuSTARJ192607+4134.1	0.777	BL	C III] Mg II Hβ [O III]	...	15
433	NuSTARJ193114-7241.8	0.723	BL	Mg II	Quality B	16
435	NuSTARJ193241-7242.4	0.599	NL	[O II] [O III]	...	23
436	NuSTARJ193246-7233.8	0.287	NL	[O II] Ca$^\dagger_{H,K}$ G-band† Hβ [O III] Mg Ib†	Caccianiga et al. (2004)	L
438	NuSTARJ195204+0234.6	1.173	BL	C III] Mg II	...	24
444	NuSTARJ202339+3347.7	...	Gal	CaT†	Counterpart uncertainty	17
445	NuSTARJ202351+3354.3	...	Gal	CaT†	Counterpart uncertainty	17

Table A.2 – continued from previous page

ID	NuSTAR Name	z	Type	Lines	Notes	Run
447	NuSTARJ202420+3347.7	...	Gal	Ca$^\dagger_{H,K}$ CaT†	Possibly incorrect counterpart due to high source density	31
448	NuSTARJ202421+3350.9	...	...	Hδ† Hγ† Hβ† Hα†	Counterpart uncertainty	37
449	NuSTARJ202828+2543.4	0.014	NL	...	Koss et al. (2016b)	L
450	NuSTARJ203956-0054.6	0.319	NL	[O II] Hβ [O III] Hα [N II] [S II]	...	37
451	NuSTARJ204020-0056.1	0.601	NL	[O II] [O III]	...	2
455	NuSTARJ204342-1040.4	0.816	NL	Mg II [Ne V] [O II] [Ne III] Hβ [O III]	...	29
459	NuSTARJ205829-4236.6	0.232	BL	...	Caccianiga et al. (2008)	L
460	NuSTARJ211459+0606.3	...	...	...	Continuum detected	38
461	NuSTARJ211506+0607.6	0.689	BL	Mg II [Ne V] [O II] [Ne III] Hδ Hγ Hβ [O III]	...	31
462	NuSTARJ211517+0608.7	0.400	BL	Mg II [O II] Hδ Hγ Hβ [O III] Hα [N II]	...	37
465	NuSTARJ212800+5651.8	...	...	Hβ Hα	Possibly incorrect counterpart due to high source density	10
469	NuSTARJ215218-3027.0	0.379	BL?	Mg II [O II] [Ne III] Hγ Hβ [O III] Hα [N II]	...	37
472	NuSTARJ220135-3153.3	0.097	...	...	de Carvalho et al. (1997)	L
473	NuSTARJ220530-0157.6	1.619	BL	...	Barcons et al. (2007)	L
474	NuSTARJ220633+1011.3	0.291	NL	Mg II [O II] Hβ [O III] Hα [N II] [S II]	...	10
475	NuSTARJ220714+1014.6	0.484	NL?	Mg II [Ne V] [O II] Hβ [O III] Hα	...	10
476	NuSTARJ220901-4716.4	0.976	BL	C III] Mg II	...	24
477	NuSTARJ220926-4715.2	0.405	BL	[Ne V] [O II] Hγ Hβ [O III] Hα	...	24
479	NuSTARJ222657+3614.4	0.873	BL	C III] Mg II [Ne V] [O II] [Ne III] Hδ Hγ Hβ [O III]	...	31
481	NuSTARJ223738+3422.6	1.099	BL	C III] Mg II [Ne V] [O II] [Ne III] Hδ Hγ	...	28
483	NuSTARJ224225+2942.0	0.304	BL	Mg II [Ne V] [O II] [Ne III] Hδ Hβ [O III] Hα [N II] [S II]	...	28
484	NuSTARJ224231+2939.3	0.121	NL	[Ne V] [O II] Hα [N II] [S II]	...	28
486	NuSTARJ225433-1732.6	0.229	BL	Mg II [Ne V] [O II] [Ne III] Hγ Hβ [O III] Hα [N II]	...	37
490	NuSTARJ231410+1449.8	0.289	NL	Mg II [Ne V] [O II] [Ne III] Hδ Hγ Hβ [O III] Hα [N II] [S II]	Companion NLAGN galaxy at 2.8″ offset and z = 0.291	30
492	NuSTARJ231840-4223.0	0.464	NL	[O II] Ca$^\dagger_{H,K}$ Hβ [O III]	...	18

Continued on next page

Table A.2 – continued from previous page

ID	*NuSTAR* Name	z	Type	Lines	Notes	Run
494	NuSTARJ232728+0849.3	3.430	BL	Lyα C IV C III]	Lyman alpha forest; highest red-shift	31
495	NuSTARJ232744+0850.1	...	...	...	Continuum detected	30
496	NuSTARJ233408−2345.5	0.507	BL	Mg II [Ne V] [O II] [Ne III] Hγ He II Hβ [O III]	...	32
497	NuSTARJ233426−2343.9	0.000	Gal	Ca$^{\dagger}_{\mathrm{H,K}}$ G-band† Mg Ib† Fe I$_{\mathrm{E2}}^{\dagger}$ Na$^{\dagger}_{\mathrm{D1,D2}}$ Hα	...	32
498	NuSTARJ235924−6056.1	1.295	BL	He II C III] C II] Mg II	...	24

Figure A.1: Optical spectra for the *NuSTAR* serendipitous survey sources. The horizontal axis shows the wavelength in units of Å, and the vertical axis shows the flux (f_ν) in units of erg s^{-1} cm^{-2} Hz^{-1}. The identified emission and absorption lines are labelled and marked with vertical dashed gray lines.

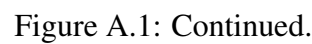Figure A.1: Continued.

Figure A.1: Continued.

Figure A.1: Continued.

Figure A.1: Continued.

Figure A.1: Continued.

Figure A.1: Continued.
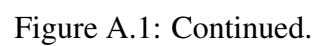
Figure A.1: Continued.

Figure A.1: Continued.

Figure A.1: Continued.

Figure A.1: Continued.

Figure A.1: Continued.

Figure A.1: Continued.

Figure A.1: Continued.

Figure A.1: Continued.

Figure A.1: Continued.

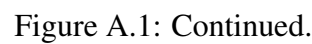Figure A.1: Continued.

Figure A.1: Continued.

Figure A.1: Continued.

Figure A.1: Continued.

Figure A.1: Continued.

Figure A.1: Continued.
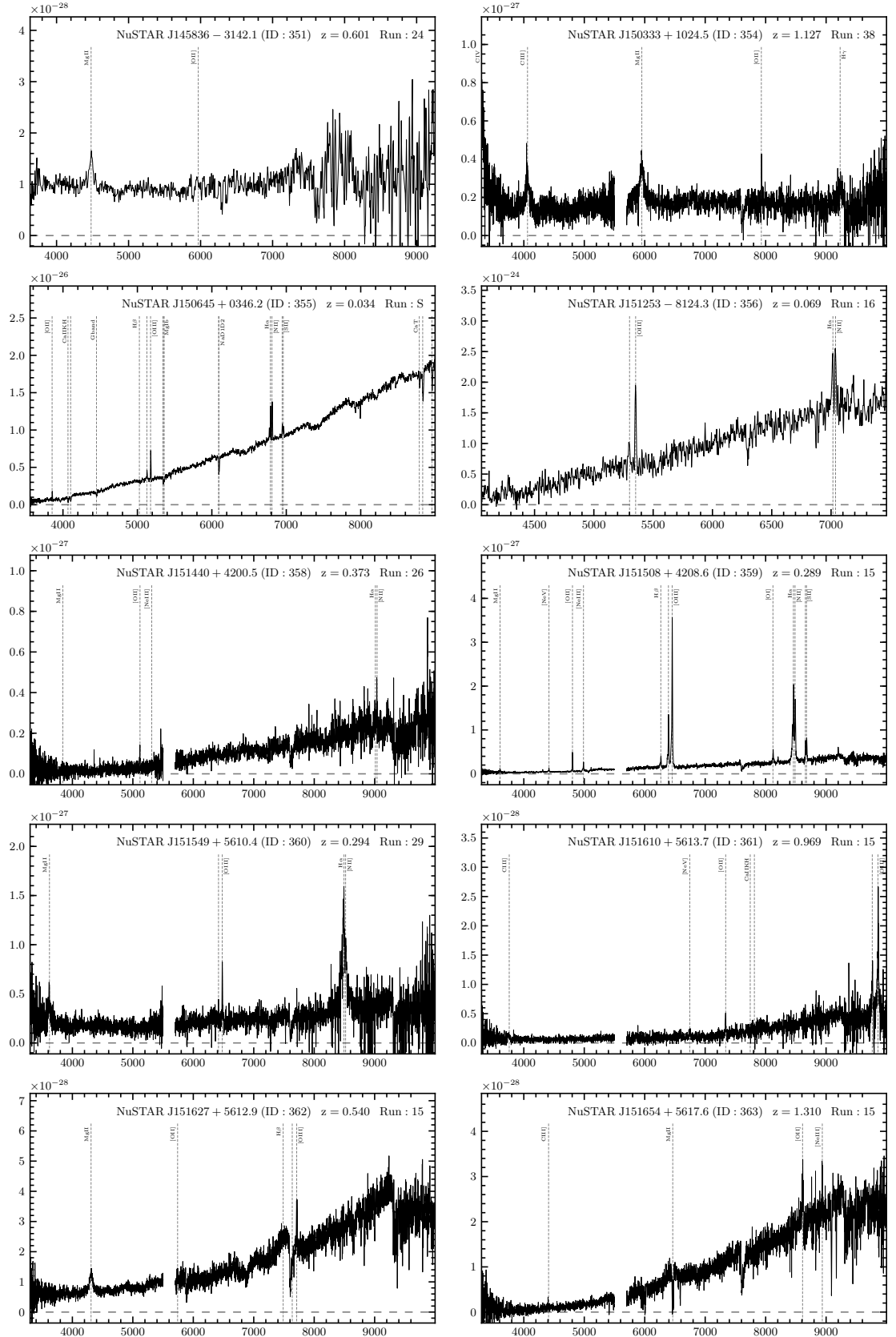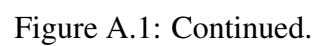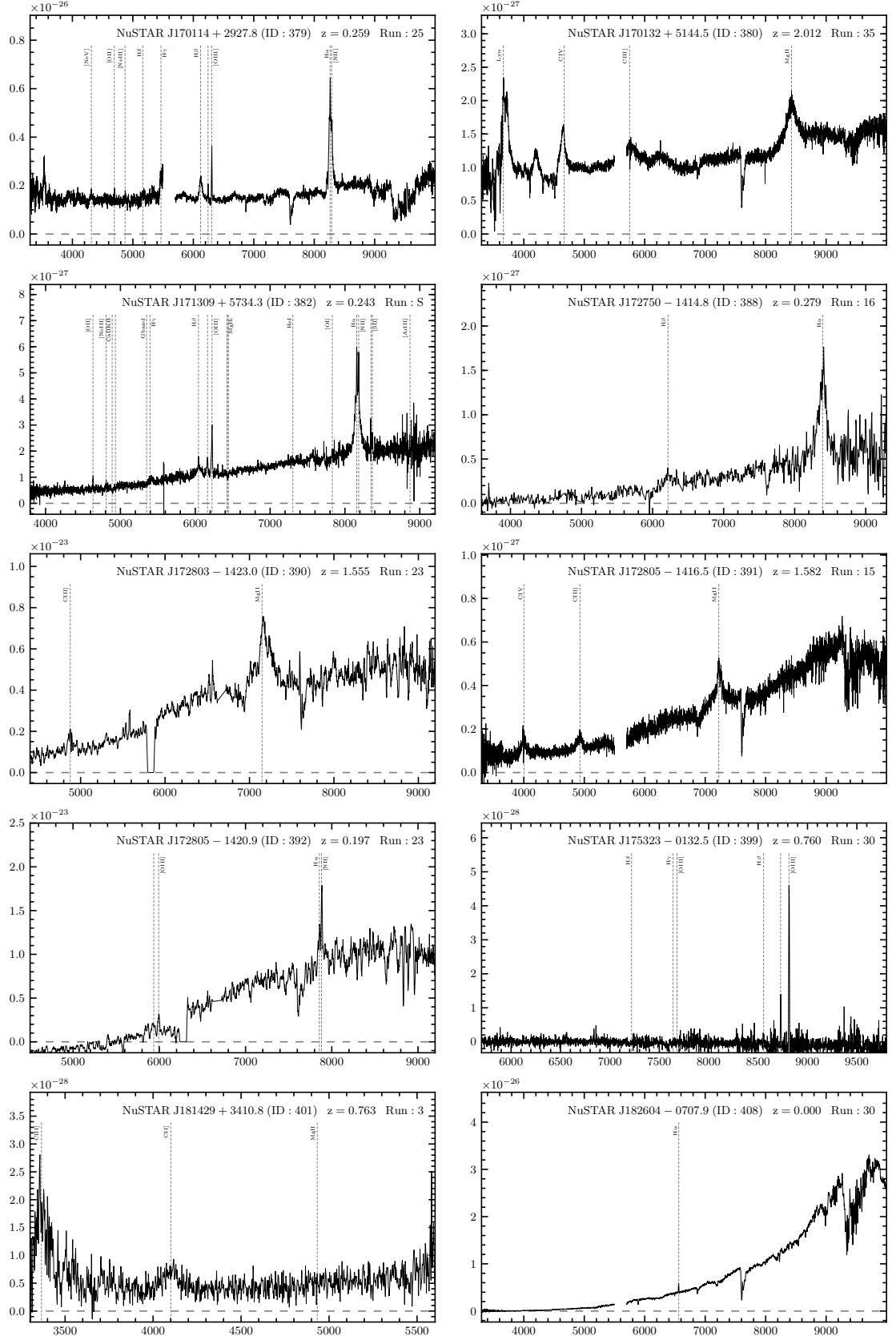
Figure A.1: Continued.
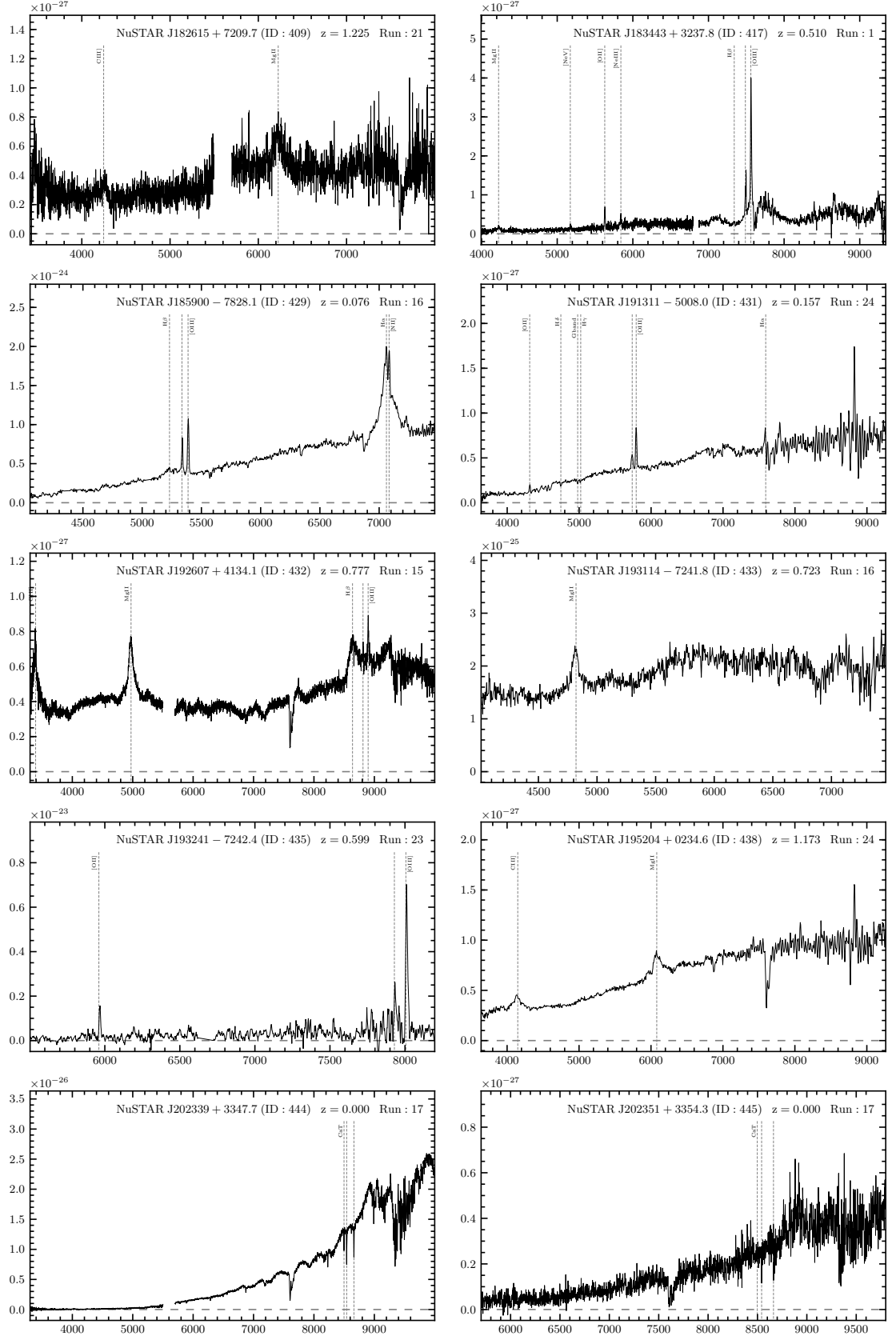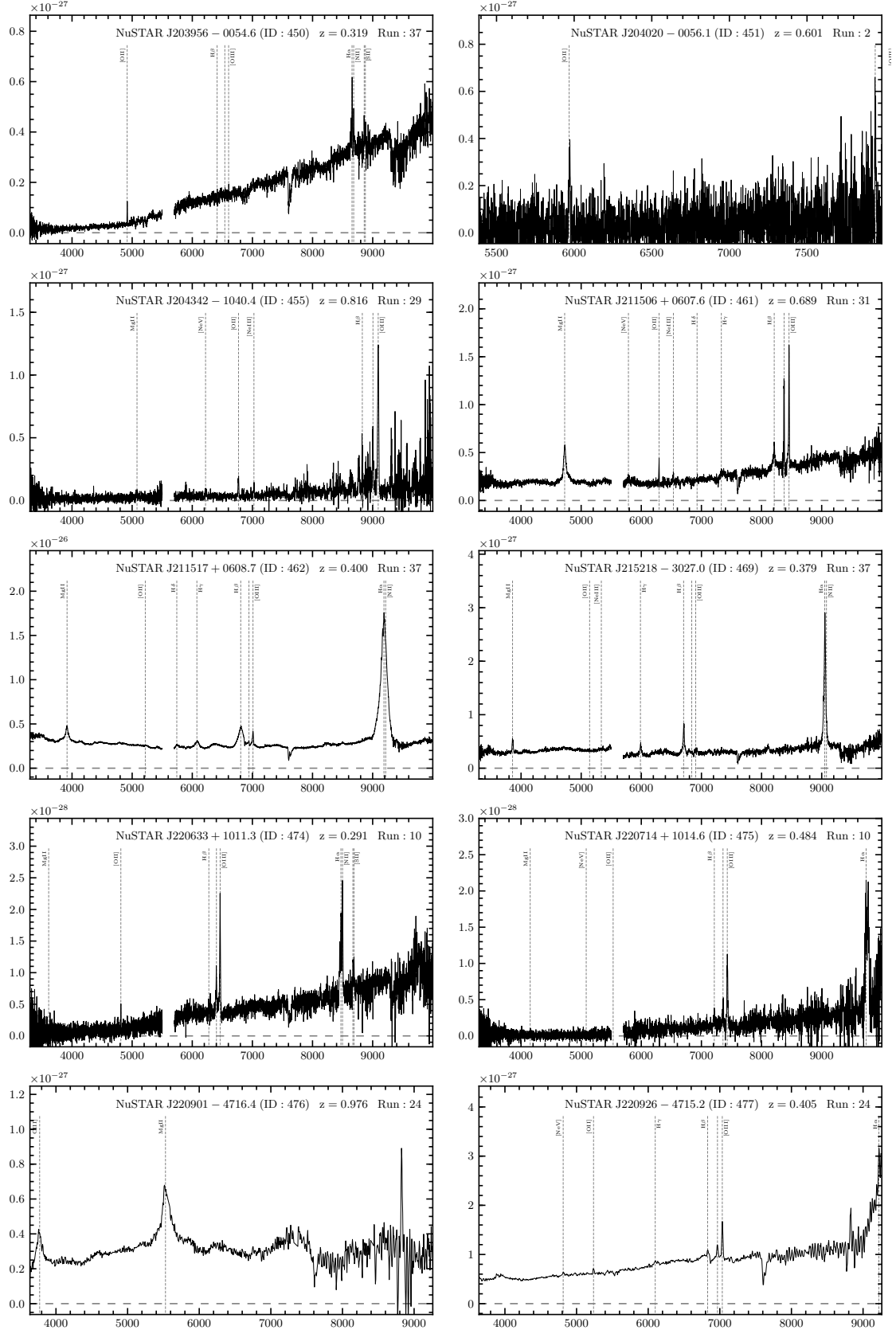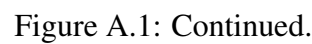
Figure A.1: Continued.

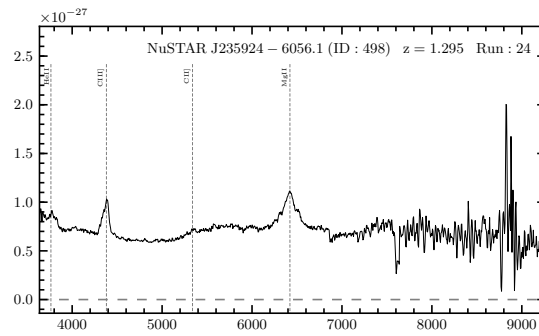Figure A.1: Continued.

Figure A.1: Continued.

Figure A.1: Continued.

A.3 Description of the Secondary Source Catalogue

Here we provide a secondary catalogue of 64 *NuSTAR* sources identified using an independent source detection approach. This independent (or "secondary") method uses `wavdetect` to search for significant emission peaks in the FPMA and FPMB data separately (see Section 2.1.1 of Alexander et al. 2013) and in the combined A+B data. The method was developed alongside the primary one (Section 5.2.3 of this chapter) in order to investigate the optimum source detection methodologies for *NuSTAR*, and to identify sources in regions of the *NuSTAR* coverage which are automatically excluded in the primary source detection. We emphasise that these secondary sources are not used in any of the science analyses presented in this chapter. The results in this work therefore correspond to a single, well-defined sample. Nevertheless, these secondary sources are robust *NuSTAR* detections, some of which will be incorporated in future *NuSTAR* studies (e.g., Chen et al., in prep.; Tomsick et al., in prep.), and many for which (33 out of the 41 sources with spectroscopic identifications) we have obtained new spectroscopic redshifts and classifications through our followup program.

The columns for the secondary source catalogue are summarized in Table A.3. The *NuSTAR* columns are equivalent to the primary catalogue columns described in Section A.1, with the exception that the count rates (columns 20–25) are aperture-corrected values. The photometric columns are blank where the A+B data prohibit reliable photometric constraints. The final column assigns a character to each source, indicating the reason for not being included in the primary catalogue. These are categorised into four groups: (E) the source is within or very close to the peripheral region of the *NuSTAR* mosaic, which is excluded from the primary source detection (33% of cases); (T) the source is narrowly offset from the central science target position for the *NuSTAR* observation (and thus automatically excluded; see Section 5.2.3), or from another bright source in the field (11%); (X) the source lies in a region which is masked out, or in a *NuSTAR* field which is excluded, from the primary source detection (44%; e.g., due to highly contaminating stray light or a bright science target); or (L) the source has a comparatively low detection significance (12%).

In Table A.4 we tabulate details of the optical spectroscopic properties of individual sources from the secondary catalogue with spectroscopic coverage. The columns are

Table A.3: Column Descriptions for the Secondary *NuSTAR* Serendipitous Source Catalogue

Column number	Description
1	Unique source identification number (ID).
2	Unique *NuSTAR* source name.
3, 4	Right ascension (R.A.) and declination (decl.).
5–16	Total, background, and net source counts for the three standard energy bands, and associated errors.
17–19	Net vignetting-corrected exposure times at the source position, for the combined A+B data.
20–25	Net source count rates for the three standard energy bands, and associated errors.
26–31	Fluxes in the three standard bands and associated errors.
32–34	Observatory name and coordinates (R.A. and decl.) for the lower-energy X-ray counterpart.
35–37	Reference and coordinates (R.A. and decl.) for the optical or *WISE* counterpart.
38	Spectroscopic redshift.
39	Non-absorption-corrected, rest-frame 10–40 keV luminosity.
40	Character indicating the reason for not appearing in the primary catalogue.

Notes. Machine readable versions of the full table are available online.

equivalent to those in Table A.2. For 77% of these sources the spectroscopic constraints are from our dedicated followup program (with Keck, Palomar, NTT, and Magellan), and 23% they are from the SDSS or the literature. Individual source spectra (F_ν versus λ) are shown in Figure A.2.
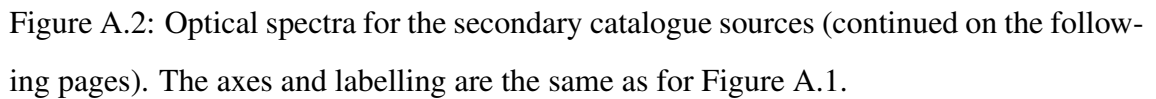
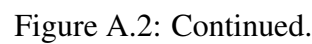Table A.4: Summary of the optical spectroscopy for the secondary catalogue sources.

ID (1)	NuSTAR Name (2)	z (3)	Type (4)	Lines (5)	Notes (6)	Run (7)
1	NuSTARJ001639+8139.8	0.000	Gal	...	Bright star	28
3	NuSTARJ001844-1022.6	0.076	NL	[O II] Ca$^\dagger_{H,K}$ G-band† H$\beta^\dagger$ Mg Ib† Na$^\dagger_{D1,D2}$ Hα [N II] [S II]	...	S
4	NuSTARJ011018-4612.1	...	...	...	Continuum detected	11
5	NuSTARJ011053-4602.6	0.626	NL	[O II] Hγ Hβ [O III]	...	18
6	NuSTARJ022801+3115.9	1.857	BL	Lyα C IV C III] Mg II	...	31
8	NuSTARJ023459-2944.6	0.446	BL	...	Caccianiga et al. (2008)	L
9	NuSTARJ031602-0221.0	0.821	NL	[O II] Hβ [O III]	...	31
10	NuSTARJ033313-3612.0	...	...	...	Two possible counterparts at $z \approx 1$; Wong et al. (2008)	L
11	NuSTARJ033342-3613.9	0.559	NL	[O II] Hβ [O III]	...	11
12	NuSTARJ033406-3603.9	0.910	BL	Mg II	...	11
13	NuSTARJ034403-4441.0	0.275	NL?	Ca$^\dagger_{H,K}$ G-band† [O III] Mg Ib† Na$^\dagger_{D1,D2}$ [O I] Hα [N II] [S II]	...	32
15	NuSTARJ043754-4716.0	0.337	NL	[O II] Hβ Hα [N II]	...	23
17	NuSTARJ081911+7046.6	0.720	NL	[O II] Hβ [O III]	[O III] asymmetry	13
18	NuSTARJ090223-4039.4	0.087	BL	Hβ [O III] [O I] Hα [N II]	...	11
20	NuSTARJ092418-3142.2	0.000	Gal	...	Continuum detected	22
21	NuSTARJ094734-3104.2	...	...	...	Continuum detected	24
22	NuSTARJ101600-3329.6	0.231	NL	[O II] [O III] Hα [N II]	...	22
27	NuSTARJ105008-5958.8	0.000	Gal	Hδ Hγ Hβ Na$^\dagger_{D1,D2}$ Hα	...	11
28	NuSTARJ110445+3811.1	0.144	NL	[O II] [Ne III] Ca$^\dagger_{H,K}$ H$\delta^\dagger$ H$\gamma^\dagger$ Hβ [O III] Mg Ib† Na$^\dagger_{D1,D2}$ [O I] Hα [N II]	...	S
30	NuSTARJ120259+4430.4	0.465	NL	[S II] Hβ [O III]	...	14
31	NuSTARJ120711+3348.4	0.135	BL	[O II] [Ne III] Ca$^\dagger_{H,K}$ Hγ Hβ [O III] Hα [N II]	...	S
33	NuSTARJ121027+3929.1	0.615	BL Lac	Ca$^\dagger_{H,K}$ H$\delta^\dagger$ G-band† H$\gamma^\dagger$ H$\beta^\dagger$ [O III] Mg Ib†	Morris et al. (1991)	S
34	NuSTARJ121038+3930.7	1.033	NL	C III] C II] [Ne IV] Mg II [Ne V] [O II] [Ne III] Hβ [O III]	...	15

Table A.4 – continued from previous page

ID	*NuSTAR* Name	z	Type	Lines	Notes	Run
35	NuSTARJ121049+3928.5	0.023	NL	[O II] Ca$^\dagger_{H,K}$ G-band† Hγ Hβ [O III] Mg 1b† Na$^\dagger_{D1,D2}$ [O I] Hα [N II]	...	S
36	NuSTARJ121854+2958.0	0.175	NL?	[O II] [Ne III] Hδ Hγ Hβ [O III] [O I] Hα [N II] [S II] [Ar III] [S II] CaT†	...	S
37	NuSTARJ123559-3951.9	0.000	Gal	...	Star	L
38	NuSTARJ125021+2635.9	0.751	BL	Mg II [Ne V] [O II] [Ne III] Hβ [O III]	...	27
39	NuSTARJ125605+5643.8	0.984	NL	Mg II [O II] [Ne III]	...	12
40	NuSTARJ125711+2748.1	0.306	NL	[O II] Ca$^\dagger_{H,K}$ [O III] Hα [N II]	...	15
41	NuSTARJ125715+2746.6	...	...	CaT†	Counterpart uncertainty	15
42	NuSTARJ125744+2751.2	0.325	NL	[O II] Ca$^\dagger_{H,K}$ [O III] Hα [N II]	...	15
43	NuSTARJ130157-6358.1	0.000	Gal	...	Krivonos et al. (2015)	L
45	NuSTARJ130616-4930.8	0.284	BL?	Hβ [O III] Hα [N II]	...	16
46	NuSTARJ134447+5554.0	0.458	BL?	Mg II Hβ [O III]	...	14
48	NuSTARJ143256-4419.3	0.119	NL	Ca$^\dagger_{H,K}$ G-band† H$\beta^\dagger$ Mg 1b† Na$^\dagger_{D1,D2}$	Cluster ABELL 3602	24
49	NuSTARJ155520-3315.1	0.551	NL	[O II] Hβ [O III]	...	23
50	NuSTARJ165050-0126.6	0.791	BL	Mg II Hβ	...	24
51	NuSTARJ165104-0127.2	0.852	NL	[Ne V] [O II] [Ne III] [O III]	...	30
52	NuSTARJ170016+7840.7	0.778	BL	Mg II [O II] [O III]	...	9
53	NuSTARJ172822-1421.4	0.688	NL	[O II] Hγ Hβ [O III]	...	23
55	NuSTARJ175307-0123.7	0.451	NL?	[O II] [Ne III] Hβ [O III]	...	24
56	NuSTARJ181417+3411.6	0.714	BL	Mg II [Ne V] [O II] Hβ [O III]	...	30
63	NuSTARJ223654+3423.4	0.148	NL	[O II] [O III] Hα [N II]	...	31
64	NuSTARJ224037+0802.6	1.418	BL	C IV C III] Mg II [O II]	...	30

Figure A.2: Optical spectra for the secondary catalogue sources (continued on the following pages). The axes and labelling are the same as for Figure A.1.

Figure A.2: Continued.

Figure A.2: Continued.